Modelling of directional thermal radiation and angular correction on land surface temperature from space

Huazhong Ren

To cite this version:

Huazhong Ren. Modelling of directional thermal radiation and angular correction on land surface temperature from space. Other. Université de Strasbourg; Beijing Normal University, 2013. English. NNT : 2013STRAD014 . tel-00967047

HAL Id: tel-00967047
https://theses.hal.science/tel-00967047

Submitted on 27 Mar 2014

N° d'ordre:

École Doctorale Mathématiques, Sciences de l'Information et de l'Ingénieur

UdS – INSA – ENGEES

THÈSE

présentée pour obtenir le grade de

Docteur de l'Université de Strasbourg
Discipline: Electronique
Spécialité: Télédétection

par

Huazhong REN

Modelling of directional thermal radiation and angular correction on land surface temperature from space

Soutenue publiquement le 24 Mai 2013

Membres du jury

Directeur de thèse: **Mme Françoise Nerry, Directeur de recherches CNRS**
Co-Directeur de thèse: **M. Guangjian Yan, Professeur de BNU**
Rapporteur externe: M. Alain Royer, Professeur des Université, Sherbrooke
Rapporteur externe: **M. Liangfu Chen, Directeur de recherches RADI**
Examinateur: **M. Zhao-Liang Li, Directeur de recherches CNRS**
Examinateur: **M. Qinhuo Liu, Directeur de recherches RADI**

ICube **UMR7357**

Acknowledgements

As a joint student, I would like to express my sincere gratitude to my supervisors, Dr. Guangjian Yan of Beijing Normal University in China, and Dr. Françoise Nerry of Université de Strasbourg in France, for their constructive criticism and encouragement in my PhD thesis, and also for their agreement of the joint supervision of my doctoral thesis.

I appreciate Dr. Zhao-Liang Li of Université de Strasbourg for his help in my application of the Ph.D candidate, and his valuable comments and instructions. His profound knowledge in the thermal infrared field inspires me with confidence in my study. I am thankful to Dr. Qiang Liu and his colleagues of the Institute of Remote Sensing and Digital Earth, Chinese Academy of Sciences, for their collection and processing of airborne multi-angular images.

I would like to thank the members of my thesis committee for their encouragements and insightful comments.

My sincere thanks also go to Drs. Wuming Zhang, Donghui Xie, Xihan Mu, Jindi Wang, Shunlin Liang and Suhong Liu of Beijing Normal University for their details discussion of my thesis, and to my colleagues in Beijing Normal University: Ling Chen, Jie Zhou, Tianxing Wang, Jie Cheng, Xiaodong Mu, Jing Li, Yingjie Yu, Haoxing Wang, Zhen Zhu, Jing Zhao, Yaokai Liu, Ronghai Hu, Kai Yan, Shuai Huang, Xia Meng and Yiming Chen, and to the colleagues in Université de Strasbourg: Sibo Duan, Jing Lu, Yuan Liu, Shi Qiu, Xiwei Fan, Pei Leng, Hongyuan Huo, Caixia Gao, Guoliang Luo, Nicolas Albalat, Jérôme Colin, Raphaël Luhahe and Jelila Labed. Thanks for their help in my study and daily life. I really cherish the happy time spent with them.

Special thanks are given to my wife Rongyuan Liu for her unselfish support. Her coming to my world makes my life more pleasant and exciting. Sincere thanks are also given to my parents for their giving birth to me, supporting my life and education all the time, and to my parents-in-law for their supports and encouragements, and to my relatives. I do not let them be disappointed.

It is difficult for me to quote everyone here. I simply make a point of saying that I appreciate everyone who helped me in the past.

This thesis was financed by the National Basic Research Program of China (973 Program), the National High-Tech Research and Development Program (863 Program), the National Natural Science Foundation of China, the European Commission (Call FP7-ENV-2007-1 Grant no. 212921) as part of the CEOP-AEGIS project, and the China Scholarship Council project.

Contents

Résumé

Dans les dernières décennies, les études des bilans d'énergie à la surface, de l’aménagement des bassins versants, des processus biophysiques et des catastrophes naturelles ont attiré l’intérêt des communautés scientifiques. Le succès de telles études exige une importante base de données sur l'état de surface de la terre, de l’océan, de l’atmosphère et même des activités humaines. La télédétection permet les observations à long terme et à faible coût et nous fournit un moyen prometteur pour obtenir ces données au niveau régional et global. Avec les données de télédétection provenant soit de plates-formes aéroportées soit de systèmes spatiaux, les scientifiques ont proposé une variété d’algorithmes pour obtenir différents types de paramètres de surface de la terre et de son atmosphère et ces paramètres ont été utilisés dans de nombreux domaines pertinents.

La température de surface de la terre (LST) est l'un des paramètres les plus importants intervenant dans les bilans énergétiques et hydrologiques de l’échelle locale à l’échelle globale. La connaissance de la LST fournit des informations sur les variations temporelles et spatiales de l'état d'équilibre de la surface et est d'une importance fondamentale dans de nombreuses applications. Par conséquent, la LST est largement utilisée dans de nombreux domaines, y compris l'évapotranspiration, le changement climatique, le cycle hydrologique, la surveillance de la végétation, le climat urbain et les études environnementales, entre autres. Elle et a été reconnue comme l'un des paramètres prioritaires du programme International Geosphere and Biosphere Program (IGBP), l'un des plus importants du Earth System Data Records (ESDR) identifié par la NASA (http://lst.jpl.nasa.gov/background) et un des produits justificatifs pour les variables climatiques de l'ESA (http://tinyurl.com/globtemperature).

La détermination de la LST par télédétection thermique infrarouge TIR a attiré beaucoup d'attention et son histoire remonte aux années 1970. Cependant, l'estimation directe de la LST n'est pas une tâche facile, et il faut tout d’abord déterminer l'émissivité et les effets atmosphériques, car les radiances mesurées par les radiomètres dépendent non seulement des paramètres de surface (température et émissivité) mais également de l’atmosphère. L'émissivité, définie comme le rapport entre le rayonnement émis par les cibles naturelles au rayonnement émis par un corps noir à la même température, varie selon les types de surface terrestre et structure, la longueur d'onde, la texture du sol, l'humidité et l’angle de vue. Le couplage de l'émissivité avec la LST fait que la détermination de la LST est mathématiquement insoluble: pour un capteur à N canaux infrarouges, on a N mesures pour N + 1 inconnues (N émissivités canal et 1 température). Pour résoudre ce problème sous déterminé, une contrainte supplémentaire est par conséquent nécessaire. En outre, le rayonnement émis par la surface est tout d'abord contaminé par la radiance atmosphérique réfléchie et est ensuite atténué par l'atmosphère sur le trajet de la surface vers le satellite. La correction des effets atmosphériques nécessite une connaissance précise des profils verticaux de vapeur d'eau atmosphérique et de température qui sont très variables.

Fondées sur la théorie du transfert radiatif dans le TIR, diverses méthodes ont été développées pour obtenir la LST à partir des données de télédétection avec un moyen

permettant de supprimer les effets de l'émissivité et de l’atmosphère. Par exemple peut être citée la méthode qui consiste à déterminer l’émissivité à partir d’une relation linéaire empirique avec des données du domaine visible/proche-infrarouge ou encore la méthode basée sur la classification. Les deux méthodes suivantes peuvent permettre d’obtenir la LST depuis l'espace: la première est l'algorithme de canal unique qui utilise un seul canal TIR, tel que celui du capteur Thematic Mapper du canal 6 (TM6); la deuxième méthode est l'algorithme de Split-Window qui supprime l'effet atmosphérique à l'aide de l'absorption atmosphérique différentielle dans deux canaux adjacents centrés à 11 et 12 µm et qui applique ensuite une combinaison linéaire (ou non) des températures de brillance des deux canaux adjacents. Car ils ne nécessitent pas d'informations précises sur les profils atmosphériques au moment de l'acquisition, de nombreux algorithmes de Split-Window ont été développés et modifiés pour extraire avec un certain succès les LST de plusieurs capteurs comme AVHRR, MODIS et SEVIRI. En revanche, pour le cas de l'émissivité, plusieurs méthodes ont été conçues pour obtenir à la fois les LST et émissivités à partir de données multi canaux et/ou multi temporelles. Par exemple citons la méthode des indices spectraux indépendants de la température (TISI) : une paire d’image de jour et de nuit dans les domaines thermiques MIR et TIR donne accès à l’émissivité dans ces deux canaux lesquelles permettent de calculer la LST directement par inversion de la Loi de Planck ou l'algorithme de Split-Window mentionné ci-dessus. De même, la méthode deux températures (TTM) dissocie les deux paramètres d'après des observations de deux canaux TIR de jour et de nuit en supposant les émissivités invariantes au cours de ces deux observations. En outre, si le nombre de canaux MIR et de TIR est suffisant (au moins sept), l'algorithme physique de jour/nuit peut être combiné pour obtenir les LST et les émissivités ainsi que d'autres paramètres. De plus, la LST et les émissivités peuvent être également obtenues à partir des données TIR multi canaux corrigées de l'atmosphère en utilisant la relation entre les émissivités des différents canaux, telle que la méthode de séparation de température/émissivité (TES) principalement conçue pour les cinq canaux TIR de ASTER et récemment étendue aux trois canaux TIR de MODIS. Avec l'apparition des capteurs hyperspectraux TIR (IASI, par exemple), des milliers de canaux de bande passante étroite peuvent fournir suffisamment de résolution verticale pour permettre l'extraction d'information atmosphérique et peuvent également fournir des contraintes physiques supplémentaires pour séparer avec précision la LST de l'émissivité.

Un ensemble d’hypothèses soustend ces algorithmes : la surface est considérée comme homogène et isotherme et la température de surface est indépendante du canal et de l’angle. Cette hypothèse est raisonnable, car elle permet de réduire le nombre d'inconnues. Cependant, en pratique, la LST varie avec l'angle zénithal (VZA). Cette variation angulaire pour surfaces tridimensionnelles résulte principalement de la variation angulaire de l'émissivité des pixels et du poids relatif des différents composants (par exemple, végétation et sol), qui ont des températures différentes dans un pixel non isotherme. En effet, la différence de la LST mesurée au nadir et hors-nadir peut être supérieure à 5 K pour les sols nus et même 10 K pour les zones urbaines. Pour la plupart des satellites sur orbite polaire (MODIS, AVHRR) qui analysent la terre dans le sens transversal à la trajectoire avec différents VZA variant de -65º à +65º, les variations angulaires de la LST sont inévitables, rendant les LST des différents pixels dans la même image incomparables et causant des résultats erronés dans leur utilisation. Cet effet angulaire se produit également avec les satellites géostationnaires comme SEVIRI

MSG et entre les LST obtenues avec différents capteurs ou à des moments différents. Il est donc crucial d'examiner cet effet sur la LST.

Une méthode pour prendre en compte l'effet angulaire sur la LST consiste à simplement attribuer la variation angulaire de la température apparente mesurée au comportement directionnel de l'émissivité du pixel. Toutefois, comme il est difficile d'obtenir l'émissivité directionnelle des surfaces naturelles à l'échelle du pixel, cette technique s’avère toujours inutilisable. Une autre technique consiste à séparer les températures des composants ou leur rapport des données multi-angulaires TIR (ATSR et AATSR) et de calculer la température effective dans une direction spécifique (par exemple au nadir) en pondérant les températures des composants avec leurs fractions correspondantes. De cette façon, la fraction des différents composants observés sous un angle spécifique peut être calculée à l'aide du modèle de la fonction de distribution des réflectances bidirectionnelles (BRDF) mesurée dans le visible et le proche infrarouge. Cette méthode peut être une voie prometteuse, mais cependant l'exigence d'observation multi-angulaire ne peut pas être satisfaite pour la plupart des capteurs TIR et la précision est loin d'être satisfaisante. Il n'y a donc encore à l’heure actuelle aucun moyen pratique pour effectuer une normalisation angulaire des LST satellitaires en raison de la complexité de cette question.

Basée sur l'état d'avancement de l'étude sur la détermination des LST et des émissivités, cette thèse est axée sur l'anisotropie du rayonnement thermique à l'aide de méthodes empiriques et physiques. Elle est divisée en sept chapitres.

Dans le chapitre 1 nous avons donné en introduction la motivation de ce travail de thèse après une brève discussion sur l'état de l’art et la nécessité d'étudier l'anisotropie de l'émission thermique de surface.

Le chapitre 2 présente les détails de l'état actuel sur la détermination des LST et des émissivités depuis l'espace. Ce chapitre débute par la description de la radiance mesurée par un capteur au sommet de l'atmosphère et des contributions de l'atmosphère en émission ainsi que le rayonnement solaire réfléchi sur la base de l'équation de transfert radiatif thermique. Ensuite, plusieurs définitions de l'émissivité pour des surfaces mixtes composées de plusieurs constituants sont données : ***r***-émissivité, ***e***-émissivité et émissivité apparente. Cependant, cette thèse utilisera exclusivement le concept de la ***r***-émissivité car seul ce type d'émissivité est accessible à partir des données satellitaires et l'émissivité est considérée comme la caractéristique intrinsèque de la surface et ne varie pas avec la température de la surface comme c’est la cas pour le concept de l'émissivité apparente. De plus, plusieurs bases de données d’émissivité dont la bibliothèque spectrale ASTER et la bibliothèque de l'Université de Californie à Santa Barbara (UCSB) ont également été présentées dans ce chapitre ; la variation spectrale de la végétation et des échantillons de sol est abordée.

Quant à l'effet atmosphérique sur le rayonnement thermique, nous donnons une brève description du modèle de transfert radiatif atmosphérique communément utilisé MODTRAN pour les capteurs de résolution modérée et le code de 4A/OP pour les capteurs hyper ou super spectraux. Nous présentons diverses ressources de données atmosphériques (p. ex. base de données initiale thermodynamique (TIGR)), le sondeur vertical à bord (MODIS) ou les prévisions météorologiques, comme le National Center for Environmental Prediction (NCEP) et le European Center for Medium-Range Weather Forecasts (ECMWF).

Les méthodes de détermination de la LST depuis l'espace sont examinées en fonction du statut de l'émissivité et des données atmosphériques. Avec une émissivité connue qui peut être calculée à partir soit de relations empiriques avec des données VNIR, soit de la méthode de la classification ou de la combinaison de jour et nuit d'observations dans les canaux de MIR et de TIR à l'aide de la méthode TISI, la méthode mono-canal et les algorithmes de Split-Window sont décrits ainsi que leurs avantages et leurs inconvénients et les conditions préalables à leurs applications.

L'algorithme Split-Window a été discuté en fonction des angles, de la colonne de vapeur d'eau et des effets dus à l'émissivité. Si l'émissivité est inconnue mais les données atmosphériques définies, les méthodes qui permettent d'extraire la LST et l'émissivité simultanément sont décrites, y compris la méthode TES proposée pour ASTER, la méthode corps gris conçue pour plusieurs canaux TIR avec la même émissivité pour au moins deux des canaux, la méthode TTM développée pour les données TIR observées à deux moments différents et l'algorithme physique jour/nuit (D/N) utilisé pour les sept canaux MODIS dans le MIR et le TIR. La comparaison croisée entre les méthodes TTM et D/N est aussi présentée. Pour les cas d'émissivité et de données atmosphériques non connues, les méthodes qui donnent accès simultanément à la LST, l'émissivité et certains paramètres atmosphériques sont exposées également. Toutefois, peu de littérature existe à ce sujet et uniquement des rapports ont été étudiés. Ce chapitre présente également les algorithmes qui permettent d'extraire la LST (et l'émissivité) à partir de données TIR hyperspectrales et micro-ondes.

Enfin, nous avons examiné les méthodes actuelles pour la modélisation et le paramétrage du rayonnement thermique directionnel et de l'émissivité pour les milieux homogènes et hétérogènes et pour le pixel satellitaire. Ces méthodes ont été divisées en quatre catégories : les modèles géométriques optiques (GO), les modèles de transfert radiatif (RT), les modèles hybrides (GORT) et les méthodes de simulation numérique. De plus, les moyens d'obtenir la température des composants provenant de données multi-angulaires ou de plusieurs données TIR sont présentés. Cette partie est importante pour la thèse car elle a fourni l'inspiration originale pour notre étude sur le rayonnement thermique et l'émissivité directionnelles en utilisant les modèles à noyaux BRDF et les méthodes de fréquence d'intervalle.

Dans le chapitre 3, on extrait, pour la première fois, les émissivités directionnelles de plusieurs couvertures naturelles à l'échelle du pixel à partir des produits d'émissivité MODIS qui utilisent l'algorithme jour/nuit. D'après la littérature, de nombreuses études se sont attaquées à ce thème mais concernent essentiellement des mesures au sol ou des simulations mathématiques mais rarement des études au niveau du pixel par un manque de données. L'algorithme jour/nuit qui permet de séparer la température et l'émissivité ainsi que certains paramètres atmosphériques (colonne de vapeur d'eau, température de l'air) en utilisant un couple de données MODIS jour et nuit dans les canaux de MIR (CH20: 3,66 ~ 3,84 µm, CH22 : 3,93 ~ 3,99 µm, CH23: 4,02 ~ 4,08 µm) et canaux TIR (CH29: 8,4 ~ 8,7 µm, CH31: 10,78 ~ 11,28 µm, CH32: 11,77 ~ 12,27 µm, CH33: 13,19 ~ 14,49 µm) a généré des produits LST et d'émissivité globales à 5 ou 6 km sur plus de dix ans. Puisque l'angle zénithal de MODIS peut aller jusqu'à 65°, le produit émissivité nous a fourni l'occasion d'examiner les effets directionnels. En outre, MODIS fournis chaque année des produits de couverture de surface (collection 4) à 1 km et la classification de l'IGBP (total de 17 types de couvert) a été utilisée pour exploiter des informations de classification. Une méthode de diagnostic à huit-connectivité a été appliquée pour assurer la correspondance spatiale de l'émissivité et des produits de couverture de surface.

Des résultats statistiques sur 5 années d'émissivité et de produits couverture de surface sur la majeure partie de l'Asie ont montré que l'émissivité de plusieurs couvertures naturelles (prairies, terres labourables, forêt d'arbres à feuilles caduques ou persistantes, forêt mixte, arbustes ouverts et zones arides) augmente dans les canaux MIR, mais diminue dans les canaux TIR avec l'augmentation de l'angle de zénithal et que l'émissivité directionnelle varie de l'ordre de 0,01 ~ 0,02 du nadir à 65°. Cependant, cette variation peut être ignorée pour les angles zénithaux inférieurs à 45°. Le comportement de l'émissivité directionnelle à l'échelle du pixel TIR est comparable à celui obtenu par des études antérieures à l'échelle de la canopée, mais cela est difficile à vérifier pour les canaux MIR car aucune littérature sur l'anisotropie de l'émissivité n'existe dans ce domaine de longueur d'onde.

L'émissivité directionnelle obtenue a été appliquée à l'algorithme Split-Window pour extraire la LST à la résolution de 1 km des données MODIS. En comparant cette LST avec les produits MODIS LST originaux, il a été constaté que cette LST est généralement plus élevée que celle d'origine et que la différence varie entre -1 K à 3 K. Les grands angles de vue entrainent les différences les plus importantes. Enfin, dans ce chapitre nous avons également examiné les effets d'échelle spatiale entre la LST à 1 km et 5 km. Les résultats montrent que l'on peut ignorer ces effets dans notre étude probablement du fait qu'il n'y n'a presque aucun effet d'échelle inclus dans l'algorithme Split-Window. En outre, deux lookup tables d'émissivité directionnelle ont été créées pour une perspective à venir.

Le chapitre 4 vise à la paramétrisation physique de l'émissivité directionnelle et du rayonnement thermique d'une canopée homogène. On utilise le modèle SAIL thermique (diffusion par feuilles arbitrairement inclinées; ci-après appelé TIR-SAIL) qui a été étendu du VNIR à l'infrarouge thermique pour simuler l'émissivité directionnelle de la canopée. Il a été utilisé avec deux grands types de méthodes pour effectuer le paramétrage de l'émissivité directionnelle avec des caractéristiques géométriques et de surface connues: tout d'abord, l'émissivité directionnelle est obtenue à partir du complémentaire à la réflectivité hémisphérique bidirectionnelle conformément à la Loi de Kirchhoff. La réflectivité hémisphérique directionnelle peut être intégrée à partir du modèle BRDF dans le demi hémisphère. Deux modèles BRDF ont été utilisés: le modèle BRDF à noyaux (ci-après appelé K-BRDF) et le modèle BRDF semi-empirique (ci-après appelé S-BRDF). Les réflectivités bidirectionnelle proviennent du modèle SAILH, découlant du modèle SAIL mais incorporant les effets de hotspot. Deuxièmement, l'émissivité directionnelle est estimée directement par une pondération des émissivités des composants et des fractions, observées dans une direction d'observation particulière. Les fractions sont toujours estimées à partir de la théorie de fréquence d'intervalle et nous avons utilisé deux des méthodes de François et al, celles élaborées en 1997 et 2002, ci-après appelés FRA97 et FRA02 respectivement.

Les résultats de la comparaison ont montré que les modèles K-BRDF et S-BRDF sont en très bon accord avec l'émissivité directionnelle du modèle SAIL-TIR pour les végétations éparses à moyennement dense mais cet accord se dégrade avec l'augmentation du LAI. Bien que les deux modèles aient une erreur relative plus élevée pour la canopée dense, cette erreur peut être ignorée, en particulier pour le modèle K-BRDF. En général, les deux modèles BRDF ont presque une différence minime pour l'émissivité directionnelle. Cependant, les résultats ont montré le paramètre ***k*** dans le S-BRDF qui devrait se situer entre 0 et 1 est supérieur à 1, ce qui réduit la signification physique du modèle S-BRDF. Par conséquent, le modèle S-BRDF n'est pas recommandé, au moins pour la réflectivité bidirectionnelle et l'émissivité directionnelle. De plus, dix échantillons de végétation et dix-sept échantillons de sol ont été choisis dans la bibliothèque des émissivités pour contrôler les relations entre les coefficients du modèle à trois noyaux K-BRDF, et il a été constaté que ces coefficients sont linéaires et reliés entre eux, surtout pour les LAI faibles. Ainsi si l'un des trois coefficients peut être obtenu, les deux autres seront par conséquent déterminés par des relations linéaires. Cependant, cette relation linéaire disparaît pour la canopée avec végétation dense (LAI = 4.0). Les plages de valeurs des coefficients ont aussi été obtenus et seront utilisés comme connaissance préalable dans le chapitre 5. Les résultats de la comparaison des FRA97 et des FRA02 avec le modèle de SAIL-TIR ont montré que l'émissivité directionnelle de FRA97 était plus proche du modèle SAIL-TIR mais que l'effet de cavité tenant compte des diffusions multiples doit être mis à jour selon le modèle SAIL-TIR.

Dans ce chapitre, la température de brillance directionnelle (DBT) a été modélisée en pondérant les composantes des températures (feuilles et sol ensoleillé et ombragé) et leurs fractions estimées en utilisant un modèle paramétré de SAIL-TIR. Le nouvel effet de cavité décrit plus haut a été utilisé pour simuler la contribution de diffusion multiple à la DBT. De plus, le modèle K-BRDF a été modifié en remplaçant la réflectivité bidirectionnelle par le DBT du modèle d'origine, lequel a été utilisé pour ajuster le DBT dans l'hémisphère supérieur. Les résultats ont montré que le modèle K-BRDF peut très bien représenter la DBT hémisphérique avec une erreur inférieure à 0,5 K. Toutefois, étant donné que la même cible ne peut être observée que dans un certain nombre de directions, il est nécessaire de trouver le groupe local et même global d'observations angulaires optimales qui permet au modèle K-BRDF d'avoir une erreur minimale. Deux méthodes différentes ont été appliquées : le modèle monopoint et le modèle rangée linéaire. Le modèle monopoint propose certains critères pour le candidat du groupe observation angulaire optimale et finit par trouver que le groupes (0°, 0°), (0°, 30°), (180°, 50°) est l'optimum local pour le modèle K-BRDF trois angles. Basé sur ce résultat, nous avons étendu le modèle à trois rangées linéaires (nadir, plan avant et plan arrière) et discuté de l'influence de l'angle zénithal sur le résultat du modèle K-BRDF. Les résultats ont montré que l'angle zénithal dans le groupe nadir ne doit pas dépasser 45° pour s'assurer d'une erreur inférieure à 1,0 K.

Le chapitre 5 est consacré à la normalisation angulaire de l'émissivité et de la température de surface de la Terre à partir d’images multi-angulaires MIR et TIR. Dans ce chapitre, on propose une méthode TISI diurne (ci-après appelée D-TISI) pour extraire l'émissivité directionnelle et la température effective en combinant le modèle K-BRDF et la méthode TISI. Dans la méthode D-TISI, la surface ést considérée comme non isothermique et les TISIE des canaux MIR et TIR sont supposés indépendants des angles. Par conséquent, l’extraction de l'émissivité et de la température conduit alors à quatre inconnues : les coefficients de trois noyaux et le TISIE. Si une cible est observée dans plus de quatre directions, ces inconnues peuvent être obtenues par les équations de transfert radiatif, et ensuite basée sur la Loi de Kirchhoff, l'émissivité MIR est calculée comme 1- réflectivité directionnelle hémisphérique qui a été estimée à partir de l'intégration du modèle K-BRDF sur l'hémisphère. Enfin l'émissivité TIR est par conséquent déduite de l'émissivité MIR et du TISIE. Deux groupes de canaux MIR et TIR du capteur MODIS avec des bandes spectrales étroites et le système WiDAS (Wide-angle infrared Dual-mode line/area Array Scanner) avec une bande large ont été utilisés pour étudier l'influence de la largeur de la bande sur l'exactitude de la restitution. Le système WiDAS a été l'un des principaux capteurs aéroportés lors de la campagne de terrain et a fourni sept observations angulaires avec des caméras MIR et de TIR. Quatre groupes de combinaisons angulaires ont servi à trouver les combinaisons optimales angulaires locales pour l’extraction de l'émissivité et de la température, et six cas de températures des composants ont été appliqués pour illustration.

L’analyse de sensibilité du modèle montre que la nouvelle méthode permet d’obtenir une émissivité directionnelle et une température avec une erreur inférieure à 0,015 et 2,0 K respectivement si le bruit de la température mesurée et des données atmosphériques ne dépassent pas 1,0 K et 10 %, respectivement. On a également constaté que l'erreur sur la détermination de l'émissivité TIR diminue d'abord puis augmente avec les LAI croissants. Des grands intervalles d’angle parmi les observations angulaires et un plus grand VZA par rapport au nadir peuvent améliorer la précision de la restitution de l'émissivité et de la température, parce que ces conditions entrainent des variations significatives des composants des fractions et de la température directionnelle sous différentes directions d'observation, et des canaux étroits peuvent conduire à de meilleurs résultats que les larges. De plus, les résultats analytiques de six groupes de températures des composants ont montré qu'au même niveau de différence de température du composant, le cas avec une température de brillance relative plus faible peut conduire à un meilleur résultat pour l'émissivité dans le canal TIR ainsi que la réflectivité bidirectionnelle et l'émissivité dans le canal MIR. Cependant, cela dépend toujours des situations spécifiques, y compris des conditions atmosphériques et des structures de la canopée.

La méthode proposée de D-TISI a été appliquée sur les images multi-angulaire acquises par le système de WiDAS dans la campagne de terrain du printemps à l'été 2008 sur le versant de la rivière de Heihe dans l'ouest de la Chine, pour extraire les TISIE, les émissivités directionnelles MIR et TIR ainsi que la température dans la zone d'étude. Les résultats ont montré que les TISIE sont distribués principalement dans la gamme de [0,95, 1,01] comparables à d’autres résultats antérieurs et sont généralement plus forts pour les pixels avec végétation que sur des sols nus et des bâtiments, car le composant de la végétation dans le pixel augmente la valeur du TISIE. Les émissivités MIR et TIR se situent principalement dans les fenêtres [0,88, 0,94] et [0.96, 0,98], respectivement. La différence d'émissivité MIR entre des pixels avec et sans végétation est supérieure à celle dans le TIR. La température effective directionnelle a été calculée à partir de l'inversion de l'équation de transfert radiatif dans le canal TIR en utilisant l'émissivité directionnelle obtenue et les données atmosphériques connues. Elle a été normalisée à une température nadir en utilisant le modèle K-BRDF modifié. Il a été constaté que la température effective au nadir était généralement supérieure à celle dans les directions hors-nadir, et leurs différences pour les pixels sans végétation sont plus élevées que pour les pixels avec végétation. Il est donc nécessaire pour les pixels sans végétation d'effectuer cette normalisation angulaire. En outre, la comparaison des produits émissivité ASTER et l'émissivité TIR retrouvée illustre que cette dernière émissivité est supérieure aux produit ASTER avec un RMSE de 0,012. Ceci est probablement dû à la variation spatio-temporelle et spectrale de l'émissivité.

Le chapitre 6 est axé la détermination des incertitudes dans la mesure terrain du TBD dans le cas des rangées de culture et analyse l'impact de l'empreinte du capteur. La modélisation DBT pour les rangées de culture a été plus difficile que pour la canopée homogène en raison de l'effet de rangée qui a causé la variation de la densité de volume du de feuillage (FAVD) et de la longueur optique d'un endroit à l'autre. Une hypothèse cruciale dans les modèles actuels est que la rangée a une extension infinie. Par conséquent, les modèles traitent les fractions des composants à l'aide d'une structure de ligne entière. Cette hypothèse est raisonnable, mais l'hypothèse que la direction d'observation est un faisceau parallèle est rarement conforme à la réalité car les différentes régions à l'intérieur de l'empreinte du champ de vue du capteur (FOV) qui a permis de recueillir des données de terrain DBT ont des azimuts et zéniths différents. Dans ce chapitre, on a mis au point un nouveau modèle de transfert radiatif (FovMod) pour simuler la DBT du feuillage en rang en tenant compte de l'empreinte du capteur dans les mesures au sol. Le FovMod tout d'abord divise l'empreinte circulaire ou elliptique du capteur en petites cellules et ensuite estime des fractions des composants (p. ex., feuilles baignées de soleil et le sol, sol ombragé) dans chaque cellule basée sur la théorie de probabilité d'écart. La DBT de la canopée est finalement obtenue en pondérant les températures de brillance des composants et de leurs fractions en utilisant la fonction de propagation gaussienne (PSF) de la réponse du capteur.

Nous avons également évalué dans ce chapitre la sensibilité et la cohérence du nouveau modèle avec les principaux paramètres d'entrée : la largeur de la haie et l'environnement, la valeur du LAI, la position centrale du champ de vue du capteur, la position solaire et les températures de brillance des composants. Les principales constatations indiquent qu'une faible empreinte au sol conduit la distribution du DBT à être fortement dominée par la direction de la rangée et la température du composant mais est peu influencée par la position solaire. Au contraire, une grande empreinte lisse l'effet de rangée et conduit la DBT à être distribuée comme une canopée uniforme et continue. Les paramètres de LAI et la position centrale du champ de vue du capteur change le mode de répartition de la DBT, surtout quand la position centrale va du sol au haut de la haie. De plus, afin de répondre à la question "quelle est la taille optimale de l'empreinte pour acquérir des DBT représentatives pour valider un modèle parallèle avec la moindre erreur, nous avons introduit un index, appelé le nombre de périodes (NP) indépendant des observations et de la hauteur de la canopée pour examiner l'empreinte optimale qui peut se traduire par la plus petite différence de DBT entre le FovMod et le modèle parallèle. Les résultats ont démontré que la différence DBT entre les deux modèles atteint toujours son minimum lorsque NP est de l'ordre de 1,5 ~2.0 ce qui a suggéré que si le diamètre de l'empreinte circulaire du capteur au nadir couvre 1,5 ~ 2,0 fois la largeur totale d'une rangée, l'effet d'empreinte serait essentiellement éliminé et la DBT mesurée peut théoriquement servir pour évaluer le modèle parallèle.

Enfin, le modèle FovMod a été validé sur une canopée de maïs. Dans les mesures terrain, un système d'Observation Multi-Angle (MAOS) a été conçu pour acquérir automatiquement et rapidement les TBD de la canopée pour différents angles azimutal et zénithal. Une caméra thermique a été utilisée en parallèle avec le MAOS, et les températures de brillance des composants ont été extraites manuellement de l'image de la caméra acquise simultanément avec chaque mesure angulaire du MAOS. Les autres paramètres nécessaires au nouveau modèle, tels que le LAI, la largeur et la hauteur de la canopée ont également été mesurés. Les résultats ont montré que la majeure partie des DBT simulées par le FovMod se situent à ± 1 K de la mesure, avec un RMSE de 1,2 K, ce qui est inférieur de 0,5 K du modèle parallèle (RMSE = 1,7K). Les variations angulaires de la DBT dans quatre plans azimutaux (plan principal et perpendiculaire solaire et plan principal et perpendiculaire de la rangée) ont été également présentées pour démontrer la supériorité du modèle FovMod. Dans ce chapitre, nous avons également examiné l'extension du modèle de la gamme thermique FovMod à la gamme VNIR, l'inversion de la température des composants de ce modèle et la validation future sur des rangées de cultures d'un type différent.

Le chapitre 7 présente et discute les principales conclusions de cette thèse ainsi que les perspectives et les limites rencontrées.

Par exemple, concernant les limites, au chapitre 3, l'émissivité directionnelle à l'échelle du pixel à partir des produits MODIS pourrait être également causée ou influencée par une erreur résiduelle dans les données atmosphériques ou les variations temporelles et spatiales de l'émissivité elle-même. Le nouveau facteur d'effet de cavité décrit dans le chapitre 4 ne peut servir que pour les modèles SAIL et il peut entrainer des incertitudes à d'autres modèles de transfert radiatif. Le paramétrage du DBT pour la canopée résulte du calcul effectué avec des canaux VNIR, mais n'a pas pu être validé en raison du manque de données terrain. En outre, la méthode D-TISI dans le chapitre 5 a ignoré la variation temporelle de la température de surface et a considéré la variation de la température comme entièrement causée par les changements d'angles de vue, car il n'y a, à l'heure actuelle, aucune méthode opérationnelle qui permette la normalisation des DBT multi-angulaire mesurées.

De manière générale, les travaux de cette thèse ont permis d'améliorer notre compréhension de l'anisotropie du rayonnement thermique de surface et de perfectionner la méthode de séparation de l'émissivité et de la température de surface à partir de données de télédétection et ce, surtout pour les surfaces hétérogènes et non isothermiques. Les travaux futurs sur cette question viseront à résoudre les problèmes, comme indiqués ci-dessus.

(1) La méthode de D-TISI proposée peut être appliquée aux données des satellites géostationnaires, qui mesurent au même endroit et à une fréquence élevée et il est facile d'obtenir des observations multi-angulaires sur la base des changements de positions solaires tant que la correction atmosphérique est opérationnelle.

(2) La correction angulaire de la LST pourrait résulter de mesures de l'indice de végétation. Puisque la température directionnelle est considérablement influencée par la fraction de la végétation (FVC), il est possible d'établir une relation entre la température directionnelle et la FVC basée sur la méthode du triangle FVC-température à partir de la distribution spatiale des deux variables dans la zone d'étude et l’utilisation d’une relation pour normaliser la température directionnelle dans la direction nadir.

(3) La correction angulaire de la LST peut être liée aux températures des composants qui peuvent être obtenus à partir de mesures multi-angulaires ou à canaux multiples ou des données hyperspectrales TIR.

(4) La correction angulaire de la LST peut être effectuée en utilisant différents capteurs. La combinaison des satellites en orbites polaires et géostationnaires peut être une autre façon de corriger la LST s’ils observent le même endroit dans des directions différentes en même temps ou en quasi-simultanéité.

Cette thèse a été réalisée dans le cadre d’une co-tutelle entre la Beijing Normal University, China, et l’Université de Strasbourg, France, et financée par le National Basic Research Program of China (973 Program), le National High-Tech Research and Development of China (863 Program), le Natural Science Foundation of China, la commission européenne (Call FP7-ENV-2007-1 Grant no. 212921) part du projet CEOP-AEGIS et le China Scholarship Council project.

地表热辐射方向性建模与温度的角度纠正

中文摘要

近几十年来，国内外科学家对地表能量平衡、流域管理、地表生物物理变化过程和各种自然灾害等开展了广泛研究。但是，传统的点测量方式受人力、物力和财力的限制难以满足需求。遥感技术具有全天候、长时间序列和低成本等特点，在区域或全球尺度获取地表、海洋、大气以及人类活动信息具有优势，可为相关领域研究提供有效数据。迄今为止，已有成百上千的在轨传感器以不同的方式获取地表信息，所获取的各种地表、大气相关参数被广泛应用于各个行业。

地表温度(land surface temperature, LST)是地表能量平衡和温室效应的一个重要指标，是区域与全球尺度地表物理过程的关键因子。它将地-气相互作用及其能量交换结合了起来。任何绝对温度大于 0 K 的物体都要向外辐射能量，利用遥感探测器接收到的热辐射信息来反演陆地表面温度是热红外遥感反演的主要目标。目前，地表温度产品被广泛地应用于全球气候变化、区域蒸散发、土壤水分检测、作物估产、城市热岛、森林火灾、地震预报与检测、地质勘查等各个研究领域。因此，地表温度数据被多个国际著名组织和工程当作最重要的地表参数之一。例如，国际地圈生物圈计划(International Geo-sphere and Biosphere Program，IGBP)将地表温度视为高优先级地表参数，美国宇航局(NASA)将其作为最重要的地球系统长期记录数据之一，以及欧空局(ESA)将地表温度当作是气候变化研究中的支撑数据。

从遥感观测的热红外数据中反演地表温度可以追溯到上世纪七十年代，并引起了科学家的广泛关注。但是，由于从地表到达卫星传感器的辐射同时包含了地表和大气信息，所以从热红外数据直接反演地表温度必须同时消除大气效应和地表本身的发射率效应，而这并非易事。首先，地表发射率定义为自然地表的热辐射与同温同波长下黑体（对达到其表面的辐射全部吸收）热辐射的比值，其随着地表类型和构成、土壤纹理和水分、观测波长和观测角度等而发生变化。对于大部分自然地表来说，它们的热辐射往往小于黑体热辐射，即发射率小于 1，地表温度和发射率的相互耦合使得地表温度的遥感反演必须考虑发射率的影响，从而在数学上形成一个“欠定”问题：某一传感器提供 $\boldsymbol{N}$ 个通道的观测数据值，却对应 $\boldsymbol{N}$+1 个未知数（$\boldsymbol{N}$ 个通道的发射率和 1 个地表温度），未知数个数总大于观测方程数。要求解这样的欠定问题，往往需要引入其它限制条件或者附加信息来减少未知数的个数。与发射率效应相比，大气对地表热辐射的影响更为显著。大气对地表热辐射的影响主要体现在：大气下行辐射和上行辐射对热辐射的贡献以及对地表热辐射在从地面到卫星的传输过程中的削弱作用。与地表自身热辐射相比，大气效应可以增加或减少到达传感器的总辐射，这主要取决于地表自身热辐射、发射率和大气热辐射之间相对大小关系。要消除大气效应，精确的大气辐射传输方程式和大气参数廓线（气温、水汽含量、气压等）必不可少，但这些参数却很难在大范围内获得，并且表现出明显的时空差异。

截至目前，基于热红外的辐射传输方程，人们发展了多种消除发射率与大气效应的方法以从热红外遥感数据中反演出地表温度，其大致可以分为三类：（1）分步法，首先从可见光-近红外数据（例如 NDVI 阈值法）或地表分类产品（Classification-based method）中获得发射率，然后再将其运用于单通道算法或者劈窗算法中反演出地表温度。（2）在已知大气条件的情况下，从多时相、多光谱数据中同时反演出地表温度与发射率，例如在假设发射率短时间内不随时间变化的基础上而发展起来的双温度法(Two-Temperature Method)和日夜算法(Day/night algorithm)，以及适合于 ASTER 传感器的 TES 方法(Temperature and emissivity separation method)等；（3）基于一定的先验知识和对未知数的简化，从多光谱或高光谱数据（例如 IASI）中同步反演地表温度、发射率和大气参数信息。

目前地表温度的反演算法常常假设地表是同温朗伯体，其温度不随传感器的观测通道和观测角度而发生变化。对于浓密植被和水体来说，这样的假设是合理的，并且能够有效的减少未知数的个数。但是，正如前人所发现的那样，对于那些三维结构明显（例如稀疏植被、城市建筑）的非同温混合像元来说，其温度是随着通道与观测角度变化的，那么以上假设将不再成立。在像元尺度上，由于其内部具有复杂的三维结构且存在不同的组分，而不同组分具有不同的发射率和温度，且不同组分对像元热辐射贡献的有效权重也随着太阳-地物-观测几何的变化而变化，因此像元的热辐射表现出明显的方向性。以往的研究发现，不同的观测角度可以导致垂直方向上和倾斜方向上的裸土温差高达 5 K，城市地表温差高达 10 K，而温度 1 K~3 K 的误差将在通量估算结果中引入高达 100W/m^2 的误差。此外，对于若干具有大视场的传感器来说，以 MODIS 为例，其可以在[-65º, 65º]的天顶角范围内观测地表，不同的像元对应不同的观测角度，温度的角度效应降低了像元之间的温度可比性，以及降低了地表温度产品在各个领域的使用精度。因此，在地表温度反演过程中考虑其角度效应对于提高反演精度是十分必要的。

对于同温像元来说，地表温度的角度效应可以归结于像元的发射率随着角度的变化。理论上，只要已知像元的方向性发射率，就可以通过反解辐射传输方程来消除地表温度的角度效应。该方法简单，但是由于难以获得自然地物在像元尺度上的方向性发射率，此种方法往往难以实际应用。若考虑非同温像元，可以首先通过多角度、多波段数据来反演出组分温度或者温度比例，然后利用特定观测方向上各个组分的比例来加权获取该方向上的等效温度。在假设地表未发生显著变化的情况下，各个组分比例可以通过多次观测的数据利用 BRDF(Bi-directional Reflectance Distribution Function)模型拟合得到。此类方法在理论上是有效的，但是至今仅有 ATSR 系列传感器拥有 2 个观测角度，还无法真正满足全球温度产品的角度纠正需求。因此，迄今尚未形成一种有效、可运作的地表温度的角度纠正方法。

本文以热辐射的方向性为切入点，基于经验模型和物理模型，在冠层尺度和像元尺度上讨论地物的发射率随着观测角度的变化情况，以及这种角度效应对地表温度的影响；明确非同温像元方向性等效地表温度的定义，并在同时考虑方向性发射率与不同组分温度的条件下，建立非同温均匀像元方向性热辐射估算模型，进而发展从多角度中红外与热红外数据中同时反演方向性发射率与等效温度的新算法；针对温度地面验证时测量数据的不确定性，发展新的辐射传输模型来探讨地面传感器视场大小对行播作物冠层方向性热辐射（亮温）的影响，并针对模型的验证给出在实际测量中的最优视场。因此，本文将从经验方法、物理建模、遥感反演和地面验证等几个方面来研究热辐射的方向性和地表温度的角度纠正方法，研究成果希望能够为未来星载或机载多角度热红外传感器的设计及地面测量提供参考。本文总共分为七章，各种的主要内容如下：

第一章主要引出对方向性热辐射研究的必要性以及本文的切入点；

第二章主要介绍目前地表温度和发射率的反演算法以及方向性热辐射建模思路。

首先，这一章将给出热红外传感器获取信息过程的辐射传输方程，以及讨论大气效应和发射率效应对地表辐射信号的影响。为了明确像元尺度，特别是非同温像元尺度地表温度和发射率的定义，还阐述了目前国际上使用的多种地表温度和发射率定义的异同，并最后选择 ***r-emissivity*** 及其对应的等效温度来作为本文研究的基础。基于 ASTER 数据库和美国加州大学圣巴巴拉分校数据库(UCSB)的若干植被与土壤样本数据，讨论了发射率随波长和地类的变化情况。以 MODTRAN 为例，讨论了大气辐射传输模型在热红外数据的大气纠正和正向模拟中的运用，从而为后文的研究做铺垫。其次，该章重点回顾了现有从热红外（和中红外）遥感数据中反演地表温度、发射率的各种方法。若按使用的通道和角度进行方法分类，可分为单通道算法、多通道算法、多角度算法以及多通道多角度算法。若按大气参数和发射率已知与否进行分类，则可分为分步法、地表温度与发射率分离方法以及大气参数、地表温度与发射率一体化反演算法，本文按照第二种分类方式简单地介绍了各种反演方法。最后，这一章节还回顾了目前在冠层尺度和像元尺度进行方向性辐射建模和参数化的主要思路和方法。总的来说，目前的方法主要可以分为四类：几何光学模型(GO)，辐射传输模型(RT)，混合模型(GORT)以及计算/数值模拟模型。

然而，目前算法却存在诸多不足之处。在热辐射方向性研究方面，这些不足将表现在如下几个方面：（1）首先，缺乏真正的像元尺度的方向性发射率。尽管国内外学者已经从地面观测和数学建模等方面对方向性发射率进行了若干研究，并得到了一些颇有价值的结论。但是由于测量技术的限制，至今未有通过实测数据获得中等分辨率像元尺度的方向性发射率，从而无法得知该尺度上发射率的角度变化规律；（2）没有充分利用多角度观测数据信息。利用多角度数据是实现地表温度角度纠正的一个重要途径。然而，由于技术的限制，现有的在轨传感器仅有 ATSR 系列能够提供 2 个角度的热红外数据，有关机载多角度热红外数据的报道也鲜有所见，并且现有的多角度观测数据主要用于反演地表温度或者组分温度。因此，至今尚未形成一套从多角度数据中同时获取地表温度和发射率的有效方法，离地表温度的角度纠正还相差甚远；（3）缺少地表温度的角度纠正的有效方法。尽管利用方向性发射率是消除同温像元地表温度角度效应的一种有效方法，但是，正如前文所述，至今并没有有效的遥感像元尺度的方向性发射率。另一种地表温度的角度纠正方法是建立地表温度与观测几何角度的转换关系。当这种转换关系的系数从有限的观测数据获得，那么在理论上就可以获得任意观测角度下的地表温度。BRDF 模型不失为其中的一种有效途径；（4）缺乏方向性热辐射地面测量数据的精度评估方法。地面测量数据常作为“真值”来检验遥感反演的地表温度与方向性热辐射模型精度。但是，地面测量数据本身也存在误差，其自身精度在很大程度上决定了检验的结果。鉴于此，本文针对于以上问题的不足之处展开了相关研究。

第三章以 MODIS 的发射率产品为基础提取了像元尺度的方向性发射率以及其对地表温度的影响和空间尺度效应。

基于日夜算法反演的 5 年 MODIS 发射率产品和地表分类产品研究了公里级像元尺度上多种自然地物发射率(***Grassland, Cropland, Evergreen Broadleaf Forest, Mixed Forest, Open Shrublands, and Barren or Sparsely Vegetated*** 等)在中红外通道（CH20: 3.66~3.84 μm, CH22: 3.93~3.99 μm, CH23: 4.02~4.08 μm）和热红外通道（CH29: 8.4~8.7 μm, CH31: 10.78~11.28 μm, CH32: 11.77~12.27 μm）的角度变化。结果表明，在像元尺度上，地类在中红外通道的发射率整体上随着观测天顶角的增大而增大，热红外通道的发射率随着观测天顶角的增大而减小。中红外通道发射率的角度变化约高于热红外通道，两个通道发射率在 0°~65°观测天顶角范围内的角度变化分别集中在 0.01~0.02 和 0.01 附近，但是

当观测天顶角小于 45°，两个通道发射率的角度变化几乎可以忽略。基于提取的方向性发射率，建立了发射率与观测天顶角的经验关系，并构建了两种不同结构的发射率查找表。将方向性发射率用于 MODIS 的劈窗算法中反演了研究区不同时期的地表温度，并与 MODIS 原有劈窗算法的地表温度产品进行了比较。比较结果说明，新反演的地表温度整体上高于 MODIS 的地表温度产品，它们的差值主要集中在-1.0~3.0 K 之间，并且差值的 RMSE 随着观测角度的增大而增大，说明在大角度观测时，利用方向性发射率对地表温度进行一定程度的角度纠正是十分必需的。最后，还进一步讨论了方向性发射率的空间尺度效应对劈窗算法反演地表温度的影响，结果表明不同尺度上温度的差异整体上小于 0.5 K，尺度效应不明显。

然而，尽管日夜算法动态反演两种大气参数（近地表大气温度和大气水汽）来调整大气廓线初值，在理论上可以提高观测数据的大气纠正精度，但仍不排除大气残余信息以及太阳辐射误差对发射率角度效应的影响。由于研究范围的限制，这一章节仅获得 6 种地物的方向性发射率，在一定程度上影响了其在更大范围内的使用。此外，由于缺乏土壤水分数据，本文不得不忽略土壤水分对发射率的影响。因此，为了更精确地获取在像元尺度上的更多地类的方向性发射率，从而为地表温度反演提供必要的先验知识，相关工作还需要进一步研究。

第四章主要介绍方向性发射率与热辐射的参数化以及 BRDF 模型在地表温度角度纠正过程中的适用性分析与观测角度需求。

基于热红外波段的 SAIL 模型(TIR-SAIL)的模拟结果，探讨了 4 种方向性发射率的参数化方案，即核驱动 BRDF 模型、半经验 BRDF 模型以及间隙率模型 FRA97 和 FRA02。结果发现，核驱动 BRDF 模型能够较为精确地反映出冠层发射率随着角度的变化情况，特别是在低植被冠层；考虑了植被与植被组分多次散射的参数化间隙率模型 FRA97 也能较好地刻画发射率随角度的变化情况，但是需要更新模型中原有模型总表示多次散射的参数“cavity”效应因子。基于更新的参数以及 SAILH 模型的“景合成”参数化模型，本文提出了一种模拟非同温均匀冠层方向性亮温的新方法，其模拟结果很好地反映了方向性亮温的半球空间分布和热点效应。

为了验证核驱动 BRDF 模型在热红外领域的适用性，本文利用方向性亮温代替原核驱动 BRDF 模型（简称 K-RBDF 模型）中的二向性反射率，并将其运用于拟合半球空间的方向性亮温。结果表明新改成的 K-BRDF 模型可以很好地拟合出半球空间的方向性亮温，其误差不超过 0.3 K。其意义在于，如果知道了 K-BRDF 模型的 3 个核系数，理论上就可以拟合出任意方向上的亮温，从而为方向性亮温的角度归一化研究提供了一种有效的途径。通过 2 种方式（即单点模式和线阵模式）来检验 K-BRDF 模型进行角度归一化的可靠性以及对观测角度的需求。基于单点模式的分析结果，本文获得了 K-BRDF 模型在拟合半球空间亮温和垂直方向亮温时的局部三角度最优组合[(0°, 0°), (0°, 30°), (180°, 50°)]，并将此角度组合应用到三线阵模式。根据对太阳天顶角和太阳方位角以及冠层 LAI 对模型拟合结果的分析，本文发现距离线阵中心位置越近，三线阵同一位置像元列对应的观测角度差异越大，K-BRDF 模型拟合的亮温精度越高；相反地，距离线阵边缘越近，像元列对应的观测角度差异越小，K-BRDF 模型拟合的亮温精度越低。总的来说，要使 K-BRDF 模型在三线阵的多数像元列下的误差小于 1.0 K，像元在垂直线阵上的观测天顶角应不超过 45°，并且中等太阳天顶角、中等植被或浓密植被可以提高 K-BRDF 模型拟合亮温的精度。这样的结果希望为未来多角度热红外传感器设计提供若干参考。

但是，本文仅使用了包括 TIR-SAIL 模型和 SAILH 模型在内的 SAIL 系列模型来模拟方向性发射率和亮温，所以更新的“cavity”效应因子并不一定适用其它辐射传输模型。模型模拟得到的方向性发射率和方向性亮温由于缺少地表均匀冠层数据而未能进行地面验证。此外，仅讨论 K-BRDF 最小的角度需求：3 个角度观测的情况，并强制它们的方位角位于同一平面。对于解决“利用核驱动模型精确拟合方向性亮温到底需要多少个角度的观测，需要哪些角度？”这一科学问题仍然需要进行更多更广泛的研究。但是本文的相关结果可以为进一步研究提供参考。

第五章发展了利用多角度数据反演方向性发射率与等效温度的新模型，并利用改进的核驱动 BRDF 模型实现温度的角度纠正。

针对于非同温像元，明确了方向性等效温度的定义。基于 BRDF 核驱动模型和 TISI 方法，提出了利用白天观测的中红外和热红外多角度数据反演方向性发射率和等效温度的新方法，简称为 D-TISI 法。该方法通过多角度观测信息来消除原有 TISI 算法对白天和夜晚双时相遥感数据的需求，将反演问题转化为对核驱动模型的三个核系数和 TISIE 的反演，从而降低了未知数的个数。基于结论第四种中所提出方法模拟的冠层方向性亮温，对模型进行敏感性分析。结果表明，具有大角度倾斜观测、角度间隔明显的观测组合能提高发射率和温度的反演精度。这是因为在这种角度组合条件下，不同方向上的组分比例和方向性亮温均有显著差异；本文同时也讨论了中红外与热红外通道宽度、冠层 LAI、组分温度分布和 TISIE 等对反演精度的影响。总的来说，当观测的方向性亮温和大气参数的噪声分别不超过 1.0K 和 10%时，新方法反演发射率和温度（等效温度）的误差分别小于 0.015 和 1.5K。

将 D-TISI 方法应用于机载白天时刻中红外、热红外通道的多角度观测数据上，反演了方向性发射率和等效温度。与 ASTER 发射率产品的交叉比较发现，新方法反演的垂直方向上的发射率大于 ASTER 发射率产品，它们的均方根误差约为 0.012。并利用核驱动 BRDF 模型将实际观测的方向性等效温度归一化到垂直方向上。对绝大多数植被像元，垂直方向上的等效温度和实际观测方向上的最小等效温度之间相差 0.5~2.0K，而对于大多数的非植被像元，两者温度之间却可高达数 K。因此，为了提高精度，有必要对地表温度进行角度归一化，特别是非植被像元。

然而，在实际过程中，地表温度同时也受区域气象条件、太阳光照条件变化而引起的时间变化。本文在利用机载数据进行反演时忽略了时间变化对温度的影响，而是将像元温度的变化全部归咎于观测角度的变化。尽管使用的数据连续观测时间间隔短，但不考虑温度的时间变化会降低反演的精度。大气纠正误差也将降低反演精度。此外，在探测单元的瞬时视场角(IFOV, instantaneous field of view)保持不变的情况下，同一探测单元在不同的角度观测时对应不同面积大小的地面像元，这可能导致不同角度的像元拥有不同的组分，尤其是对于非均匀地表。因此，在未来多角度传感器发展中，需要根据观测的角度大小来设计具有不同瞬时视场角的探测单元，使得在不同角度下观测到同样的地面面积。

第六章主要是在考虑了视场效应的基础上构建了模拟行播作物冠层方向性亮温的新模型，并提出了地面验证过程中需要的最佳视场。

在考虑地面测量传感器的视场大小的基础上，构建了模拟行播作物冠层的方向性亮温新模型(FovMod)。FovMod 模型采用圆形（垂直观测）或椭圆形（倾斜观测）来刻画传感器在冠层上的投影视场，并将该视场划分为多个小面元，分别计算各个面元内植被、

光照土壤与阴影土壤的比例。然后，按照高斯分布的点扩散函数来计算每个面元对整个视场辐射的权重，并加权得到整个视场内各个组分比例。最后，利用组分比例和组分亮温的加权和来获得冠层的方向性亮温。研究结果表明，当传感器视场较小时，行播作物冠层的方向性亮温分布主要取决于行播作物本身的行向方位角和单一组分温度，而几乎与太阳的位置无关；而当传感器视场较大时，冠层的行结构却在很多程度上得以平滑，使得方向性亮温的分布模式与均匀连续冠层相当，因此选择合适的传感器视场角对于获取的行播作物冠层亮温的空间分布十分重要。

针对平行光模型地面验证过程对传感器视场的需求，研究发现当传感器在垂直方向上的视场覆盖 1.5~2.0 倍行结构周期宽度时，地面仪器测量到的方向性亮温可等效地当作单一观测方向上的亮温，在理论上可以用来验证平行光模型，而无需考虑传感器的视场效应。最后，利用玉米行播作物冠层的实测数据来验证了 FovMod，验证结果证明新模型 FovMod 的模拟数值与实测值相当，二者的均方根误差为 1.2 K，优于平行光模型的均方根误差 1.7 K。此外，由于 FovMod 同时考虑了观测几何、冠层结构和视场大小，该模型还可以用来评价地面测量数据因观测角度控制误差、或者结构参数测量误差而导致的亮温不确定性，从而为测量数据的评价提供依据。

新模型的不足之处在于没有考虑行播作物冠层内组分之间的多次散射，并忽略了大气下行辐射的影响，因此模型的模拟值理论上小于实际值。新模型需要的冠层结构和观测几何参数比较繁多，在利用该模型发展组分温度反演算法时，需要对模型开展进一步的参数化或简化过程。此外，新模型还需要针对处于不同生长期的更多行播作物冠层开展地面验证工作。

第七章主要总结本文的主要工作和成果，并且对未来的研究做出了相关展望。

本文从理论上对地表热辐射的方向性进行了系统分析，有助于促进人们更好的了解热辐射方向性以及提高现有遥感温度产品的精度，所得结论可为星载或机载多角度热红外传感器的设计及地面测量提供参考。此外，还可以从几个方面来进一步深化本文的研究工作：

（1）理论上，本文提出的 D-TISI 方法使用的多角度数据不需要在同一时间段内观测，因此适用于具有中红外与热红外波段的静止卫星。此类卫星可在短时间内对同一地物以相同的观测方向进行连续观测，通过太阳位置的移动来获取同一地物的多角度观测几何数据。只要能够实现各次观测时的大气纠正，D-TISI 方法就可以从这些数据中反演出发射率和温度。鉴于这样的思路，在地表没有发生显著变化的前提下，MODIS 和 AVHRR 等传感器也可以通过多天对同一地物的多次观测来提供多角度数据；

（2）本文所需要的方向性发射率或者多角度数据在目前并非多见，算法的应用受到一定的限制，因此需要在未来研究中发展地表温度角度纠正的新方法。例如，利用植被覆盖度与地表温度的空间信息，首先可基于二者特征空间来建立地表温度与植被覆盖度的经验关系，然后再通过 BRDF 模型获得垂直方向上的植被覆盖度，并进一步获取垂直方向上的地表温度；结合静止卫星和极轨卫星，利用它们同步或者准同步信息来发展地表温度纠正算法；

（3）从高光谱或超高谱传感器的成百上千的观测数据中提取像元的组分温度，然后再利用植被指数或者覆盖度获得垂直方向上地表温度也可能是一种地表温度角度纠正的有效方法；

（4）由于缺少地面实测数据，D-TISI 方法实际反演的发射率和温度没有进行地面验证，需要在以后研究中更注重星-机-地同步配合实验。尽管针对玉米行播冠层验证了新发展的行播作物冠层方向性亮温模型，但是在未来研究中，仍需要利用更多种类的行播作物（例如小麦、玉米、果园等）冠层在不同生长期的方向性亮温数据来对新模型进行验证。

本文由北京师范大学(Beijing Normal University, China)和斯特拉斯堡大学(Université de Strasbourg, France)双方导师共同指导完成，并得到了中国国家重点基础研究发展计划项目（973 计划）、国家高技术研究发展计划（863 计划）、国家自然科学基金、国家公派留学基金以及国际合作项目 FP7(CEOP-AEGI)的联合资助。谨此致谢！

List of Figures

List of Tables

Chapter 1

Introduction

In the recent decades, the studies of land surface energy balance, watershed management, biophysical process and disasters have attracted worldwide interests. The achievement of those subjects requires a huge database about the status of land surface, ocean, atmosphere and even the human activities. The advent of remote sensing technique, featured with rapid revisit, long-term observation and low cost, provides us a promising way to obtain those data at regional and global scales rather than the traditional point measurement. With the remotely sensed data from airborne and spaceborne platforms, scientists have proposed different algorithms to retrieve different types of parameters about the Earth's surface and its atmosphere cycle, and these parameters have been used in many relevant fields.

The land surface temperature (LST) is one of the most important parameters in the physical processes of surface energy and water balance at local through global scales. Knowledge of the LST provides information on the temporal and spatial variations of the surface equilibrium state and is of fundamental importance in many applications. As such, the LST is widely used in a variety of fields including evapotranspiration, climate change, hydrological cycle, vegetation monitoring, urban climate and environmental studies, among others (Mildrexler et al. 2011; Rodriguez-Galiano and Chica-Olmo 2012; Sims et al. 2008; Tang et al. 2010; Van Leeuwen et al. 2011), and has been recognized as one of the high-priority parameters of the International Geo-sphere and Biosphere Program (IGBP) (Townshend et al. 1994), as one of the most important Earth System Data Records (ESDR's) identified by NASA (http://lst.jpl.nasa.gov/background), and as one of the supporting products for the ESA climate variables (http://tinyurl.com/globtemperature).

The retrieval of the LST from remotely sensed thermal infrared (TIR) data has attracted much attention, and its history dates back to the 1970s (McMillin 1975). However, the direct estimate of the LST is not an easy task and it has to deal with the emissivity and atmospheric effects, because the radiances measured by the radiometers onboard satellites depend not only on surface parameters (temperature and emissivity) but also on atmospheric effects (Li and Becker 1993; Ottlé and Stoll 1993; Prata et al. 1995). The emissivity, defined as the ratio of the radiance emitted by natural targets to the radiance emitted by a blackbody at the same temperature, varies with land surface types and structure, wavelength, soil texture and moisture and viewing angle (Becker 1987; François et al. 1997; Schmugge et al. 1998; Sobrino et al. 2008). The coupling of the non-unity emissivity for most natural surface with the LST causes the retrieval of the LST from space is mathematically underdetermined and unsolvable: for a sensor with $\boldsymbol{N}$ infrared channels, N measurements have $\boldsymbol{N} + 1$ unknown ($\boldsymbol{N}$ channel emissivities and 1 temperature). To solve this underdetermined problem, some extra constraints are consequently needed. As for the atmospheric effect, the surface-emitted radiance is firstly contaminated by the reflected atmospheric downward radiance, and then attenuated by atmosphere on the path from the surface to the sensor onboard satellite. Correcting for the atmospheric effect requires accurate knowledge of the vertical profiles of atmospheric water vapor and temperature both of which are highly variable (Perry and Moran 1994).

Based on the radiative transfer theory in the TIR, a variety of methods have been developed to retrieve LST from remotely sensed data with different way to remove the effect of emissivity and atmosphere. For example, with known emissivity from the linear empirical relationship with visible/near-infrared data or classification-based method (Snyder et al. 1998; Sobrino et al. 2008; Zhou et al. 2003), two popular methods can used to retrieve LST from space: one is the single-channel algorithm that was proposed to obtain LST with only one TIR channel, such as the Thematic Mapper channel 6 (TM6) onboard Landsat and HJ-1B (Duan et al. 2008; Jiménez-Muńoz and Sobrino 2003; Qin et al. 2001); the other is the split-window algorithm that removed the atmospheric effect using the differential atmospheric absorption in the two adjacent channels centered at 11 µm and 12 µm, and finally applied the linear or nonlinear combination of brightness temperatures of the TIR channels to get the LST. Because it does not require accurate information about the atmospheric profiles at the time of the acquisition, a variety of split-window algorithms have been developed and modified to successfully retrieve LST from several sensors, such as AVHRR, MODIS, and SEVIRI (Becker and Li 1995; Sobrino et al. 1993; Sun and Pinker 2007; Tang et al. 2008; Wan and Dozier 1996). On the other hand, with the cases of unknown emissivity, several methods were designed to retrieve both LST and emissivity from multiple-channel and/or multiple temporal observations. For example, the Temperature-Independent Spectral Indices (TISI) method firstly used a pair of day and night observations in middle and thermal infrared channels to retrieve emissivity in both channels, and then used the retrieved emissivity to calculate LST directly from the inversion of the Planck’s law or from the split-window algorithm aforementioned (Becker and Li 1990; Goïta and Royer 1997; Jiang et al. 2006; Nerry et al. 1998). Similarly, Two-Temperature Method (TTM) decouples the two parameters from two TIR channel’s observations in day and night observations by assuming channel emissivities were invariant during the two observations (Peres and DaCamara 2004a; Watson 1992). Moreover, if the number of MIR and TIR channels is enough (no less than seven), the physical day/night algorithm can be unitized to retrieve LST and emissivity along with some other parameters from day and night observations (Wan and Li 1997). Besides, both LST and emissivity can be also retrieved from atmospherically corrected multiple-channel TIR data by using relationship between channel emissivities, such as the Temperature/emissivity separation method (TES) primarily designed for ASTER five TIR channels and then extended to MODIS three TIR channels (Gillespie et al. 1998; Gustafson et al. 2006; Hulley and Hook 2011; Sabol et al. 2009). With the appearance of hyperspectral TIR sensors (e.g. Infrared Atmospheric Sounding Interferometer, IASI), the thousands of narrow bandwidth channels in TIR can supply enough vertical resolution to allow extraction of atmospheric information and can also provide more physical constraints to accurately separate the LST and emissivity (Wang 2011).

An important assumption included in these current algorithms is that the surface is considered as homogeneous and isothermal, and the surface temperature is channel-independent and angle-independent. This assumption is reasonable because it can reduce the number of unknowns and make the LST retrievable. However, in practice, as reported by some authors by (Chehbouni et al. 2001; Lagouarde and Irvine 2008; Lagouarde et al. 1995; Li et al. 2004a), the LST varies with viewing angle, and its angular variation for three-dimensional surfaces results primarily from the angular variation of the pixel emissivity and the relative weights of different components (e.g., vegetation and background soil) with different temperatures in a non-isothermal pixel. The difference in the LST measured in nadir and off-nadir observations can be as large as 5 K for bare soils and even 10 K for urban areas. For most polar-orbit satellites (e.g. MODIS, AVHRR) that scan the land surface in the cross-track direction with different viewing zenith angles (VZA) varying from -65º to +65º, angle-dependent variations in the retrieved LST are inevitable, making the LSTs of different pixels in the same orbit incomparable and causing erroneous results in application. This angular effect also occurs in the geostationary satellite such as Spinning Enhanced Visible and Infrared Imager (SEVIRI) onboard MSG and among LSTs obtained from different sensors or at different times. Therefore, it is very crucial to consider this effect in the retrieved LST.

One method of considering the angular effect on LSTs is to simply attribute the angular variation of the measured effective temperature derived from area-weighted emitted radiances to the directional behavior of the pixel emissivity, as proposed by (Li et al. 1999). However, the directional emissivity defined in this manner is usually not measurable from space and the assumption that there is no downward environmental thermal radiance may cause some unexpected errors in the normalized result (Li et al. 2012; Norman and Becker 1995). Another technique for this effect is to separate the components' temperatures or their ratio from multi-angular TIR data (Jia et al. 2003; Li et al. 2001; Liu et al. 2012; Menenti et al. 2001; Shi 2011; Zhan et al. 2011), and calculate the effective temperature in a specific direction (e.g., at nadir) by weighting the components' temperatures with their corresponding fractions. The fractions of various components under a specific viewing angle can be calculated using the bi-directional reflectance distribution function (BRDF) model in the visible and near infrared spectral regions. This method might be a promising way, but the requirement of multi-angular observation cannot be satisfied for most TIR sensors, and its accuracy is still far from satisfactory. Therefore, there is still no any practical way to perform angular normalization of satellite-derived LSTs due to the complexity of this issue.

From this point of view, the study of this thesis focuses on the retrieval of directional emissivity from spaceborne and airborne data using empirical and physical methods, and its applications on the angular correction of the LST. It also aims at the simultaneously retrieve directional emissivity and temperature from multi-angular middle and thermal infrared data. Besides, for the field angular measurement of surface temperature, this thesis also develops a hybrid radiative transfer model to consider the sensor's footprint effect on the measured directional brightness temperature. Therefore, this thesis is organized into seven chapters:

Chapter 2 describes the fundamental radiometric theory, and reviews the current status of retrieving LST and emissivity from remotely sensed data, and the issue of modeling of directional thermal radiation for homogeneous and heterogeneous surface.

Chapter 3 aims at the extraction of directional emissivity based on MODIS standard emissivity product for several land cover types, and establishment of empirical expression of directional emissivity at pixel scale. The directional emissivity is finally applied to the split-window algorithm for retrieving LST with angular correction.

Chapter 4 presents the parameterizations of the directional emissivity and thermal radiance and discussion about the application of the kernel-driven BRDF model in the angular normalization of land surface temperature and its requirement of viewing angles.

Chapter 5 depicts the newly developed model for the retrieval of directional emissivity and effective temperature from daytime multi-angular MIR and TIR images. Analysis of model consistency to several key parameters is also presented. Finally, the new method is applied to an aircraft dataset collected by airborne system in the field campaign, and validated by using ASTER products.

Chapter 6 develops a new hybrid GORT model to simulate the directional brightness temperature for row-structured canopy by considering the footprint effect of the sensor in the ground measurement. Based on the new model named FovMod, this chapter provides the optimum footprint for the validation of the previous relevant models.

Chapter 7 concludes the work of this thesis and gives out some discussions about the future efforts on the topic of directional behavior of LST and emissivity.

Chapter 2

Fundamental radiometric theory, and reviews of LST and emissivity retrieval methods and modeling of directional thermal radiation

This chapter firstly presents the basic theory of radiative transfer model, along with defining the LST and emissivity for space pixel, and then reviews the current popular methods of retrieving land surface temperature and emissivity. Finally, it describes the methods for modeling of directional thermal radiation. Based on the analysis on of the drawbacks of the current work, it introduces briefly the main objectives of this thesis.

2.1 Radiative transfer theory

According to the Planck's law, all targets with absolute temperature larger than 0 K emits radiance. The spectral radiance emitted from a blackbody is expressed as:

$$\boldsymbol{B}_{\lambda}(\boldsymbol{T}) = \frac{\boldsymbol{C}_1}{\lambda^5[\exp(\boldsymbol{C}_2/\lambda\boldsymbol{T}) - 1]}, \tag{2.1}$$

where, $\boldsymbol{B}_{\lambda}(\boldsymbol{T})$ is the spectral radiance (W.m^{-2}.μm^{-1}.sr^{-1}) at temperature $\boldsymbol{T}$ (K) and wavelength λ (μm); $\boldsymbol{C_1}$ and $\boldsymbol{C_2}$ are physical constants ($\boldsymbol{C_1}$=1.191×10^{8} W.μm^{4}.m^{-2}.sr^{-1}, $\boldsymbol{C_2}$=1.439 ×10^{4} μm.K). Because most natural targets are non-black bodies, the emissivity ε, which is defined as the ratio of the radiance of a target to that of a black body at the same temperature, must be taken into account. According to the definition of emissivity, only the blackbody has an emissivity 1, and the natural targets are usually non-unity, i.e. $0 < \varepsilon_{\lambda} < 1$. The spectral radiance of a non-black body is given by the spectral emissivity multiplied by Planck's law as shown in Eq.(2.1).

The measured radiance by a sensor onboard the satellite or the aircraft is contributed by both surface and atmosphere. For a cloud-free sky, several different sources of the radiance at the Top Of Atmosphere (TOA) are presented in Fig.2-1 in details and the measured radiance in an infrared channel $\boldsymbol{i}$ is given by:

$$\boldsymbol{I_i}(\theta_v, \varphi_v) = \boldsymbol{R_i}(\theta_v, \varphi_v) \cdot \tau_i(\theta_v, \varphi_v) + \boldsymbol{R}_{ati\uparrow} + \boldsymbol{R}_{sli\uparrow}. \tag{2.2}$$

The first term of the right-hand side of Eq.(2.2) is the measured surface-leaving radiance after attenuation passing through the atmosphere (path ① in Fig.2-1), and the second and third terms are the contribution of upward atmospheric emission $\boldsymbol{R}_{ati\uparrow}$ and scattered solar radiance $\boldsymbol{R}_{sli\uparrow}$ (paths ② and ③). The surface-leaving radiance $\boldsymbol{R}_{\boldsymbol{i}}(\theta_{\boldsymbol{v}}, \varphi_{\boldsymbol{v}})$ is written as:

$$\begin{aligned}\boldsymbol{R}_{\boldsymbol{i}}(\theta_v,\varphi_v) = \varepsilon_{\boldsymbol{i}}(\theta_v,\varphi_v)\boldsymbol{B}_{\boldsymbol{i}}(\boldsymbol{T}_s) + [1-\varepsilon_{\boldsymbol{i}}(\theta_v,\varphi_v)]\cdot \boldsymbol{R}_{\boldsymbol{ati}\downarrow} + [1-\varepsilon_{\boldsymbol{i}}(\theta_v,\varphi_v)]\cdot \boldsymbol{R}_{\boldsymbol{sli}\downarrow} \\ + \rho_{\boldsymbol{i}}(\theta_s,\varphi_s,\theta_v,\varphi_v)\cdot \boldsymbol{E}_{\boldsymbol{i}}\cos(\theta_s)\tau_{\boldsymbol{i}}(\theta_s,\varphi_s)\end{aligned}, \qquad (2.3)$$

where, $\theta_{\boldsymbol{v}}$ and $\varphi_{\boldsymbol{v}}$ are the viewing zenith angle and azimuth angles, while $\theta_{\boldsymbol{v}}$ and $\varphi_{\boldsymbol{v}}$ are solar zenith and azimuth angles. $\tau_{\boldsymbol{i}}$ is the atmospheric transmittance. This first term of the right-hand side of Eq.(2.3) is the surface thermal radiation (path ④), while $\varepsilon_{\boldsymbol{i}}(\theta_{\boldsymbol{v}}, \varphi_{\boldsymbol{v}})$ is the surface emissivity in the viewing direction, and $\boldsymbol{B}(\boldsymbol{T}_{\boldsymbol{s}})$ is the surface emission calculated from the Planck's law at the temperature $\boldsymbol{T}_{\boldsymbol{s}}$. The second and third terms are the downward atmospheric radiance and solar scattering radiance reflected by the surface at the viewing direction (paths ⑤ and ⑥, respectively); the last part (path ⑦) of Eq.(2.3) presents the solar direct illumination reflected by the surface with the bi-directional reflectivity $\rho_{\boldsymbol{i}}(\theta_{\boldsymbol{s}}, \varphi_{\boldsymbol{s}}, \theta_{\boldsymbol{v}}, \varphi_{\boldsymbol{v}})$. For the middle infrared channel (3~5μm) in nighttime and the thermal infrared channel (8~14μm), the reflected solar radiance (the third and fourth terms in Eq.(2.3)) are negligible.

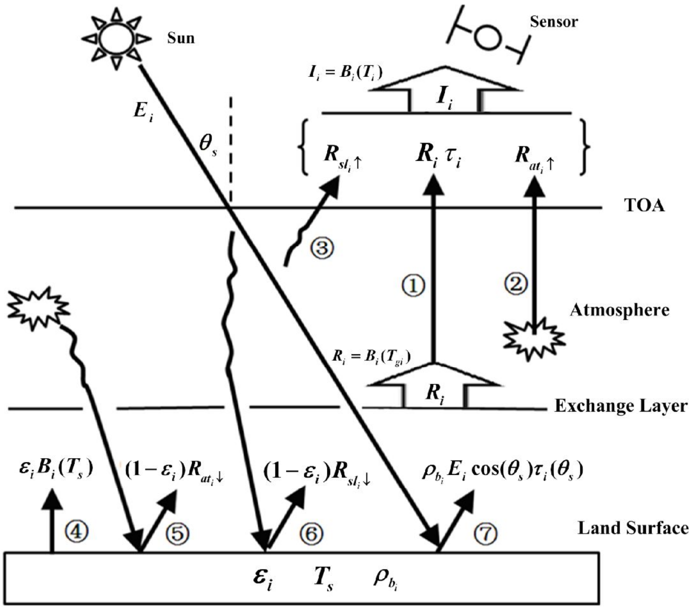

Fig.2-1. Illustration of radiative transfer equation in the infrared regions (Li et al. 2013a)

It is worth noting that all variables/parameters in Eqs. (2.2) and (2.3), except for the angles ($\theta_{\boldsymbol{s}}$, $\varphi_{\boldsymbol{s}}$, $\theta_{\boldsymbol{v}}$ and $\varphi_{\boldsymbol{v}}$), are channel-effective values. Most satellite sensors measure the outgoing radiation within a finite spectral bandwidth. The channel-effective quantity $\boldsymbol{X}_{\boldsymbol{i}}$ of interest is therefore a weighted average from spectral quantities $\boldsymbol{x}_{\lambda}$ and the channel's filter function $\boldsymbol{f}(\lambda)$ in the range (λ_1, λ_2) , expressed as:

$$\boldsymbol{X}_{\boldsymbol{i}} = \frac{\int_{\lambda_1}^{\lambda_2} \boldsymbol{f}_{\boldsymbol{i}}(\lambda)\boldsymbol{x}_{\lambda}\boldsymbol{d}\lambda}{\int_{\lambda_1}^{\lambda_2} \boldsymbol{f}_{\boldsymbol{i}}(\lambda)\boldsymbol{d}\lambda}. \qquad (2.4)$$

2.2 Definition of temperature and emissivity for land surface

As noted in (Prata et al. 1995), the definition of the surface temperature may depend strongly on the type of application and the method of measurement. Because the surface temperature $\boldsymbol{T_s}$ in Eq.(2.3) is defined using the radiance emitted by a surface, this temperature is called the radiometric temperature (or the skin temperature) that corresponds to the radiation emitted from depths less than the penetration depth of a given wavelength (Becker and Li 1995; Norman and Becker 1995). The penetration depth is usually within a few millimeters in the TIR region (Wan 1999) . This radiometric temperature physically differs from other definition of temperatures, such as the thermodynamic temperature defined for a medium in thermal equilibrium and measured by a thermometer. For homogeneous and isothermal surfaces, the radiometric and thermodynamic temperatures are reported to be equivalent. As the thermodynamic temperature is actually hard to measure in reality, even for water bodies, the radiometric temperature is often the only practical measurement for the homogeneous and isothermal surface. However, most surfaces are not in equilibrium and for heterogeneous and non-isothermal surfaces, these two temperatures are different. Considering that the spatial resolution of the current onboard systems varies approximately from 10^{-2} to 10 km^2, there may be several surface types with different temperatures and emissivities within one pixel, which complicates the physical understanding of the LST values retrieved from space and the relation of the radiometric temperature at large scales to other temperatures used in different applications. In that case, because of the coupling of the temperature and emissivity, the definition of temperature depends on that of the emissivity.

There are currently several definitions of the emissivity, such as the ***r-emissivity*** (Becker and Li 1995), the ***e-emissivity*** (Norman and Becker 1995) and the apparent emissivity (Li et al. 1999).

A. ***r-emissivity***

For a pixel made up of $\boldsymbol{N}$ homogeneous components with known emissivity in given spectral domain and viewing angles, the ensemble emissivity of a mixed pixel along the viewing direction ($\theta_{\boldsymbol{v}}$ and $\varphi_{\boldsymbol{v}}$) can be expressed as:

$$\varepsilon_{\boldsymbol{r}}(\theta_v,\varphi_v)=\sum_{\boldsymbol{k}=1}^{\boldsymbol{N}}\boldsymbol{a_k}\varepsilon_{\boldsymbol{k}}(\theta_v,\varphi_v)\,, \tag{2.5}$$

where $\boldsymbol{a_k}$ is the relative proportion of the $\boldsymbol{k}$th components in the pixel, and the sum of all $\boldsymbol{a_k}$ is unity. According to Eq.(2.5), Wan and Dozier (1996) further defined the band-average emissivity by adding the channel's filter function to Eq.(2.5) and applied it to retrieve LST from MODIS TIR data. The ***r-emissivity*** is a characteristic of the surface, and independent on the components' temperatures. Furthermore, for most of the common terrestrial surfaces, this emissivity is the complement to the hemispherical-directional reflectance $\rho(\theta_{\boldsymbol{v}}, \varphi_{\boldsymbol{v}})$, following the Kirchhoff's law, by ensemble in the same spectral domain and view direction:

$$\varepsilon_{\boldsymbol{r}}(\theta_{\boldsymbol{v}},\varphi_{\boldsymbol{v}})=1-\rho(\theta_{\boldsymbol{v}},\varphi_{\boldsymbol{v}})=1-\int_0^{2\pi}\int_0^{\pi/2}\rho(\theta_{\boldsymbol{s}},\varphi_{\boldsymbol{s}},\theta_{\boldsymbol{v}},\varphi_{\boldsymbol{v}})\sin\theta_{\boldsymbol{s}}\sin\theta_{\boldsymbol{s}}\boldsymbol{d}\theta_{\boldsymbol{s}}\boldsymbol{d}\varphi_{\boldsymbol{s}}\,. \tag{2.6}$$

In the above equation, the last part describes the integration of bi-directional reflectance in the upper hemisphere. One of the advantages of ***r-emissivity*** is its measurability from space and its scale invariability. However, this type of definition makes the definition of LST wavelength- and viewing-angle-dependent and also dependent on the distributions of surface temperature and emissivity within a pixel.

B. ***e-emissivity***

The emissivity is defined as the ratio of the radiance of an ensemble of natural surface to the radiance of that ensemble with the same temperature distribution, and each component is assumed a blackbody in the same spectral domain and viewing angle:

$$\varepsilon_{\boldsymbol{e}}(\theta_v,\varphi_v)=\frac{\sum_{\boldsymbol{k}=1}^{\boldsymbol{N}}\boldsymbol{a}_{\boldsymbol{k}}\varepsilon_{\boldsymbol{k}}(\theta_v,\varphi_v)\boldsymbol{B}(\boldsymbol{T}_{\boldsymbol{k}})}{\sum_{\boldsymbol{k}=1}^{\boldsymbol{N}}\boldsymbol{a}_{\boldsymbol{k}}\boldsymbol{B}(\boldsymbol{T}_{\boldsymbol{k}})}, \tag{2.7}$$

where, $\boldsymbol{B}(\boldsymbol{T}_{\boldsymbol{k}})$ is the radiance of ***k***th component at its temperature $\boldsymbol{T}_{\boldsymbol{k}}$. From this definition, the ***e-emissivity*** depends on the temperature distribution of the ensemble components and on the characteristic of the components. Besides, Eq.(2.7) implies that the denominator is an equivalent black body at a temperature $\boldsymbol{T}$. However, this temperature varies with channels because an equivalent black body at a given temperature, composed of black bodies at different temperatures, does not exist.

C. ***Apparent emissivity***

In order to keep the Planck's law and BRDF-derived emissivity unchanged in the heterogonous and non-isothermal pixels, Li et al.(1999) proposed the apparent emissivity, defined by adding an apparent emissivity increment caused by the temperature difference of non-isothermal surface into the ***r-emissivity*** to make the definition of LST independent of viewing angle and wavelength:

$$\varepsilon_{\boldsymbol{app}}(\theta_v,\varphi_v)=\varepsilon_{\boldsymbol{r}}(\theta_v,\varphi_v)+\Delta\varepsilon=\varepsilon_{\boldsymbol{r}}(\theta_v,\varphi_v)+\boldsymbol{K}_\lambda(\boldsymbol{T}_0)\sum_{\boldsymbol{k}=1}^{\boldsymbol{N}}\boldsymbol{a}_{\boldsymbol{k}}\varepsilon_{\boldsymbol{k}}(\theta_v,\varphi_v)\Delta\boldsymbol{T}_{\boldsymbol{k}}, \tag{2.8}$$

where, $\boldsymbol{T}_0$ is the reference temperature that is independent with the wavelength and viewing angle, and $\Delta\boldsymbol{T}_{\boldsymbol{k}}$ is the difference between this reference temperature and the ***k***th component temperature. $\boldsymbol{K}_\lambda(\boldsymbol{T}_0)$ is a function of both wavelength and temperature, written as $\boldsymbol{K}_\lambda(\boldsymbol{T}_0) = \boldsymbol{B}'(\boldsymbol{T}_0)/\boldsymbol{B}(\boldsymbol{T}_0)$, in which $\boldsymbol{B}'(\boldsymbol{T}_0)$ is the first derivation of the Planck's law at the reference temperature $\boldsymbol{T}_0$. Although the LST derived from the apparent emissivity is invariant with wavelength and viewing angle, the apparent emissivity itself varies with wavelength and temperatures ($\boldsymbol{T}_0$ and $\boldsymbol{T}_{\boldsymbol{k}}$). If the reference temperature $\boldsymbol{T}_0$ is inaccurately determined, the apparent emissivity may be consequently larger than unity. Besides, the reference and the components' temperatures cannot be obtained in practice.

These definitions are the same for homogeneous and isothermal surface, but because natural surfaces observed from space are usually heterogeneous, the assumptions of homogeneity and thermal equilibrium are often violated in reality, especially in measurements with low spatial resolution. Therefore, the differences between these definitions are evident in many cases. Since the ***r-emissivity*** is invariant with the temperature and measurable from bi-directional thermal reflectance at space and ground levels, it provides an access to estimate the emissivity separately before LST retrieval by offline computer simulation or from vegetation index. Therefore, the ***r-emissivity*** is often recommended for LST retrieval from space and will be used in this thesis for illustration. However, one should note that the ensemble emissivity presented in Eq.(2.5) is a not completely accurate since it ignores the single and multiple scattering within a pixel, and the angular behavior of the emissivity mainly due to the angular variation of the relative fractions $\boldsymbol{a_k}$ rather than to the component emissivity $\varepsilon_{\boldsymbol{k}}$ which is almost independent on the viewing angle for most natural targets.

2.3 Atmospheric transmittance code and atmospheric data

The most popular transmittance codes, such as the series of MODTRAN (Berk et al. 2003) and 4A/OP(Chaumat et al. 2009), have been widely used to perform atmospheric corrections and/or to simulate satellite TIR data. MODTRAN (MODerate spectral resolution atmospheric TRANsmittance and radiance code) was developed by Air Force Research Labs (AFRL) in collaboration with Spectral Sciences, Inc(SSI). MODTRAN calculates atmospheric transmittance and radiance for frequencies from 0 to 50,000 cm^{-1} at moderate spectral resolution, primarily 2 cm^{-1} (20 cm^{-1} in the UV). The original development of MODTRAN was driven by a need for higher spectral resolution and greater accuracy than that provided by the LOWTRAN series of band model algorithms. Except for its molecular band model parameterizations, MODTRAN adopts all the LOWTRAN 7 capabilities, including spherical refractive geometry, solar and lunar source functions, and scattering (Rayleigh, Mie, single and multiple), and default profiles (gases, aerosols, clouds, fogs, and rain) (http://imk-msa.fzk.de/Software/Modtran/MODTRAN.htm).

The most recently released version of the code, MODTRAN 5, provides a spectral resolution of 0.2 cm^{-1} using its 0.1 cm^{-1} band model algorithm. However, this thesis did not have the access to get this latest version, and thus replaced it with MODTRAN 4, which implemented a correlated-k algorithm for accurate calculation of multiple scattering, added the azimuth dependent DISTORT option and upgraded the ground BRDF model and database. All of these refinements made the calculation of MODTRAN 4 more accuracy than the former versions. Therefore, it was widely used since its release in 2000 and modification in 2003.

4A/OP (Operational release for 4A radiative transfer model) is a fast and accurate line-by-line radiative transfer model particularly efficient in the infrared region of the spectrum. Compared with MODTRAN, 4A/OP uses a comprehensive database (GEISA) of monochromatic optical thicknesses for up to 43 atmospheric molecular species and to simulate transmittance and radiance at high spectral resolution (the nominal spectral resolution is 5×10^{-4} cm^{-1} but it can be changed by users) in the spectral range of 600 ~ 3000 cm^{-1}(about 3.3 μm ~16.6 μm). Therefore, 4A/OP is more suitable for the calculation of (super) hyperspectral TIR data, such as Infrared Atmospheric Sounding Interferometer (IASI) onboard METOP. More detains are included in (Chaumat et al. 2009).

The accuracy of the calculation of those codes depends on that of the code itself and input atmospheric data. As reported by (Wang et al. 1996), the agreement of MODTRAN is usually within a few percent root-mean-square error (RMSE) and seldom exceeds 5%. MODTRAN provides six standard atmospheric profiles: tropical, mid-latitude summer, mid-latitude winter, sub-arctic summer, sub-arctic winter and 1976 U.S standard. Each profile contains 36-layer atmospheric data: altitude, air pressure, air temperature, water vapor density, and layer concentration of ozone, carbon dioxide, carbon monoxide, methane, nitrous oxide, oxygen, nitric oxide, sulphur dioxide, nitrogen dioxide, and ammonia. In addition to the six standard atmospheres, MODTRAN also provides the New Model Atmosphere option to accept the atmosphere defined by user from radiosoundings data (e.g. Thermodynamic Initial Guess Retrieval (TIGR) database), onboard vertical sounder (e.g. MODIS) or meteorological forecasting models, such as the National Centers for Environmental Prediction (NCEP) and the European Centre for Medium-Range Weather Forecasts (ECMWF). Some other instrument, for example CE318 Sunphotometer, can also provide the column water vapor and near surface air temperature for the MODTRAN.

Fig.2-2 presents the spectral atmospheric transmittance simulated by MODTRAN with 1976 U.S. atmosphere, which indicates that sensors onboard the satellite for the retrieval of LST and emissivity must be built in the “atmosphere windows” of about 3 ~ 5 μm (middle infrared, MIR) and 8 ~ 14 μm (thermal infrared, TIR), where the atmosphere is mostly transparent for the surface radiance.

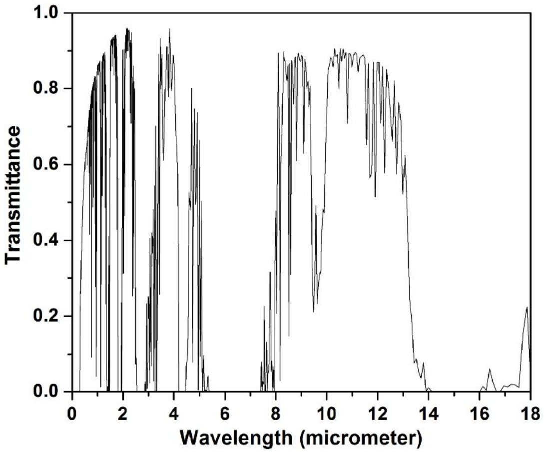

Fig.2-2. Atmospheric transmittance in the range of 0 ~ 18 μm under 1976 U.S. standard atmosphere profile

2.4 Emissivity spectra database

Emissivity of natural surface at ground can be measured on basis of the direct inversion of spectral radiative transfer equation (i.e. Eq.(2.3)) or from the complementary to the hemispheric-directional reflectivity (Salisbury and D'Aria 1992). Two popular emissivity spectra databases that are currently used for the algorithm development are the ASTER spectral library (Baldridge et al. 2009) and the University of California Santa Barbara library (UCSB) (Snyder et al. 1998), respectively. The ASTER spectral library was released since 2008 and contains about 1330 emissivity spectra in the range of 3 ~ 14 μm for natural and man made materials, collected from three other spectral libraries: the Johns Hopkins University (JHU) Spectral Library the Jet Propulsion Laboratory (JPL) Spectral Library, and the United States Geological Survey (USGS - Reston) Spectral Library. The data in the UCSB spectral library was measured by the Institute for Computational Earth System Science at the University of California, Santa Barbara, which included 123 land surface emissivity spectra. The surfaces in those databases mainly include vegetation, rock, sand, water, snow/ice, and manmade materials. Fig.2-3 displays the spectral variation of several samples selected from the libraries. It indicates that the spectral emissivity of water and green grass is almost flat in the atmosphere windows 3 ~ 5 μm and 8~14 μm, while that of soils and dry grass varies significant and has a larger value range. Therefore, an accurate estimate of soil emissivity turns out to be more crucial than that of vegetation for accurately retrieving LST from remotely sensed data. Besides, the channel emissivity of a sensor can be calculated from the spectral value with the spectral response function using Eq.(2.4).

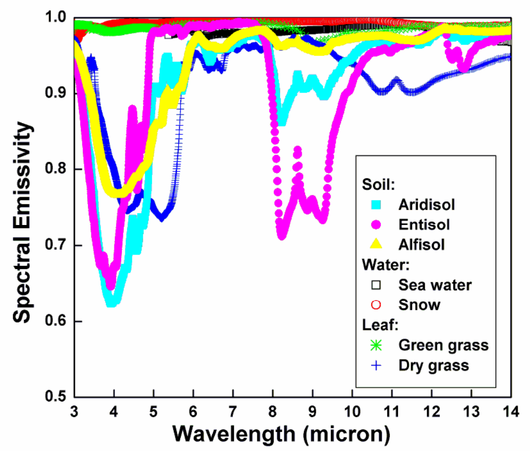

Fig.2-3. Spectral emissivity of several samples including water, soil and leaf

2.5 Estimate of LST and emissivity from space

To date, many algorithms have been developed to retrieve LST from remotely sensed data with different way of removing emissivity and atmospheric effect. Apart from the atmospheric effect, the methods of retrieving LST and emissivities can be grouped to two categories: stepwise retrieval method and simultaneous retrieval of both variables.

2.5.1 Stepwise retrieval method

In this case, LST and emissivity are retrieved step by step: the emissivity is firstly determined, and then LST is retrieved with the determined emissivity as a prior. Two types of methods estimating land surface emissivity (LSE) are respectively the semi-empirical classification-based method and the empirical relationship between the normalized difference vegetation index (NDVI), derived from the VNIR data. The combination of day and night observations in MIR and TIR channels is also promising to obtain emissivity in advance.

There are two common methods that retrieve LST with known emissivity, which are the single-channel method and the split-window method.

(1) Classification-based emissivity retrieval method (CBEM).

This method generally uses the conventional land-cover classification information to determine the emissivity of the pixel. The key points of this method are the emissivity database and the land-cover products. For example, Snyder et al. (1998) developed an emissivity database in MODIS TIR channels by using three kernel-driven BRDF models based on the laboratory emissivity spectra and canopy structural parameters (Snyder and Wan 1998), driven from approximate descriptions of the cover type. In the model, the emissivity was calculated from the hemispheric-directional reflectance based on the integration of BRDF over an angle range from 0° to 65°, and the Kirchhoff's law. Finally, emissivities for 14 distinct land covers in the IGBP (International Geosphere-Biosphere Programme) were obtained and saved in a Look-up table (LUT). With this emissivity LUT, the emissivities of MODIS 31 and 32 channels are determined directly from the IGBP classification product with consideration of seasonal and dynamic states, and consequently applied in the generalised split-window algorithm to retrieve LST. Similarly, the emissivity of a pixel mixed by several land covers can be estimated using a linear mixing equation as Eq.(2.5).

Because of its operability, this method has already been applied to other satellite data, such as the AATSR on ENVISAT, the METEOSAT Second Generation-1 (MSG) data (Peres and DaCamara 2005; Trigo et al. 2008) and Geostationary Operational Environmental Satellite (GOES) data (Sun and Pinker 2003). However, the accuracy of this method highly depends on the land cover. The seasonal variation of the vegetation cover and moisture will cause some uncertainty to the emissivity and then degrade the accuracy of the retrieved LST. Besides, since the emissivity is derived from LUT and land covers, a problem about the spatial discontinuity is consequently raised.

(2) Empirical emissivity algorithm

This method is based on some empirical relationship between the vegetation index derived from the VNIR data and the emissivity in the TIR channels. Griend and Owe (1993) first found a very high correlation between the emissivity in the TIR channels covering 8 ~ 14 μm and the logarithmic NDVI. Subsequently, Valor and Caselles (1996) applied this method to estimate the effective emissivity of a rough row-distributed system. Starting from the method proposed in (Valor and Caselles 1996), Sobrino and Raissouni (2000) reduced the complexity and formulated an operational NDVI threshold method to derive the emissivity from space, with three linear functions corresponding to conditions in which a pixel is composed of full vegetation, of full soil or of mixed soil/vegetation:

$$\varepsilon_\lambda = \begin{cases} \boldsymbol{a}_\lambda + \boldsymbol{b}_\lambda \rho_{\boldsymbol{red}} & \boldsymbol{NDVI} < \boldsymbol{NDVI_s}\,(\text{bare soil}) \\ \varepsilon_{\boldsymbol{v},\lambda} \boldsymbol{f_v} + \varepsilon_{\boldsymbol{g},\lambda}(1-\boldsymbol{f_v}) + \boldsymbol{d}\varepsilon_\lambda, & \boldsymbol{NDVI_s} < \boldsymbol{NDVI} < \boldsymbol{NDVI_v}\,(\text{mixed}), \\ \varepsilon_{\boldsymbol{v},\lambda} + \boldsymbol{d}\varepsilon_\lambda & \boldsymbol{NDVI} > \boldsymbol{NDVI_v}\,(\text{full vege}) \end{cases} \quad (2.9)$$

where, $\boldsymbol{a}_\lambda$ and $\boldsymbol{b}_\lambda$ are channel-dependent regression coefficients, $\rho_{\boldsymbol{red}}$ is the reflectance of the red channel, $\boldsymbol{NDVI_s}$ and $\boldsymbol{NDVI_v}$ are the NDVI corresponding to the bare soil and full vegetation, respectively. $\varepsilon_{v,\lambda}$ and $\varepsilon_{\boldsymbol{g},\lambda}$ are the vegetation and soil emissivities, respectively. Both of them can be measured in the field (Rubio et al. 1997; Rubio et al. 2003) or obtained from the emissivity database (Baldridge et al. 2009). $\boldsymbol{f_v}$ is the fraction of vegetation that can be derived either from the NDVI (Carlson and Ripley 1997; Valor and Caselles 1996) or from the variable atmospherically resistant index (VARI$_{\text{green}}$) and spectral-mixture analysis (SMA) techniques (Sobrino et al. 2008), $d\varepsilon_\lambda$ means cavity effect of multiple scattering, and can take values of 0.02 and higher from numerical simulation (Valor and Caselles 1996). $\boldsymbol{NDVI_s}$ and $\boldsymbol{NDVI_v}$ can be estimated from the histogram for the entire scene (Dash et al. 2005; Sobrino et al. 2008). For its simplicity, this method can be applied to any sensor that has red and near-infrared channels to calculate NDVI, such as the AVHRR, MODIS, TM, SEVIRI, ATSR and CHRIS (Sobrino et al. 2004b; Sobrino et al. 2003). Similar to the CBEM, this method also causes spatially discontinuous emissivity values of regions transitioning from soil-type to vegetation-type, because the emissivities in those regions are calculated from different formulae, and its accuracy will be degraded by the errors included in the vegetation and soil emissivity, and the fraction of vegetation as well as the NDVI thresholds used to distinguish bare soil and full vegetation.

(3) Temperature-independent spectral indices (TISI) method.

Based on two assumptions that the Planck's law can be approximated using a power function for a MIR or TIR channel and the pixel emissivities have no significant change during daytime and nighttime observations, Becker and Li (1990a), and Li and Becker (1990) first proposed a TISI-based method to perform spectral analysis in the TIR region. Subsequently, assuming that the $\boldsymbol{TISI_{ij}}$ ($\boldsymbol{i}$ is the MIR channel and $\boldsymbol{j}$ is the TIR channel) in the daytime without the contribution of solar illumination is the same as the $\boldsymbol{TISI_{ij}}$ in the nighttime, Li and Becker (1993) and Li et al. (2000) further developed a day/night TISI-based method to first extract the bi-directional reflectivity in MIR channel $\boldsymbol{i}$ by eliminating the emitted radiance during the day in this channel by comparing the $\boldsymbol{TISI_{ij}}$ in the daytime and the nighttime. Once the bi-directional reflectivities in an MIR channel are retrieved, the directional emissivity in that MIR channel can be estimated as the complementary to the hemispheric-directional reflectivity following the Kirchhoff's law. The hemispheric-directional reflectivity can be estimated from a bi-directional reflectivity data series using either an angular form factor (Li et al. 2000), a semi-empirical phenomenological model(Petitcolin et al. 2002a, b) or a kernel-driven bi-directional reflectivity model(Jacob et al. 2004; Jiang and Li 2008a). Finally, based on the concept of the TISI, the emissivities in the TIR channels can be obtained from the two-channel TISI (Jiang et al. 2006; Li et al. 2000). Once the emissivities are known, the LST can be retrieved using single-channel method or split-window method.

The TISI-based method allows us to obtain emissivity without any prior information about the emissivity itself, as long as there is no occurrence of precipitation, snow or dew during the two observations, and the radiance is atmospherically corrected. However, since the TISI-based method needs the daytime and nighttime observation at the same target in a short time, its application cannot be achieved to those sensors that have no ability to fill this requirement. In order to deal with this problem, Goïta and Royer (1997) extended the original TISI method to make it available for the emissivity retrieval from two consecutive datasets acquired at the same daytime, by introducing more simplifications on the TISI and the characteristics of the bi-directional reflectivity. Besides, they also obtained the TISI using a linear regression model from the ratio of the atmospherically corrected radiances of the MIR and TIR channels. However, their simplifications, especially the case of TISI = 1, will cause some unexpected error to the retrieved emissivity and then the LST. Besides, the mismatch in space and viewing angle between the two observations might reduce the retrieval accuracy of emissivity.

(4) Single-channel LST retrieval method

With the emissivity calculated in advance, the single-channel method uses the radiance measured by the satellite sensor in a single channel, chosen within an atmospheric window, to retrieve LST from the inversion of the radiative transfer model given in Eqs. (2.2) and (2.3) by correcting the radiance for residual atmospheric attenuation and emission using atmospheric transmittance/radiance code that requires input data on the atmospheric profiles. The atmospheric profiles can be generally obtained either from ground-based atmospheric radiosoundings, from satellite vertical sounders (e.g. MODIS, TOMS) or from meteorological forecasting models (e.g. NCEP and ECMWF). In order to reduce the dependence on atmospheric profiles, several single-channel algorithms have been proposed to estimate the LST from satellite data by parameterizing the atmospheric data. Qin et al. (2001) proposed a method to estimate the LST specifically from Landsat-5 TM data using only the near-surface air temperature and water vapor content instead of atmospheric profiles using empirical linear relationships between the atmospheric transmittance and the water vapor content and between the mean atmospheric temperature and the near-surface air temperature. Jiménez-Muñoz and Sobrino (2003) and Jiménez-Muñoz and Cristóbal (2009) developed a generalized single-channel algorithm for retrieving the LST from any TIR channel with a FWHM (full width at half maximum) of about 1 µm, provided that the emissivity and the total atmospheric water vapor content are known. This generalized single-channel algorithm requires the minimum input data and can be applied to different thermal sensors using the same equation and coefficient.

(5) Split-window LST retrieval method

The basis of this method is that the atmospheric attenuation suffered by the surface emitted radiance is proportional to the difference between the at-sensor radiances measured simultaneously in two adjacent thermal infrared channels. This method was firstly proposed by McMillin (1975) to estimate Sea Surface Temperature (SST) from satellite measurements, and then was extended to retrieve LST from space. On the basis of the first Taylor series of the radiative transfer equation, the LST is linearly related to the brightness temperatures of two adjacent TIR channels in the 10 ~ 12.5 µm regions, and a typical linear split-window algorithm can be written as Eq.(2.10) with the emissivities of these two channels are known (Atitar and Sobrino 2009; Becker and Li 1995; Becker and Li 1990b; Prata 1993; Sobrino et al. 1994; Tang et al. 2008; Wan and Dozier 1996).

$$\boldsymbol{T_s} = \boldsymbol{a}_0 + \boldsymbol{a}_1\boldsymbol{T_i} + \boldsymbol{a}_2(\boldsymbol{T_i} - \boldsymbol{T_j}), \qquad (2.10)$$

where, $\boldsymbol{T_i}$ and $\boldsymbol{T_j}$ are the brightness temperatures of the two adjacent TIR channels, and $\boldsymbol{a_i}$ ($\boldsymbol{i}$=0, 1, and 2) are coefficients that depend primarily on the spectral response function of the two channels $\boldsymbol{f_i}(\lambda)$ and $\boldsymbol{f_j}(\lambda)$, the two channel emissivities ε_i and ε_j, the column water vapor (WV) in the atmosphere, and the viewing zenith angle. They are generally pre-determined either by fitting the simulated data with a set of atmospheres and surface parameters or empirically by comparing the satellite data against ***in situ*** LST measurements. In the past decades, many split-window algorithms, with linear or non-linear relationship with the brightness temperatures of two or three TIR channels, have been developed to retrieve LST from different sensors by additionally parameterizing the coefficients $\boldsymbol{a_i}$ according to various combinations of the emissivity, WV, and the VZA (Becker and Li 1995; Coll and Caselles 1997; François et al. 1997; Minnis and Khaiyer 2000; Pinheiro et al. 2004; Sobrino et al. 2004a; Sobrino and Romaguera 2004; Sun and Pinker 2003; Sun and Pinker 2007; Wan and Dozier 1996). Because of its little requirement of atmospheric data, which is not accessible for most sensors, and also because of its easy operation, the split-window algorithm has been successfully applied to many sensors with two TIR channel, such as AVHRR, MODIS, SEVIRI, FY-3(Hulley et al. 2011; Jiang and Li 2008b; Kerr et al. 1992; Sun and Pinker 2003; Tang et al. 2008; Wan and Dozier 1996). Because the land surface shows more heterogonous than the sea surface, the LST cannot be retrieved with accuracy as high as that of the SST. However, validation results indicated that, with such an approach and considering our knowledge of surface emissivity, accuracies of 1 to 2 K are generally attainable over land surface (Wan 2008; Wan et al. 2002; Yu et al. 2008).

2.5.2 Methods of simultaneous retrievals of LST and emissivity

In the above stepwise retrieval method, if errors included in the emissivity is significant, the consequently retrieved LST will be far away from the truth. Therefore, it is often needed to retrieve both LST and emissivity simultaneously. This goal has been achieved from multiple-channel (e.g. TES method and gray body method), and multiple-time TIR data (e.g. Two-Temperature Method and physical day/night method).

(1) Temperature and Emissivity Separation method (TES)

The TES method was first developed by Gillespie et al. (1998) to decouple LST and emissivity from five atmospherically corrected TIR channels' radiance of the Advanced Spaceborne Thermal Emission and Reflection Radiometer (ASTER). It consists of three mature modules: the normalization emissivity method (NEM) (Gillespie 1995), the spectral ratio (SR), and the maximum–minimum apparent emissivity difference method (MMD) (Matsunaga 1994). This method utilizes a relationship between the minimum emissivity $\varepsilon_{\min}$ and the spectral contrast (MMD) to increase the number of equation and make the ill-posed problem become solvable, as:

$$\varepsilon_{\min} = 0.994 - 0.687\boldsymbol{MMD}^{0.737}\,. \tag{2.11}$$

Since the TES method used the spectral variation of emissivity to separate the LST and emissivity, it can perform better for those natural surfaces with high spectral contrast emissivities such as rocks and soils. Numerical simulation and some field validations have demonstrated that the TES can recover LST and LSE consistently within ± 1.5 K and ± 0.015

when the atmospheric effects are accurately corrected (Gustafson et al. 2006; Sobrino et al. 2007; Yoriko et al. 2003). However, some reports have indicated that the TES method exhibited significant errors in the LST and emissivity of surfaces with low spectral contrast emissivity (e.g., water, snow, vegetation) and under hot and wet atmospheric conditions (Coll et al. 2007; Gillespie et al. 2011; Gustafson et al. 2006; Jimenez-Munoz and Sobrino 2007; Payan and Royer 2004). To deal with those problems, TES has been modified several times (see Table 1 in (Sabol et al. 2009)) to accommodate low emissivity contrasts and errors in measured data. For example, Sabol et al. (2009) replaced the power relationship of $\varepsilon_{\min}$ and MMD in the original TES method with a linear expression, and applied the new relationship available for all materials to alleviate low contrasts problem, and Gillespie et al. (2011) used a water vapour scaling (WVS) approach proposed in (Tonooka 2001, 2005) to improve the accuracy of this method by minimizing atmospheric correction errors. Besides, Hulley and Hook (2011) recently refined the relationship between the minimum emissivity and spectral contrast to make TES algorithm available for MODIS's three TIR channels (29, 31 and 32). However, because of its requirement of at least three TIR channels in the atmospheric window, the TES method is not applicable for those sensors with only one or two channels.

(2) Gray Body Method

This method assumes the spectral emissivity for wavelengths larger than 10 μm is relatively flat and the emissivity is almost wavelength-independent. If emissivities for two or more channels can be considered to be the same, the number of the unknowns will be equal to or less than that of the radiative transfer equations, and consequently, the LST and emissivity will be determined from multiple-channel TIR data (Barducci and Pippi 1996). The advantage of this method is that it does not require the detail information about the emissivity spectra and only assumes that at least two channels have the same emissivity (no need to be the gray body) in the wavelength interval of interest. This assumption is reasonable for dense vegetation and water, but is difficult to be satisfied for those surface with high emissivity spectral contrast in multiple channels, such as bare soil, sand and sparse vegetation. Besides, since atmospheric correction on the radiance is needed, the accuracy of this method can be degraded by the error in the input atmospheric data. However, this method shows more promising for hyperspectral TIR data because two or more channels with the same emissivity out of its hundreds of channels can be expected.

(3) Two-Temperature Method (TTM)

The TTM reduced the number of unknowns by assuming the emissivity is unchanged during two observations. In this case, $\boldsymbol{N}$ TIR channel in two observations correspond to $\boldsymbol{2N}$ equations and $\boldsymbol{N}+2$ unknowns (N channels' emissivity and 2 temperatures). As a result, if a sensor has $\boldsymbol{N} \geq 2$ TIR channels, both LST and emissivity can be retrieved from two observations (Peres and DaCamara 2004a, b, 2006; Watson 1992). The main advantage of the TTM is that there is no assumption about the shape of the spectral emissivity, except that the spectral is time-invariant. However, the high correlation of the radiative transfer equation between adjacent TIR channels always causes the retrieval accuracy highly sensitive to the error in atmospheric correction and the measured data, and also its accuracy can be degraded by the mismatch of geometrical registration and pixel sizes in the different observation. As report by (Peres and DaCamara 2004b, 2006), the increase of the number of observations and temperature difference among those observations, as well as a non-linear optimization algorithm, can improve the retrieval accuracy of the TTM, but the improvement was still limited by the constraint of the method itself.

(4) Physical Day/night method (D/N)

Inspired by the day/night TISI-based method and TTM method, Wan and Li (1997) further developed a physics-based D/N method to simultaneously retrieve LST and emissivity from a combined use of the day/night pairs of MIR and TIR data. This method assumes that the emissivities do not significantly change from day to night and that the angular form factor has very small variations (<2%) in the MIR wavelength of interest to reduce the number of unknowns and make the retrieval more stable. To reduce the effect of the residual error of atmospheric corrections on the retrieval, two variables, the air temperature at the surface level ($\boldsymbol{T_a}$) and the column water vapor (***WV***), are introduced to modify the initial atmospheric profiles in the retrieval. With two measurements (day and night) in ***N*** channels, the numbers of unknowns are ***N***+7 (***N*** channel emissivity, 2 LSTs, 2 $\boldsymbol{T_a}$, 2 ***WV***, and 1 angular form factor for the MIR channels). Thus, to make the equations deterministic, ***N*** must be equal to or greater than seven. The D/N method was successfully applied on the MODIS MIR channels (CH20:3.66~3.84 μm, CH22: 3.93~3.99 μm, CH23: 4.02~4.08 μm) and TIR channels (CH29: 8.4~8.7 μm, CH31: 10.78~11.28 μm, CH32: 11.77~12.27 μm, CH33: 13.19~13.49μm), to generate global daily LST and emissivity products.

Compared with the TTM, the D/N improved the accuracy of LST and emissivity by using the data in MIR channel to reduce the high correlations of the radiative transfer equations among the TIR channels, and by refining the atmospheric data with the near-surface air temperature $\boldsymbol{T_a}$ and the column water vapor ***WV***. Besides, considering the angular variation in emissivity, the whole range of MODIS viewing zenith angles (55° was designed, but the actual value is 65° due to the Earth’s curvature) was separated into subranges and selection is done of a pair of clear-sky daytime and nighttime MODIS observations at viewing angles in the same subranges whenever it is possible (Wan and Li 1997; Wan et al. 2004). Therefore, as long as the surface emissivity does not change significantly, daytime and nighttime data collected over several days rather than 12 hours are still appropriate. Moreover, in order to improve the retrieval accuracy, the algorithm aggregated MODIS MIR and TIR channel data from 1 km to 5 km or 6 km to reduce the drawback of mis-registration of day and night observations, and combined the use of the two MODIS sensors onboard TERRA and AQUA satellites. Note that because of the requirement of at least seven channels in MIR and TIR wavelength, the D/N method have not been used by other sensor expect the MODIS until now.

2.5.3 Methods of simultaneous retrievals of LST, emissivity and atmospheric data

Atmospheric correction is required for the above algorithm, but the atmospheric data are usually unavailable synchronously with the TIR observation and errors in the atmospheric data always influence the retrieval result significantly. Therefore, an ideal way is to simultaneously derive LST, emissivity and atmospheric data from space. Ma et al. made an initial attempt by assuming that the emissivity is invariant within the MODIS MIR channels and also invariant within the TIR channels (Ma et al. 2002; Ma et al. 2000), and Wang (2011) further combined the use of principle component analysis and artificial neural technique to obtained LST, emissivity and atmospheric profile from IASI hyperspectral TIR data. Their result showed RMSEs of LST and temperature profiles in troposphere were about 1.6 K and 2.0 K, respectively; RMSE of ***WV*** was around 0.3 g/cm^2. RMSE of emissivity was less than 0.01 in the spectral interval from 10 µm to14 µm.

2.5.4 Methods for hyperspectral TIR data and microwave data

The above is a brief description of the main approaches to derive LST and emissivity from several MIR and/or TIR channels. Compared with the multiple channels data, the hyperspectral TIR data, with hundreds of channels, provide much more detailed spectral information about the atmosphere and land surface. Therefore, it is promising to use the spectral shape of the emissivity to separate LST and emissivity. For example, the iterative spectrally smooth temperature emissivity separation method (ISSTES) achieves the retrieval by minimizing the spectral smoothness iteratively in a range of temperature based on an assumption that a typical emissivity spectrum is rather smooth compared with the spectral features introduced by the atmosphere(Borel 1998; Ingram and Muse 2001). And, Wang et al. (2011) assume that the emissivity spectrum can be divided into ***M*** segments and that the emissivity in each segment varies linearly with the wavelength. As a result, the retrieval of spectral emissivity and LST becomes the retrieval of the coefficients of each line. Besides, some other algorithms, such as stepwise refining algorithm, correlation-based separation and alpha-derived emissivity method, were also proposed to decouple LST and emissivity from hyperspectral TIR data. Details can be found in the literatures (Cheng et al. 2010; Cheng et al. 2008; Kealy and Hook 1993).

Except for MIR and TIR data, the LST can be also retrieved from microwave data for all weather conditions (Chen et al. 2011; Mao et al. 2007) because it can penetrate the cloud, in which status the MIR and TIR data from the land surface was totally obscured. The combination of the MIR and TIR data with the microwave data is often considered as a promising way to generate long-term LST product. However, it is hampered by at least two factor: firstly, the retrieved temperature from microwave data is different from that of the MIR and TIR data because it actually corresponds to the emitted radiance of the profile from land surface to the depth that the microwave penetrates into the soil and depends on the wavelength, while the retrieved temperature from the MIR and TIR data result from the surface radiance in a several microns depth. Secondly, the spatial resolution of microwave data (tens of kilometers) is usually much coarser than that of the infrared data. Therefore, there is no publication about the fusion of the two kinds of temperature data and this topic is still under investigation.

2.6 Modeling of directional radiance and emissivity

The anisotropy of the surface has been observed by many researchers either at top of canopy or at TOA This anisotropy, mainly due to the 3D structure of the surface and non-isothermal conditions existing between different components, will bring large error to the computation of long-wave outgoing radiation if not being accounted for (Otterman et al. 1999; Otterman et al. 1997). Commonly, the land surface is a mixture of two elements, namely, the soil and the vegetation, which have completely different physical properties controlling their energy balances. Modeling the directional brightness temperature (DBT) or radiance of homogenous or heterogeneous canopies is a promising approach to enhance our understanding of the angular feature, and this issue has prompted numerous thermal radiative models that can generally be divided into four categories: geometrical optical (GO) models, radiative transfer (RT) models, hybrid models (GORT), and computer/numerical simulation methods. The GO models estimate the thermal radiance by combining the weights of thermal radiance of several components, with their corresponding proportions projected in the viewing direction. Because the vegetation is considered as an opaque medium, the GO model do not simulate radiative transfer between different components. In contrast, the RT models simulate directional radiance as a function of viewing direction, temperature distribution, and leaf angle distribution within the canopy as well as the atmosphere. The canopy is always statistically distributed into homogeneous horizontal layers, and the directional radiance is calculated by summing the radiative contributions of all layers. In RT models, iterations are occasionally performed to account for multiple scattering within the canopy. The hybrid models are a combination of GO and RT models that simulate the DBT over complicated heterogeneous land surfaces.

2.6.1 Modeling for homogeneous canopy at ground

A homogeneous canopy can be easily divided into several layers and its gap frequency is related to the leaf area index, leaf angle distribution and viewing direction. Several RT models and their parameterizations can be proposed to simulate the directional radiance and emissivity of the homogeneous canopy. For example, Prévot (1985) addressed a probability-based model (turbid-medium model) calculating canopy radiances as resulting from radiative interactions between the soil and the surrounding vegetation, and interactions between the leaves within the vegetation using the directional gap frequency concept. Based on the way of estimating the upward and downward flux for each layers in the VNIR spectral range, the scattering by arbitrarily inclined leaves (SAIL) model added an additional radiative resource to the original model to extend its applications to simulate the directional thermal radiance (François 2002; Liu et al. 2003; Verhoef et al. 2007). In those modes, the directional emissivity is calculated as the ratio of the simulated directional radiance to the radiance of a black body with the assumption that all components have the same temperature.

Although the RT models can estimate the directional thermal radiance and emissivity close to the reality for most cases, the use of iterative calculation usually make it time-consuming. Since the contribution of the different components are involved in this iteration calculation, there is no clear expression in mathematic about their radiances, so it is difficult to separate the components' temperatures, which are assumed to bear more physical meaning than the average temperature of the scene. As a result, the parameterization of those RT models is thus needed. A general expression of the directional radiance of the canopy mainly consisting of soil and vegetation is written as:

$$\boldsymbol{R}(\theta_v) = \tau_{\boldsymbol{o}}(\theta_v)\varepsilon_{\boldsymbol{g}}\boldsymbol{B}(\boldsymbol{T}_{\boldsymbol{g}}) + \boldsymbol{w}_{\boldsymbol{o}}(\theta_v)\varepsilon_v\boldsymbol{B}(\boldsymbol{T}_v) + \boldsymbol{R}_{\boldsymbol{multi}} + [1-\varepsilon_{\boldsymbol{c}}(\theta_v)]\boldsymbol{R}_{\boldsymbol{at}\downarrow}, \tag{2.12}$$

where, $\tau_o(\theta_v)$ is interpreted as the upward directional canopy transmittance for the soil emission, and $\boldsymbol{w}_o(\theta_v)$ is the fraction of the upward emission of the vegetation in the viewing direction θ_v; ε_g and ε_v are the emissivity of soil and component, while ε_c is the canopy's directional emissivity; $\boldsymbol{B}(\boldsymbol{T}_g)$ and $\boldsymbol{B}(\boldsymbol{T}_v)$ are respectively the black body radiances of the soil and leaves at the temperature $\boldsymbol{T}_g$ and $\boldsymbol{T}_v$. The term $\boldsymbol{R}_{multi}$ represents the multiple scattering radiations among leaves, and between soil and leaves, and the last term is the reflected atmospheric downward radiance $\boldsymbol{R}_{at\downarrow}$ by the canopy. As a result, the parameterization of the RT models is to find approximate expressions for the terms $\tau_o(\theta_v)$, $\boldsymbol{w}_o(\theta_v)$, $\boldsymbol{R}_{multi}$ and ε_c, which can be calculated easily, and causes no significant error to the final radiance. To date, several methods have been designed with different considerations on the single or multiple scattering, hotspot effect within the canopy (Chehbouni et al. 2001; François 2002; François et al. 1997; Otterman et al. 1992; Otterman et al. 1997; Otterman et al. 1995; Shi 2011; Sobrino et al. 2005; Wang 2009).

The main idea of those parameterizations is to calculate $\tau_o(\theta_v)$, $\boldsymbol{w}_o(\theta_v)$ and $\varepsilon_c(\theta_v)$ directly from gap frequency. For example, François et al. (1997) proposed an analytical way by using the directional gap frequency and hemispheric-gap frequency related to LAI and viewing angle, and introducing a parameter, named cavity effect factor, to address the multiple scattering radiance caused by leaves, and the term $\boldsymbol{R}_{multi}$ in Eq.(2.12) was consequently included in the $\boldsymbol{w}_o(\theta_v)$. As a result, only the first, second and last terms of Eq.(2.12) left. If ε_g, ε_v and $\boldsymbol{R}_{at\downarrow}$ are known as a prior, $\boldsymbol{T}_g$ and $\boldsymbol{T}_v$ are thus retrievable from observations in at least two directions. For a mixed pixel from space, Shi (2011) added a vegetation area ratio to this model to retrieve components' temperatures from AATSR. Another way of the parameterization started with the ε_c, which was firstly estimated as the complementary to the hemispheric directional reflectance of the canopy according the Kirchhoff's law, and then $\tau_o(\theta_v)$ and $\boldsymbol{w}_o(\theta_v)$ were calculated based on the gap frequency in viewing direction and the formula $\varepsilon_c(\theta_v)= \tau_o(\theta_v)+\boldsymbol{w}_o(\theta_v)$ (François 2002). The current results indicated that the emissivity of bare soil, sand, clay, and water decreased with increasing viewing angle, but for dense vegetated canopies the angular dependence is minimal.

Furthermore, if more components such as sunlit soil and shaded soil, sunlit leaves and shaded leaves rather than only soil and leaves are considered in the canopy, the hotspot effect occurring in the solar direction is another consideration in the parameterization. However, because of its complexity, rare publications exist about this issue except in the work of (Wang 2009) who used an the clumping effect proposed in (Roujean 2000) to separate the fractions of sunlit soil and shaded soil, and the work of (Smith and Ballard 2001) who performed theoretical calculations of TIR hotspot over a homogeneous canopy using a 3D vegetation model.

Additionally, Guillevic et al. (2003) proposed a three-dimensional radiative transfer model that was based on the Discrete Anisotropic Radiative Transfer (DART) model (Gastellu-Etchegorry et al. 1996) to investigate the angular thermal radiance of a vegetated canopy. Furthermore, Peng et al. (2011) used the kernel-driven BRDF model to fit the atmospherically corrected directional surface-leaving brightness temperature, and their result showed that the accuracy of fitted directional brightness temperatures was around 1 K and that the coefficients were further a good indicator for monitoring soil moisture. However, as their TIR data still contained the reflected downward atmospheric radiance, the angular effect of the brightness temperature might be smoothed to some extent.

2.6.2 Modeling for heterogeneous canopy at ground

Compared with the homogenous canopy, the space between vegetation in incomplete canopy is no longer distributed in a uniform way, which caused the optical length passing through the vegetation layer at the same azimuth angle with different zenith angle or in the same zenith angle with different azimuth angle is not equal. Therefore, the modeling of directional radiance and emissivity for heterogeneous canopy is quite different from that for homogenous one. Many authors devoted to the studies of this issue, especially for the row-structured canopy because it is widely distributed and useful for estimating crop productivity. Commonly, the main idea of this modeling was generally reported as:

$$\boldsymbol{R}(\theta_v)=\sum_{\boldsymbol{i}=1}^{\boldsymbol{N}}\boldsymbol{f_i}(\theta_v)\cdot\boldsymbol{B}(\boldsymbol{BT_i}),\ \text{or}\ \ \boldsymbol{DBT}\approx\left[\sum_{\boldsymbol{i}=1}^{\boldsymbol{N}}\boldsymbol{f_i}(\theta_v)\cdot\boldsymbol{BT_i}^4\right]^{1/4}, \tag{2.13}$$

where, $\boldsymbol{BT_i}$ and $\boldsymbol{f_i}$ are the components' brightness temperature and directional fractions, respectively. N is the number of the involved components, always less than four types: sunlit soil and shaded soil, sunlit leaves and shaded leaves. Jackson et al. (1979) firstly developed a GO model for partially covered row crop canopies to separate components' fractions from viewing angle, plant height/width ratio, row spacing, row orientation, and Kimes et al. validated and applied this model in the simulation of cotton DBT (Kimes 1981; Kimes et al. 1980). However, although Sobrino and Caselles (1990) accounted for the radiation of plant wall, and Caselles and Sobrino (1992) considered the multiple scattering between plant rows, the effect of gaps within the plant rows were ignored because the plant rows in their model were assumed opaque. In order to solve this problem, Chen et al (2002) used the directional gap frequency to refine the original model and introduced the Kuusk hotspot effect (Kuusk 1985) to account for it in the direction where viewing and solar beams are nearly overlapping. Moreover, the model of Chen et al. (2002) was further modified by Yan et al. (2003) by using the bi-directional gap frequency. Validation on wheat canopy indicated that their results were closer to the field measurement. By additionally considering the stem and small leaves between the soil plane and vegetation, Yu et al. (2004) considered that the vegetation parts were exactly placed over the soil plane with a limit distance rather than directly on the soil surface and then recalculated the components' fractions and consequently the final DBT. Based on the model of Yu et al. (2004), Du et al. (2007) took more into account the status of the crop, and divided the wheat canopy in ear stage into three layers (ear, leaves, and soil) with five components (sunlit and shaded ear, sunlit and shaded soil, and leaves), whose fractions were calculated by assuming the upper ear part of the wheat was like a cylinder. Apart from the use of the gap frequency theory, Huang et al. (2010) also extended the RGM model in VNIR to TIR range to simulate the hotspot of the row crop.

A common assumption in the above models is that the row canopy has an infinite extension and the viewing beam is parallel everywhere. Therefore, the models can treat the components' fractions in only a whole row structure. However, in filed measurements, the sensor's footprint is limited to several or tens of degrees, and different regions within the footprint data have different azimuth and zenith viewing angles rather than one unique angle. As a result, the assumption that the viewing direction is a parallel beam is rarely consistent with reality. Up to now, except for Colaizz et al. (2010), who modeled the footprint as continuous ellipses on the row canopy and estimated the sunlit and shaded components within the circular or elliptical footprint, and Chen et al. (2009), there have been no other studies that have considered the footprint effect (i.e., the FOV effect) on a row canopy's DBT, let alone any discussion of the difference in DBT between a parallel-beam model and a FOV model that accounts for variations in the viewing angle within the footprint. Therefore, a model that considers the sensor's footprint effect in the measurement of DBT on row crop canopies is strongly needed.

For the incomplete vegetation with an irregular distribution, the case becomes more complex and therefore there is a little publication about this issue. However, the Monte Carlo technique used by Chen et al.(2004) and the above method DART model and BRDF model might can be used to study the angular characteristics of radiance for those canopies.

2.6.3 Modeling for satellite pixel

Modeling the directional radiance at pixel scale is helpful to check the sensitivity of the algorithm of retrieving components' temperatures. In order to make the number of the observations larger than that of the unknowns, the pixel is usually assumed to be composed only with soil and vegetation, and the directional radiance after atmospheric correction is consequently related to the components' fractions and temperatures in a linear equation as follows:

$$\boldsymbol{B}(\boldsymbol{T}) = \boldsymbol{f}(\theta_v)\varepsilon_{\boldsymbol{v}}\boldsymbol{B}(\boldsymbol{T}_v) + [1 - \boldsymbol{f}(\theta_v)]\varepsilon_{\boldsymbol{g}}\boldsymbol{B}(\boldsymbol{T}_{\boldsymbol{g}}), \tag{2.14}$$

where, $\boldsymbol{f}(\theta_{\boldsymbol{v}})$ is the fraction of vegetation cover of the pixel, calculated from NDVI or from a linear equation of surface reflectances. The rest terms in Eq.(2.14) are defined above. Based on Eq.(2.14), Jia et al. (2003) obtained components' temperatures from ATSR's nadir and off-nadir observation, and Song and Zhao (2007) achieved this goal from MODIS multiple-channel TIR data observed at one time and single angle by using the genetic algorithm. Both methods required the components' emissivities known in advance.

In order to investigate the anisotropy of the brightness temperature at a scale of several kilometers, Pinheiro et al. (2004) reported a modified geometric projection (MGP) model, a highly parameterized model of scene TIR radiance applicable to both homogeneous and discontinuous canopies. Based on geometric optics modeling, MGP assumes that the directional TIR radiance over discontinuous canopies is due strictly to the different proportions of scene endmembers (e.g., sunlit tree crowns, background shadows) visible to a sensor at different sun-view geometries. The MGP model requires inputs on tree cover density and detailed information about the tree vegetation such as average crown height and crown width, as well as LAI to estimate the components' fractions. The tree cover density at the pixel scale was obtained from the MODIS Vegetation Continuous Fields product (Hansen et al. 2003) or from field measurement. The MGP model was used to simulate the DBT of AVHRR and SEVIRI in the place of Africa (Pinheiro et al. 2004; Rasmussen et al. 2011; Rasmussen et al. 2010), and result shows that the sun–target-sensor geometry plays a significant role in the estimated DBT, with variations more than ±3.0 K in some cases.

For the directional emissivity at pixel scale, Prata (1993) proposed a simple way to obtain the directional emissivity as $\varepsilon(\theta_v) = \varepsilon(0)\cos(\theta_v/2)$, where θ_v is the viewing angle and $\varepsilon(0)$ is the nadir emissivity. Such an equation is simple but is not applicable for all land cover types due to heterogeneity. Similar with the NDVI-based method stated above, the common calculation of the directional emissivity is written as:

$$\varepsilon(\theta) = \varepsilon_{i,v}\boldsymbol{f}(\theta) + \varepsilon_{i,g}[1-\boldsymbol{f}(\theta)] + 4 < \boldsymbol{d}\varepsilon_i > \boldsymbol{f}(\theta)[1-\boldsymbol{f}(\theta)], \tag{2.14}$$

where, $\boldsymbol{f}(\theta)$ is the fraction of vegetation cover in the direction θ, which can be obtained from NDVI. $\varepsilon_{i,v}$ and $\varepsilon_{i,g}$ are the vegetation and ground emissivity, respectively. At the pixel scale, $\varepsilon_{i,v}$ and $\varepsilon_{i,g}$ are usually channel-dependent, estimated from the land cover type and off-line emissivity database. $<d\varepsilon_i>$ is the maximum cavity term, accounting for the effect of radiance internal scattering between the different components of a structured and rough surface. $<d\varepsilon_i>$ can be set as a constant (e.g. 0.015) or parameterized using other model, such as the model proposed by Sobrino and Caselles (1990). More details about the application can be found in the literatures (Caselles et al. 2012; Phinheiro et al. 2006).

2.7 Drawbacks of current methods and possible solutions

From the above discussions, we know that much grate progress has been made in the retrieval of LST and emissivity from remotely sensed data, and in the modeling directional thermal radiation. However, there are still some drawbacks that need to be refined in the future. As for the issue on the modeling of directional thermal radiation and angular corrections on the land surface temperature, the drawbacks and their possible solutions in this thesis can be stated as follows:

(1) Lack of directional emissivity at pixel scales.

Many studies have investigated the directional emissivity from ground measurement or mathematical modeling, and consequently obtained some valuable results. However, there is still no publication about directional emissivity that was retrieved from satellite observations at pixel scale with a moderate spatial resolution. As a result, no one knows the exact shape of the angular anisotropy of the pixel emissivity. Fortunately, since those methods, such as TISI-based method, physical D/N method and TTM aforementioned, can retrieve directional emissivity directly from space data with little assumption on the shape of the directional emissivity, their retrieved directional emissivity products may provide us an opportunity to investigate the angular feature of the pixel emissivity if the same target or land cover type are observed under different directions in a short time and their corresponding directional emissivities are recovered accurately. The idea motivates our studies on the angular effect from the MODIS emissivity products, because MODIS sensor observes the land surface at viewing zenith angle ranging from 0° to 65°, and its emissivity products contain angular information of the natural surface's thermal emission. The details about this issue will be addressed in Chapter 3.

(2) Lack of multi-angular observations and the corresponding algorithms to make angular normalization of the LST

The use of the multi-angular dataset is considered as the most promising way to achieve the angular correction on temperature. However, due to the technical limitations, except ATSR sensors that can provide dual-angular observations in the TIR range, there is rare report about the multi-angular observations at spaceborne or airborne platform. As for the dual-angular observations by ATSR sensors, they were mainly used to directly retrieve LST or separate components' temperatures given pixel's emissivity or components' emissivities. As a result, no operational way exists for the angular normalization of LST from multi-angular observations due to the complexity of this issue. From this point of view, this thesis will aim at the case of non-isothermal pixels, and firstly propose a new model to simulate the thermal radiations for such pixels, and then attempt to investigate a new algorithm by combining the kernel-driven BRDF model and TISI method to retrieve temperature and emissivity simultaneously based on the multi-angular dataset in MIR and TIR channels obtained by an airborne system. In order to make the temperature with more physical meanings, this thesis will also clarify the definition of the directional effective temperature for the non-isothermal pixel. Finally, the directional effective temperature will be normalized from off-nadir to nadir with modified BRDF model. This issue is one the most important parts of this thesis and will be presented in Chapter 4 and 5.

(3) Lack of accessible way to evaluate the ground-measured temperature

The ground-measured temperature is considered as the true value to validate the retrieved LST products from remotely sensed data or simulated thermal radiation from models. However, the ground-measured data itself also includes error resulting from sensor's radiative calibration error, ambient radiation interruption, inaccurate angle controlling and so on. In order to remove or reduce this error, the ground-measured data are often averaged in time and space, or smoothen by using some filter functions. Such processing is reasonable for homogenous surface, such as dense vegetation and water, but it may cause much uncertainty for the heterogeneous surface or incomplete canopies, such as the row-structured canopy. Therefore, a new way is required to evaluate the accuracy of the ground-measured temperature. Based on the potential error in the directional brightness temperature caused by the uncertainty of sensor's footprint, this thesis will propose a new model to simulate the directional thermal radiation for row canopies by additionally considering sensor's footprint impact. Since the new model concerns on the footprint size and the variation of viewing directions in the footprint, it can be used to access the uncertainty involved in the measured data in theory and its results will show much closer to the reality than the current similar models. Furthermore, the new model will also provide the optimum footprint for the ground measurement of the validation of other similar models and the LST products from remotely sensed data. This part of work will be addressed in Chapter 6.

Chapter 3

Directional emissivity in MODIS products and its application to split-window algorithm

Angular effect of emissivity is considered one of the two reasons that cause the angular variation of the LST. However, the current land surface temperature (LST) products always ignore this effect of emissivity due to the lack of directional emissivity knowledge at pixel scale. Up to now, MODIS has observed the global surface for more than ten years, and its emissivity product retrieved from physical day/night algorithm provides us an opportunity to investigate the angular features of the natural surface's emissivity at pixel scale. From this point of view, this chapter emphasized on the statistical studies of 5-year MODIS emissivity products over most part of East Asia to obtain empirical relationships among the directional emissivity, land cover, and the seasonal variation. Consequently, two look-up tables (LUT) of directional emissivity were created for typical land cover types and then applied to the generalized split-window algorithm to modify MODIS LST. Results showed that the angular effect of emissivity could introduce a significant bias of -1.0 K~3.0 K to 1km-resolution LST. Finally, the spatial scale effects of emissivity were checked, and it was found that the temperature differences caused by scale effects fell within +/-0.5 K for most pixels if 5-km emissivity was used in 1km LST retrieval. Therefore, it is expected that widely use of the LUTs will lead to improvement for LST retrieval.

3.1 Background

Land Surface Temperature (LST) is one of the key parameters in land surface processes, and has been widely used in regional energy budget, climatic changes, and watershed management and crop assessments (Mannstein. 1987; Su 2002). The development of satellite and sensor technology in the recent decades has provided us an opportunity to retrieve LST from remotely sensed data at regional and global scales. Numerous algorithms have be reported to retrieve LST from space, such as the single-channel method (Jiménez-Muńoz and Cristóbal 2009; Qin et al. 2001), the split-window algorithm (Becker and Li 1995; Sobrino et al. 1994; Wan and Dozier 1996), the two-temperature method(Peres and DaCamara 2004a; Watson 1992), the temperature and emissivity separation method (Gillespie et al. 1998), the physical day/night algorithm (Wan and Li 1997) among others. Split-widow algorithm is the most popular one and has been used for different sensors, such as AVHRR, MODIS, ATSR, SEVIRI and FY-3(Coll and Caselles 1997; Sun and Pinker 2003; Sun and Pinker 2007; Tang et al. 2008; Wan and Dozier 1996), because it removes the atmospheric effect from the absorption difference between two adjacent TIR channels in the 10~12.5 μm regions, and relates the LST directly to linear or non-linear expression of the two channels' brightness temperatures. However, most of split-window algorithms require the land surface emissivity (LSE) of land surface known in advance, and thus the LSE plays a crucial role in the inversion of LST and its error affects the accuracy of LST. An uncertainty on the emissivity of 0.01 can lead to an error on the LST of around 0.5 K (Sobrino et al. 2005).

As reported by some authors (Chehbouni et al. 2001; Lagouarde et al. 2010; Lagouarde et al. 1995; Otterman et al. 1997), the LST varies with VZA, and some of them assumed this angular variation of the LST for isothermal pixel was mainly caused by the angular effect of LSE. Many authors made efforts to studying the angular effect of emissivity by using field and laboratory measurements, and some of them even modeled the angular LSE on the concept of radiative transfer model and/or geometrical-optic model(Chehbouni et al. 2001; Chen et al. 2004; François 2002; François et al. 1997; Otterman et al. 1992; Petitcolin et al. 2002b). Their results indicated that LSEs of bare soil, sand, clay and water decreased with increasing viewing angle, but for dense vegetated canopies the angular dependence is minimal (Sobrino et al. 2005). However, there is still rare investigation on the angular effect of the pixel emissivity at pixel scale because of the complexity of the natural surface itself and the difficulty in the measurement of the pixel's directional emissivity. Although Prata (1993) proposed a simple way to obtain the directional emissivity as $\varepsilon(\theta_{\boldsymbol{v}}) = \varepsilon(0)\cos(\theta_{\boldsymbol{v}}/2)$, where $\theta_{\boldsymbol{v}}$ is the viewing angle and $\varepsilon(0)$ is the nadir emissivity. Such an equation highly depends on the land cover and cannot be applicable for all land cover types due to heterogeneity. As a result, the LSEs used in the split-window algorithms were almost out of the consideration of the angular effect, let alone the angular correction on the LST. The directional emissivity product retrieved by the day/night algorithm (Wan and Li 1997) from the combination of daytime and nighttime MODIS MIR and TIR observations is considered as a unique data source to study the angular effect of the pixel emissivity because this product has a large range of viewing zenith angle (0°~65°), a global coverage and a long duration of more than ten years.

3.2 Method of extracting directional emissivity

3.2.1 Physical Day/Night algorithm

Similar to Eq.(2.2), the channel radiance measured by a sensor at the TOA can be approximated as (Wan and Li 1997):

$$\begin{aligned}\boldsymbol{R}(\boldsymbol{i}) &= \boldsymbol{t}_1(\boldsymbol{i})\varepsilon(\boldsymbol{i})\boldsymbol{B}_{\boldsymbol{i}}(\boldsymbol{T}_{\boldsymbol{s}}) + \boldsymbol{R}^{\uparrow}_{\boldsymbol{at}}(\boldsymbol{i}) + \boldsymbol{R}^{\uparrow}_{\boldsymbol{sl}}(\boldsymbol{i}) \\ &\quad + \frac{1-\varepsilon(\boldsymbol{i})}{\pi}[\boldsymbol{t}_2(\boldsymbol{i})\cdot\beta\cdot\boldsymbol{E}_0(\boldsymbol{i}) + \boldsymbol{t}_3(\boldsymbol{i})\boldsymbol{E}_{\boldsymbol{d}}(\boldsymbol{i}) + \boldsymbol{t}_4(\boldsymbol{i})\boldsymbol{R}^{\downarrow}_{\boldsymbol{at}}(\boldsymbol{i})]\end{aligned}, \tag{3.1}$$

where, $\varepsilon(\boldsymbol{i})$ is the channel directional emissivity, and β is the anisotropic factor for middle infrared channel, which is used to convert the bi-directional reflectivity $\rho_{\boldsymbol{i}}(\theta_{\boldsymbol{s}}, \varphi_{\boldsymbol{s}}, \theta_{\boldsymbol{v}}, \varphi_{\boldsymbol{v}})$ to the hemispheric-directional reflectivity and then linked to the directional emissivity on basis of Kirchhoff's law, as $\boldsymbol{r} = 1\text{-}\ \varepsilon(\boldsymbol{i}) = \pi\rho_{\boldsymbol{i}}(\theta_{\boldsymbol{s}}, \varphi_{\boldsymbol{s}}, \theta_{\boldsymbol{v}}, \varphi_{\boldsymbol{v}})/\beta$. $\boldsymbol{B}_{\boldsymbol{i}}(\boldsymbol{T}_{\boldsymbol{s}})$ is the channel radiance calculated from the Planck's law at temperature $\boldsymbol{T}_{\boldsymbol{s}}$. $\boldsymbol{R}^{\uparrow}_{\boldsymbol{at}}(\boldsymbol{i})$ and $\boldsymbol{R}^{\downarrow}_{\boldsymbol{at}}(\boldsymbol{i})$ are the upward and downward atmospheric thermal radiation, respectively; $\boldsymbol{E}_0(\boldsymbol{i})$, $\boldsymbol{E}_{\boldsymbol{d}}(\boldsymbol{i})$ and $\boldsymbol{R}^{\uparrow}_{\boldsymbol{sl}}(\boldsymbol{i})$ are the direct and diffuse downward and upward solar radiation. t_1, t_3 and t_4 are the atmospheric effective transmittance for the scattering radiations from land surface to the TOA, while t_2 is the transmittance for the reflected direct solar radiation. The above atmospheric parameters and solar beam can be calculated from MODTRAN given atmospheric data.

In order to retrieve the unknowns ($\varepsilon(i)$, T_s and β) in Eq.(3.1), Wan and Li (1997) used a pair of daytime and nighttime MODIS data in MIR channels (CH20: 3.66~3.84 µm, CH22: 3.93~3.99 µm, CH23: 4.02~4.08 µm) and TIR channels (CH29: 8.4~8.7 µm, CH31: 10.78~11.28 µm, CH32: 11.77~12.27 µm, CH33: 13.19~13.49µm) by assuming that the channel emissivities have no significant variation during the two observations and three MIR channels have the same anisotropic factor β due to its small spectral variation (<2%). Besides, another two atmospheric variables, near-surface air temperature T_a and column water vapor WV were added into the solution in order to increase the accuracy of the atmospheric correction. Finally, 14 radiative transfer equations of Eq.(3.1) from day and night observation in MODIS seven channels corresponds to total 14 unknowns, including 2 T_s, 2 T_a, 2 WV, 1 β and 7 ε. Considering the angular variation in emissivity, this algorithm separated the whole range of MODIS viewing zenith angles into several sub-ranges and tried to select a pair of clear-sky daytime and nighttime MODIS observations at viewing angles in the same sub-range whenever it is possible (Wan and Li 1997; Wan et al. 2004).

The atmospheric data was obtained from MODIS vertical sounders and a lookup-table off-line created by MODTRAN simulation. The initial values of the unknown were given separately by empirical linear relationships with 14 brightness temperatures as:

$$x_i = \sum_{j=1}^{14} w_{i,j} y_j + c_i, \; i,j = 1,2,\ldots,14, \tag{3.2}$$

where, x_i is the vector of 14 unknowns, and y_j is the brightness temperatures, and $w_{i,j}$ is the coefficients of y_j for the x_i. c_i is the coefficients for the offset term. Both $w_{i,j}$ and c_i were regressed from a huge dataset of land surface and atmosphere case. With the given initial values, the final solution was obtained from χ^2 optimization algorithm by minimizing an objective function like Eq.(3.3), where R_i is channel radiance observation value and $R(i)$ is the calculated channel radiance from Eq.(3.1) using the retrieved variables, and σ_i is the uncertainty in the observed radiance, related to the channels' noise equivalent differential temperature ($NE\Delta T$).

$$\chi^2 = \sum_{j=1}^{14} \{\frac{1}{\sigma_j^2}[L_j - L(j)]^2\}. \tag{3.3}$$

3.2.2 MODIS LST&LSE products and land cover products

Two types of global MODIS LST&LSE products are released since 2000. One is calculated from split-window algorithm (Wan and Dozier 1996) using MODIS 31 and 32 channels' data, whose emissivities are estimated from emissivity look-up table and land cover products; the other one is driven from the day/night algorithm aforementioned (Wan and Li

1997), which is used in this thesis.

The current version of the LST product is collection 5, updated from the collection 4 by dealing with several drawbacks (Wan 2008; Wang et al. 2007), such as pixels with cloud-contaminated LST values and those with missing valid LST values in areas under apparently clear-sky conditions. Three refinements of the total eight are interesting for us: 1) the way of detecting clear-sky conditions by varying confidence of clear-sky can increase the number of clear-sky pixels; 2) the number of sub-ranges of viewing angles in day/night algorithm is incremented from 5 to 16; and 3) the grid size of retrieved LST&LSE is changed to 6 km×6 km instead of 5 km×5 km. However, the results in this thesis were obtained using the channel emissivity (channel 20-23, 29, 31, 32) of MODIS collection 4 LST&LSE products (MOD11B1) from the day/night algorithm, covering most part of East Asia (Fig.3-1) from the years 2000 to 2004. Although the first refinement has increased the number of valid LST&LSE in our study region, the huge number of valid values of 5-years collection 4 products in our study region is enough to make our result representative of this region. In terms of the second refinement, the accuracy of retrieved emissivity in collection 5 was enhanced, but emissivity in collection 4 was also proved to be acceptable by validating LST in clear-sky (Wan et al. 2004; Wan et al. 2002). Therefore, the application of collection 4 LST&LSE product is also reliable. Table 3-1 shows the specification of the MODIS LST&LSE product.

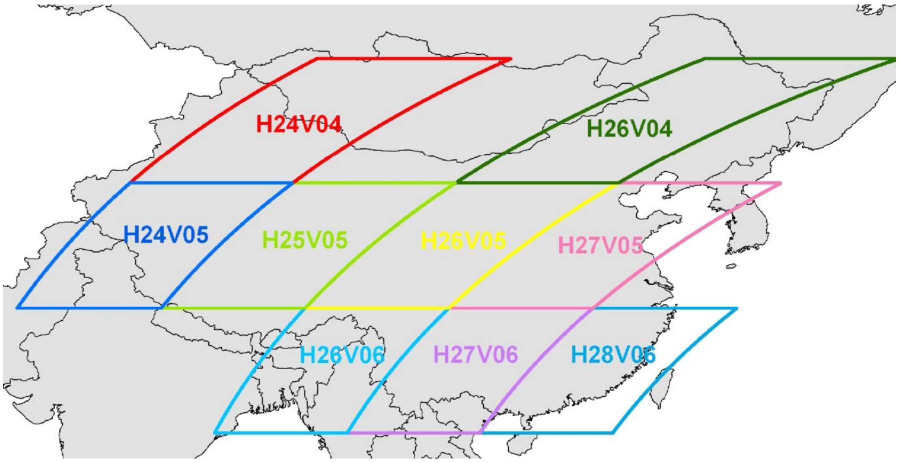

Fig.3-1. Study region locates in East Asia from $19^{o}59'$ N to $49^{o}59'$ N of latitude and from $69^{o}17'$E to $155^{o}59'$E of longitude, including most part of China, Mongolia and Russia

Table 3-1. Some specification of MODIS LST&LSE and land cover products in V004

Variables	LST/LSE product	Land Cover Product
Product ID	MOD11B1	MOD12Q1
Temporal Coverage V004	Mar. 5, 2000 – the present	Jan. 1,2000 – Jan. 1, 2004
Product Frequency	Daily	Yearly
Image Dimensions	240 rows × 240 columns	1200 rows × 1200 columns
Spatial Resolution	~5 km	~1.0 km
Dataset Layers	17	16
Projection	Sinusoidal	Sinusoidal
File Format	HDF-EOS	HDF-EOS

Another MODIS land product used in this thesis is the yearly land-cover products MOD12Q1 with a spatial resolution of 1 km. There are five groups of land covers included in this product, and the IGBP (International Geosphere-Biosphere Programme) scheme (Friedl et al. 2002), which divides global surface to total 17 land covers as shown in Table 3-2, was used in this thesis. Both products (MOD11B1 and MOD12Q1) distributed in 9 tiles covering most of East Asia (Fig.3-1) from the years 2000 to 2004. This region covers various landscapes including plateau, forest, irrigated crop, glacier, bare, desert and so on, and most fraction of the study region was observed in large viewing angles, thus angular correction of LST is strongly required.

Table 3-2. Land covers in the IGBP classification scheme

Class	Land Cover	Class	Land Cover
0	Water	9	Savannas
1	Evergreen Needleleaf Forest	10	Grassland
2	Evergreen Broadleaf Forest	11	Permanent wetlands
3	Deciduous Needleleaf Forest	12	Cropland
4	Deciduous Broadleaf Forest	13	Urban and Built-up
5	Mixed Forests	14	Cropland/Natural vegetation mosaic
6	Closed Shrublands	15	Permanent Snow and Ice
7	Open Shrublands	16	Barren or Sparsely Vegetated)
8	Woody Savannas		

3.2.3 Analysis methods

Fig.3-2 represents the flowchart of retrieval of MODIS directional emissivity in this thesis. The method started with the spatial aggregation of land cover products from 1 km to 5 km. Since both products have the same geographical system and projection, the spatial aggregation was easily performed. The new 5-km grid was considered as “pure pixel or quasi-pure pixel” if more than 23 1-km pixels among total 5×5 1-km pixels hold the same cover type. Additionally, cluster analysis was performed with ***eight-connectivity diagnosis*** method to remove isolated pixels, which requires that all surrounding pixels have the same cover type with the central pixel. Fig.3-3 shows an example of cluster analysis on MODIS tile H26V04 located on northeast corner of our study region (Fig.3-1). This shows that the 5×5 1-km pixels image is smoothed, and that only the pixels distributed over large areas remain.

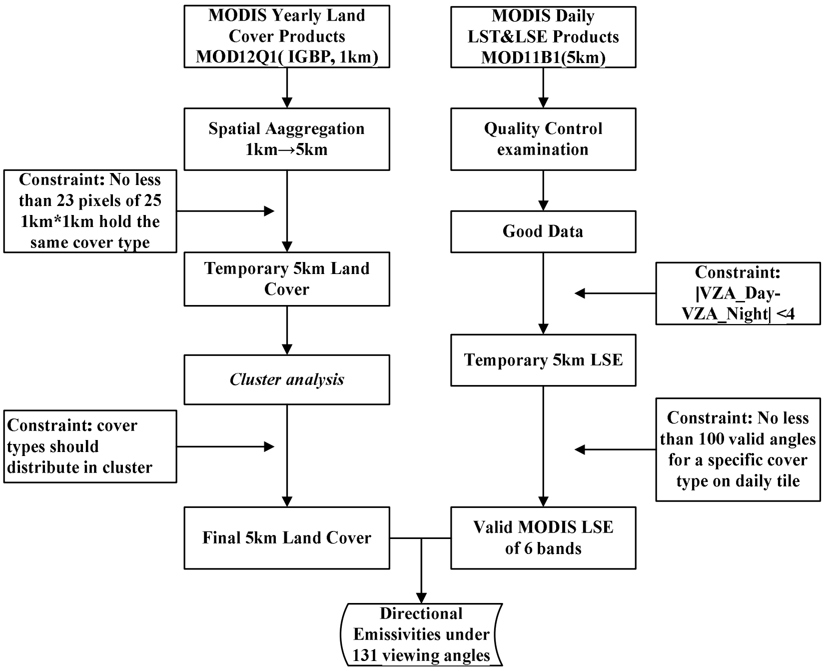

Fig.3-2. Flowchart to retrieve directional emissivity of MODIS product

In addition to the ***Quality Control*** flags included in the products, more constraints were used on the MODIS daily LST&LSE products to select the valid pixels. First, the difference of viewing angles for a pixel between daytime and night time should be smaller than 4°, and their average value was considered as the viewing angle of the pixel; second, the number of valid viewing angles for a specific cover type should be larger than 100 on daily tiles. The selected pixels from the MODIS LST&LSE products are then used to study the angular effects of emissivity.

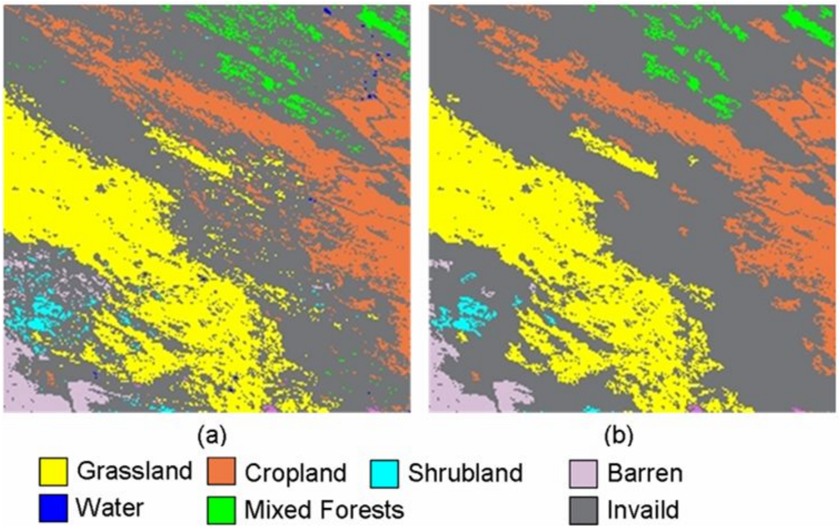

Fig.3-3. Comparison between the images before and after cluster analysis on MODIS land cover product in Tile H26V04 of 2001

3.3 Characteristics of MODIS emissivity

3.3.1 Angular variation of emissivity

With the selected valid samples from the above flowchart, the directional emissivities for six cover types were obtained in our study region. They are ***Grassland***, ***Cropland***, ***Evergreen Broadleaf Forest***, ***Mixed Forest***, ***Open Shrublands*** and ***Barren or Sparsely Vegetated*** (hereinafter abbreviated as ***Barren***). Because of space limitation, we only took ***Grassland***, ***Cropland*** and ***Barren*** as example to illustrate the angular effects of emissivity at 5km-scaled grid in MODIS 6 channels. Fig.3-4(a), (c) and (e) show directional emissivities in MIR channels, and (b), (d) and (f) present those in TIR channels. It can be found that: 1) emissivities increased with viewing zenith angles in MIR channels but decreased in TIR channels; 2) they varied slightly from 0° to 45° but significantly in the range larger than 45°; 3) the curves of directional emissivities in MIR and TIR channels (except channel 29 for ***Barren***) showed similar shapes. Table 3-3 gives some statistical information about directional emissivities of channel 23 and 32 for the three cover types. It can be found that the maximum differences in emissivities under all angles were about 0.01~0.02 in channel 23 (that means an equivalent ΔT from 0.8K to 1.5 K at T = 300 K), and about 0.006 in channel 32 (that means an equivalent ΔT about 0.5 K at T = 300 K). For other three cover types (***Evergreen Broadleaf Forest***, ***Mixed Forest***, and ***Open Shrublands***), their directional emissivities presented similar tendencies in MIR and TIR channels as ***Grassland*** and ***Cropland*** did.

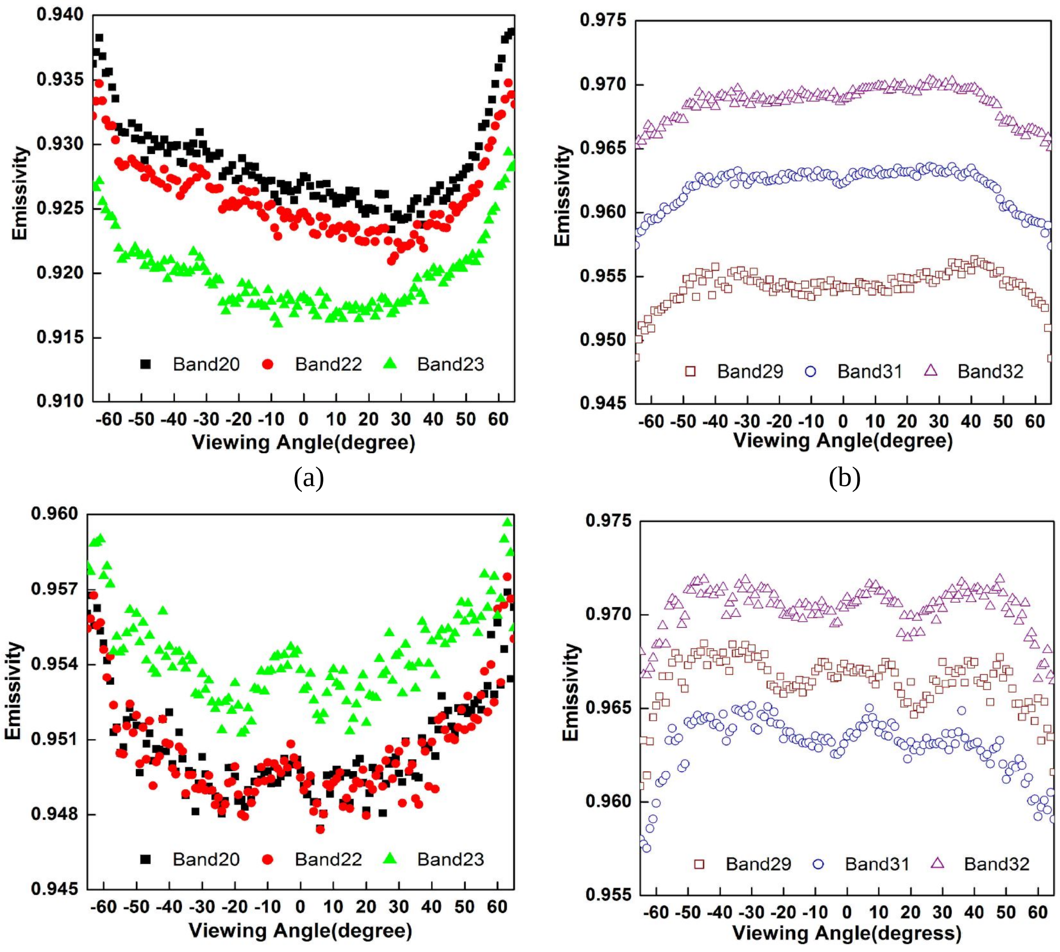

(a) (b)

(c) (d)

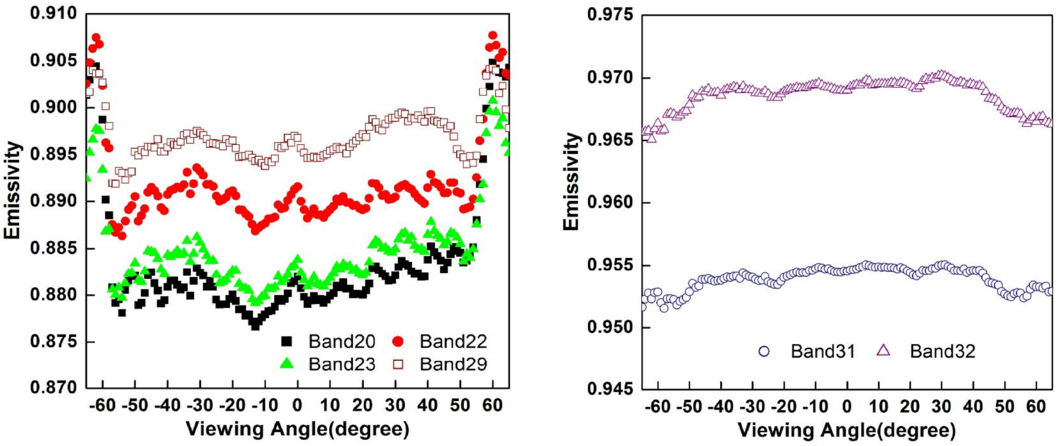

(e) (f)

Fig.3-4. Directional emissivities in MODIS MIR and TIR channels. (a) (b), for ***Grassland*** in MIR and TIR channels, (c) (d) for ***Cropland***;(e)(f) for ***Barren***. However, channel 29 emissivity for ***Barren*** varied similarly with those in MIR channel shown in (e).

Table 3-3. Analysis of emissivities under different sub-ranges of viewing angles in channels 23 and 32

	Channel No.	Channel 23		Channel 32	
	Viewing angles	±(0°~45°)	±(45° ~65°)	±(0°~45°)	±(45° ~65°)
Grassland	Mean	0.917	0.922	0.967	0.964
	STDEV	0.002	0.003	0.001	0.001
	Max	0.921	0.927	0.969	0.968
	Min	0.915	0.918	0.966	0.962
	Δ(131)*	0.012		0.007	
Cropland	Mean	0.953	0.957	0.972	0.970
	STDEV	0.001	0.002	0.001	0.001
	Max	0.955	0.960	0.973	0.972
	Min	0.952	0.954	0.971	0.967
	Δ(131)	0.008		0.006	
Barren	Mean	0.883	0.889	0.969	0.967
	STDEV	0.002	0.007	0.0004	0.001
	Max	0.888	0.901	0.970	0.960
	Min	0.879	0.880	0.968	0.965
	Δ(131)	0.022		0.010	

* Δ (131) is the maximum difference in emissivities at all of the whole 131 viewing angles

Based on the above directional emissivities, we present the relationship between emissivities and cosine values of viewing angles in channels 23 and 32 for ***Grassland*** and ***Cropland*** in Fig.3-5(a) and (b). The curve of channel 23 in Fig.3-5(a) denotes a logarithmic relationship while Fig.3-5(b) shows an exponential relationship. These relationships are simple and easy in use. Eq.(3.4) expresses the regressed results of ***Cropland***'s emissivity versus cosine view angle. Relationships for other cover types can be obtained similarly.

$$\varepsilon(\theta) = -0.01\ln[\cos(\theta)] + 0.917, \boldsymbol{R}^2 = 0.91, \text{ for channel 23,}$$

$$\varepsilon(\theta) = -0.0015\exp[-0.62\cos(\theta)] + 0.968, \boldsymbol{R}^2 = 0.86, \text{ for channel 32.} \qquad (3.4)$$

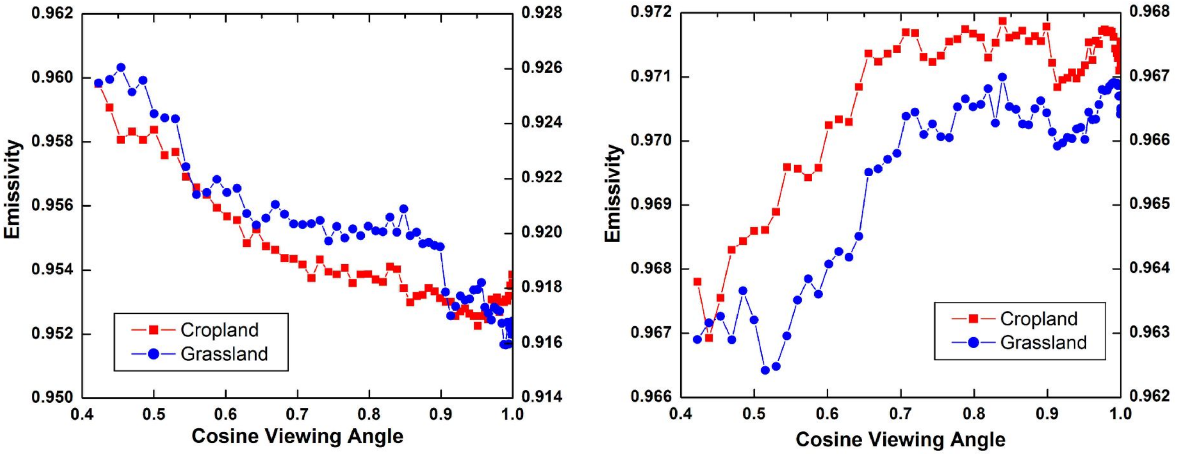

(a) Channel 23 (b) Channel 32

Fig.3-5. Directional emissivity versus the cosine of viewing angles for ***Cropland*** and ***Grassland*** in channels 23(a) and 32(b) of MODIS. The right y-axis is corresponding to the emissivity for ***Grassland***.

3.3.2 Angular variation of emissivity in different seasons

As known, emissivity is also influenced by vegetation fraction. Vegetation fraction changes cannot be ignored during the year. Seasonal averaged directional emissivities were also got in this thesis. Fig.3-6 presents seasonal directional emissivities for ***Grassland***, ***Cropland*** and ***Barren*** in channel 23 and 32. In general, angular variations are similar for the four seasons. For channel 23, emissivities in summer and autumn were smaller than those in other two seasons. The minimum emissivity value was found in summer, and the emissivity in summer was more sensitive to the change of viewing angle than that in other seasons. After changing the number of daily valid angles from 100 to 85 for each land cover, we got the seasonal averaged directional emissivities of the other four cover types (***Water***, ***Woody Savannas***, ***Urban*** and ***Built-up***, ***Permanent Snow and Ice***), and found the similar phenomena.

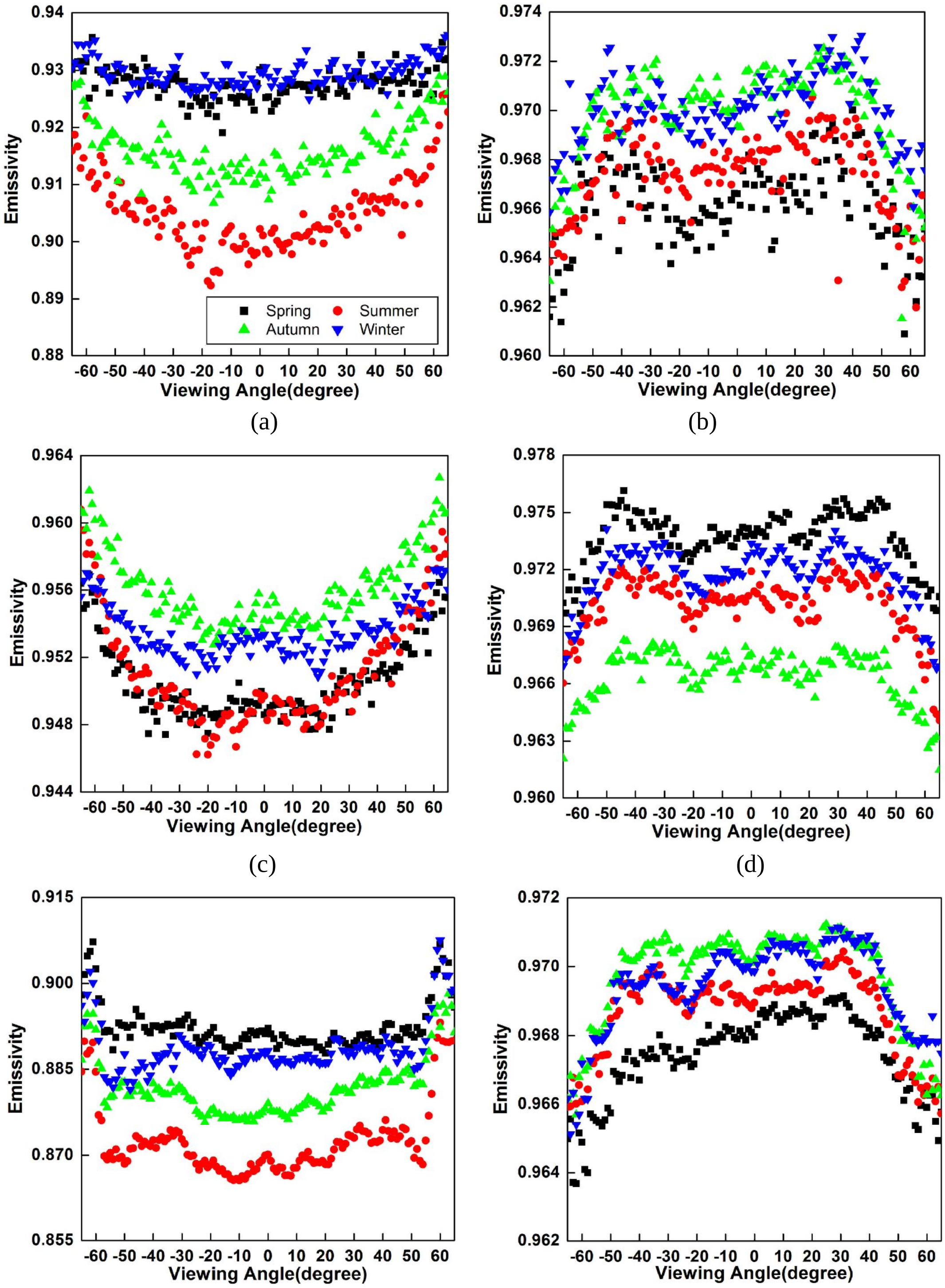

(a) (b)

(c) (d)

(e) (f)

Fig.3-6. Angular effects of emissivity in channels 23 and 32 in different seasons. (a), (c) and (e) are emissivities in channel 23 for ***Grassland***, Cropland and ***Barren***, respectively; (b), (d) and (f) are in ***channel*** 32, respectively.

3.3.3 Lookup-table for directional emissivity

Based on the directional emissivity, two look-up tables (LUTs) were created. Both LUTs depended upon cover type and viewing angle but with a slight difference that one of them relied on seasons (seasonal-dependent LUT). Their structures are described in Fig.3-7. It should be noted that emissivities in both LUTs were not calculated using Eq.(3.4) but were obtained directly from MODIS products at 5km-scale using the flowchart of Fig.3-2. Both LUTs include directional emissivities of ***Grassland***, ***Cropland***, ***Evergreen Broadleaf Forest***, ***Mixed Forest***, ***Open Shrublands*** and ***Barren or Sparsely Vegetated***. The seasonal-dependent LUT also includes directional emissivities of other four cover types: ***Water, Woody Savannas, Urban and Built-up, Permanent Snow and Ice***. Emissivities of the rest 7 cover types in the IGBP scheme were also included in the seasonal-dependent LUT but set to constant values according to Wan's paper (Wan 2008).

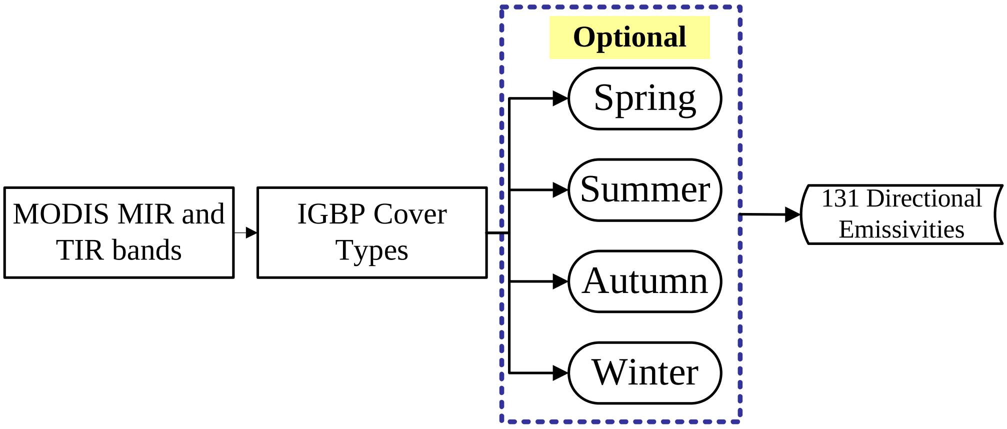

Fig.3-7. Structure of look-up tables for directional emissivity.

3.4 Applications to the split-window algorithm

3.4.1 Theory of the generated split-window algorithm

The generated split-window algorithm (Wan and Dozier 1996; Wan et al. 2004) used a linear combination of two apparent temperatures and their corresponding channel-averaged emissivities to estimate LST as follows:

$$\begin{aligned}\boldsymbol{T}_s &= \boldsymbol{C} + \left(\boldsymbol{A}_1 + \boldsymbol{A}_2\frac{1-\varepsilon}{\varepsilon} + \boldsymbol{A}_3\frac{\Delta\varepsilon}{\varepsilon^2}\right)\frac{\boldsymbol{T}_{31}+\boldsymbol{T}_{32}}{2} \\ &+ \left(\boldsymbol{B}_1 + \boldsymbol{B}_2\frac{1-\varepsilon}{\varepsilon} + \boldsymbol{B}_3\frac{\Delta\varepsilon}{\varepsilon^2}\right)\frac{\boldsymbol{T}_{31}-\boldsymbol{T}_{32}}{2}\end{aligned}, \tag{3.5}$$

where, $\boldsymbol{A_i}$, $\boldsymbol{B_i}$ ($\boldsymbol{i}$=1, 2, 3) and $\boldsymbol{C}$ are coefficients regressed from numerical simulations with the MODTRAN code; $\boldsymbol{T}_{31}$ and $\boldsymbol{T}_{32}$ are apparent brightness temperatures of channel 31 and 32 of MODIS, respectively; $\varepsilon=0.5(\varepsilon_{31}+\varepsilon_{32})$ and $\Delta\varepsilon=\varepsilon_{31} - \varepsilon_{32}$, where ε_{31} and ε_{32} are the classification-based emissivity, estimated from land cover types in each MODIS pixel through a LUT based on TIR BRDF and emissivity modeling (Snyder and Wan 1998; Snyder et al. 1998). Although a simple linear correction is made to the channel emissivities to account for the angular effect in the emissivities when the viewing zenith angle is larger than 45° for some land cover types, the refinement of directional emissivity was limited (~0.003) and their emissivity accuracy may be degraded by the spatial scale effect from simulated data to pixel scale and also by the error of identified land cover. Compared with the emissivity used in the current split-window algorithm shown in Table 3-3, the emissivity retrieved from the day/night algorithm turn out to be a little smaller for some vegetated covers (see Fig.3-6), perhaps because the mixed effect of the vegetated part and soil part in the real pixel reduce the pixel value of directional emissivity.

Table 3-4. Channel emissivity used in MODIS split-window algorithm (Wan 2008)

Cover types	ε_{31}	ε_{32}
Water	0.992	0.988
Evergreen needleleaf forest	0.987	0.989
Evergreen broadleaf forest	0.981	0.984
Deciduous needleleaf forest	0.987	0.989
Deciduous broadleaf forest	0.981	0.984
Mixed forest	0.981	0.984
Closed shrublands	0.983	0.987
Open shrublands	0.972	0.976
Woody savannas	0.982	0.985
Savannas	0.983	0.987
Grasslands	0.983	0.987
Permanent wetlands	0.992	0.988
Croplands	0.983	0.987
Urban and built-up	0.970	0.976
Cropland and mosaics	0.983	0.987
Snow and ice	0.993	0.990
Bare soil and rocks	0.965	0.972

For the isothermal pixel, the angular variation of their emissivity is assumed to fully result in the angular behavior of its temperature. In order to illustrate the angular effect of emissivity on the retrieved LST, the directional emissivities of MODIS channel 31 and 32 included in the new LUT was used in the split-window algorithm to get angular-independent LST, and comparison was further made between the new LSTs with the LSTs using the original LUT (Table 3-4).

3.4.2 Application and comparison

A total of twelve MODIS scenes (one per month in 2008) were chosen to calculate the LST, most of them located in the middle and northwest part of China. The percentage histograms of temperature differences between the modified LST with the new LUT and MODIS 1km LST products (MOD11_L2, collection 4) are shown in Fig.3-8. They indicate that the temperature differences $\Delta\boldsymbol{T}$s for most pixels fell in the range of -1.0 K to 3.0 K; the modified LSTs are generally larger than the MODIS LST products in most of cases. The peaks $\Delta\boldsymbol{T}$s of the histograms varied from 1.02 K to 2.26 K, and nine of the twelve scenes show that the temperature differences are larger than 1.5 K. Table 3-4 gives more information: about 45% to 55% pixels had the temperature differences within peak Δ$\boldsymbol{T}$ ± 1.0 K, and 53% to 64% pixels had the temperature differences within peak Δ$\boldsymbol{T}$ ± 1.5 K.

Table 3-5. Temperature differences in 12 scenes

Julian Day of 2008	Peak Δ$\boldsymbol{T}$ (K)	Percentages of pixels within the defined temperature differences (%)	
		Peak Δ$\boldsymbol{T}$±1.0 K	Peak Δ$\boldsymbol{T}$±1.5 K
001	1.02	46.4	57.9
050	1.04	50.9	62.5
068	1.33	53.8	63.7
104	1.93	54.6	64.3
126	1.90	50.7	60.5
167	2.26	45.4	55.7
199	1.57	45.0	56.2
229	1.86	45.6	56.8
259	1.75	41.5	53.2
286	1.69	49.1	59.3
312	1.59	51.7	62.7
334	1.20	50.8	62.3

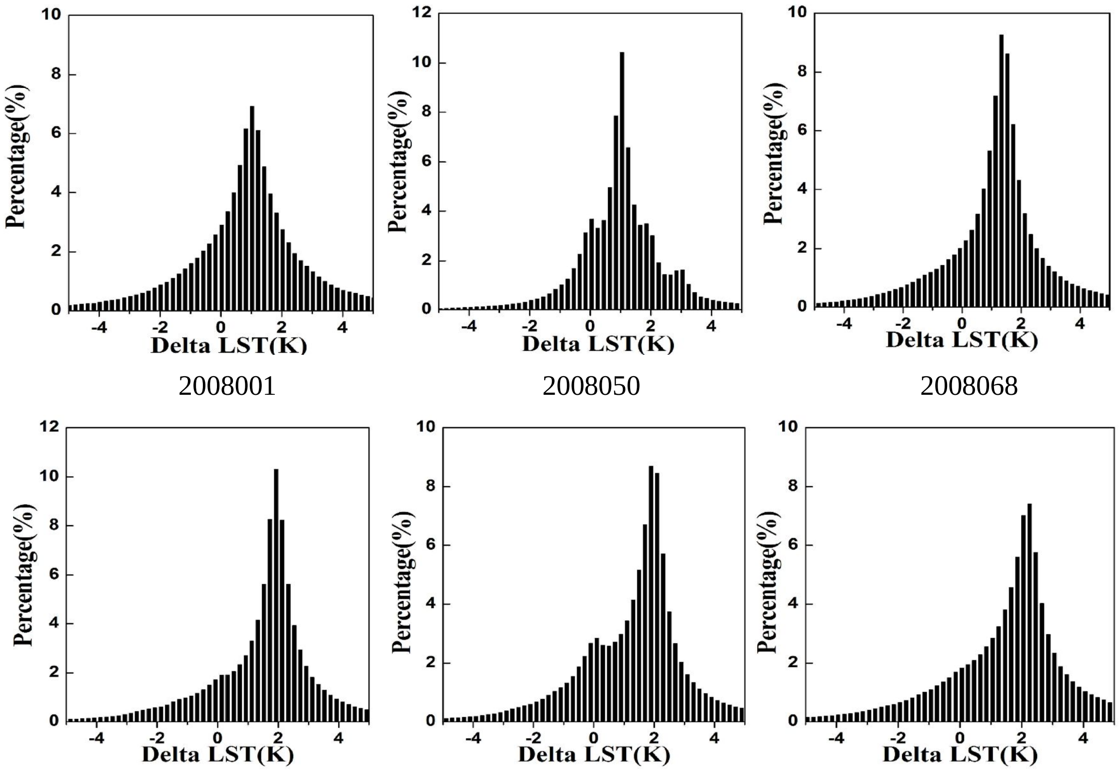

2008001 2008050 2008068

2008104 2008126 2008167

Fig.3-8. Percentage histograms of temperature difference Δ$\boldsymbol{T}$ between newly retrieved LST and MODIS LST products of 12 scenes data in 2008, locating in the middle part of China. (***to be continue***)

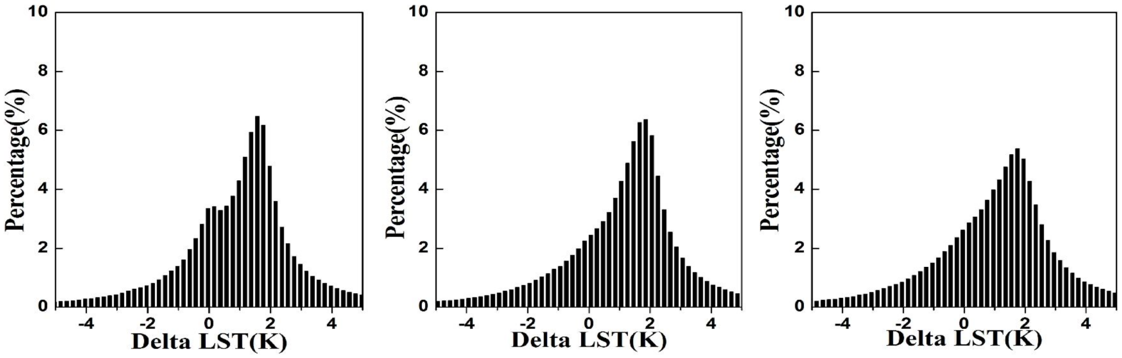

2008199 2008229 2008259

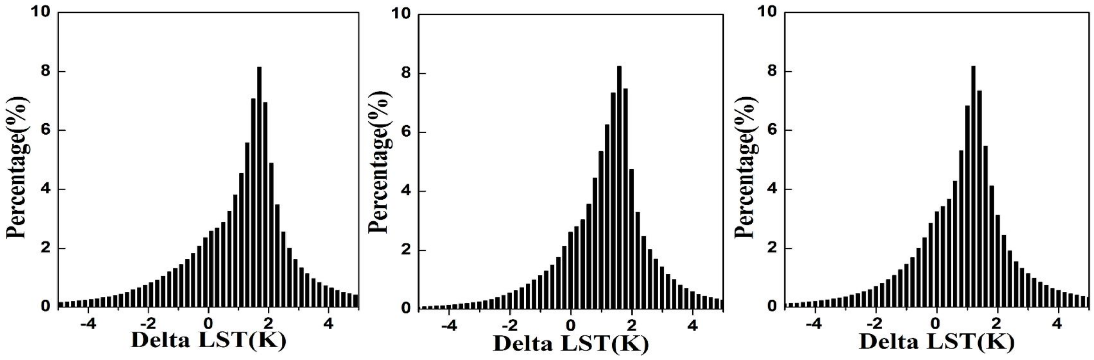

2008286 2008312 2008334

Fig. 3-8. (***continue***)

Furthermore, we divided the viewing zenith angles into seven sub-ranges with an interval of 10° and presented the temperature RMSEs of the twelve scenes in Fig.3-9. This figure shows that RMSEs in all viewing zenith angle sub-ranges are within 1.4~2.5 K and the discrepancy between the maximum and minimum RMSE is about 0.6 K. However, RMSE increases with the increase of viewing zenith angle. This is reasonable because the modified LSTs tend to be larger at large viewing angles due to the lower emissivity values. From the above results, a conclusion can be drawn that the inversion of LST with a high accuracy needs to consider the angular effects of emissivity, especially for large viewing angles.

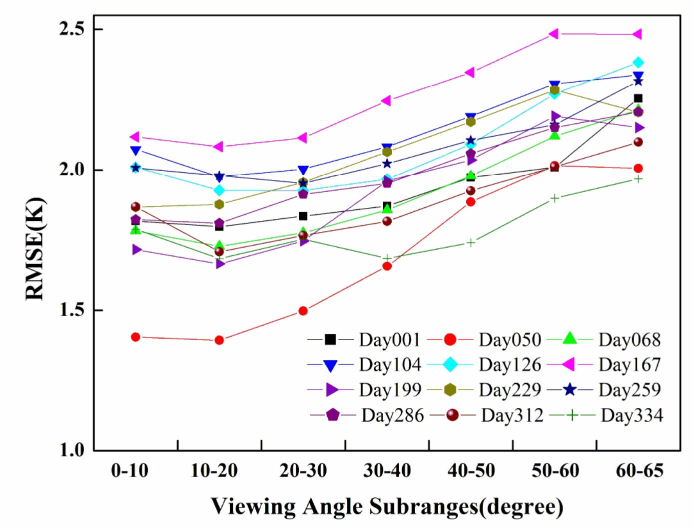

Fig.3-9. RMSEs in seven viewing zenith angle subranges

3.4.3 Spatial scale effects of emissivity

It is worth notice that emissivities in LUTs were retrieved directly from 5 km grid which was assumed to be homogeneous. However, above subsections retrieved LST at 1 km resolution. Therefore, the spatial scale effects of emissivity that may influence the accuracy of LST should be considered. In order to check the scale effects, we retrieved LST again at 5 km resolution with the same method and data applied in previous subsection. The 5 km brightness temperatures T_{31} and T_{32} in Eq.(3.5) were averaged from 5×5 1-km pixels in MODIS L1B products, and pure or quasi-pure pixels and mixed pixels were distinguished using the same constraint shown in Fig.3-2. Then the 5-km LST was retrieved (denoted as ***LST_5km***) and compared with the 5-km LST (***LST'_5km***) directly averaged from 1-km modified LST mentioned before. The temperature difference caused by the scale effects is expressed as Δ***T_5km* =*LST_5km* - *LST'_5km***. The percentage histograms of Δ***T_5km*** for pure and mixed pixels are presented in Fig.3-10. Result shows that the percentage peaks of the temperature differences is very close to 0.0 K, and the differences fall within +/-0.5K for most pixels. Therefore, the spatial effect of 5-km directional emissivity applied on the split-window algorithm at 1-km scale is very small and can be ignored, at least for the linear split-window algorithm.

3.5 Conclusions and discussions

With statistical analysis of MODIS land cover products and LST&LSE products from the physical day/night algorithm, angular effects of emissivity for several land covers were presented in East Asia. The result shows that emissivity increases in MODIS MIR channels but decreases in TIR channels with the increase of viewing angle. The angular effects makes emissivity varies in a range of 0.01~0.02 in MIR channels and about 0.01 in TIR channels. Based on directional emissivities, two LUTs at 5km were created. Both LUTs depended upon cover type and viewing zenith angle but one of them additionally relied on seasons.

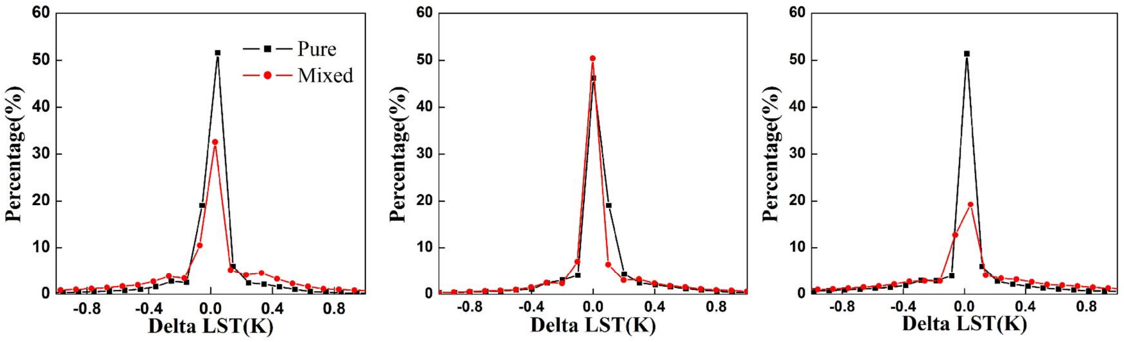

2008001 2008050 2008068

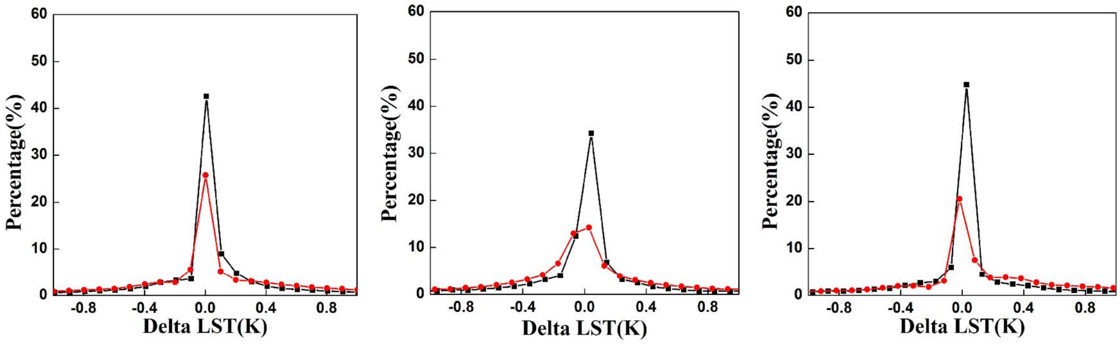

2008104 2008126 2008167

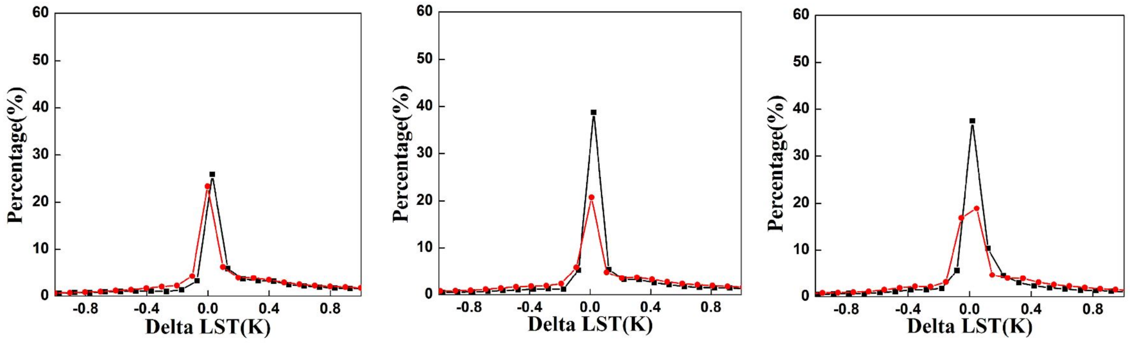

2008199 2008229 2008259

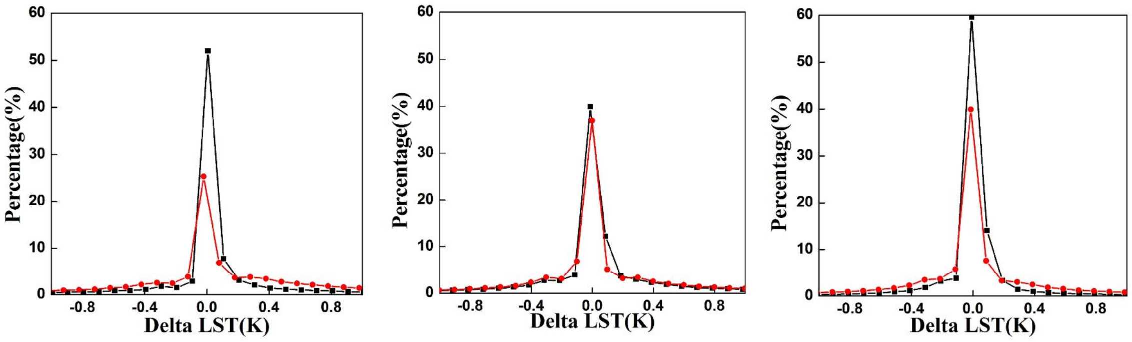

2008286 2008312 2008334

Fig.3-10. Percentage histograms of *ΔT_5km* of 12 scenes data for pure and mixed pixels at 5 km

The seasonal LUT was applied on the split-window algorithm to retrieve LST at 1km resolution. By comparing the retrieved LST with MODIS LST products, we found that the new LSTs were generally larger than the MODIS LST products and the discrepancy ranged from -1.0 K to +3.0 K. Large viewing angles will cause larger temperature differences than smaller ones. Finally, we discussed the spatial scale effects between the LST retrieval results at 1 km and 5 km, the corresponding result denoted that the spatial scale effects of emissivity could be ignored from 1 km to 5 km in our study region.

The relationship between the vegetation fraction and the emissivity had been discussed in details (Momeni and Saradjian 2007; Sobrino et al. 2001). However, the angular effect of emissivity itself was seldom cared in the past. Seasonal directional emissivities were also investigated in this study. After this framework, further researches may be done by considering the fractional vegetation cover and angular effects together in the modeling of emissivity. Besides, although the Day/Night algorithm applied near-surface air temperature and column water vapor to refine the input atmospheric data and improved the accuracy of atmospheric correction in theory, the directional emissivity obtained in this thesis may still be impacted by the residual error of atmospheric radiation. Furthermore, the soil moisture influences the emissivity, but we ignored this effect because we had no soil moisture data at 5km scale.

In addition, our study on emissivity only performed over most part of East Asia, and did not obtain directional emissivity over all land cover types described in the IGBP scheme. However, our work can be extended easily on more regions and land cover types. Currently, the modified LST after correcting the angular dependence was only compared with the original MODIS LST products. If ground-based reliable measurements over enough large areas are available in the future, the temperature validation work will be expected. By our field experiences, new data collection methods and effective equipment are needed to get more reliable in-situ LSTs.

Chapter 4

Parameterization of directional emissivity and brightness temperature, and the angular normalization of temperature using kernel-driven BRDF model

This chapter firstly compares four parameterization models of the directional emissivity based on the thermal radiative transfer model (TIR-SAIL model). Results show that the kernel-driven BRDF (K-BRDF) model accurately represents the angular variation of the canopy directional emissivity and that it has to refine the cavity effect factor related to the multiple scattering in the canopy. Then, based on the new cavity effect factor and the parameterization method of the SAILH model, we develop a new way to simulate the directional brightness temperature (DBT) of the canopy assumed to consist of leaves, sunlit and shaded soils. Finally, the availability of the K-BRDF model in the angular normalization of the DBT is investigated in two different ways: the single-point pattern and the linear-array pattern. The result of two patterns' analyses respectively finds out the local optimum three-angle combination of the K-BRDF model, and releases the requirement of the viewing zenith angle (VZA) in the designed three arrays (nadir, forward and backward) detector system. The findings of this chapter will be used in the next chapter.

4.1 Background

As stated in the previous chapter, the emissivity varied with viewing zenith angle (VZA) at pixel scale, and the angular dependence was generally significant when the VZA exceeded 45°. Such angular dependence for three-dimensional surfaces mainly results primarily from the angular variation of the relative weights of different components (e.g., vegetation and background soil) with different emissivities in the pixel. The angular dependence has been studied from field and laboratory measurements. Their results show that for bare soil surfaces emissivity values decreased with increasing viewing angle, whereas the angular dependence of dense vegetated canopies was minimal, in agreement with the usual assumption of Lambertian behavior for vegetation. However angular characteristic of sparse and middle dense vegetated canopies depends on the structure of the canopies themselves.

Up to now, different models have been developed to analyze the angular variation of directional emissivity and radiance over vegetation canopies, using the soil and vegetation emissivities as input data and based on the assumption of Lambertian behavior for these components. In those models, three ways are often used to obtain the directional emissivity: first, directional emissivity can be estimated as the weight of different components' emissivity, whose fractions were calculated from the canopy structures and the viewing geometry using the gap probability. For example, François (2002) addressed five of such models for the parameterization on the model of Prévot (1985). Second, the directional emissivity is calculated to be complementary to the hemispheric-directional reflectivity according to the Kirchhoff's law. The hemispheric-directional reflectivity can be estimated from a bi-directional reflectivity dataset by using an angular form factor (Li et al., 2000), a semi-empirical phenomenological model (Petitcolin et al., 2002a) or a kernel-driven BRDF model (Jiang and Li 2008a). Third, the directional emissivity is directly estimated as the ratio of directional thermal radiance to the blackbody radiance calculated with the Planck's law, with the assumption that all components in the scene have the same physical temperature (Liu et al., 2003). Although François (2002) and Sobrino et al. (2005) have respectively compared five parameterization models including radiative transfer (RT) and geometrical-optical (GO) models, their parameterized model was only based on the result of the model Prévot (1985), which was a probability-based model (turbid-medium model) computing the solution of the radiative transfer by summing the relative contributions of a large number of vegetation layers using the directional gap frequency concept. However, the model proposed by Prévot (1985) has not been widely validated and does not contain consideration of hotspot effect. Moreover, the coefficients from their parameterizations might not be consistent with other similar models (such as the SAIL (Scattering by Arbitrarily Inclined Leaves) model) and should be updated. The series of SAIL models have been used in this chapter because this model can deal with a much wider spectral range than the model of Prévot (1985), working in the visible/near-infrared to thermal infrared domains, and also because they have been widely used and validated. Therefore, the SAIL models can obtain the canopy's reflection and emission information together, which is helpful for the retrieval of surface parameters from both middle and thermal infrared channels. From this point of view, the objective of this chapter is to parameterize the directional emissivity based on the simulation result of SAIL model by using BRDF model and gap-frequency-based model, and refine their coefficients. Furthermore, based on the parameterization and new coefficients, we present the directional brightness temperature as the weights of three kinds of components and their multiple scattering contributions, and then validate the performance of the BRDF model in the DBT. Finally, we analyze the BRDF model in the angular normalization and discuss the angle requirement of this model.

4.2 Models of directional emissivity

4.2.1 Thermal SAIL model

The SAIL model was first proposed by (Verhoef 1984) to simulate the radiation flux interactions and bi-directional reflectivity of the canopy in the visible/near infrared (VNIR) range, and then extended to the SAILH model by modifying the single scattering contribution in the bi-directional reflectivity for the hotspot effect according to the theory of (Kussk 1985). In order to apply this model in the thermal infrared domain, Liu et al.(2003) and Verhoef et al. (2007) respectively provided additional facilities to support the calculation of internal thermal radiation. Since Verhoef et al. (2007) classified the components to sunlit and shaded leaves, and sunlit and shaded soils and Liu et al. (2003) only related to leaves and soils, the result of the former should be closer to the reality, especially for the representation of the hotspot. However, there should be no difference between the two models if the temperatures of all components are the same. In this way, the directional emissivity can be obtained as the ratio of directional radiance to the blackbody radiance from the given emissivities of leaves and soil background as well as the canopy structure. Because the model of (Verhoef et al. 2007) is not free of access, the model of Liu et al. (2003) was used for illustrations and named the TIR-SAIL model.

Similar with the primary version of SAIL, the TIR-SAIL is still based on analytical solution of four linear equations:

$$\begin{aligned}
\frac{d\boldsymbol{E_s}}{d\boldsymbol{z}} &= \boldsymbol{k_s E_s} \\
\frac{d\boldsymbol{E_-}}{d\boldsymbol{z}} &= -\sigma \boldsymbol{E_+} + \alpha \boldsymbol{E_-} - \boldsymbol{s E_s} - \boldsymbol{r} \\
\frac{d\boldsymbol{E_+}}{d\boldsymbol{z}} &= -\alpha \boldsymbol{E_+} + \sigma \boldsymbol{E_-} + \boldsymbol{s' E_s} + \boldsymbol{r} \\
\frac{d\boldsymbol{E_o}}{d\boldsymbol{z}} &= \omega \boldsymbol{E_s} + \upsilon \boldsymbol{E_-} + \mu \boldsymbol{E_+} - \boldsymbol{k_o E_o} + \boldsymbol{r_o}
\end{aligned} , \qquad (4.1)$$

where, $\boldsymbol{E_s}$, $\boldsymbol{E_-}$, $\boldsymbol{E_+}$ and $\boldsymbol{E_o}$ are respectively the direct solar irradiance on a horizontal plane, the diffuse downward irradiance, the diffuse upward irradiance and the irradiance in the direction of observation. $\boldsymbol{z}$ is the height counting from the top of the canopy. α is the attenuation coefficients for the upward and downward diffuse flux, and σ is the fraction of reflected upward (or downward) diffuse radiation that is scattering downward (or upward). $\boldsymbol{s}$ and $\boldsymbol{s'}$ are respectively the fraction of the upward and downward scattering from the solar irradiance, while $\boldsymbol{k_s}$ and $\boldsymbol{k_o}$ are respectively the attenuation coefficients in the solar and observation direction. Actually, there is no solar irradiance $\boldsymbol{E_s}$ in the TIR domain and only a small value in the MIR domain. $\boldsymbol{r}$ represents the upward or downward thermal radiation of the canopy itself, and $\boldsymbol{r_o}$ is the thermal radiation in the observation direction. The two parameters can be estimated as Eq.(4.2):

$$\boldsymbol{r} = \boldsymbol{FAVD} \cdot \varepsilon_{\boldsymbol{v}} \cdot \boldsymbol{B}(\boldsymbol{T_v}), \boldsymbol{r_o} = \boldsymbol{FAVD} \cdot \boldsymbol{F_o} \cdot \varepsilon_{\boldsymbol{v}} \cdot \boldsymbol{B}(\boldsymbol{T_v}) . \qquad (4.2)$$

In Eq.(4.2), $\varepsilon_{\boldsymbol{v}}$ and $\boldsymbol{T_v}$ are the leaves' emissivity and the physical temperature and $\boldsymbol{B}(\boldsymbol{T})$ is the blackbody radiance. $\boldsymbol{FAVD}$ is the foliage area volumetric density and $\boldsymbol{F_o}$ is the ratio of the projected leaves' area to the total leaves' area in the observation direction. The term $\boldsymbol{FAVD} \bullet \boldsymbol{F_o}$ equals to the term $\boldsymbol{k_o}$ that is used in the primary SAIL model. The bottom layer of the canopy is the soil emission and the reflected downward thermal radiance by the soil, written as:

$$\boldsymbol{E_+}(\boldsymbol{h}) = [\boldsymbol{E_-}(\boldsymbol{h}) + \boldsymbol{E_s}(\boldsymbol{h})] \cdot \rho_{\boldsymbol{g}} + \varepsilon_{\boldsymbol{g}} \cdot \boldsymbol{B}(\boldsymbol{T_g}) , \qquad (4.3)$$

where, $\boldsymbol{T_g}$ is the soil temperature, and $\varepsilon_{\boldsymbol{g}}$ and $\rho_{\boldsymbol{g}}$ are the emissivity and reflectivity of the soil (generally $\rho_{\boldsymbol{g}} = 1 - \varepsilon_{\boldsymbol{g}}$ for the opaque soil). More details about the TIR-SAIL can be found in

(Liu et al. 2003).

Fig.4-1(a) shows the directional emissivity at different viewing zenith angles (VZA) with vegetation and soil emissivity of 0.98 and 0.94 in the thermal wavelength, respectively. The spherical LAD (leaf angle distribution) was assumed for the canopy. The results obtained show a low angular variation for high vegetation cover canopy, which means almost a Lambertian surface. However, for low vegetation cover canopy, emissivity increases with increasing VZA due to the larger vegetation cover observed. The angular variation of emissivity is within 0.01 between nadir and 70°, but as large as 0.02 between nadir and horizontal observation. Note that for LAI < 1.5, the emissivity decreases at large angles (> 80°) because the multiple scattering contribution of the canopy has been reduced in such large angles. Fig.4-1(b) shows the result with vegetation and soil emissivity of 0.98 and 0.96. Comparison of the two figures illustrates that a smaller difference of soil and vegetation emissivity can reduce the angular variation of the canopy. However, such variation still exists even if soil and vegetation have the same emissivity, because in this case, the scattering contribution varies with viewing angles. Furthermore, the emissivity of all cases converged to the point about 0.99 in the horizontal direction, in which only vegetation component is observed. This point is called ***limit emissivity*** that will be addressed in the following part.

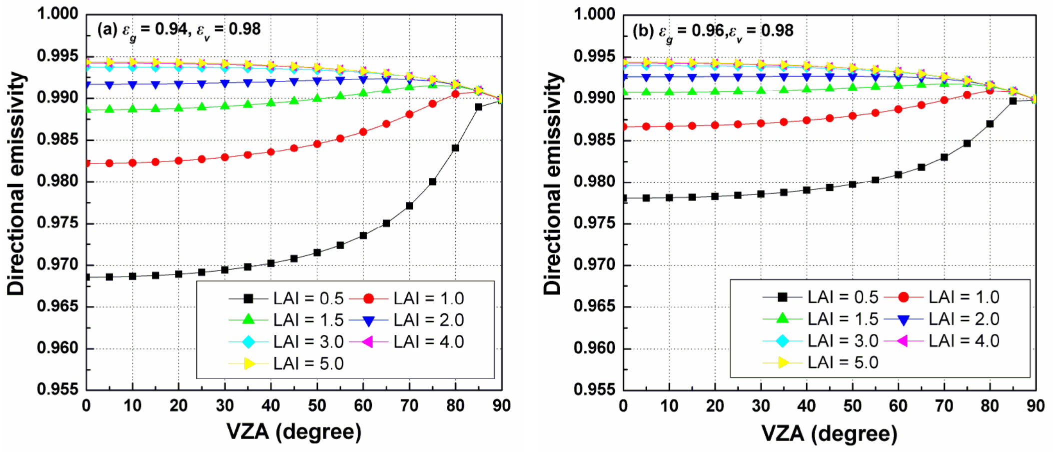

Fig.4-1. Angular variation of canopy emissivity at different LAI cases, with soil and vegetation emissivity of (a) 0.94 and 0.98, and (b) 0.96 and 0.98, respectively.

4.2.2 Parameterization models

As reported by some previous studies, the SAIL series model generally provides acceptable simulation results and therefore is used in many relevant fields (Jacquemoud et al. 2009). However, this model is time-consuming because it has to interactively calculate the upward and downward flux by dividing the canopy into several layers. Therefore, there is no exact mathematical expression for the directional emissivity or temperature, which makes it difficult to be used directly in the retrieval of some parameters from remote sensed data such as the component temperatures. As a result, it is needed to approximate the SAIL model using some variables that are easily obtainable from space.

To date, two major types of methods have been developed for the parameterization of the directional emissivity with known viewing geometrical and surface characteristics: First, the directional emissivity is estimated directly as a weight of components emissivity and their fractions in a particular viewing direction, and the additional term of multiple scattering. For example, Sobrino and Caselles (1990) estimated the directional emissivity for row crops by weighting the proportions of the hedgerow top, wall and soil and the corresponding scattering of those components. On basis of their method, the NDVI threshold method was subsequently proposed to retrieval emissivity from remote sensed data. The vegetation-cover method (Valor and Caselles 1996) used the fraction of vegetation cover to average the soil and vegetation emissivity, and introduced a term $d\varepsilon$ to consider the multiple scattering at pixel scale. Second, the directional emissivity is obtained from the complementary to the hemispheric-directional reflectivity according to the Kirchhoff's law. For example, based on the geometrical model of (Li and Strahler 1992) for a sparse canopy composed by soil and vegetation, Snyder and Wan (1998) integrated the BRDF model over the hemisphere to obtain hemispheric-directional reflectivity, and then generated emissivities for IGBP-scheme land cover classes. Li et al. (2000) and Petitcolin et al. (2002a) respectively used an angular form factor and a semi-empirical phenomenological model to obtain such emissivity from bi-directional reflectivity. François et al. (1997) firstly developed an analytical parameterization using the gap frequency function and cavity effect factor, and François (2002) calculated the hemispheric-directional reflectivity from gap frequency theory by accounting for the scattering between soil and vegetation interface. This thesis will check the performance of four models: the kernel-driven BRDF model (Jiang and Li 2008a), semi-empirical BRDF model (Li et al. 2000), the analytical model (François et al. 1997) and the multiple-scattering model (François 2002). The kernel-driven BRDF model will be used in next chapter to retrieve directional emissivity from multi-angular observation data, and the updated cavity effect factor in (François et al. 1997) on basis of the TIR-SAIL model, will be applied in simulation of directional thermal radiance. The other two models are used for comparisons among those models.

A. The kernel-driven BRDF model: K-BRDF

The kernel-driven BRDF model (hereafter called as K-BRDF) was firstly proposed to fit bi-directional reflectivity from several different viewing directions. This model usually consists of three parts: the isotropic scattering, the volumetric scattering and the geometric-optical scattering, written as:

$$\rho(\theta_v,\theta_s,\varphi) = \boldsymbol{k_{iso}} + \boldsymbol{f_{vol}} \cdot \boldsymbol{k_{vol}}(\theta_v,\theta_s,\varphi) + \boldsymbol{f_{geo}} \cdot \boldsymbol{k_{geo}}(\theta_v,\theta_s,\varphi)\,, \tag{4.4}$$

where, $\boldsymbol{f_{iso}}$ is the isotropic scattering term, $\boldsymbol{f_{vol}}$ is the coefficient of the volumetric kernel $\boldsymbol{k_{vol}}$, and $\boldsymbol{f_{geo}}$ is the coefficient of the geometric kernel $\boldsymbol{k_{geo}}$. Such model is promising for the directional correction of the reflectance in the visible spectral range because it links to the viewing geometry of the solar-target-sensor using the kernels and relates to the components' characteristics through the observed reflectances. This model may also provide us an opportunity to achieve the angular normalization of temperature if the target's temperatures or brightness temperatures at least in three viewing directions are known.

A suitable expression of $\boldsymbol{k_{vol}}$ was derived by Roujean et al. (1992), which was called the Ross-Thick kernel for its assumption of a dense leaf canopy. It is a single-scattering solution of the radiative transfer equation by (Ross 1981) for plane-parallel dense vegetation canopy with uniform leaf angle distribution, a Lambertian background and equal leaf transmittance and reflectance. It does not account for the hotspot effect.

$$\boldsymbol{k_{vol}}(\theta_v,\theta_s,\varphi)=\frac{(\pi/2-\xi)\cos\xi+\sin\xi}{\cos\theta_v+\cos\theta_s}-\frac{\pi}{4}, \tag{4.5}$$

where, ξ is the phase angle, related to the sun-target-observer position as:

$$\xi=\cos\theta_v\cos\theta_s+\sin\theta_v\sin\theta_s\cos\varphi\,. \tag{4.6}$$

The Li-Sparse kernel derived by (Wanner et al. 1995) was reported to work well with the observed data. This kernel is derived from the geometric-optical mutual shadowing BRDF model (Li and Strahler 1992). The original form of this kernel is not reciprocal in the viewing and solar directions, a property that is expected from homogeneous natural surface viewed at coarser spatial resolution, but then was refined to be reciprocal by assuming the sunlit component in the viewed scene simply varies as $1/\cos\theta_S$. As a result, the reciprocal model was Li-SparseR kernel:

$$\begin{aligned}\boldsymbol{k_{geo}}(\theta_v,\theta_s,\varphi)&=\boldsymbol{O}(\theta_v,\theta_s,\varphi)-\sec\theta'_v-\sec\theta'_s\\&+\frac{1}{2}(1+\cos\xi')\sec\theta'_v\sec\theta'_s\end{aligned}, \tag{4.7}$$

with,

$$\boldsymbol{O}=\frac{1}{\pi}(\boldsymbol{t}-\sin\boldsymbol{t}\cos\boldsymbol{t})(\sec\theta'_v+\sec\theta'_s)$$

$$\cos\boldsymbol{t}=\frac{\boldsymbol{h}}{\boldsymbol{b}}\frac{\sqrt{\boldsymbol{D}^2+(\tan\theta'_v\tan\theta'_s\sin\varphi)^2}}{\sec\theta'_v+\sec\theta'_s}$$

$$\boldsymbol{D}=\sqrt{\tan^2\theta'_v+\tan^2\theta'_s-2\tan\theta'_v\tan\theta'_s\cos\varphi}$$

$$\cos\xi'=\cos\theta'_v\cos\theta'_s+\sin\theta'_v\sin\theta'_s\cos\varphi$$

$$\theta'_v=\tan^{-1}\left(\frac{\boldsymbol{b}}{\boldsymbol{r}}\tan\theta_v\right),\theta'_s=\tan^{-1}\left(\frac{\boldsymbol{b}}{\boldsymbol{r}}\tan\theta_s\right).$$

where, $\boldsymbol{O}$ is the overlap area between the view and solar shadows. The term $\boldsymbol{cost}$ should be constrained to the range [-1, 1], as values outsides of this range imply no overlap and should be disregarded. The ratio $\boldsymbol{h/b}$ and $\boldsymbol{b/r}$ are the dimensionless crown relative height and shape parameters, respectively, and should be preselected. In this thesis, $\boldsymbol{h/b}$ = 2 and $\boldsymbol{b/r}$ = 1, i.e. the spherical crowns are separated from ground by half their diameter.

The integration of the BRDF model will generate the hemispheric-directional reflectivity and the directional emissivity is calculated with the Kirchhoff's law:

$$\varepsilon_{\boldsymbol{i}}(\theta_{\boldsymbol{v}},\varphi_{\boldsymbol{v}})=1-\int_0^{2\pi}\int_0^{\pi/2}\rho(\theta_{\boldsymbol{s}},\varphi_{\boldsymbol{s}},\theta_{\boldsymbol{v}},\varphi_{\boldsymbol{v}})\sin(\theta_{\boldsymbol{s}})\cos(\theta_{\boldsymbol{s}})\boldsymbol{d}\theta_{\boldsymbol{s}}\boldsymbol{d}\varphi_{\boldsymbol{s}}\,. \tag{4.8}$$

According to Eq.(4.4), the integration of the bi-directional reflectivity in the upward hemisphere equals to the result of integrating the three kernels ($\boldsymbol{k_{vol}}$, $\boldsymbol{k_{geo}}$, and 1) in the same angle range because the values of the kernels' coefficients are fixed for all angles. Jiang and Li (2008a) calculated the integration of the Ross-Thick volumetric kernel ($\boldsymbol{Ik_{vol}}$) and Li-SparseR ($\boldsymbol{Ik_{geo}}$) with solar zenith angle varying from 0° to 80° and azimuth angle from 0° to 360° in a step 0.05°, and then related $\boldsymbol{Ik_{vol}}$ and $\boldsymbol{Ik_{geo}}$ to the viewing zenith angle ($\theta_{\boldsymbol{v}}$) using an exponent growth function and Gaussian function, respectively.

$$\boldsymbol{Ik_{vol}}(\theta_{\boldsymbol{v}})=\boldsymbol{A}_0+\boldsymbol{A}_1\exp(\theta_{\boldsymbol{v}}/\boldsymbol{t}_1)\,,\ \text{ and }\ \boldsymbol{If_{geo}}(\theta_{\boldsymbol{v}})=\boldsymbol{B}_0+\frac{\boldsymbol{B}_1}{\omega\sqrt{\pi/2}}\exp\left[-2\left(\frac{\theta_v-\theta_c}{\omega}\right)^2\right], \tag{4.9}$$

where, $\boldsymbol{A}_0$ (= -0.0299), $\boldsymbol{A}_1$ (= 0.01278), $\boldsymbol{t}_1$ (= 21.43823), $\boldsymbol{B}_0$ (= -2.01124), $\boldsymbol{B}_1$ (= -29.40855), ω (= 68.88171) and $\theta_{\boldsymbol{c}}$ (= 90.95449) are the regressed coefficients. The unit of $\boldsymbol{t}_1$ and $\theta_{\boldsymbol{c}}$ is degree and the other terms are unitless.

B. The semi-empirical BRDF model: S-BRDF

The semi-empirical BRDF model (hereafter called as S-BRDF) was first proposed by (Minnaert 1941) and then modified by (Li et al. 2000) by adding the terms of the azimuth angle to describe the bi-directional characteristics of the surface as:

$$\rho(\theta_{\boldsymbol{v}},\theta_{\boldsymbol{s}},\varphi)=\rho_0\cos^{\boldsymbol{k}-1}\theta_{\boldsymbol{v}}\cos^{\boldsymbol{k}-1}\theta_{\boldsymbol{s}}[1+\boldsymbol{b}(1-\boldsymbol{k}^2)\sin\theta_{\boldsymbol{v}}\sin\theta_{\boldsymbol{s}}\cos\varphi], \tag{4.10}$$

where, ρ_0 is the reflectivity with viewing and incident zenith angle at nadir observation. $\boldsymbol{k}$ is a parameter between 0 and 1. For a Lambertian surface, $\boldsymbol{k}$ equals to 1. The term $\boldsymbol{b(1-k^2)}$ term is called anisotropy factor. This anisotropy factor is positive if backscattering is significant and negative when forward-scattering is dominant. The integration of Eq.(4.10) like Eq.(4.8) will conduct the directional emissivity from hemispheric directional reflectivity as:

$$\varepsilon(\theta_{\boldsymbol{v}})=1-\frac{2\pi}{\boldsymbol{k}+1}\rho_0\cos^{\boldsymbol{k}-1}\theta_{\boldsymbol{v}}\,. \tag{4.11}$$

Although the directional emissivity in Eq.(4.11) is not related to the term $\boldsymbol{b}$ in Eq.(4.10), it still needs at least three bi-directional reflectivity to solve the coefficients ρ_0, $\boldsymbol{k}$ and $\boldsymbol{b}$.

C. The analytical parameterization model: FRA97

Based on the radiative transfer model of (Prévot 1985), François et al.(1997) developed the following analytical parameterization model (hereafter called as FRA97) using the gap frequency theory:

$$\varepsilon(\theta_{\boldsymbol{v}})=1-\rho=1-\boldsymbol{b}(\theta_{\boldsymbol{v}})\boldsymbol{M}(1-\varepsilon_{\boldsymbol{g}})-\alpha[1-\boldsymbol{b}(\theta_{\boldsymbol{v}})\boldsymbol{M}](1-\varepsilon_{\boldsymbol{v}})\,, \tag{4.12}$$

where, ε_{g} and ε_{V} are the emissivity of soil and vegetation, respectively. $\boldsymbol{b}(\theta)$ is the directional gap frequency and $\boldsymbol{M}$ is the hemispheric gap frequency of the canopy. For a canopy with spherical leaf angle distribution and random dispersion, they can be expressed as:

$$\boldsymbol{b}(\theta)=\exp[-\frac{0.5}{\cos\theta}\boldsymbol{LAI}],\ \text{and}\ \ \boldsymbol{M}=\frac{1}{\pi}\int_{-\pi/2}^{\pi/2}\boldsymbol{b}(\theta)\boldsymbol{d}\theta=\exp(-0.825\boldsymbol{LAI})\,. \qquad (4.13)$$

The second term of the right side of Eq.(4.12) is the hemispheric-directional reflectivity of the soil in the viewing direction, and the third term is the hemispheric-directional reflectivity of the vegetation. α is cavity effect factor that expresses the part of the incident beam which is reflected by the leaves is absorbed by the canopy. Therefore, α is used for the multiple scattering inside the canopy and its values in different viewing zenith angles were provided in (François 2002).

D. The multiple-scattering model in (François 2002): FRA02

Similar with FRA97, the model proposed by (François 2002) (hereafter called as FRA02) estimated the directional emissivity based on hemispheric-directional reflectivity but paid more attentions to the multiple scattering in the interface of soil and vegetation layers, written as:

$$\varepsilon(\theta_v)=1-\rho=1-[1-\boldsymbol{b}(\theta_v)](1-\varepsilon_v)-\boldsymbol{M}\cdot\boldsymbol{b}(\theta_v)(1-\varepsilon_g)/[1-(1-\varepsilon_g)\sigma_f(1-\varepsilon_v)]. \qquad (4.14)$$

The term σ_f is the hemispherical shielding factor, linked to the hemispherical gap frequency $\boldsymbol{M}$ in Eq.(4.13) as $\sigma_f = 1-\boldsymbol{M}$. the other terms have been defined above. The second term of the right-hand side is the reflectivity of vegetation in the viewing direction, and the third term is the sum of the soil single-scattering reflectivity and the multiple-scattering reflectivity in the interface of soil and vegetation layers. The term $\sigma_f(1-\varepsilon_v)$ stands for the downward hemispheric albedo of the vegetation layer, and the denominator in Eq.(4.14) was approximated from the infinite series: $1+(1-\varepsilon_v)\sigma_f(1-\varepsilon_v)+[(1-\varepsilon_v)\sigma_f(1-\varepsilon_v)]+[(1-\varepsilon_v)\sigma_f(1-\varepsilon_v)]^3\ldots$ for the multiple scattering. Compared with the FRA97, FRA02 takes more cares in multiple scattering behaviors occurring in the interface of the soil and vegetation layers, while FRA97 pays more attention to the inside vegetation-to-vegetation multiple scattering.

4.3 Parameterization result of directional emissivity

4.3.1 Comparison of the TIR-SAIL and BRDF models

The bi-directional reflectivity used in the K-BRDF and S-BRDF models to obtain their respective coefficients is simulated by the SAILH model developed by (Verhoef 1989), which is reported to simulate canopy's bi-directional reflectivity of the canopy more accurately than other series of this model because it adds the hotspot effect in the solar direction. With a fixed viewing beam, the integration of the bi-directional reflectivity in the upper hemisphere generates the directional-hemispheric reflectivity. Since the directional-hemispheric reflectivity equals to the hemispheric-directional reflectivity on the basis of the reciprocity theory in the BRDF field, the directional emissivity is finally calculated as one minus the hemispheric-directional reflectivity according to the Kirchhoff's law. However, we find out that the directional emissivity (ε_i) from the above integration differs from simulated result direct from the above TIR-SAIL model (ε_t), and that it is needed to correct the integrated emissivity using a linear function for most cases (i.e, $\varepsilon_t = \boldsymbol{a}\cdot\varepsilon_i + \boldsymbol{b}$, $\boldsymbol{a}$ and $\boldsymbol{b}$ are coefficients, and depend on LAI). This correction leads an error less than 0.002 to the integrated emissivity.

Based on the bi-directional reflectivity simulated by the SAILH model with soil and vegetation emissivity of 0.94 and 0.98, the coefficients in the K-BRDF and S-BRDF models are first analytical regressed, and then are used to calculate the directional emissivity respectively using Eqs. (4-8) and (4-11). As reported in the literatures (Snyder and Wan 1998; Sobrino et al. 2005), the K-BRDF model presents much uncertainty for the large viewing zenith angle. Therefore, only the bi-directional reflectivity with viewing zenith angle no larger than 65° is used, but we illustrate the directional emissivity value up to 80° in Fig.4-2, which displays the comparison of the directional emissivity from the TIR-SAIL model, the K-BRDF and S-BRDF models with (a) LAI = 0.5, (b) LAI = 1.0, (c) LAI = 2.0 and (d) LAI = 4.0, respectively. It shows that the three models have the similar tendency for LAI =0.5 and LAI =1.0, and the difference of their directional emissivity is very small, even at the large viewing zenith angle (i.e., beyond 65°). However, for LAI = 2.0 and 4.0, significant difference of their directional emissivity occurred, especially at larger angles. For example, in Fig.4-2(c), the emissivity increases with the VZA all the time in the two BRDF models but it decreases with VZA in the TIR-SAIL model after 65°.

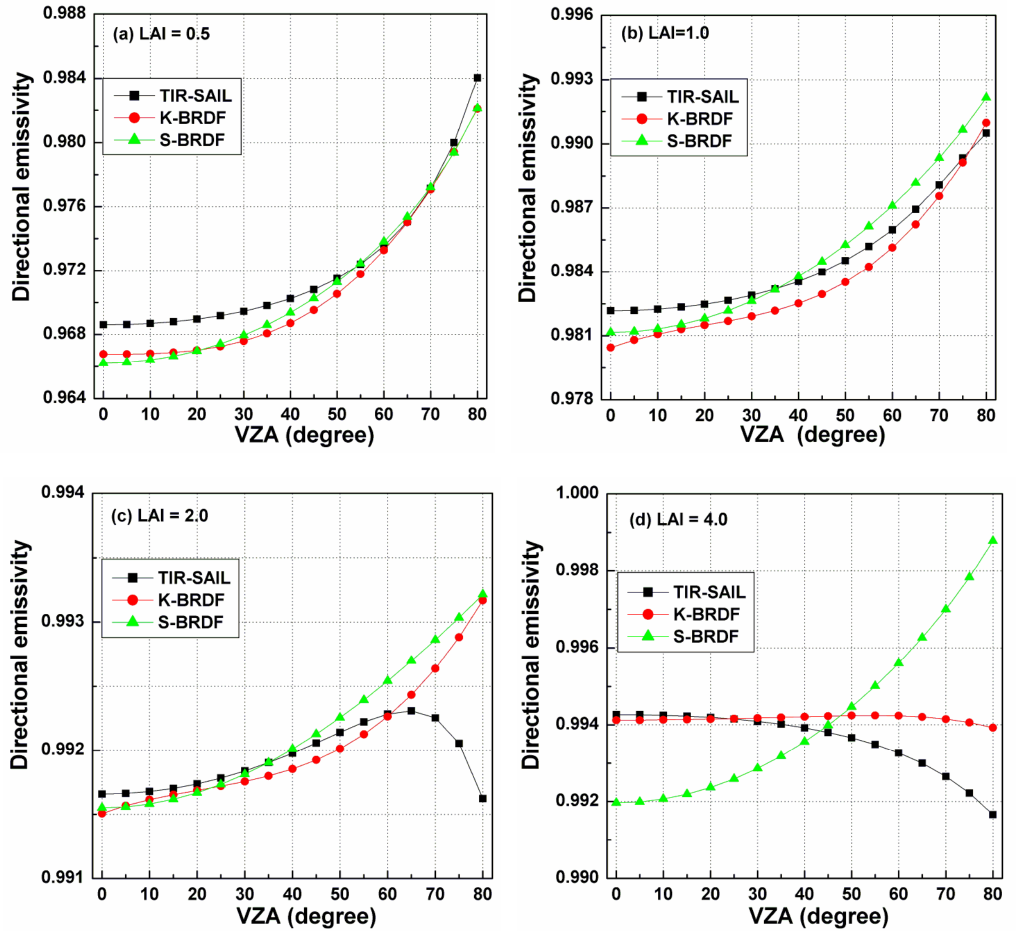

Fig.4-2. Comparison of directional emissivity respectively from TIR-SAIL model, K-BRDF model and S-BRDF model at (a) LAI = 0.5, (b) LAI = 1.0, (c) LAI = 2.0 and (d) LAI = 4.0.

In Fig.4-2(d), the S-BRDF model almost has the different tendency with the TIR-SAIL model, and their values differ from each other. On the contrary, the emissivity of the K-BRDF model is close to that of the TIR-SAIL model, especially under small VZAs, but its angular variation is much less than the TIR-SAIL model. Although the emissivity curve of the K-BRDF model seems to be similar with that of the TIR-SAIL model, the curve actually first increases with the VZA and decreases after 65°. Comparison of the coefficients of the K-BRDF model among those different LAIs illustrates that the volumetric scattering coefficient $\boldsymbol{f_{vol}}$ for Fig.4-2(d) is negative and the others are all positive, which therefore makes the emissivity of this model decreases in large VZAs.

From the above discussion and the result of Fig.4-2, we find out that both the K-BRDF and S-BRDF model generally perform well in the presentation of the directional emissivity, especially for sparse and middle dense vegetation canopy. Although they have a relative higher error in the dense canopy, this error (less than 0.002) can be ignored, especially for the K-BRDF model. Besides, the two BRDF models almost have small difference in the directional emissivity except for the case of Fig.4-2(d). However, one should note that the parameter $\boldsymbol{k}$ in the S-BRDF was required between 0 and 1, which will result in a series of directional emissivity decreasing rather than increasing with the VZA in theory. On the contrary, the result of Fig.4-2 is actually obtained with $\boldsymbol{k}$ larger than 1. Although the S-BRDF model performs well in fitting mathematically the bi-directional reflectivity, the parameter $\boldsymbol{k}$ larger than 1 reduces its physical meaning. Therefore, the S-BRDF model is not recommended, at least for the bi-directional reflectivity and directional emissivity from the SAIL series models.

Furthermore, we chose ten vegetation samples and seventeen soil samples from UCSB Emissivity Library (Snyder and Wan 1998; Snyder et al. 1998), and calculated their channel emissivity with the MIR spectral response function that will be stated in the next chapter. The bi-directional reflectivity for each combination (total 170) of soil and vegetation was simulated using the SAILH model and then was used to fit the three kernel coefficients of the K-BRDF model. Fig.4-3 shows the relationship among those three coefficients for different LAIs, which indicates that there is a linear relationship between those kernel coefficients, especially for small LAIs. If any one of the three coefficients can be obtained, the other two will be consequently determined from this linear relationship. As a result, the number of unknowns is reduced. However, this linear relationship almost disappears or is eliminated for the dense vegetated canopy, such as the case LAI = 4.0 (see Fig.4-3(d)). The application of such linear relationship might cause much uncertainty to the result in this case.

Besides, as seen from Fig.4-3, it is found that the value ranges of the coefficients $\boldsymbol{f_{geo}}$, $\boldsymbol{f_{vol}}$ and $\boldsymbol{f_{iso}}$ mainly distributed within [0.0, 0.9], [-0.3, 0] and [0, 0.3], respectively, and become narrower with the increasing LAIs. This information is generally useful in the retrieval of those coefficients from remotely sensed data and will be used as a prior knowledge in the process of recovering emissivity from multi-angular data that will be presented in the next chapter.

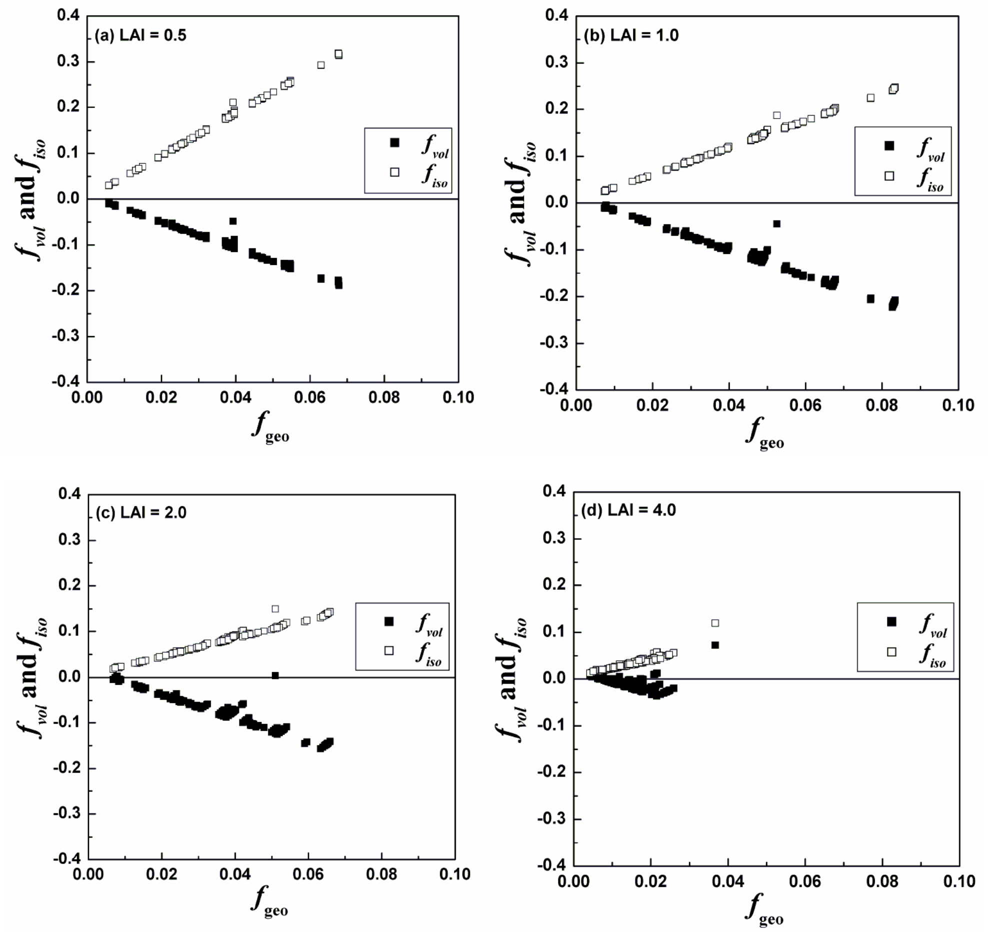

Fig.4-3. Relationship between the three coefficients of the K-BRDF model at (a) LAI =0.5, (b) LAI =1.0, (c) LAI =2.0, and (d) LAI = 4.0, respectively.

4.3.2 Comparison of the TIR-SAIL and gap-frequency-based models

Fig.4-4 displays the directional emissivity respectively from the TIR-SAIL model (black square), FRA97 (red circles) and FRA02 (blue downward-pointing triangles) at different LAIs. It shows that the emissivity of both FRA97 and FRA02 parameterization models is totally smaller than that of the TIR-SAIL model. The reason for the difference between the TIR-SAIL and FRA02 model might be explained as that the FRA02 parameterization model only deals with the multiple scattering in the interface of soil and vegetation layers and ignores the multiple scattering inside the vegetated layers. The TIR-SAIL model iteratively calculates the upward and downward flux between two adjacent vegetated layers and only accounts for single scattering between soil and the upper vegetation layers. On the other hand, because the FRA97 model handles the contributions from the two scattering paths in the TIR-SAIL model, its results are closer to the TIR-SAIL model than the FRA02 model, and has a similar tendency with the TIR-SAIL model as shown in Fig.4-4.

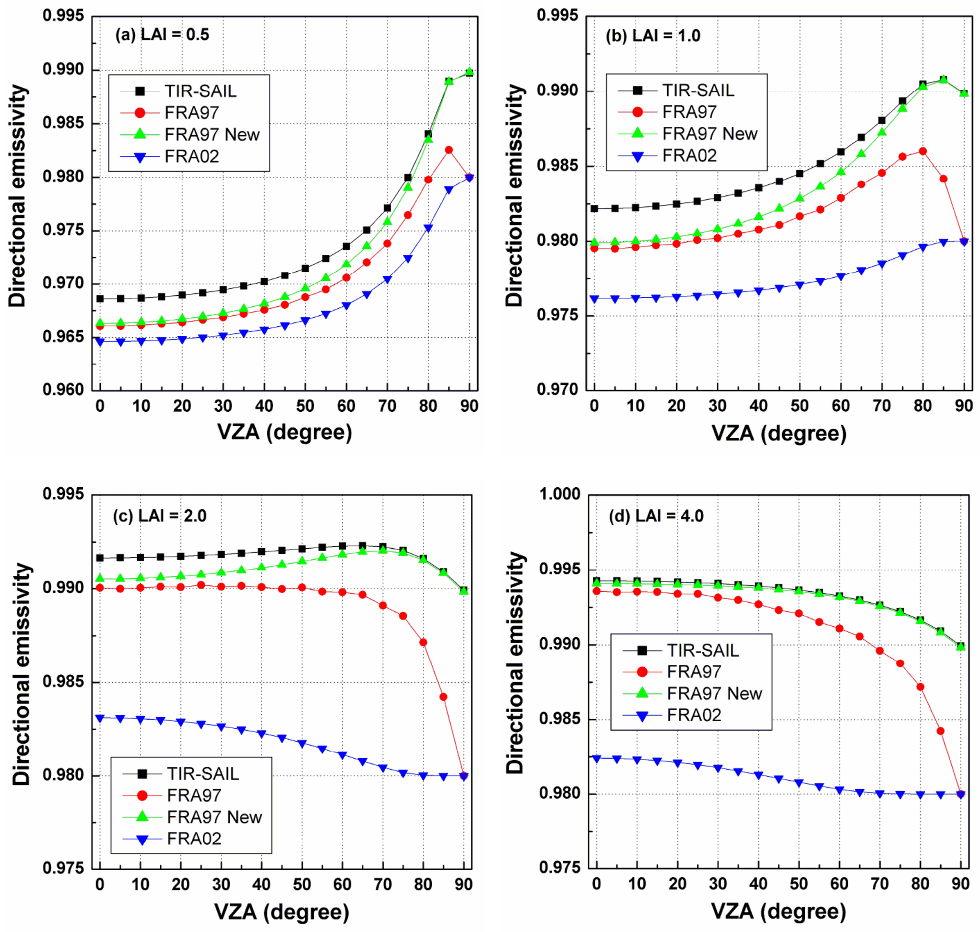

Fig.4-4. Comparison of directional emissivity respectively from the TIR-SAIL model, FRA97 model with previous and new cavity effect factors, and FRA02 models at (a) LAI = 0.5, (b) LAI = 1.0, (c) LAI = 2.0 and (d) LAI = 4.0.

However, the emissivity difference between the FRA97 and the TIR-SAIL model also cannot be ignored, especially for some large VZAs. It needs to update the cavity effect factor α, which is an indicator of the multiple scattering in the canopy and generally represents the proportion of the radiation that penetrates into the canopy and is reflected out of the canopy. Based on the radiative transfer model of (Prévot 1985), François et al. (1997) found that the canopy directional emissivity at a specified VZA always reached a limit emissivity ε_{lim} which only depended on the vegetation emissivity and VZA rather than on the background soil emissivity. Fig.4-5(a) and (b) present the directional emissivity at VZA = 0° and 55° at different LAIs simulated from the TIR-SAIL model. The vegetation emissivity is 0.98 and the soil emissivity is 0.90, 0.92, 0.94 and 0.96, respectively. It releases that the canopy emissivity for all soil cases reaches the same point, i.e., the limit emissivity ε_{lim}, which is about 0.9944 and 0.9935 respectively for VZA = 0° and 55°, larger than the vegetation emissivity 0.98 due to the multiple scattering. Furthermore, Fig.4-5(c) shows that the limit emissivity ε_{lim} increases with the vegetation emissivity. François et al. (1997) developed a method to calculate the cavity effect factor α as (ε_v is the vegetation emissivity):

$$\alpha = (1-\varepsilon_{\text{lim}})/(1-\varepsilon_v)\,. \tag{4.15}$$

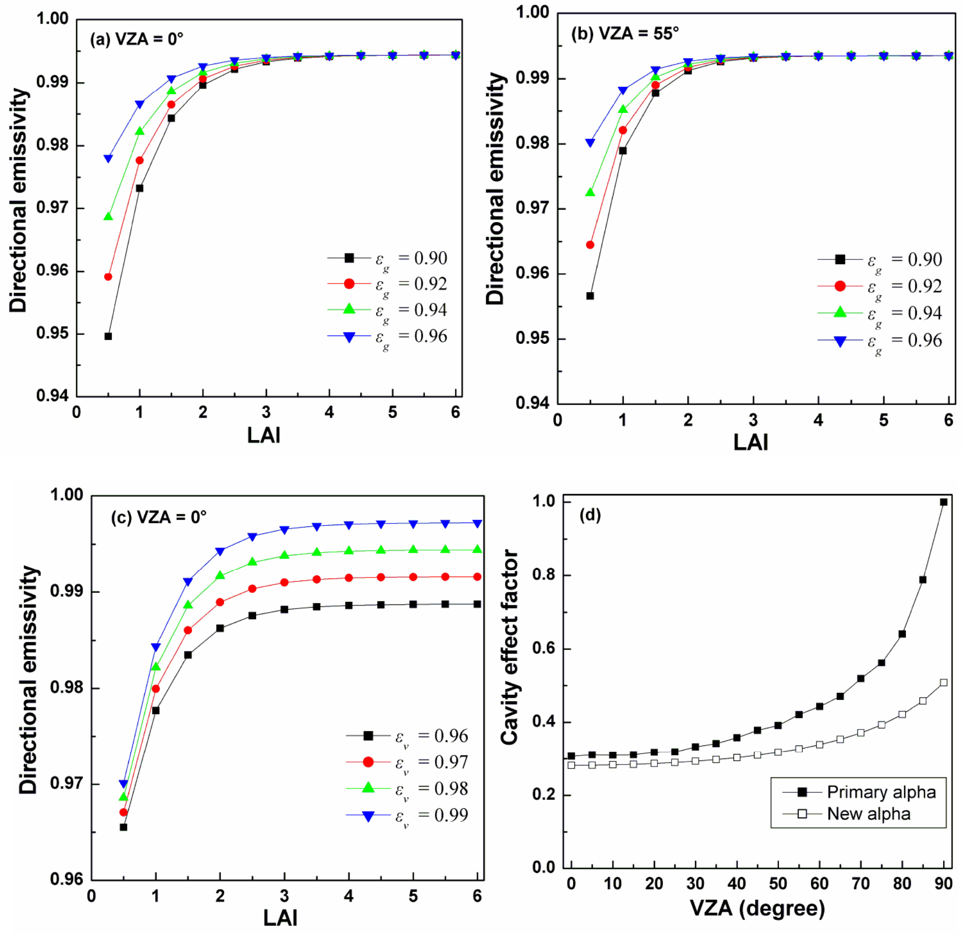

Fig.4-5. Limit emissivity at different conditions. (a) and (b): the limit emissivity of the canopy at VZA = 0° and 55° with vegetation emissivity 0.98 but different soil emissivity, respectively. (c): the limit emissivity at VZA = 0° with soil emissivity 0.94 but different vegetation emissivity. (d): the primary and new cavity effect factors at different viewing zenith angles.

Based on the directional emissivity from the TIR-SAIL model and the FRA97 parameterization model, new cavity effect factor α for the TIR-SAIL model was calculated and presented in Fig.4-5(d) along with those reported in (François et al. 1997). The cavity effect factor actually slightly varies with vegetation emissivity but the variation is very small and can be ignored. As seen from Fig.4-5(d), the new α is totally smaller than those of (François et al. 1997), especially for the large VZAs, which indicates that multiple scattering still contributes to the directional emissivity at VZA = 90° in the TIR-SAIL model, while this scattering disappears in the model of (Prévot 1985). We use the new factor in Eq.(4.12) to recalculate the directional emissivity and present the result in Fig.4-4 (green triangles, denoted as ***FRA97 New***). Compared with the result of the FRA97 model using previous version of the factor, the directional emissivity of the ***FRA97 New*** is closer to the TIR-SAIL model, especially for the large VZAs, because the difference of the new and previous α is more significant in large VZAs than the smaller one, as shown in Fig.4-5(d).

4.4 Parameterization of directional brightness temperature

Up to now, modeling the directional brightness temperature (DBT) of homogenous or heterogeneous canopies has attracted many attentions. For example, except for the aforementioned TIR-SAIL models, Kimes (1983) simulated the DBT of the row canopy by treating the row structure as a rectangular cross section for the first time and calculated the fractions of different components from the row structure. Inspired by this concept, several similar models have been developed by considering the bi-directional gap, hotspot effect or crop growth stages (Chen et al. 2002; Du et al. 2007; Huang et al. 2010; Yan et al. 2003; Yu et al. 2004). Pinheiro et al. (2006) developed a Modified Geometric Projection (MGP) model by highly parameterizing the geometric-optics (GO) model to first separate the components' fractions with given canopy structure and observation variables and then weighted those fractions with components' brightness temperatures to generate the DBT for homogeneous or discontinues canopies. The MGP was further used to investigate the angular variation of surface temperature for the sensors AVHRR and SEVIRI (Phinheiro et al. 2006; Rasmussen et al. 2011; Rasmussen et al. 2010). The MGP can present the hotspot of the LST at pixel scale, but it ignores the contribution of multiple scattering in the canopy, which reduces the DBT in theory. Besides, it is difficult to provide the input data about the tree density and width and height, which hampers its wide application.

As stated above, this thesis used the TIR-SAIL to simulate the directional emissivity. To unify the directional emissivity, the way of simulating DBT should also come from the SAIL series model. However, since the TIR-SAIL model developed by (Liu et al. 2003) only concerns on two components (soil and vegetation), its DBT was only dependent on the VZA but independent on viewing azimuth angle (VAA). Therefore, the TIR-SAIL model of (Liu et al. 2003) was unable to character the hotspot. Although the 4-component SAIL model proposed by (Verhoef et al. 2007) separated the components to four parts: sunlit and shaded leaves, and sunlit and shaded soil, we have no access to get the code of this model. To the end, the parameterization model of the SAILH model by (Li et al. 2010), who presented the primary SAILH model by weighting four components' (sunlit and shaded leaves, and sunlit and shaded soil) reflectivity and their fractions estimated from given canopy structures, was employed to parameterize the DBT for the homogenous canopy, written as:

$$\boldsymbol{L} = \sum_{\boldsymbol{i}=1}^{\boldsymbol{N}} \boldsymbol{f_i} \cdot \varepsilon_{\boldsymbol{i}} \cdot \boldsymbol{B_i}(\boldsymbol{T_i}) + \boldsymbol{L_{multi}}, \tag{4.16}$$

$$\boldsymbol{L_{multi}} = \sigma_{\boldsymbol{f}} \boldsymbol{L_{leaf}} (1-\varepsilon_{\boldsymbol{g}}) + (1-\alpha)[1-\boldsymbol{b}(\theta)(1-\sigma_{\boldsymbol{f}})] \cdot [1-\boldsymbol{b}(\theta)](1-\varepsilon_{\boldsymbol{v}}) \cdot \boldsymbol{L_{leaf}}, \tag{4.17}$$

where, $\boldsymbol{L}$ is the directional thermal radiance (the inversion of $\boldsymbol{L}$ according to the Planck's law will produce the DBT). $\boldsymbol{f_i}$ is the fractions of different components and can be estimated from the parameterization model of (Li et al. 2010), provided the solar and viewing directions, canopy structure and model parameters. $\boldsymbol{T_i}$ and $\varepsilon_{\boldsymbol{i}}$ are the temperature and emissivity of the components. Only three components (leaves and sunlit and shaded soils) are concerned in this thesis, because the temperature difference between sunlit and shaded leaves is very small compared to the temperature difference between the sunlit and shaded soils. $\boldsymbol{L_{multi}}$ is the multi-scattering between soil and leaves, and between leaves inside the canopy. The first part of the right-hand side of Eq.(4.17) is the reflected leaves' radiation by the soil, and the second part is the multi-scattering inner the canopy. The terms in this equation have been defined above. The cavity effect factor used the updated one based on the TIR-SAIL model. Table 4-1 lists the main input variables of the simulation DBT including the solar zenith and azimuth angles, LAI of the canopy, the temperature of leaf ($\boldsymbol{T_{leaf}}$), sunlit soil ($\boldsymbol{T_{sun\_soil}}$) and shaded soil ($\boldsymbol{T_{shd\_soil}}$), and the emissivity of vegetation (ε_v) and soil (ε_g). Note that the simulated DBT is assumed to be atmospherically corrected.

Table 4-1. The main input parameters for the DBT simulation

SAA	SZA	LAI	$\boldsymbol{T_{leaf}}$	$\boldsymbol{T_{sun\_soil}}$	$\boldsymbol{T_{shd\_soil}}$	ε_v	ε_g
120°	30°	0.5:0.5:5.0	305 K	320 K	315 K	0.985	0.95

Besides, we also used the kernel-driven BRDF model to fit the hemispheric DBT by replacing the bi-directional reflectivity in the left-hand side of Eq.(4.4) with the DBT, as reported by (Peng et al. 2011). Since we aim at the non-isothermal pixel and the components' fractions vary with solar and viewing azimuth angles, the DBT is consequently depends on the azimuth angles.

$$\boldsymbol{DBT}(\theta_v,\theta_s,\varphi)=\boldsymbol{k}'_{\boldsymbol{iso}}+\boldsymbol{f}'_{\boldsymbol{vol}}\cdot\boldsymbol{k}_{\boldsymbol{vol}}(\theta_v,\theta_s,\varphi)+\boldsymbol{f}'_{\boldsymbol{geo}}\cdot\boldsymbol{k}_{\boldsymbol{geo}}(\theta_v,\theta_s,\varphi)\,. \tag{4.18}$$

The Ross-Thick and Li-SparseR kernels are used as the volumetric and geometrical scattering kernels in Eq.(4.18). Based on the input variables shown in Table 4-1 for the DBT simulation using Eq.(4.16) and the SAILH parameterization model (Li et al. 2010), Fig.4-6 displays the simulated DBT distribution (the first column) and the fitted DBT from the K-BRDF model (the second column) and their temperature difference (the third column) at (a) LAI = 0.5, (b) LAI = 1.0 and (c) LAI = 2.0. The maximum zenith angle is constrained to 60° because the K-BRDF model was reported to obtain unacceptable result for larger zenith angle (Snyder and Wan 1998; Sobrino et al. 2005).

As seen from Fig.4-6, the angular variation of the DBT is up to about 3.0 K for the simulation conditions (Table 4-1). However, this angular variation relies on the components' temperature difference and canopy structure: larger temperature difference generally leads to larger angular variation. The K-BRDF model fits well the distribution of DBT, only leading to error lower than 0.3 K. The hotspot effect in the solar direction is significant and but it is also found that the maximum temperature difference occurs around this direction and the DBT from the K-BRDF model is generally larger than that from the simulation result in the directions around the solar beam. The increase of LAI totally decreases the DBT because the fraction of leaves increases and the leaves' temperature is lower than that of soils. Furthermore, the LAI also influences the temperature difference caused by regression process of the K-BRDF model. Fig.4-7 shows the RMSE (root-mean-square-error) and the maximum temperature difference with LAIs. It indicates that the RMSE is smaller than 0.1 K and the maximum temperature is smaller than 0.3 K, and both of them reach their global maximum at about LAI = 2.

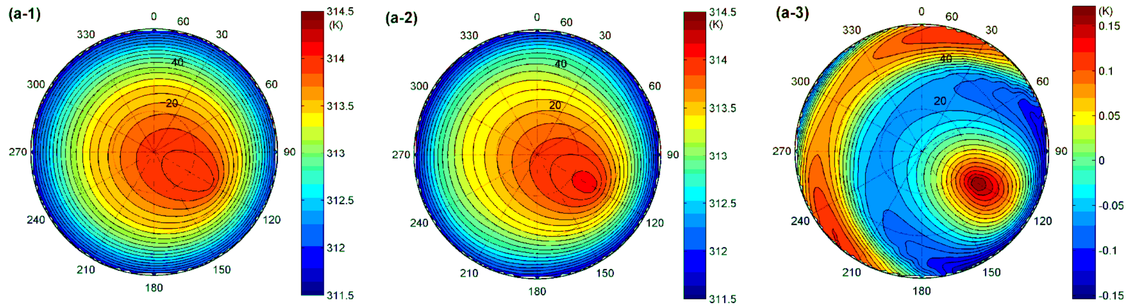

(a) LAI = 0.5

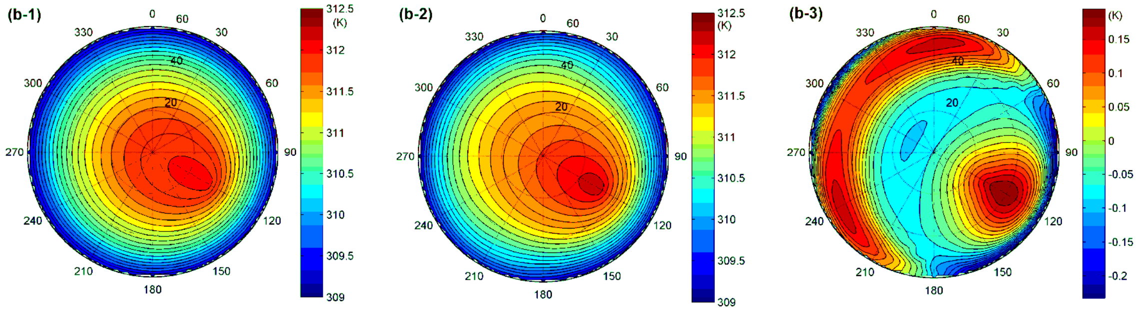

(b) LAI = 1.0

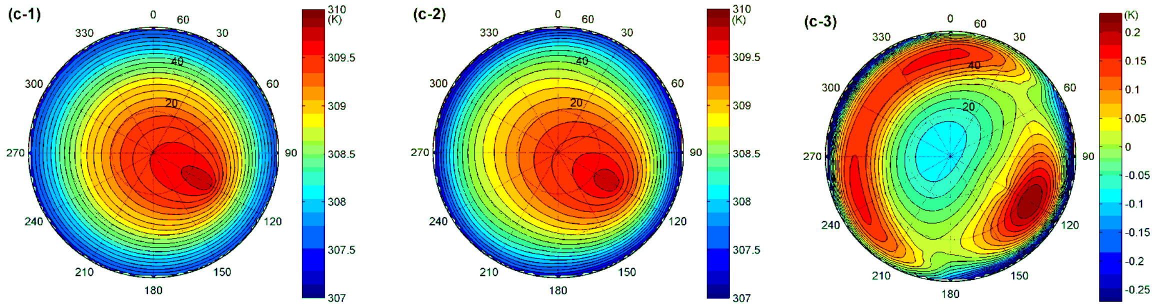

(c) LAI = 2.0

Fig.4-6. The hemispheric distribution of the simulated DBT from Eq.(4.16) (the first column), the fitted DBT from kernel-driven model (the second column) and their temperature difference (the third column) at (a)LAI =0.5, (b) LAI =1.0 and (c) LAI = 2.0, respectively.

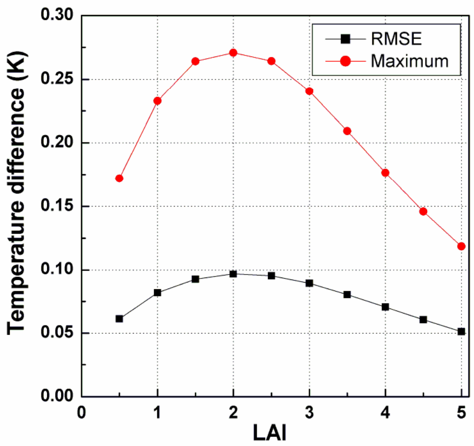

Fig.4-7. The influence of LAI on the error of the kernel-driven BRDF model

Furthermore, we also checked the K-BRDF model in different solar positions, components' temperatures and emissivities, and canopy structures, and the results further confirmed the availability of the K-BRDF model in the presentation of the DBT distribution. Therefore, according to the above discussions and results, a conclusion can be drawn that Eq.(4.16) can represent the hemispheric distribution of the DBT very well and the K-BRDF model can fit the DBT distribution robustly, without leading significant error if no noise is included in the data. Note that, because the components' emissivity is considered as angle-independent and consequently the DBT of bare surface is isotropic, we only discuss at the level of canopy rather than the case of bare surface.

The above result is obtained by using the K-BRDF model for all viewing zenith and azimuth angles. However, it is almost impossible to observe the same target under so many directions in reality. On the contrary, only several angular observations are usually conducted. Consequently, a problem is raised: how many observations and under what viewing angles are needed for the K-BRDF model to fit the DBT accurately? In order to find out the optimum observation groups, this thesis used two different ways in the following discussions: single-point pattern and linear-array pattern.

4.4.1 Single-point pattern for the optimum angular combination

According to Eq.(4.18), at least three angular observations are needed to complete the K-BRDF model. More observations can make the fitted coefficients more reliable in theory but the error in those observations could cause more uncertainty to the fitted result. Therefore, we start with only three viewing angles. The objective of this work is to find out the local optimum viewing angle combination that can cause the smallest error from the K-BRDF model, and also to provide some suggestion for the future development of the multi-angle airborne or space-borne TIR sensors. Therefore, for the achievable purpose in the mechanical design of the sensors, we herein assume that all observations are made with the azimuths in the same plane, i.e. their azimuths equal *to* φ or $\varphi + \pi$.

Taking $\varphi = 0$ for example, the three observations' zenith angles vary in the azimuth plane ($0 \sim \pi$), at a step of 10° with the maximum 60° in the zenith direction. Observations are forbidden to have the same value of zenith and azimuth angles. As a result, there are 126 groups of the three angles. To find out the optimum group, we use firstly Eq.(4.16) to simulate the hemispheric DBT under different cases of solar positions (SAA from 0° to 330° with a step 30°, SZA=10°, 30° and 50°), LAIs (0.5~5.5 with a step 0.5) and the components' temperatures and emissivities in Table 4-1, resulting in a total of 396 cases. Consequently, the three coefficients of Eq.(4.18) are obtained from the DBT of three angles, and this process is controlled additionally by an optimization algorithm. Table 4-2 shows the frequency of the RMSE in [0.0, 0.5] K, [0.5, 1.0] K and the number of the occurrences of the maximum and minimum RMSEs, respectively. The cases without nadir viewing direction is not displayed here because they do not have better results and also because of the limited space.

Some criteria are proposed to filter out the final optimum angle combinations:

(1) Most of the RMSE of the K-BRDF model should fall in the range of 0.0~0.5 K;

(2) The maximum difference seldom occurs in the angle combinations;
(3) Most of the minimum difference should be obtained in the combinations;
(4) Observation in very large zenith angle is not recommended, and the interval of the adjacent zenith angles should be as large as possible.

According to the above four criteria and the results shown in Table 4-2, it is found that large viewing zenith angles could make the fitted error smaller, and several angle combinations can be considered as the candidate for the optimum groups: ① [(0°, 0°)，(0°, 30°)，(180°, 50°)]; ② [(0°, 0°)，(0°, 40°)，(180°, 50°)] and ③ [(0°, 0°)，(0°, 40°)，(180°, 60°)]. Although the combination [(0°, 0°)，(0°, 50°)，(180°, 60°)] has the maximum occurrences for the minimum error, the occurrences (five times) in the maximum error and large viewing zenith angles make this group unavailable.

Among the three candidates, group ③ cannot be recommended because of its large viewing zenith angle in the direction (180°, 60°), whose pixel sizes is as large as four times of the pixel size at nadir observation if the sensor’s IFOV(instantaneous field of view) keeps the same in every direction. Compared with group ①, group ② works slightly better. However, the final decision cannot be made without any sensitivity analysis to the errors involved in observed data.

Table 4-2. The frequency of the root-mean-square error (RMSE) in different three angle combinations

1st VAA	1st VZA	2nd VAA	2nd VZA	3rd VAA	3rd VZA	RMSE [0.0~0.5]K	RMSE [0.5~1.0]K	Max*	Min#
0	0	0	10	180	10	195	44	122	0
0	0	0	10	180	20	241	43	49	1
0	0	0	10	180	30	299	40	16	2
0	0	0	10	180	40	316	33	15	0
0	0	0	10	180	50	337	7	1	12
0	0	0	10	180	60	323	4	5	11
0	0	0	20	180	10	243	42	45	1
0	0	0	20	180	20	295	18	11	0
0	0	0	20	180	30	315	34	14	4
0	0	0	20	180	40	337	20	2	3
0	0	0	20	180	50	359	3	1	15
0	0	0	20	180	60	354	7	19	11
0	0	0	30	180	10	299	39	17	2
0	0	0	30	180	20	316	34	14	4
0	0	0	30	180	30	351	16	0	7
0	0	0	30	180	40	361	3	0	6
0	0	0	30	180	50	360	0	0	14
0	0	0	30	180	60	373	0	2	9
0	0	0	40	180	10	316	35	16	0
0	0	0	40	180	20	337	20	2	3
0	0	0	40	180	30	361	2	0	6
0	0	0	40	180	40	364	1	0	3
0	0	0	40	180	50	373	0	0	26
0	0	0	40	180	60	373	0	1	47
0	0	0	50	180	10	336	8	1	14
0	0	0	50	180	20	359	4	1	16
0	0	0	50	180	30	360	0	0	14
0	0	0	50	180	40	373	0	0	26
0	0	0	50	180	50	353	2	2	14
0	0	0	50	180	60	365	8	5	69
0	0	0	60	180	10	322	5	4	10
0	0	0	60	180	20	354	8	22	12
0	0	0	60	180	30	373	0	1	10
0	0	0	60	180	40	373	0	1	47
0	0	0	60	180	50	365	8	3	69
0	0	0	60	180	60	349	0	21	0

*Max stands for the frequency of maximum temperature difference, while #Min stands for the frequency of minimum temperature difference.

In order to investigate the sensitivity of the different angle groups to the DBT errors, some artificial noises within [-0.5, 0.5] K and [-1.0, 1.0] K in a uniform distribution were respectively added to the simulated DBT of Eq.(4.16). The three coefficients of the K-BRDF model were recalculated and then used to obtain the hemispheric DBT. The output of the K-BRDF model was constrained by the optimization algorithm as that the DBT must reach the maximum value in the solar direction.

Fig.4-8 shows the RMSE histograms of the temperature difference caused by the three-angle K-BRDF model using the angles groups ①~③ by responding to the DBT noise of [-0.5, 0.5] K and [-1.0, 1.0] K, respectively. It illustrated that group ③ obtained the smallest errors for two noise conditions, followed by group ② and ①. The RMSE percentages of the three angle groups ①~③ in the range of 0.0~1.0 K are about 92.4%, 96.6% and 96.3% for the noise condition [-0.5, 0.5] K, 80.1%, 88.5% and 91.1% for the noise condition [-1.0, 1.0] K. Those results indicates that the three groups have the ability to obtain an error of temperature better than 1.0 K for most cases if the noise involved in the observed DBT data is no more than 1.0K. However, it is obvious that group ② and ③ are less sensitive to the noise in the observed data. As stated above, group ③ cannot be used as the optimum viewing angle combination because of the large viewing zenith angle and the occurrence of maximum errors. As a result, group ② should be the optimum one in theory. However, as the pixel size increases with the increasing VZA, the ratios of pixel area at VZA = 30°, 40° and 50° to that of nadir are 1.32, 1.70 and 2.40, respectively. It's necessary to need a pixel with a middle area to connect the observations from nadir to large VZAs, especially for heterogeneous surfaces. In this case, the zenith angle in group ① leads a more continues series of pixel sizes (1, 1.3 and 2.4 times of nadir pixel size). Besides, the angle intervals in the slant direction of group ① (i.e., 20°) is larger than that of group ② (i.e., 10°), which makes group ① less sensitive to the error included in the observation angle itself in theory. Therefore, we prefer to the angle combination of group ①, and take this group as the local optimum angle combination for the DBT regression using three-angle K-BRDF model.

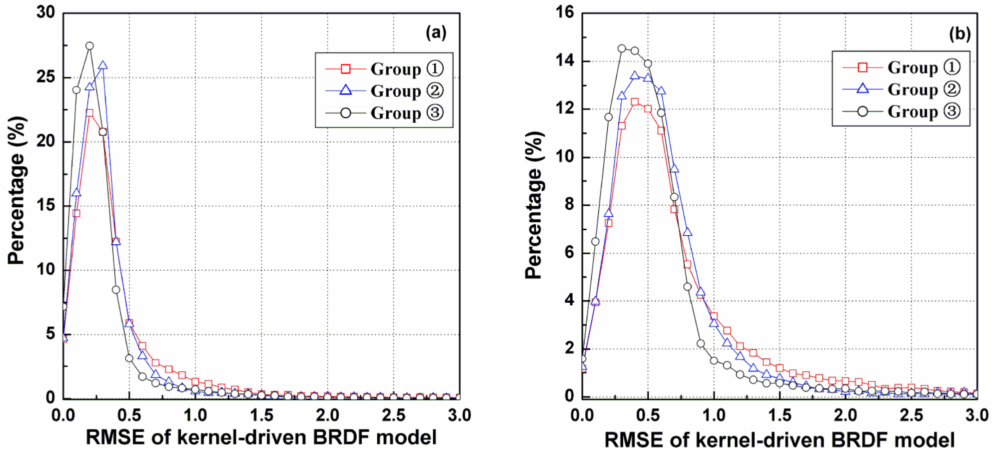

Fig.4-8. RMSE histogram of the three-angle kernel-driven model for DBT noise within (a) [-0.5, 0.5] K and (b) [-1.0, 1.0] K.

4.4.2 Linear-array pattern

For most sensors onboard the polar-orbit satellite, it scans the surface in the crossing-track direction by rotating the mirror toward the target or using the array detectors to monitor the earth under different relative zenith angles to the nadir direction or by taking photos under central projection manner. In this study, we take the way of the array detectors for example and suppose that a sensor is equipped with three arrays of detectors to observe the earth at nadir, forward and backward directions and that all detectors have the same spectral and radiative characteristics. Based on the result from the above section 4.4.1, we use the combination of group ① [(0°, 0°), (0°, 30°), (180°, 50°)] as the optimum one to investigate the case of the array observations. Fig.4-9 shows the array detectors (or pixels) for the nadir, forward and backward directions. Each array has 27 pixels from left to right with an interval of 5° in the range of ±65° at the Nadir array. If assume the satellite flies in the north-south direction and ignore the influence of the rotation of the earth itself, the azimuth angle of the left part of the Nadir array is 90° and that of the right part is 270°. The viewing zenith and azimuth angles (VZA and VAA) in the backward and forward arrays can be calculated as:

$$\theta_{i,k} = \arctan(\tan\theta_k / \tan\theta_{i,0}), \quad \varphi_{i,k} = \arctan\left(\sqrt{\tan^2\theta_k + \tan^2\theta_{i,0}}\right), \qquad (4.19)$$

where, $\theta_{i,k}$ is the viewing zenith angle of the ***i***th pixel in the backward or forward arrays. $\theta_{i,0}$ is the viewing zenith angle of the ***i***th pixel in the Nadir array. θ_k is the zenith angle of the backward or forward arrays relative to the nadir, i.e. θ_k = 30° or 50°. $\varphi_{i,k}$ is the relative angle between the azimuths of the ***i***th pixel in the nadir and off-nadir directions. The absolute azimuth angle will be finally determined by $\varphi_{i,k}$ and the position of the ***i***th pixel in the Nadir array.

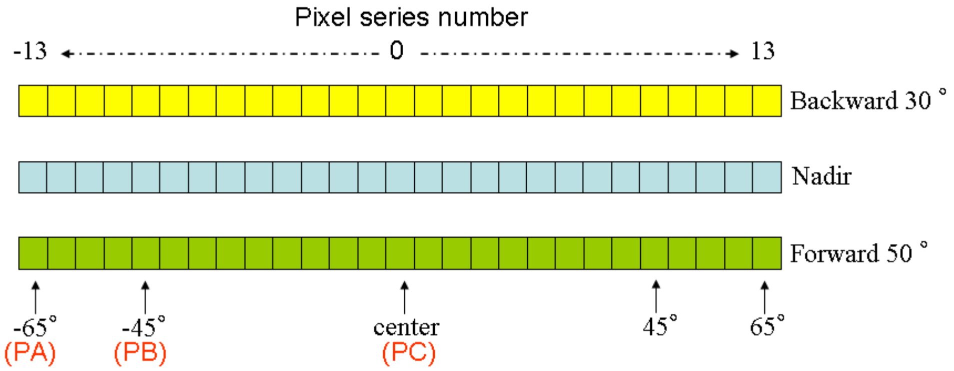

Fig.4-9. The illustration of three linear-arrays. The “pixel series number” was the number of each pixel corresponding with Fig.4-10; the pixels marked with “PA”, “PB” and “PC” were used for analysis.

Based on Eq.(4.19), the azimuth and zenith angles for each pixel in the three linear-arrays of Fig.4-9 are consequently calculated and displayed in Fig.4-10. As seen from Fig.4-10, the differences of VZA and VAA of the same pixels in the three arrays are significant in the middle part of those arrays, but decrease with the pixels getting close to the edges of the arrays. Since the angle difference will influence the temperature difference between different viewing directions, a small difference in viewing angles might cause large errors into the K-BRDF model, which will be illustrated in following discussion.

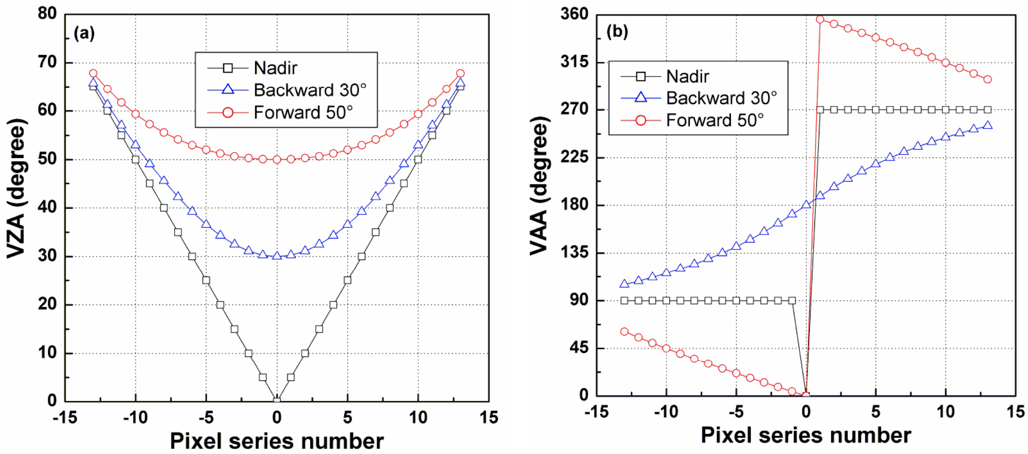

Fig.4-10. (a) Viewing zenith angles (VZA) and (b) azimuth angles (VAA) of the three arrays. The pixel series number can be found in Fig.4-9.

In order to check the availability of the K-BRDF model on the array observation pattern and analyze the influence of the three angles in different places of the arrays, we firstly simulated some hemispheric DBT with varying LAIs and solar positions, and then added some uniform-distributed noise in [-0.5, 0.5] K to the simulated data and finally compared the fitted DBT from the K-BRDF model with the truth DBT from the simulations. The following parts will discuss the influence of SZA, SAA and LAI on the DBT residual caused by the K-BRDF model in the total hemisphere and on the DBT difference at nadir observation that is usually considered as the reference direction for the angular correction of temperature.

4.4.2.1 The influence of solar position

Since the VZA and VAA of each pixel in the arrays are fixed, the solar position impacts the fractions of sunlit soil, shadow soil and leaves as well as the components' temperatures in each pixel. To analyze the sensitivity of the K-BRDF model to the solar position, we simulate the hemispheric DBT by changing SAA from 0° to 330° with a step of 30°, with SZA equal 10°, 30° and 50° for each SAA. A total of 5 LAIs (0.5, 1.0, 2.0, 3.0 and 4.0) are used for each solar position. Artificial noise is added to the simulated DBT. All pixels in Nadir, backward or forward array include the same noise, respectively, but different arrays have different noises.

A. The influence of SZA on the K-BRDF model

Fig.4-11 shows the RMSE histograms for the temperature difference resulted from the K-BRDF model at different SZAs. Fig.4-11(a) shows the RMSE for all pixels, which indicated that the percentage of RMSE within [0,1.0] K for SZA=10° is larger than the other two SZAs. A small SZA can lead to a low uncertainty for the estimated DBT and presents less sensitivity to the noise. Fig.4-11(b), (c) and (d) show RMSE histograms of three pixels marked with PC, PB and PA in Fig.4-9, which corresponds to VZA = 0°, 45° and 60° in the Nadir array, respectively. It is found that the case of the pixel PC has the most robust ability to deal with the noise (Fig.4-11(b)). The pixels (e.g. PA) closed to the edge of the array have more errors in the estimated DBT because as shown in Fig.4-10, the difference of their VZA and VAA in the three arrays are very small, which causes a small variation of the components' fractions between three viewing angles, and consequently leads to a small temperature difference in the observed DBT data. To the end, the K-BRDF model turned out to be highly sensitive to the noise included in the DBT. Therefore, a better result from the K-BRDF model requires a significant difference between the viewing angles.

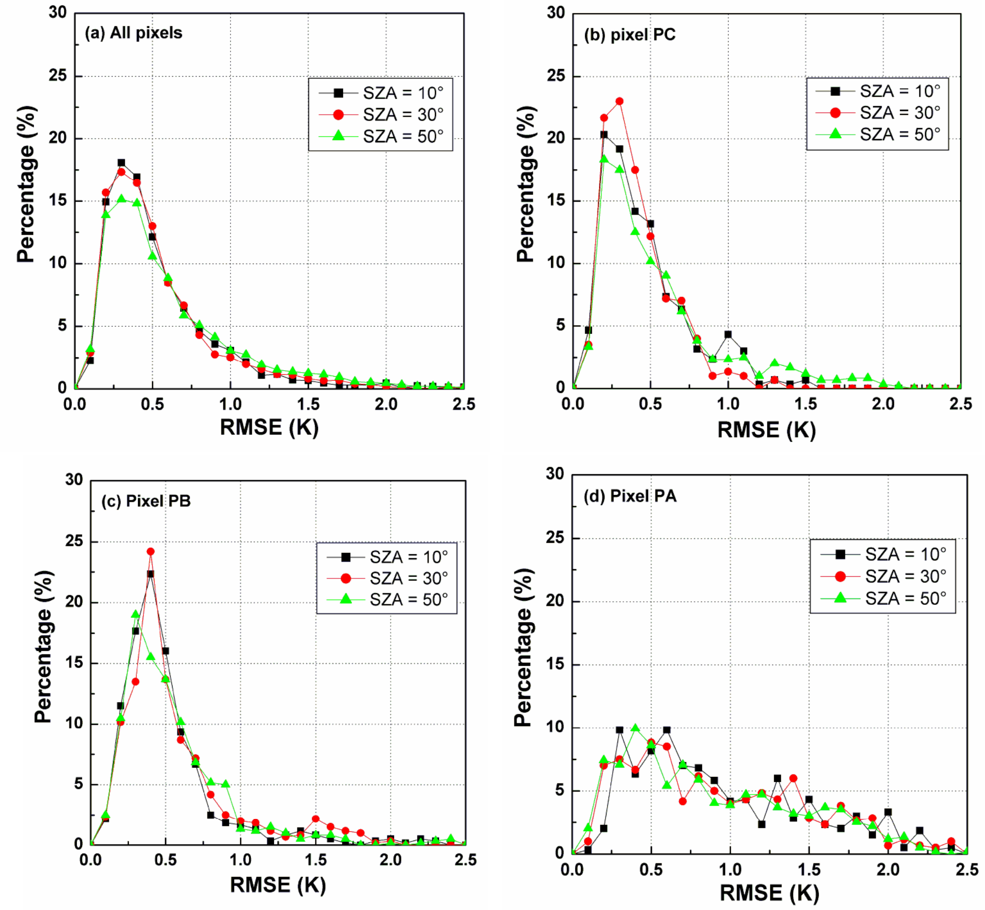

Fig.4-11. RMSE histograms of DBT difference for different pixels and SZAs

Based on the results of Fig.4-11, the cumulative percentage of RMSE ranging in [0.0, 1.0] K has been calculated for each pixel and SZA, and shown in Fig.4-12. The VZA of the X-axis is the zenith angle of the pixel in the Nadir array. Fig.4-12 indicates that such cumulative percentage generally decreases with the increase of VZA, especially in the range of VZA larger than 45°. For SZA = 10° and 30°, their cumulative percentages are about 95% at VZA smaller than 45°, and even near 100% at nadir direction. On the contrary, such percentage for SZA = 50° is about 85%, much lower than the other two SZAs. Therefore, as seen from the Fig.4-12, an angular observation with the maximum VZA less than 45° at Nadir array and a relative small SZA is necessary to make sure that the cumulative percentage of the temperature error in the range of 0.0~1.0 K caused by the K-BRDF model is no less than 85%.

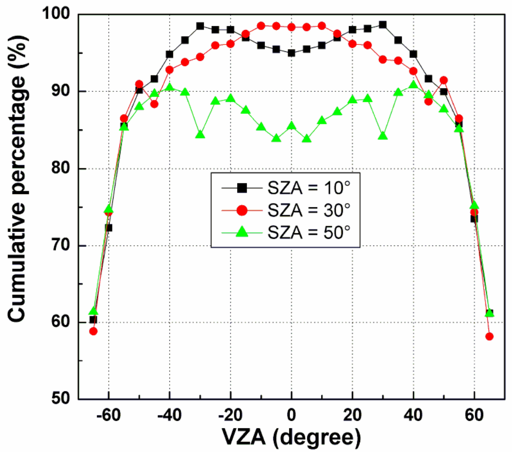

Fig.4-12. The cumulative percentages of RMSE in [0.0, 1.0] K for different pixels in Nadir array and SZA.

B. The influence of SZA on DBT difference at nadir observation

Once the three kernel coefficients of the K-BRDF model are determined, the DBT in any other direction can be estimated in theory. Nadir direction is taken as the reference direction in this thesis, and the DBT is normalized from other direction to the nadir observation. Fig.4-13(a) displays the histograms of the temperature difference between the normalized DBT at nadir from the K-BRDF model and the truth nadir value in the simulation. It releases that most of the difference ranges in [-1.0, 1.0] K with a bias about 0.2 K. Similar results are obtained for the three SZAs although the case of SZA = 30° performed a little better than the other two SZAs. The occurrence of the sawtooth in the curves of the graphs in Fig.4-13(a) might be caused by a lack of enough simulations. Fig.4-13(b) shows the cumulative percentage of DBT difference in [-1.0, 1.0] K for different pixels and SZAs. Similar to the Fig.4-12, the percentages decrease with the increasing of VZA and almost are distributed in symmetry with respect to the central pixel. For those pixels with small VZAs, the K-BRDF model works well at all of the three SZAs, but its accuracy is degraded for the pixels near the edges of linear arrays. These results are similar to those of the previous section, which further indicate that the requirement of an angular observation with middle SZA, and VZA at Nadir array less than 45° is necessary for an acceptable result.

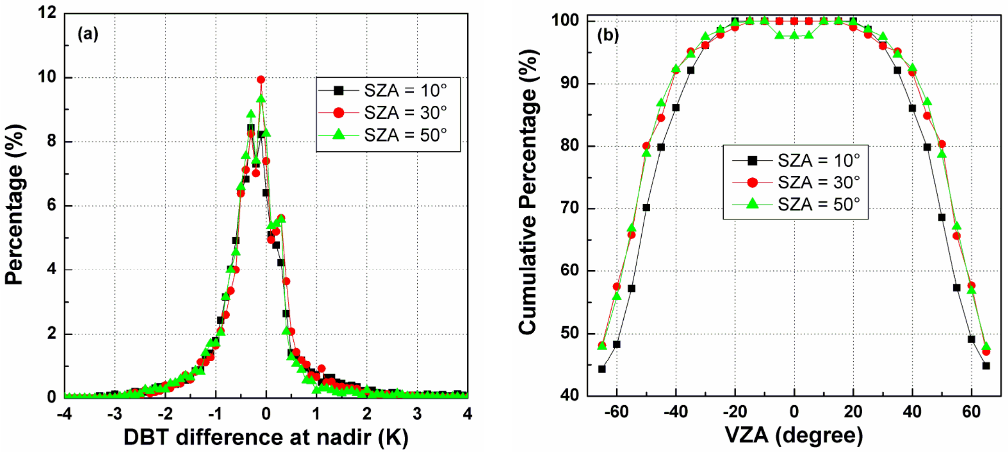

Fig.4-13. (a) The histograms of DBT difference at nadir, and (b) the cumulative percentages of DBT difference in [-1.0, 1.0] K for different viewing angles and SZAs

C. The influence of SAA on the K-BRDF model

Similar to Fig.4-11, Fig.4-14 shows the RMSE histograms for the temperature difference resulted from the K-BRDF model at different SAAs. It is also found the result of the pixel (e.g. Fig.4-14(d)) near the edges of the array showing more uncertainty than the other pixels. It is difficult to decide which SAA is the best for all pixels but as seen from Fig.4-14(a), the error of the K-BRDF model is generally smaller at the solar position closer to the viewing azimuth (0°~180°). The case of SAA = 90° generally provides the worst result perhaps because this solar position results in the smallest variation in components' fractions and temperatures.

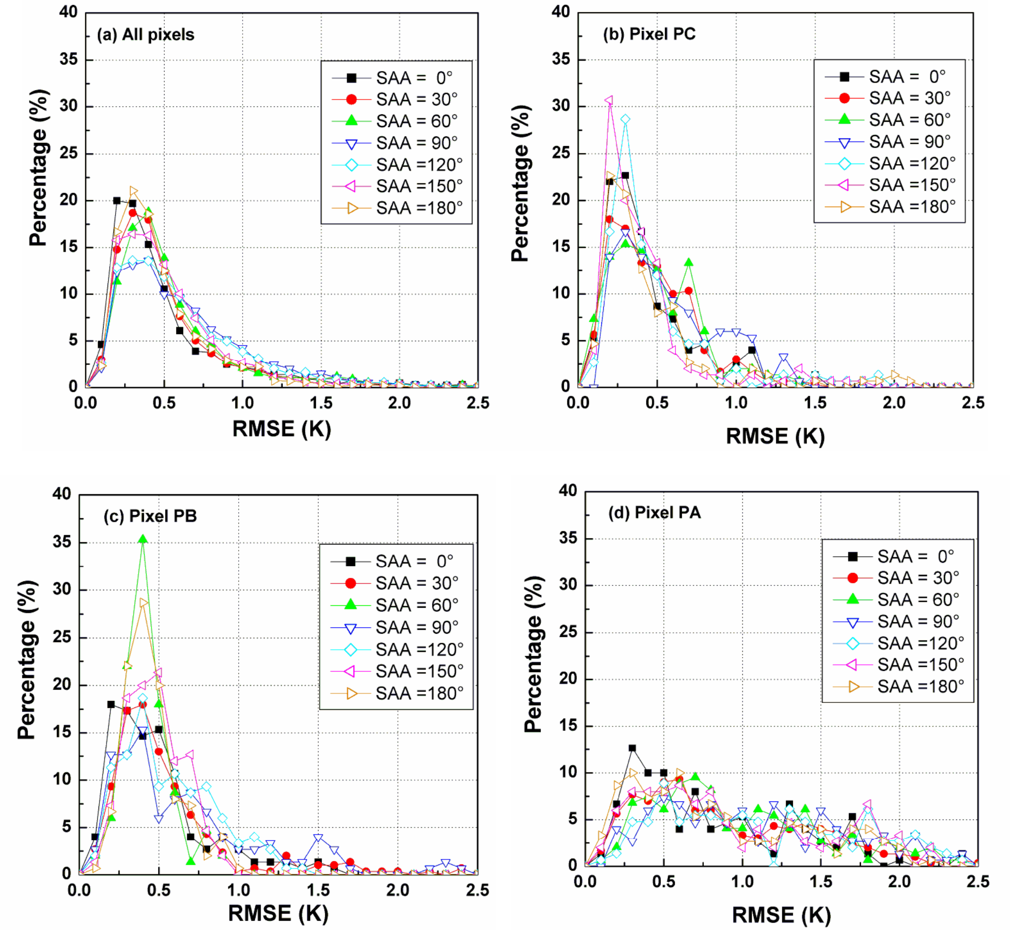

Fig.4-14. RMSE histograms of DBT difference for different pixels and SAAs

Fig.4-15 displays the angular variation of the cumulative percentages of temperature RMSE within [0.0, 1.0] K. The percentages are not symmetric with respect to the central pixel for SAA = 30°, 60° and 90° as those in Fig.4-12. For example, the percentages in the right-hand side of SAA = 30° is larger than those in the left-hand side, while the right-hand side of SAA = 60° is generally smaller than those in the left-hand side. The curve of SAA = 90° varies significantly with the VZA. However, the cases of SAA = 0°, 120°, 150° and 180° are almost symmetric with the central pixel's location. These different patterns for different SAAs are caused by the difference of the viewing angles in the backward and forward arrays. According to the VAAs for each pixels of the three arrays shown in Fig.4-10(b) and the results of Fig.4-14, a cautious conclusion can be drawn that the larger the difference between the solar azimuth and the azimuth angles of array Forward50° is, the better the result of the K-BRDF model will be.

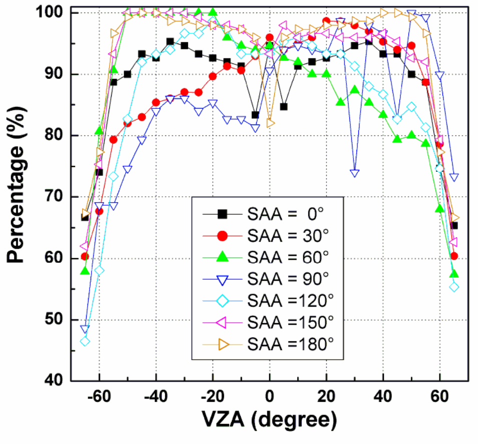

Fig.4-15. The cumulative percentages of RMSE in [0.0, 1.0] K for different pixels in Nadir array and SAA.

D. The influence of SAA on DBT difference at nadir observation

Fig.4-16(a) shows the histograms of the temperature difference between the normalized DBT at nadir from the K-BRDF model and the truth nadir value in the simulation. It illustrates that there is almost no difference among those SAA. Fig.4-16(b) is the corresponding cumulative percentages with DBT difference in [-1.0, 1.0] K. The results of the SAA = 30°, 60°, 90° and 120° turned out to be better in one side than the other, perhaps because of the different viewing zenith angles in the backward and forward arrays. As seen from both Fig.4-15 and Fig.4-16, the requirement on the error of no less than 85% pixels falls in the error range [0.0, 1.0] K, needs the maximum VZA in Nadir array smaller than 45° for most SAAs but still depends on the SAA.

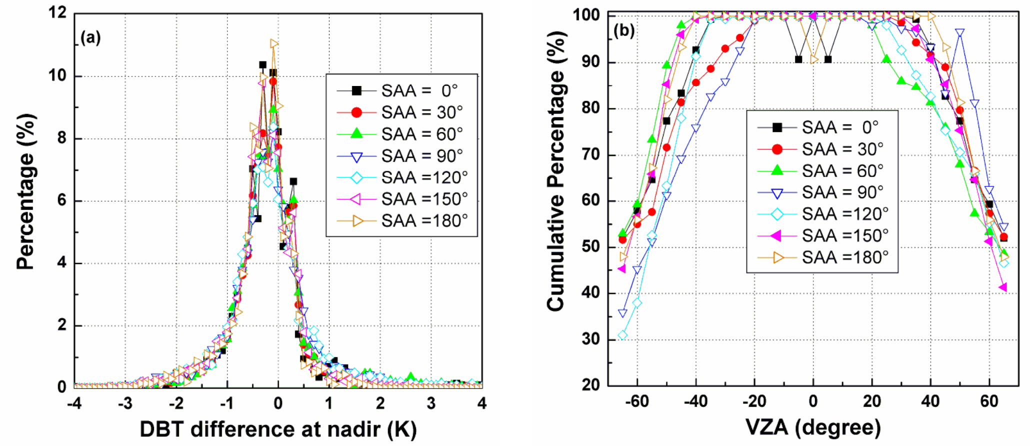

Fig.4-16. (a) The histograms of DBT difference at nadir for different SAAs, and (b) the cumulative percentages of nadir DBT difference in [-1.0, 1.0] K for different viewing angles and SAAs.

4.4.2.2 The influence of LAI

LAI impacts the gap frequency of the canopy and consequently influences the fractions of leaves and soils. As the leaves usually has a lower temperature than the soil, large LAIs lead to smaller temperature for the canopy. Using the same methods than above, we have checked the influence of the LAI on the result of the K-BRDF model with LAI equal 0.5, 1.0, 2.0, 3.0 and 4.0. The other simulation conditions keep the same with the above discussion.

A. The influence of LAI on the K-BRDF model

Fig.4-17 shows the RMSE histograms for different LAIs when there are noises of [-0.5, 0.5] K included in the DBT data, which indicates that the K-BRDF model is not very sensitive to the noise for the case of larger LAIs, especially with LAI larger than 2.0. However, the K-BRDF model causes a relative larger error to LAI = 1.0 than to LAI =0.5, possibly because the changes from soil-dominated canopy (small LAI) to vegetation-dominated canopy (large LAI) degrade the accuracy of the regression process in the K-BRDF model.

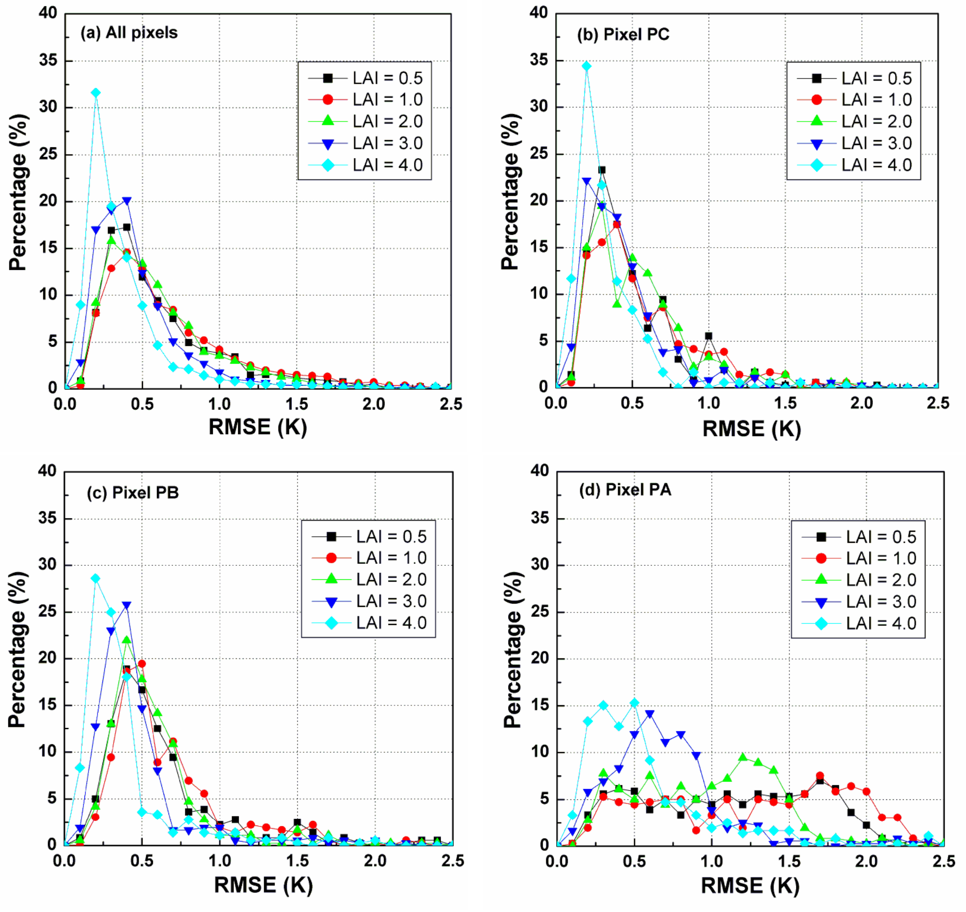

Fig.4-17. RMSE histograms of DBT difference for different pixels and LAIs

Fig.4-18 is the variation of cumulative percentages of the temperature RMSE within [0.0, 1.0] K for the VZAs in the Nadir array and different LAIs. Similar to the influence of the solar position, the pixels closer to the edges of the arrays has smaller cumulative percentages and larger uncertainties, while the pixels in the range of [-45°, 45°] obtain more reliable results from the K-BRDF model. As stated previously, the VZAs smaller than 45° are required to obtain reliable fitted DBT from the K-BRDF model.

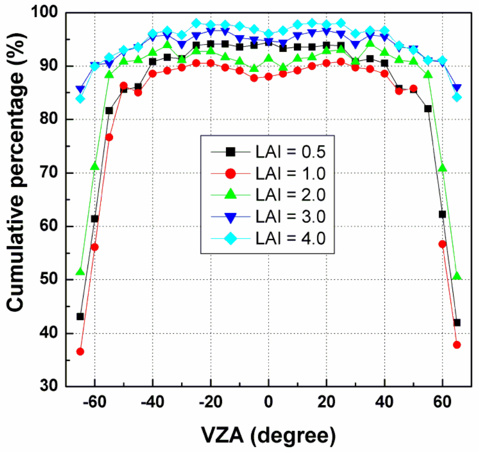

Fig.4-18. The cumulative percentages of RMSE in [0.0, 1.0] K for different pixels in Nadir array and LAIs.

B. The influence of LAI on DBT difference at nadir observation

Fig.4-19(a) shows the histograms of the temperature difference between normalized DBTs at nadir from the K-BRDF model and the truth nadir value in the simulation at different SAAs. It illustrates, except for the case of LAI = 4 which obviously presents largest percentage in the [-1.0, 1.0] K, that no significant difference between the histogram of the other LAIs can be observed. Fig.4-19(b) is the variation of cumulative percentages of the nadir DBT difference in [-1.0, 1.0] K with the viewing angles in the Nadir array and different LAIs. This figure shows that there are no difference in the cumulative percentage for all LAIs in the range of small VZAs (i.e. -20° ~20°), but larger LAIs can generally generate higher percentages in large viewing zenith angles. Therefore, the K-BRDF model is more reliable for dense vegetated canopy than for relative sparse canopy. The case of LAI =1.0 has the smallest percentages perhaps because of the mixed effect described above. Similarly, an acceptable cumulative percentages (>85%) for all LAIs requires the viewing zenith angle to be less than 45°.

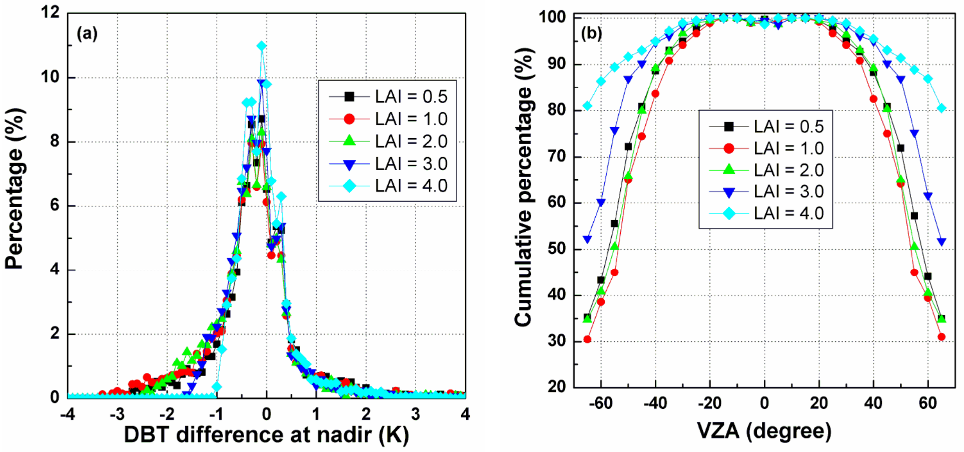

Fig.4-19. (a) The histograms of DBT difference at nadir for different LAIs, and (b) the cumulative percentages of DBT difference in [-1.0, 1.0] K for different viewing angles and LAIs.

From the above discussion about the three linear-array pattern, we find that the VZA in Nadir array has to be smaller than 45° in order to enable most of the temperature error from the K-BRDF model no more than 1.0 K, and that the middle SZA and partly and dense vegetated surface can improve the accuracy of the model.

4.5 Conclusions and discussions

This chapter firstly compares four parameterization models for the directional emissivity of canopy based on the result of the TIR-SAIL model developed by (Liu et al. 2003). The four models are respectively the kernel-driven BRDF model (K-BRDF) with Ross-Thick volumetric kernel and Li-SparseR geometric-optic kernel, the semi-empirical BRDF model S-BRDF (Li et al. 2000), the analytical parameterization model FRA97 (François et al. 1997) and the multiple scattering model FRA02 (François 2002). Results show that both K-BRDF and S-BRDF model can accurately represent the angular variation of the canopy directional emissivity for low and middle LAIs. However, for dense vegetated canopy, such as LAI = 4.0, the S-BRDF model almost has an opposite tendency pattern for the directional emissivity to the result of the TIR-SAIL model, and the emissivity difference between the two model is as large as 0.007 for larger VZAs. On the contrary, the K-BRDF model presents a relative higher accuracy because it holds a similar angular pattern of the directional emissivity to the TIR-SAIL model with emissivity difference less than 0.002. Besides, we find out that the factor $\boldsymbol{k}$ of the S-BRDF is always larger than 1.0, an outlier of its physical value between 0 and 1.0. As a result, comparison between the K-BRDF model and the S-BRDF model indicates that the former performs a litter better than the latter in the parameterization of the directional emissivity. Therefore, the K-BRDF model will be used in the further analysis of the angular normalization of the land surface temperature. Besides, linear relationships between the three kernel coefficients of K-BRDF model are found from the simulation data composed with ten vegetation and seventeen soil samples chosen from emissivity database. Moreover, results also show that the FRA02 model has large error in the parameterization of directional emissivity simulated from the TIR-SAIL model perhaps because the FRA02 ignores the multiple scattering between the vegetation layers inside the canopy. Besides, the cavity effect factor developed by (François et al. 1997) based on the (Prévot 1985) in the FRA97 model is found to be no longer suitable for the TIR-SAIL model, so it has been refined according to the TIR-SAIL model, and the new value consequently increases the accuracy of the FRA97 model, especially at large VZAs.

Using the refined cavity effect factor and the parameterization method of the SAILH model (Li et al. 2010), we have developed a new way to simulate the directional brightness temperature (DBT) of the canopy which is assumed to be composed with leaves, sunlit and shaded soils. The hemispheric DBT simulated from the new method can obviously present the hotspot effect of the DBT. Based on the simulated DBT, analysis results show that the K-BRDF model, refined by replacing the bi-directional reflectivity in the primary model with the DBT, performs well in the regression of the hemispheric DBT, leading to an error lower than 0.3 K. If the three kernel coefficients of the K-BRDF model are known, the DBT in any other direction is obtainable in theory. Therefore, the K-BRDF model gives us an opportunity to make angular normalization of the DBT. To check the availability of this model in the angular normalization and find out the optimum angle combination for this model, two different ways are used for investigation: single-point pattern and linear-array pattern. The single-point pattern finally selects the angle combination [(0°, 0°), (0°, 30°), (180°, 50°)] from many three-angle groups as the optimum angle combination because the K-BRDF model using the DBT under this angle combination give out a robust result and because the pixel resolution of this angle combination keeps a finer continuity from fine to coarse scales. Furthermore, we extend this optimum angle combination to the three linear-array pattern (Nadir, Forward 50° and backward 30°, respectively), which are assumed to be onboard of polar-orbit satellite and use to observe the earth’s surface in multiple angles as the satellite moves forward. Investigations of the consistency of the K-BRDF model to the solar position and LAIs show that a middle SZA, and a SAA along satellite track direction, and a relative higher LAI is more appropriate to enable a reliable fitted DBT from the K-BRDF model. However, the results depend on the pixel location in the arrays as the closer to the edges of the arrays, the worse the result will be. Because the VZA and VAA differences of the pixels in the position of different arrays gradually become smaller as the pixel moves from the centre position to the edge of arrays. As a result, it reduces the angular variation of the DBT observed by the edge pixels in different arrays and consequently caused the K-BRDF model more sensitive to the noise in the observed DBT data. Finally, based on the analysis of the temperature RMSE and the temperature difference of the nadir DBT, we find out that the VZA in the Nadir array cannot be larger than 45° to enable the temperature RMSE within [0.0, 1.0] K and the temperature difference of the nadir DBT within [-1.0, 1.0] K for most cases (85%). These results may provide some suggestion to design the multi-angular observation system onboard the satellite.

However, in this thesis we only use the SAIL series models including TIR-SAIL and SAILH models to simulate the directional emissivity and brightness temperature, so the new cavity effect factor may not be suitable to other radiative transfer models. The DBT simulated from the proposed new method is not yet validated with field data because of a lack of field data on homogenous canopy. Furthermore it is only used to provide the DBT data resource for the illustration of the K-BRDF model in the angular correction of the land surface temperature and for the algorithm development of the retrieval of directional emissivity and DBT from the multi-angular observations in Chapter 5. Future work should concern on field validation. Besides, in this thesis, we only discuss the case of three angular observations and force their azimuths to be in the same plane. Therefore, the angle combination [(0°, 0°), (0°, 30°), (180°, 50°)] is only a local optimum for the development of three linear-array detector system. To answer the question “how many observations under what viewing angles are needed for the kernel-driven BRDF model to fit the DBT accurately?” still requires more work.

Chapter 5

Angular normalization of land surface temperature and emissivity from multi-angular middle and thermal infrared images

Based on the result of previous chapter, this chapter proposes a daytime TISI (temperature-independent spectral indices) method to retrieve directional emissivity and effective temperature from daytime multi-angular observed images in both middle and thermal infrared (MIR and TIR) channels by combining the kernel-driven BRDF (bi-directional reflectance distribution function) model and the TISI method. Four groups of angular combinations and two groups of MIR and TIR channels with narrow and broad bandwidth were used to investigate the influence of the angular observations and the bandwidth on the retrieval accuracy. Model sensitivity analysis indicated that the new method can obtain directional emissivity and temperature with an error less than 0.015 and 1.5 K if the noise included in the measured directional brightness temperature and atmospheric data was no more than 1.0 K and 10%, respectively. The analysis also indicated that (1) large-angle intervals among the angular observations and a larger viewing zenith angle (VZA) with respect to nadir direction can improve the retrieval accuracy of emissivity and temperature because those angle conditions can result in significant difference for component fractions and directional brightness temperatures under different viewing directions, and (2) narrow channels can produce better results than broad channels. The new method was finally applied to a multi-angular MIR and TIR dataset acquired by an airborne system, and a modified kernel-driven BRDF model was used for angular normalization to the surface temperature for the first time. The difference of the retrieved emissivity and ASTER emissivity was found to be approximately 0.012 in the study area.

5.1 Background

Land surface temperature (LST) is strongly required for many applications, including agrometeorology, climate and environmental studies. Thermal infrared images from aircraft and spaceborne satellites provide a unique opportunity to map this parameter at regional and even global scales. However, the determination of LST from remotely sensed data needs to solve two types of problems. The first is atmospheric correction, which aims to remove the contribution of atmospheric emission and scattering to the target radiation in the path from the surface to the sensor. The other involves accounting for the emissivity effect on the LST to allow the retrieval of LST from the radiance measured at the surface. Many methods have been proposed to retrieve LST from remotely sensed data depending on different specifications of thermal infrared sensors and the atmospheric and emissivity data situations, reviews of those methods can be found in Chapter 2. For operational purposes, those methods often take the observed pixel as a homogeneous and isothermal target, and this assumption is reasonable for pure or quasi-pure pixels, such as bare soil, sand, snow and dense vegetated surface. However, for mixed pixels including two or more components at different temperatures and emissivities, the pixel temperature actually presents spectral and angular variations. As a result, the above assumption will be incorrect, and at least, the retrieved LST only presents the effective temperature at its corresponding viewing direction and cannot be directly taken as the temperature at nadir or under other directions in theory.

The angular behavior of LST has been investigated in many previous studies (Chehbouni et al. 2001; Coret et al. 2004; Lagouarde et al. 2004; Lagouarde et al. 1995; Li et al. 2004b; Minnis and Khaiyer 2000; Rasmussen et al. 2011), and this angular variation results primarily from the angular variation of the pixel emissivity for three-dimensional surfaces and the relative weights of more than one component (e.g., vegetation and background soil) with different temperatures included in the scene. Some ground measurements have indicated that the LST difference at nadir and off-nadir observations can be as large as 5 K for bare soils and even 10 K for urban areas. For satellite images, the pixels also face a similar situation because the pixels in the same image are usually observed with significantly different viewing angles. For example, Moderate Resolution Imaging Spectroradiometer (MODIS) scans the land surface in the cross-track direction with viewing zenith angle (VZA) varying from -65° to +65°, and thus, angle-dependent variations in the retrieved LST are inevitable, which make the LSTs of different pixels in the same image incomparable and eventually lead to large errors. Similar cases can be observed in other satellite sensors, such as Advanced Very High Resolution Radiometer (AVHRR), Spinning Enhanced Visible and InfraRed Imager (SEVIRI), and so on. Therefore, it is crucial to make angular corrections to the LST.

Until recently, there have been two types of methods for solving this angular LST problem. One method focused on the modeling of directional emissivity, and the other method is aimed at the retrieval of pixel components' temperatures. The former simply attributes the angular variation of the measured effective temperature to the directional behavior of the pixel emissivity. If the directional emissivity at the viewing direction is known, LST can be retrieved by taking the inverse of the radiative transfer model, and the result is consequently assumed to be angle independent. However, because this method ignores the angular variation caused by the component temperatures, and it is always difficult to determine the directional emissivity at the pixel scale, the results of this method are far from satisfactory. In contrast, the retrieval of component temperatures is more promising for achieving LST angular correction because once the components' temperatures are obtained from multi-angle observations (Jia et al. 2003; Li et al. 2001; Menenti et al. 2001), vegetation indices (Liu et al. 2012) or spatial patterns (Zhan et al. 2011), the thermal radiance at any direction can be theoretically calculated by weighting the component temperatures with their corresponding fractions. However, this method always requires the component emissivities and their fractions to be known in advance, but those parameters are seldom easily obtained in practice. As a result, there has been no practical way until now to perform LST angular correction due to the complexity of this issue.

Multi-angular observation on the same targets is considered the most promising way to solve this problem. However, there are still rare reports about LST angular correction or simultaneous retrieval of directional emissivity and temperature from multi-angular TIR images because no more than two angular observations were designed for satellite sensors (e.g., the ATSR/AATSR, Advanced Along Track Scanning Radiometer), and the number of the observation was less than that of the unknowns. On the other hand, more angular observations can be obtained easier from airborne sensors than from spaceborne sensors, such as the WiDAS system (Liu et al. 2012) in the WATER campaign (Li et al. 2009). From the view of this point, the objective of this chapter is to develop a new method for simultaneously retrieving directional emissivity and temperature from the multi-angular observation of middle and thermal infrared (MIR and TIR) data using the TISI method and the kernel-driven BRDF model, and to achieve angular correction on the temperature using modified BRDF model. It is organized as follows: Section 5.2 will present some basic theory on retrieval of emissivity and temperature data from multi-angular observations in both MIR and TIR channels; Section 5.3 will discuss the model sensitivity analysis with respect to some input parameters and errors; Section 5.4 will be devoted to the application of the new method to an aircraft dataset consisting of MIR and TIR images at several viewing angles, which were obtained in the WATER campaign (Li et al. 2009), and the cross validation of the results; and finally, some discussion and conclusions will be presented in the last section of this chapter.

5.2 Algorithm for retrieving angular temperature and emissivity

5.2.1 Radiative transfer equation

For a cloud-free sky, the radiance measured by an infrared channel onboard a satellite or an aircraft can be approximated as Eq.(5.1) (Li et al. 2013a).

$$\boldsymbol{I}(\theta_s,\theta_v,\varphi)=\boldsymbol{R}(\theta_s,\theta_v,\varphi)\cdot\tau(\theta_s,\theta_v,\varphi)+\boldsymbol{R}_{a\uparrow}+\boldsymbol{R}_{sl\uparrow}\,. \tag{5.1}$$

The first term of the right-hand side of Eq.(5.1) is the measured surface-leaving radiance after attenuation passing through the atmosphere, and the second and third terms are the contribution of upward atmospheric emission $\boldsymbol{R}_{a\uparrow}$ and scattered solar radiance $\boldsymbol{R}_{sl\uparrow}$, respectively. The surface-leaving radiance $\boldsymbol{R}(\theta_s, \theta_v, \varphi)$ is written as the following:

$$\begin{aligned}\boldsymbol{R}(\theta_s,\theta_v,\varphi)=\varepsilon(\theta_v,\varphi_v)\boldsymbol{B}[\boldsymbol{T}(\theta_s,\theta_v,\varphi)]+[1-\varepsilon(\theta_v,\varphi_v)]\cdot(\boldsymbol{R}_{a\downarrow}+\boldsymbol{R}_{sl\downarrow})\\+\rho(\theta_s,\theta_v,\varphi)\cdot\boldsymbol{E}_{sun}\end{aligned}\,, \tag{5.2}$$

where, θ_v and θ_s are the viewing zenith angle (VZA) and solar zenith angle (SZA), whereas φ_v is the relative azimuth angle between the viewing azimuth angle φ_v (VAA) and solar zenith angles φ_s (SAA). τ is the atmospheric transmittance. This first term of the right-hand side of Eq.(5.2) is the surface thermal radiation, whereas $\varepsilon(\theta_v, \varphi_v)$ is the surface emissivity in the viewing direction. Because the emissivity is assumed to be VAA-independent in this thesis as reported by (Chehbouni et al. 2001; François 2002; François et al. 1997), the term $\varepsilon(\theta_v, \varphi_v)$

will be replaced with $\varepsilon(\theta_v)$ in the following discussion. $\boldsymbol{B}[\boldsymbol{T}(\theta_s, \theta_v, \varphi)]$ is the surface thermal emission calculated using the Planck's law at the effective temperature $\boldsymbol{T}(\theta_s, \theta_v, \varphi)$, which will be defined from directional emissivity in the next section and varies with the viewing geometry for the non-isothermal pixel rather than an angle-independent value as indicated in some previous studies. The second term is the downward atmospheric radiance $\boldsymbol{R}_{a\downarrow}$ and solar scattering radiance $\boldsymbol{R}_{sl\downarrow}$, reflected by the surface at the viewing direction. The last part of Eq.(5.2) presents the solar direct illumination reflected by the surface with the bi-directional reflectivity $\rho(\theta_s, \theta_v, \varphi)$. For the middle infrared channel at nighttime and the thermal infrared channel, no reflected solar radiance ($\boldsymbol{R}_{sl\downarrow}$ and $\boldsymbol{E}_{sun}$ in Eq.(5.2)) contributes to the surface-leaving radiance. Note that, Eqs. (5.1) and (5.2) are similar to Eqs. (2.2) and (2.3), respectively. However, the variables included in Eqs. (5.1) and (5.2) are related to the viewing and solar azimuth angles because the two equations concern on the non-isothermal pixel, while Eqs. (2.2) and (2.3) conduct the isothermal pixel.

5.2.2 Daytime TISI method

The TISI method was initially developed to separate temperature and emissivity from daytime and nighttime MIR and TIR images, and the method has been successfully applied to retrieve bi-directional reflectivity in the MIR channel and emissivity from the AVHRR, MODIS and SEVIRI onboard MSG (Dash et al. 2005; Goïta and Royer 1997; Jiang et al. 2006; Li et al. 2013b; Li et al. 2000; Nerry et al. 1998; Petitcolin et al. 2002a; Petitcolin and Vermote 2002). According to the TISI method, the Planck's law can be approximated using a power function for the MIR or TIR channel:

$$\boldsymbol{L} = \varepsilon \cdot \boldsymbol{m} \cdot \boldsymbol{T}^{\boldsymbol{n}}, \tag{5.3}$$

where, the coefficients $\boldsymbol{m}$ and $\boldsymbol{n}$ are channel-dependent. Furthermore, the surface-leaving radiance can be consequently expressed as $\boldsymbol{R} = \varepsilon.\boldsymbol{m}.\boldsymbol{T}^{\boldsymbol{n}}.\boldsymbol{C}$, with $\boldsymbol{C}$ accounting for the reflected downward atmospheric radiations. A two-channel emissivity ratio, $\boldsymbol{TISIE}_{\boldsymbol{ij}}$, between one MIR channel (denoted as $\boldsymbol{i}$) without solar illumination and one TIR channel (denoted as $\boldsymbol{j}$) was defined by (Li and Becker 1993; Li et al. 2000) to improve the retrieval of emissivity and consequently LST as follows:

$$\boldsymbol{TISIE}_{\boldsymbol{ij}} = \frac{\varepsilon_{\boldsymbol{i}}}{\varepsilon_{\boldsymbol{j}}^{\boldsymbol{n}_{\boldsymbol{ij}}}} = \frac{\boldsymbol{R}_{\boldsymbol{i}}}{\boldsymbol{R}_{\boldsymbol{j}}^{\boldsymbol{n}_{\boldsymbol{ij}}}} \cdot \frac{\boldsymbol{m}_{\boldsymbol{j}}^{\boldsymbol{n}_{\boldsymbol{ij}}}}{\boldsymbol{m}_{\boldsymbol{i}}} \cdot \frac{\boldsymbol{C}_{\boldsymbol{j}}^{\boldsymbol{n}_{\boldsymbol{ij}}}}{\boldsymbol{C}_{\boldsymbol{i}}} = \frac{\boldsymbol{R}_{\boldsymbol{i}}}{\boldsymbol{R}_{\boldsymbol{j}}^{\boldsymbol{n}_{\boldsymbol{ij}}}} \cdot \boldsymbol{M}_{\boldsymbol{ji}} \cdot \boldsymbol{C}_{\boldsymbol{ji}}, \text{ with } \boldsymbol{n}_{\boldsymbol{ij}} = \boldsymbol{n}_{\boldsymbol{i}} / \boldsymbol{n}_{\boldsymbol{j}}. \tag{5.4}$$

Introducing Eq.(5.4) into Eq.(5.2) obtains the expression to calculate the bi-directional reflectivity as follows:

$$\rho_{\boldsymbol{i}}(\theta_s, \theta_v, \varphi) = \frac{1}{\boldsymbol{E}_{\boldsymbol{sun}}}[\boldsymbol{R}_{\boldsymbol{i}} - \boldsymbol{TISIE}_{\boldsymbol{ij}} \cdot \boldsymbol{R}_{\boldsymbol{j}}^{\boldsymbol{n}_{\boldsymbol{ij}}} \cdot \boldsymbol{M}_{\boldsymbol{ij}} \cdot \boldsymbol{C}_{\boldsymbol{ij}}]. \tag{5.5}$$

The final solution of Eq.(5.5) requires the value of $\boldsymbol{TISIE}_{\boldsymbol{ij}}$, which is assumed to be the same at daytime and nighttime if there is no occurrence of rain, snow or dew, and the nighttime $\boldsymbol{TISIE_{ij}}$ can calculated directly using Eq.(5.4) from the nighttime observations in both the MIR and TIR channels. However, because the TISI method requires daytime and nighttime observation of the same target in a short time frame, its application cannot be achieved for the sensors that only provide daytime observations. To solve this problem, Goïta and Royer (1997) extended the original TISI method to retrieve emissivity from two consecutive datasets acquired at the same time during daytime by simplifying the TISIE and the characteristics of the bi-directional reflectivity. However, their simplifications, especially the case of TISIE = 1, will introduce some unexpected error into the retrieved emissivity and, consequently, the LST.

Inspired by the results of (Jiang and Li 2008a), a new daytime TISI method is proposed that uses the TISI method and the kernel-driven BRDF model to simultaneously retrieve emissivity and temperature from a sufficient number of angular observations. First, the bi-directional reflectivity in the MIR channel can be expressed as Eq.(5.6) on the basis of the kernel-driven BRDF model:

$$\rho_i(\theta_s,\theta_v,\varphi) = \boldsymbol{f_{iso}} + \boldsymbol{f_{vol}} \cdot \boldsymbol{k_{vol}}(\theta_s,\theta_v,\varphi) + \boldsymbol{f_{geo}} \cdot \boldsymbol{k_{geo}}(\theta_s,\theta_v,\varphi)\,, \tag{5.6}$$

where, $\boldsymbol{f_{iso}}$ is the isotropic scattering term, $\boldsymbol{f_{vol}}$ is the coefficient of the volumetric kernel $\boldsymbol{k_{vol}}$, and $\boldsymbol{f_{geo}}$ is the coefficient of the geometric kernel $\boldsymbol{k_{geo}}$. The Ross-Thick volumetric kernel and the Li-SparseR geometric kernel are used in this thesis (Jiang and Li 2008a). If the bi-directional reflectivity ρ is known for at least three viewing directions, the three kernel coefficients ($\boldsymbol{f_{iso}}$, $\boldsymbol{f_{vol}}$ and $\boldsymbol{f_{geo}}$) can be regressed using the least squares method. In contrast, if the three kernel coefficients are known in advance, the bi-directional reflectivity ρ in arbitrary direction can be estimated from Eq.(5.6). Therefore, the retrieval of ρ will be equivalent to the retrieval of those kernel coefficients. Moreover, combining Eqs. (5.4) and (5.6) into to Eq.(5.2) will produce a new formula:

$$\boldsymbol{R_i}(\theta_s,\theta_v,\varphi) = \boldsymbol{TISIE_{ij}} \cdot \boldsymbol{R_j^{n_{ij}}}(\theta_s,\theta_v,\varphi) \cdot \boldsymbol{M_{ij}} \cdot \boldsymbol{C_{ij}} + (\boldsymbol{f_{iso}} + \boldsymbol{f_{vol}} \cdot \boldsymbol{k_{vol}} + \boldsymbol{f_{geo}} \cdot \boldsymbol{k_{geo}}) \cdot \boldsymbol{E_{sun}}\,. \tag{5.7}$$

In Eq.(5.7), the terms $\boldsymbol{R_i}$ and $\boldsymbol{R_j}$ are the measured radiance in the MIR and TIR channels, respectively; the solar illumination $\boldsymbol{E_{sun}}$ can be estimated from atmospheric data (Nerry et al. 1998); $\boldsymbol{M_{ij}}$ and $\boldsymbol{n_{ij}}$ are channel-dependent and can be fitted using laboratory-simulated data; the index $\boldsymbol{C_{ij}}$ is complicated because it relies on both surface and atmospheric conditions and can be approximated as $\boldsymbol{C_{ij}} = [1 - \boldsymbol{R}_{ai\downarrow}/\boldsymbol{B_i}(\boldsymbol{T_{max}})] / [1 - \boldsymbol{R}_{ai\downarrow}/\boldsymbol{R_i}]$ (Jiang et al. 2006), with $\boldsymbol{T_{max}}$ is the maximum the brightness temperature in the TIR channel under different viewing angles. The rest of the terms of Eq.(5.7) are the unknown variables, including the three coefficients of the BRDF model and the TISIE. Although the emissivities of both MIR and TIR channels (i.e., ε_i and ε_j) vary with the viewing angle, the angular variation of TISIE is not significant and is less than 0.01 for most cases. Therefore, it is reasonable to use only one average TISIE in Eq.(5.7) to reduce the number of unknowns. As a result, there are only four unknowns that remain (TISIE, $\boldsymbol{f_{iso}}$, $\boldsymbol{f_{vol}}$ and $\boldsymbol{f_{geo}}$) in Eq.(5.7). If the same target is observed at more than four directions, those unknown $\boldsymbol{X}$ can be retrieved from the linear equation group such as $\boldsymbol{Y} = \boldsymbol{AX}$, where $\boldsymbol{A}$ is the coefficient matrix composed by the terms in Eq.(5.7) and $\boldsymbol{Y}$ denotes $\boldsymbol{R_i}$.

Once the three coefficients of the BRDF model are obtained, the directional emissivity in the MIR channel can be estimated as one minus the hemisphere-directional emissivity on the basis of Kirchhoff's law (Jiang and Li 2008a; Lucht and Roujean 2000; Roujean et al. 1992; Wanner et al. 1995).

$$\varepsilon_{\boldsymbol{i}}(\theta_v) = 1 - \int_0^{2\pi}\int_0^{\pi/2} \rho(\theta_s, \theta_v, \varphi)\sin(\theta_s)\cos(\theta_s)\boldsymbol{d}\theta_s\boldsymbol{d}\varphi\,. \tag{5.8}$$

According to Eq.(5.6), the integration of the reflectivity in the upward hemisphere is equal to the result of integrating the three kernels ($\boldsymbol{k_{vol}}$, $\boldsymbol{k_{geo}}$, and 1) in the same angle range because the values of the kernel coefficients are fixed for all angles. Jiang and Li (2008a) calculated the integration of the Ross-Thick volumetric kernel ($\boldsymbol{Ik_{vol}}$) and Li-SparseR geometric kernel ($\boldsymbol{Ik_{geo}}$) with SZA varying from 0° to 80° and SAA varying from 0° to 360° with a step 0.05° and then related $\boldsymbol{Ik_{vol}}$ and $\boldsymbol{Ik_{geo}}$ to the VZA (θ_v) using an exponent growth function and a Gaussian function, respectively. Finally, based on the concept of the two-channel TISIE defined in Eq.(5.4), the emissivity in the TIR channels can be obtained from the TISIE and the emissivity in the MIR channel (Jiang et al. 2006; Li et al. 2000).

$$\varepsilon_{\boldsymbol{j}}(\theta_v) = \left(\frac{\varepsilon_{\boldsymbol{i}}(\theta_v)}{\boldsymbol{TISIE_{ij}}}\right)^{1/\boldsymbol{n_{ij}}}. \tag{5.9}$$

The advantage of the above daytime TISI method (hereafter called the D-TISI method) is that it eliminates the requirement of daytime and nighttime measurements in the original TISI method by using at least four angular daytime observations in both MIR and TIR channels, and it requires only one atmospheric correction for all angular observations rather than two times, respectively, for the daytime and nighttime observations. However, because the temperature difference between those angular observations is not as large as that of the daytime and nighttime observations, the relatively high correlations in the radiative transfer equations like Eq.(5.7) may make the model sensitive to data error. Therefore, an optimization algorithm is needed to avoid outliers.

It is worth noting that all variables/parameters in the above equations, except for the angles, are channel-effective values. The channel-effective quantities of interest are calculated as a weighted value from monochromatic values using the spectral response function $\boldsymbol{f}(\lambda)$: (Li et al. 2013a):

$$\boldsymbol{X_i} = \frac{\int_{\lambda_1}^{\lambda_2} \boldsymbol{f_i}(\lambda)\boldsymbol{X}_\lambda \boldsymbol{d}\lambda}{\int_{\lambda_1}^{\lambda_2} \boldsymbol{f_i}(\lambda)\boldsymbol{d}\lambda}, \tag{5.10}$$

where, λ_1 and λ_2 are the lower and upper response wavelength of the $\boldsymbol{i}$th channel, respectively, and $\boldsymbol{X}$ stands for $\boldsymbol{B}(\boldsymbol{T})$, $\boldsymbol{R}$, $\boldsymbol{L}$, $\boldsymbol{R_{a}}\downarrow$, $\boldsymbol{R_{a}}\uparrow$, $\boldsymbol{R_{sl}}\uparrow$, ε, τ, or ρ. Eqs. (5.1) and (5.2) are actually approximations of the theoretical radiative transfer equation in which monochromatic quantities are replaced with channel-effective values, and those approximations are only reliable for a narrow channel.

5.3 Model analysis

5.3.1 Channel specifications

We were concerned with the MIR and TIR channels from two sensors: the airborne WiDAS (Wide-angle infrared Dual-mode line/area Array Scanner) system (Fang et al. 2009; Liu et al. 2012) used in the WATER field campaign (Li et al. 2009), and the MODIS channels 20 and 31. The MIR and TIR images of WiDAS will be used in the next section for the validation of the D-TISI method. However, as shown in Fig.5-1, the bandwidths of the WiDAS's two channels are up to 4 μm and 11 μm, respectively, which are rare in current airborne or spaceborne sensors and will reduce the accuracy of the approximations of the radiative transfer function from the monochromatic value to the channel-effective value as stated in Eq.(5.8), in addition to degrading the accuracy of the approximation of the exponent expression of the channel radiance using Eq.(5.3). In contrast, the bandwidths of the MODIS's MIR and TIR channels are relatively narrower, and such narrow bandwidths are usually observed for several sensors. Therefore, although this thesis will not use the MODIS data to validate the D-TISI method due to the lack of the multi-angular observation images, the following analysis will discuss the retrieved result from the MODIS's two channels in detail rather than the WiDAS, to make the findings of this thesis more representative and reliable. We also provide the general results for the WiDAS system.

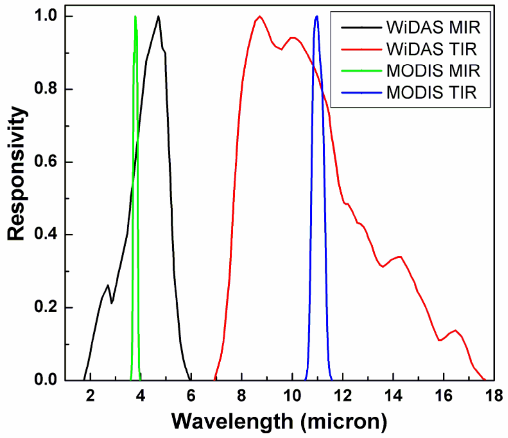

Fig.5-1. Spectral response functions of the MIR and TIR channels for the WiDAS system and the MODIS sensor, respectively.

Table 5-1 shows the coefficients ***m*** and ***n*** in Eq.(5.3) for the channels of MODIS and WiDAS. Two temperature ranges, 270 K to 300 K and 300 K to 330 K, were used for the power approximation with a higher accuracy. The ***m*** and ***n*** can be determined with the measured TIR brightness temperature.

Table 5-1. Parameters m, n, and error (**rms** and **max**) for the MIR and TIR channels of MODIS and WiDAS

Sensor& Channel		270 K ~ 300 K				300K ~ 340 K			
		$Ln(m)$	n	ΔL (*rms*)	ΔL (*max*)	$Ln(m)$	n	ΔL (*rms*)	ΔL (*max*)
MODIS	MIR	-76.68	13.32	0.002	0.006	-68.43	11.87	0.009	0.032
	TIR	-24.18	4.64	0.014	0.036	-21.46	4.16	0.029	0.078
WiDAS	MIR	-60.57	10.67	0.003	0.011	-54.74	9.65	0.014	0.047
	TIR	-26.01	4.95	0.012	0.032	-23.49	4.51	0.027	0.073

5.3.2 Simulation conditions

Many surface and atmospheric conditions have to be designed to simulate the bi-directional reflectivity in the MIR, directional emissivity and measured radiance of the MIR and TIR channels. Because the D-TISI method addresses the atmospherically corrected radiance, only the surface-leaving radiance is used. We considered the middle-latitude summer atmospheric models included in the MODTRAN 4.0 radiative transfer code. The rural aerosol model was assumed with a visibility of 10, 15, 20, 25, 30, 40 and 50 km, and the column water vapor was set with 0.25 WV_{max}, 0.5 WV_{max} and 0.75 WV_{max}, where WV_{max} is the maximum water content in the atmospheric model.

The SAILH model (Verhoef 1989) was used to simulate the bi-directional reflectivity in the MIR channel and the directional emissivities in both the MIR and TIR channels. The SAILH model was inherited from the SAIL (scattering by arbitrarily inclined leaves) model (Verhoef 1984), which incorporated the foliage hotspot effect according to the theory of Kuusk (1985), and the results of the SAILH model should be closer to reality than the original model. The input variables of the SAILH model include the canopy parameters (e.g., leaf area index, hotspot factor) and component properties (e.g., reflectivity and transmittance). The SAILH model outputs the bi-directional reflectivity at any designed viewing geometry. Furthermore, the hemisphere-directional reflectivity of the canopy is integrated from the bi-directional reflectivity in the hemisphere, and the directional emissivity is estimated as the complement of the hemisphere-directional reflectivity based on Kirchhoff’s law. Although this thesis concerns non-isothermal surfaces, the emissivity is assumed to be independent of the temperature distribution of the surface (Li et al. 1999). As a result, Kirchhoff’s law is still suitable at least for the above calculation of the directional emissivity over the non-isothermal surface. Note that, in the Chapter 4, we simulated the directional emissivity from the TIR-SAIL model (Liu et al. 2003) or from the complement of hemispheric-directional reflectivity integrated from the SAILH model, and found that a slight difference existed between the two ways. Details can be found in section 4.3.1. Since we parameterized the directional emissivity simulated from the TIR-SAIL model, for context coherence reasons, this chapter should use the TIR-SAIL model to simulate directional emissivity of the canopy. However, in order to uniform the bi-directional reflectivity and directional emissivity in MIR channel as well as in TIR channel, and also to remove the error in the simulated dataset for the model analysis, we only used the SAILH model in this chapter.

Table 5-2. The channel emissivity for the MODIS and WiDAS system, chosen from UCSB emissivity database

MODIS MIR	MODIS TIR	WiDAS MIR	WiDAS TIR	Sample Name
Vegetation Samples				
0.9566	0.9626	0.9572	0.9572	Leaf of Maple
0.9384	0.9535	0.9096	0.9664	Dry Grass (Averaged over 9 Sets)
0.9392	0.9540	0.9103	0.9669	Dry Grass3 (Averaged over 9 Sets)
0.9691	0.9601	0.9677	0.9617	Fresh leaf of Eucalyptus tree
0.9724	0.9714	0.9714	0.9742	Laurel leaf
0.9586	0.9563	0.9577	0.9525	Leaf Magnolia
0.9642	0.9617	0.9638	0.9621	Leaf of Evergreen Pear
0.9856	0.9908	0.9860	0.9914	Leaf of Green Spruce from Canada
0.9841	0.9807	0.9844	0.9809	Leaf of Pine(New)
0.9781	0.9792	0.9786	0.9787	Leaf of Pine(Old)
Soil Samples				
0.9248	0.9681	0.9369	0.9618	Salty Soil (Averaged over 19 Sets)
0.8392	0.9581	0.9242	0.9012	Sand Sample 2 from Orchard
0.8467	0.9719	0.8694	0.9571	No.88p2535S from Nebraska Soil Lab
0.6816	0.9590	0.7503	0.9531	No.88p3715S from Nebraska Soil Lab
0.8252	0.9789	0.8597	0.9656	No.88p4643S from Nebraska Soil Lab
0.6066	0.9477	0.6869	0.9380	No.90p3101S from Nebraska Soil Lab
0.6918	0.9712	0.7519	0.9532	No.90P4172S from Nebraska Soil Lab
0.7793	0.9746	0.8347	0.9586	No.90P4255S from Nebraska Soil Lab
0.8501	0.9760	0.8885	0.9656	Soil Sample 1 from Concord, MA
0.7858	0.9828	0.8408	0.9535	Soil Sample 10 from Oklahoma
0.7842	0.9767	0.8431	0.9497	Soil Sample 13 from Oklahoma
0.8712	0.9744	0.8938	0.9631	Soil Sample 3 from Concord, MA
0.8493	0.9673	0.9077	0.9568	Soil Sample 4 from Death Valley, CA
0.8548	0.9758	0.9047	0.9512	Soil Sample 5 from Oklahoma
0.8346	0.9679	0.8700	0.9438	Soil Sample 7 - Hard Pan
0.7569	0.9661	0.8602	0.9301	Soil Sample 7 from Death Valley, CA
0.8418	0.9725	0.8905	0.9449	Soil Sample 9 - Hard Pan, Ground

We chose 10 vegetation and 17 soil samples from the UCSB spectral emissivity databases and obtained their channel emissivity for the MIR and TIR channels using Eq.(5.10), which resulted in a total of 170 combinations of vegetation and soil samples. Table 5-2 shows the channel emissivity of the MODIS and WiDAS. Because the wavelength range (3~14 μm) of the sample emissivities did not cover all the response wavelengths of the WiDAS's two channels, the spectral emissivity out of the 3~14 μm was not used in the integration procedure from monochromatic emissivity to the channel emissivity. Note that sample emissivities were assumed to be angle-independent. Furthermore, those samples' reflectivity input to the SAILH model was calculated as the complement of the channel emissivity listed in Table 5-2, and the transmittance of the samples equaled zero. A spherical canopy was assumed in the SAILH model, and the LAI varied from 0.5 to 5 with a step of 0.5.

As shown in Fig.5-2, the simulated TISIE in the MODIS channels mainly distributes in the range [0.95, 1.1], whereas some TISIE values are smaller than 0.9 because of the low emissivity of some soil samples in the MIR channel and the small LAIs. According to the results obtained by Jiang et al. (2006), the pixel TISIE were mostly larger than 0.96 for several different combinations of the MIR and TIR channels. Therefore, we only consider the case of TISIE larger than 0.92, which covers approximately 92% of the total samples.

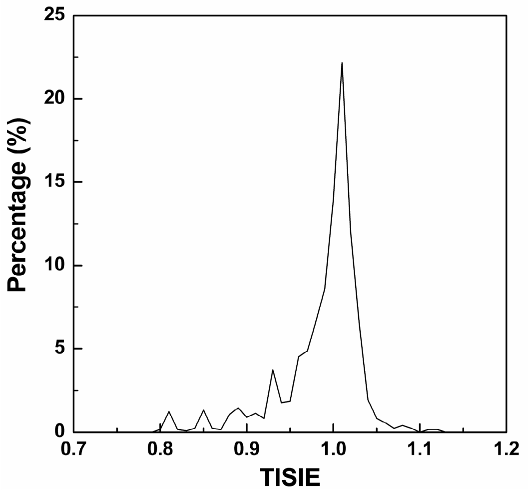

Fig.5-2. Histogram of TISIE in the MODIS simulated dataset

The non-isothermal canopy was assumed to consist of three components: leaves, sunlit soil and shaded soils. Six groups of those three component temperatures were used, as shown in Table 5-3. T-groups 1 and 2 represent low component temperatures with small and large differences, respectively. T-groups 3 and 4 represent middle temperatures with small and large differences, respectively. Finally, T-groups 5 and 6 represent high temperatures, and their temperature differences are generally larger than the other groups because this case may occur in sparse canopies and/or in summer.

Table 5-3. Different groups of components' temperatures used for simulations

T-group No.	T_{leaf}(K)	T_{sun_soil} (K)	T_{shd_soil} (K)
1	270	280	273
2	270	285	275
3	290	300	293
4	290	305	295
5	310	325	315
6	310	330	320

5.3.3 Canopy directional radiance and directional effective temperature

Based on the simulation conditions as stated above, the bi-directional reflectivity and emissivity were simulated with the SAILH model, and the downward atmospheric radiance and solar radiance in Eq.(5.2) were determined from MODTRAN 4.0. The canopy directional effective radiance in Eq.(5.2) (i.e., $\boldsymbol{L_e}(\theta_s, \theta_v, \varphi)= \varepsilon(\theta_v)\, \boldsymbol{B}[\boldsymbol{T}(\theta_s, \theta_v, \varphi)]$) was further simulated as follows:

$$\boldsymbol{L_e}(\theta_s,\theta_v,\varphi)=\sum_{k=1}^{3}\boldsymbol{f_k}(\theta_s,\theta_v,\varphi)\cdot\boldsymbol{L_k}+\boldsymbol{L_{multi}}, \tag{5.11}$$

$$\boldsymbol{L_{multi}}=\sigma_f\boldsymbol{L_{leaf}}(1-\varepsilon_g)+(1-\alpha)[1-\boldsymbol{b}(\theta_v)(1-\sigma_f)]\cdot[1-\boldsymbol{b}(\theta_v)](1-\varepsilon_v)\cdot\boldsymbol{L_{leaf}}. \tag{5.12}$$

The first term of Eq.(5.11) is the weighted radiance by the component fraction $\boldsymbol{f_k}$, calculated from a parameterization model of the SAILH model by (Li et al., 2011) at the viewing geometry (θ_s, θ_v, φ) and the component emitted radiance $\boldsymbol{L_k}$ calculated from the emissivity (see Table 5-1) and temperature (see Table 5-2) using Planck’s law. The second term of Eq.(5.11) is the radiance scattering between the leaves and soil (first part of the right-hand side of Eq.(5.12)) and between leaves (second part of the right-hand side of Eq.(5.12)) in the canopy. $\boldsymbol{b}(\theta)$ is the directional gap of the canopy, and σ_f is the hemispheric leave fraction, both of them can be determined by using canopy LAI and viewing angles. α denotes the cavity effect accounting for the multiple scattering inside the canopy. More details about the calculation of $\boldsymbol{b}(\theta)$, σ_f and α can be found in Chapter 4. On the basis of the $\boldsymbol{L_e}(\theta_s, \theta_v, \varphi)$ simulated from Eq.(5.11), we defined the directional brightness temperature (DBT) and the directional effective temperature ($\boldsymbol{T_e}$) for the non-isothermal canopy as Eq.(5.13). $\boldsymbol{B}[]^{-1}$ is the inversion of Planck’s law. Note that the consideration of the non-isothermal canopy causes $\boldsymbol{T_e}$ to vary with channels, which does not satisfy the requirement of the D-TISI method that the temperature must be the same in the MIR and TIR channels. To satisfy the requirement, the $\boldsymbol{T_e}$ of the MIR channel was forced to equal that of the TIR channel in our simulated dataset. However, the DBTs were channel-dependent.

$$\boldsymbol{DBT}(\theta_s,\theta_v,\varphi)=\boldsymbol{B}\big[\boldsymbol{R}(\theta_s,\theta_v,\varphi)\big]^{-1},\ \text{and}\ \ \boldsymbol{T_e}(\theta_s,\theta_v,\varphi)=\boldsymbol{B}\left[\frac{\boldsymbol{L_e}(\theta_s,\theta_v,\varphi)}{\varepsilon(\theta_v)}\right]^{-1}. \tag{5.13}$$

5.3.4 Multi-angular combinations

As stated above, at least four angular observations are required to solve the four unknowns. A previous study indicated that a large difference among VZAs can reduce the correlations between radiative transfer equations and can obtain more accurate results in the retrieval of emissivity and temperature (François et al. 1997). To illustrate the influence of the different angular observations on the retrieval accuracy, we used four groups of angular observations (Table 5-4): (1) five angles: nadir, forward and backward 10° and 30°; (2) five angles: nadir, forward and backward 30° and 50°; (3) five angles: nadir, forward and backward 20° and 40°; and (4) seven angles: nadir, forward and backward 10°, 20° and 40°, respectively. The forth group is the designed angular combination of the WiDAS system. In addition, we assumed that the backward direction has an azimuth angle 180°, and the forward direction has an azimuth angle 0°.

Table 5-4. Different angle combinations

Case No.	Angle combination (VAA, VZA)	description
1	(0°, 0°); (0°, 10°), (0°, 30°) and (180°, 10°) , (180°, 30°)	five angles: nadir, forward and backward 10° and 30°
2	(0°, 0°); (0°, 30°), (0°, 50°) and (180°, 30°), (180°, 50°)	five angles: nadir, forward and backward 30° and 50°
3	(0°, 0°); (0°, 20°), (0°, 40°) and (180°, 20°), (180°, 40°)	five angles: nadir, forward and backward 20° and 40°
4	(0°, 0°); (0°, 10°), (0°, 20°), (0°, 40°); and (180°, 0°), (180°, 20°), (180°, 40°)	seven angles: nadir, forward and backward 10°, 20° and 40°

5.3.5 Initial values of the four unknowns

The initial value of the TISIE can be obtained using a similar relationship between the TISIE and the ratio of the MIR and TIR surface-leaving radiance, as proposed by (Goïta and Royer 1997). With the known atmospheric downward radiance from atmospheric data, we first used $\varepsilon_{\boldsymbol{j}} = 0.98$ ($\boldsymbol{j}$ denotes the TIR channel) to retrieve the $\boldsymbol{T_e}$ in the TIR channel and applied $\boldsymbol{T_e}$ in the radiative transfer equation (i.e., Eq.(5.2)) to calculate the bi-directional reflectivity with an approximation $\rho(\theta_s, \theta_v, \varphi) = 1 - \varepsilon(\theta_v)$, and then we estimated the three coefficients ($\boldsymbol{f_{iso}}$, $\boldsymbol{f_{vol}}$ and $\boldsymbol{f_{geo}}$) from the BRDF model shown in Eq.(5.6). These initial values were consequently input into an optimization algorithm to obtain the final solution of the four unknowns.

5.3.6 Model analysis

Because the observed data always included some noise from the instrument noise, atmospheric correction and angle-controlling error, the retrieval accuracy may be consequently degraded. To evaluate the model's consistency with the LAI, angular combination, as well as temperature and TISIE themselves, some artificial noise was introduced into those data. The noise included in the atmospheric data ranged from [-10%, 10%] of the data itself, and the noise introduced in the DBT of the MIR and TIR channels was within [-0.5, 0.5] K and ± [0.5, 1.0] K. The two types of DBT noise were used to investigate the reliability of the above four angular combinations. All noise was provided with a uniform distribution. Note that the results shown from Fig.5-3 to Fig.5-7 came from the MIR and TIR channels of the MODIS sensor, whereas the results of Fig.5-8 are for the WiDAS system.

A. Influence of LAI

The root-mean-square error (RMSE) of the retrieved TIR emissivity is displayed in Fig.5-3 for the equivalent temperature noise within [-0.5, 0.5] K, included in simulated DBT, and in Fig.5-4 for the noise within ± [0.5, 1.0] K. As observed in the two figures, the RMSE initially decreases and then increases with the increasing LAIs. As for the sparse (e.g., LAI = 0.5) or dense (e.g., LAI > 4) vegetated surfaces, their angular variations of the component fractions and DBT were not remarkable, and consequently, the solution of Eq.(5-7) was sensitive to the noise included in the MIR and TIR brightness temperatures and atmospheric data. In contrast, for the partly vegetated surface (e.g., LAI =1.5, 2.0), the variation of the component fractions and DBT caused by the different viewing angle becomes relatively more significant, whereas the retrieval process is less influenced by the noise in the input data.

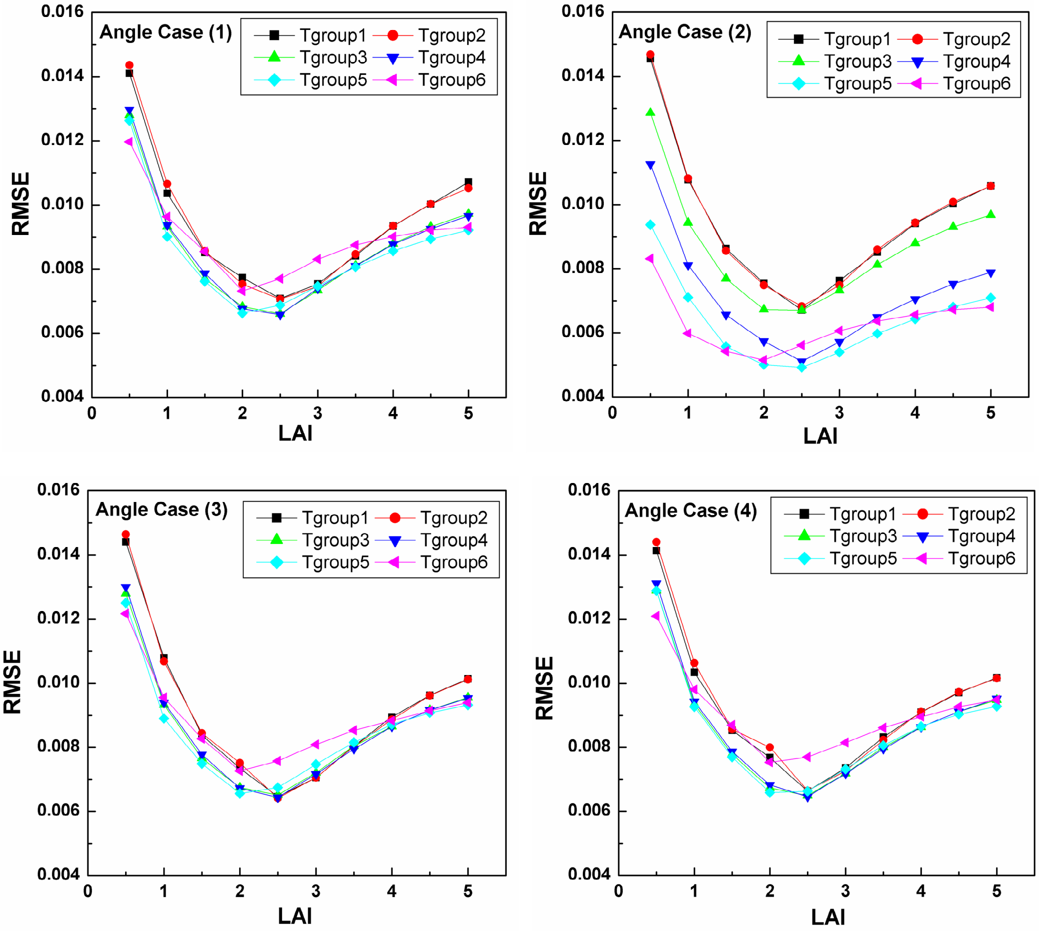

Fig.5-3. RMSE of TIR emissivity at different angular observations and LAIs, with DBT noise of the MIR and TIR channels within [-0.5, 0.5] K included in the DBT of both MIR and TIR channels.

B. Influence of angular combinations

As stated above, four groups of angular observations were used to determine the “best” combination for the retrieval of the bi-directional reflectance and emissivity. The retrieval RMSE for most cases in Fig.5-3 is smaller than 0.01, and all of them are less than 0.015, whereas for most cases in Fig.5-4, the RMSEs are less than 0.015. A greater noise included in the DBT produced larger error in the retrieved emissivity. A comparison between the results from different cases of the angular combinations indicates that case (2) performs better than the others, especially for the DBT noise within [-0.5, 0.5] K, most likely because case (2) had the largest off-nadir observation (i.e., VZA = 50°) and the largest angle interval (i.e., ΔVZA =

30° or 20°) (see Table 5-4), which corresponded to the largest difference in the component fractions and DBT between the different viewing angles and consequently reduced the correlation of the radiative transfer equations, resulting in more reliable retrieval result. On the other hand, the smallest off-nadir observation (i.e., VZA = 50°) and angle interval (i.e., ΔVZA = 10° or 20°) in case (1) enhanced the correlations of their radiative transfer equations, leading to the lowest retrieval accuracy. Comparing the results of case (3) and (4), case (3) performed slightly better than case (4), especially for T-groups 1 and 2. This better performance might be because although case (4) has more angular observations (seven) than case (3), the correlations of the radiative transfer equations were increased by the smaller angle interval in case (4), and the error included in the additional angular observation can also degrade the retrieval accuracy. Therefore, more observations will not always obtain more accurate results unless the angle interval is large enough.

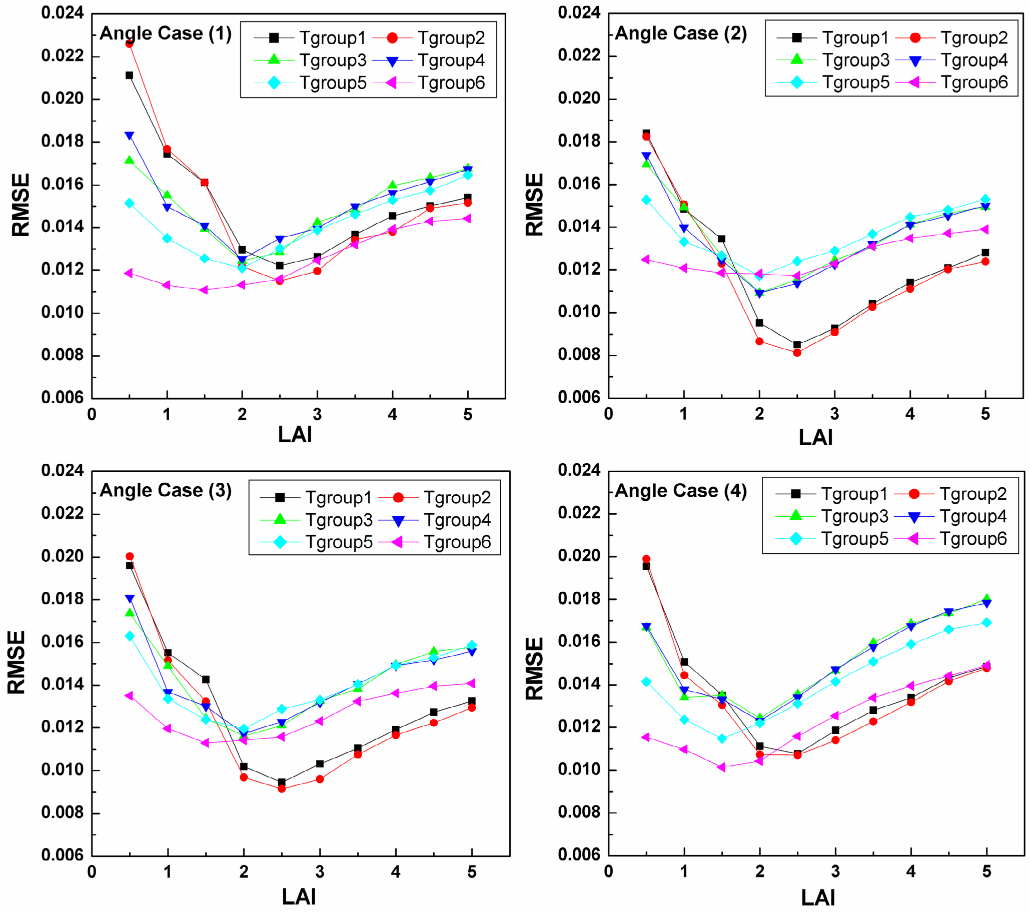

Fig.5-4. Similar to Fig.5-3, but with DBT noise within ± [0.5, 1.0] K.

From the above discussion and the results shown in Fig.5-3 and Fig.5-4, we determined that case (2) is the best angular combination among the four examined angle cases, and these results are similar to a previous study (François et al. 1997). However, these results do not mean that case (2) involves the best angular combinations for the retrieval, as it is actually difficult to determine the best combination from numerous combinations with different viewing angles in the upper hemisphere. Although a large viewing angle can improve the retrieval accuracy, it is not recommended to use a viewing angle larger than 55° because the pixel size of such viewing angle is approximately 4 times the size of the nadir observation, and the different pixels size may result in the presentation of different components and/or their temperatures, especially for heterogeneous surfaces.

C. Influence of components' temperatures

The correlation between the radiative transfer equations of different viewing angles is related to the temperature discrepancy of the components in the scene. Large temperature discrepancies can reduce this correlation, whereas small temperature discrepancies can lead to a higher correlation. As shown in Table 5-3, T-groups 1 and 2 had a similar level of different component temperatures, but the temperature discrepancy for T-group 2 was larger than T-group 1. Therefore, as the correlation of the angular observation is less significant in T-group 2, the retrieval error of T-group 2 is smaller than T-group 1, as shown in Fig.5-3 and Fig.5-4. A similar case was found for T-groups 3 and 4 and 5 and 6. However, this difference of the retrieval errors between T-groups 1 and 2, 3 and 4, and 5 and 6 was so limited that it almost disappeared in some results, as observed in Fig.5-3, perhaps because the relatively smaller temperature difference in T-groups 1, 3 and 5 is large enough to reduce the influence of the temperature difference and also because of the influence of noise included in the measured data.

Fig.5-4 also shows that the retrieval errors of T-groups 1 and 2 were almost smaller than those of the other T-groups with higher DBT, especially for the angle cases (2) and (3). These results indicate that the increase of DBT could not enable a better retrieval result because at the same level of the component temperatures' difference, the increase of component temperatures inversely reduced the angular variation of the DBT between the angular observations. Fig.5-5 presents the histograms of the difference $\Delta T' = \Delta T_1 - \Delta T_{\boldsymbol{x}}$ of temperature discrepancies between the nadir and off-nadir 50° observations, where $\Delta T_1 = T_{nadir} - T_{50°}$ in T-group 1 and $\Delta T_{\boldsymbol{x}} = T_{nadir} - T_{50°}$ ($\boldsymbol{x}$ = 3 and 5) in T-groups 3 and 5. It was observed that the temperature discrepancy between the nadir and off-nadir 50° in T-group 1 was larger than that of T-groups 3 and 5, especially for the MIR channel. As for the T-group 1 and 3 (see filled squares in Fig.5-5(a) and (b)), the temperature discrepancy ΔT_1 was notably larger than ΔT_3 for both the MIR and TIR channels, and all of the $\Delta T'$ values in the TIR channel ranged from 0.0 K to 0.2 K, whereas most of the $\Delta T'$ values in the MIR channel were more than 1.0 K. Consequently, this variation in the temperature discrepancy of nadir and off-nadir directions, from a lower temperature to a higher temperature but with similar difference of component temperatures, caused a corresponding higher correlation in radiative transfer equations and finally led the retrieval process from T-group 3 to be more sensitive to the noise than that from T-group 1. As for T-groups 1 and 5 (see unfilled squares in Fig.5-5(a) and (b)), the $\Delta T'$ between ΔT_1 and ΔT_5 of the MIR channel was notable and generally larger than the $\Delta T'$ between ΔT_1 and ΔT_3. However, as seen from Fig.5-5(b), most of the ΔT_1 were smaller than ΔT_5, which means that the temperature discrepancy between the nadir and off-nadir 50° was enlarged in the TIR channel from T-group 1 to T-group 5. As a result, this variation might cause T-group 5 to obtain a more accurate result than T-group 3 in theory. However, because temperature discrepancies in the MIR channel were remarkably reduced, the retrieval accuracies from T-group 5 were generally lower than that from T-group 1, and even lower than that from T-group 3 in some cases. Similar reasons can be used to explain the variation between T-groups 2 and 4. T-group 6 had a better result because it had a larger component temperature discrepancy than the other groups. From the above discussions, a cautious conclusion can be drawn that at the same level of component temperature differences, the case with a relatively lower brightness temperature will lead to better results for the retrieval emissivity in the TIR channel, as well as for the bi-directional reflectivity and emissivity in the MIR channel. However, the results still depend on the specific situation, including the atmospheric conditions and canopy structures.

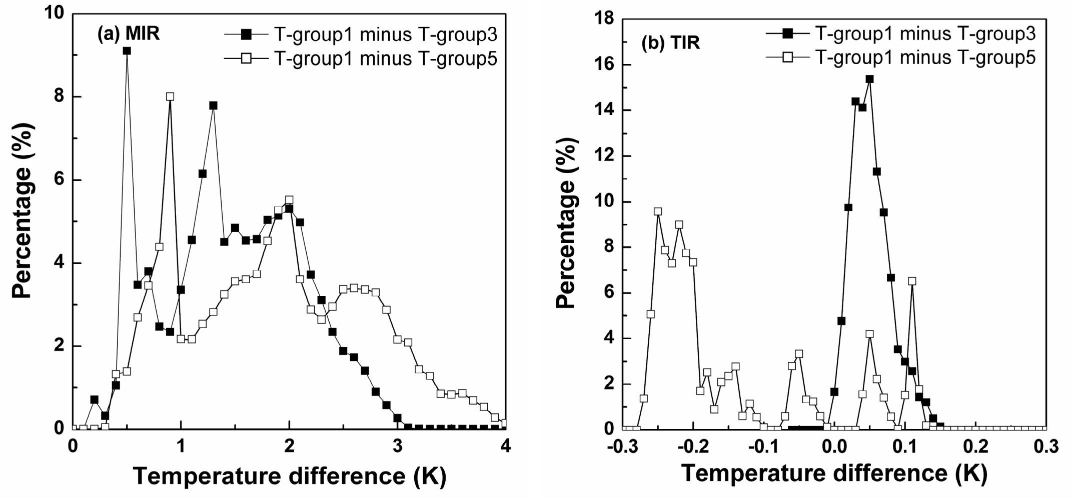

Fig.5-5. Histograms for the difference of the temperature discrepancy between nadir and off-nadir 50°.

D. Influence of TISIE

Fig.5-6 presents the RMSE for the retrieved TIR emissivity, which varies with the TISIE for two noise conditions. Only angle case (2) was used for illustration. These data show that the RMSEs for TISIE within [0.92, 1.06] were smaller than 0.015, which is the accuracy required for some sensors (Gillespie et al. 1998). According to the histogram in Fig.5-2, this part of the TISIE covers approximately 91% of all samples and approximately 98% of the samples with a TISIE larger than 0.92. Moreover, this range of TISIE also covers the values of most natural surfaces as reported by (Jiang et al. 2006) on satellite data. However, for those larger TISIEs (i.e., > 1.05) resulting from dense vegetated surfaces or sparse surfaces whose MIR emissivity is relatively larger and TIR emissivity is relatively smaller, the retrieval accuracy might be degraded by the small angular variation of the component fractions and DBT as described above.

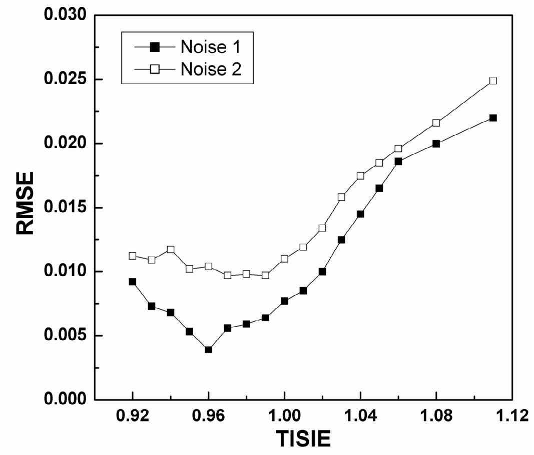

Fig.5-6. Influence of TISIE on the retrieval accuracy by using angle case (2)

Fig.5-7(a) displays the histograms of the residual error for the retrieved bi-directional reflectivity in the MIR channel and emissivity in the TIR channel with DBT noise within [-1.0, 1.0] K. These results show that the bias of reflectivity was close to 0 but that of the TIR emissivity was larger than 0 and nearly 0.004, which indicates that the retrieved TIR emissivity was generally larger than the true value and that the accuracy of the retrieved reflectivity was higher than that of the TIR emissivity. This result is reasonable because, from Eq.(5.7) and the kernel-driven BRDF model in Eq.(5.6), the accuracy of the bi-directional reflectivity is only influenced by the three coefficients driven from Eq.(5.7), whereas that of the TIR emissivity is not only dependent on the three coefficients and TISIE but also relies on the parameter $\boldsymbol{C_{ij}}$ described in Eq.(5.4). The error in the estimated $\boldsymbol{C_{ij}}$ can degrade the accuracy of the TISIE solution, and the errors in TISIE and the MIR emissivity calculated from the BRDF model using the retrieved three coefficients can be further enlarged by the exponent conversion of Eq.(5.9).

Fig.5-7(b) and (c) are the histograms of the residual error for the directional effective temperature ($\boldsymbol{T_e}$) (see Eq.(5.13)) calculated from the inversion of the radiative transfer equation using the retrieved TIR emissivity with true DBT and downward atmospheric radiance, and with noised DBT and downward atmospheric radiance, respectively. Therefore, Fig.5-7(b) can be considered as the temperature residual error only caused by the error of the TIR emissivity, whereas Fig.5-7(c) can be considered as the residual error caused by the error of the TIR emissivity as well as the noise included in the DBT itself and the atmospheric radiance. As observed in Fig.5-7(b), the temperature residual error mainly (96%) fell into a range of [-1.0, 1.0] K, and the maximum percentage of the histogram was close to 0. To investigate the results of Fig.5-7(c), Fig.5-7(d) presents the theoretical temperature error caused by emissivity error (±0.02 at true $\varepsilon = 0.98$) under different temperatures and downward atmospheric radiances and indicates that the temperature error increased with temperature itself but decreased with the downward atmospheric radiance. It is possible for an emissivity error of 0.02 to lead to a temperature error within [-1.0, 1.0] K, especially for low temperatures and/or large downward atmospheric radiance. Therefore, the results shown in Fig.5-5(b) are reasonable. Compared with Fig.5-7(b), the actual range of the temperature residual error in Fig.5-7(c) was relatively larger, and the residual error within [-0.8, 0.5] K is at a similar percent because of the influence of the noise included in the DBT and the atmospheric radiance. However, Fig.5-7 still demonstrates that the bi-directional reflectivity and emissivity can be retrieved within an error lower than 0.015, and the DBT can be obtained with an error within 1.5 K for most cases from multi-angular observations using the angle combination of case (2).

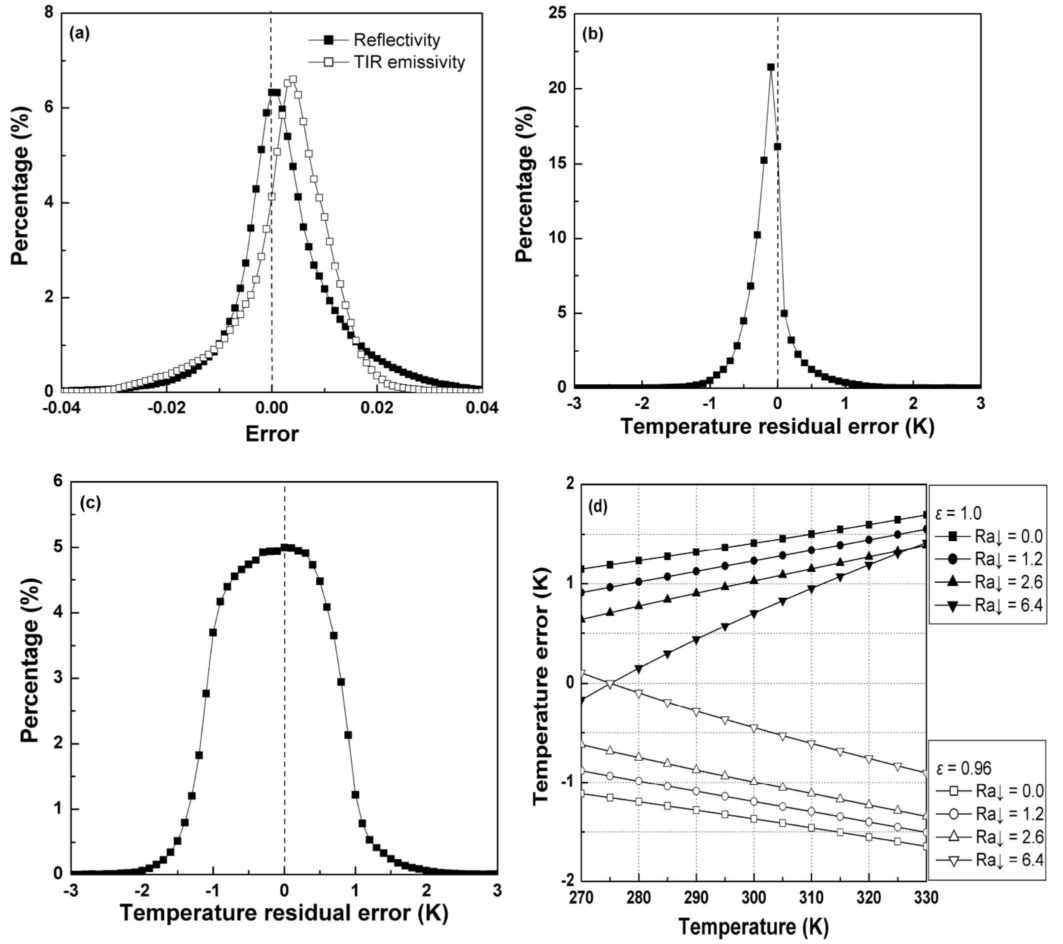

Fig.5-7. (a) The histograms of the retrieval error for the bi-directional reflectivity in MIR channel and emissivity in TIR channel at DBT noise within [-1.0, 1.0] K; (b) Histogram of the residual error of directional effective temperature ($\boldsymbol{T_e}$) calculated from the retrieved TIR emissivity, and the directional radiance and atmospheric data without noise; (c) Histogram of the residual error of $\boldsymbol{T_e}$ calculated from the retrieved TIR emissivity, and the directional radiance and atmospheric data with noise. (d) The theoretical temperature error caused by emissivity error (±0.02 at true $\varepsilon = 0.98$) under different temperatures and downward atmospheric radiances (unit: W/m^2/sr/μm).

The above model analysis concerned on the MIR and TIR channels of the MODIS sensor because this sensor has narrower bandwidth than the WiDAS system and is more representative of most current sensors. However, it is necessary to illustrate the result for the WiDAS system because its MIR and TIR data will be used to validate the D-TISI method. Fig.5-8(a) displays the variation of the RMSE of the TIR emissivity, retrieved from the DBT at noise within [-1.0, 1.0] K and downward atmospheric radiance at noise within [-10%, 10%], with the canopy LAIs and component temperature combinations. The angle case (4) was used because this angle case was designed for the WiDAS system. Compared with Fig.5-3(d) and Fig.5-4(d), the RMSE for the WiDAS system is similar to that of the MODIS, except for the RMSE (up to 0.035) in the lower LAIs of T-group 1 and T-group 2.

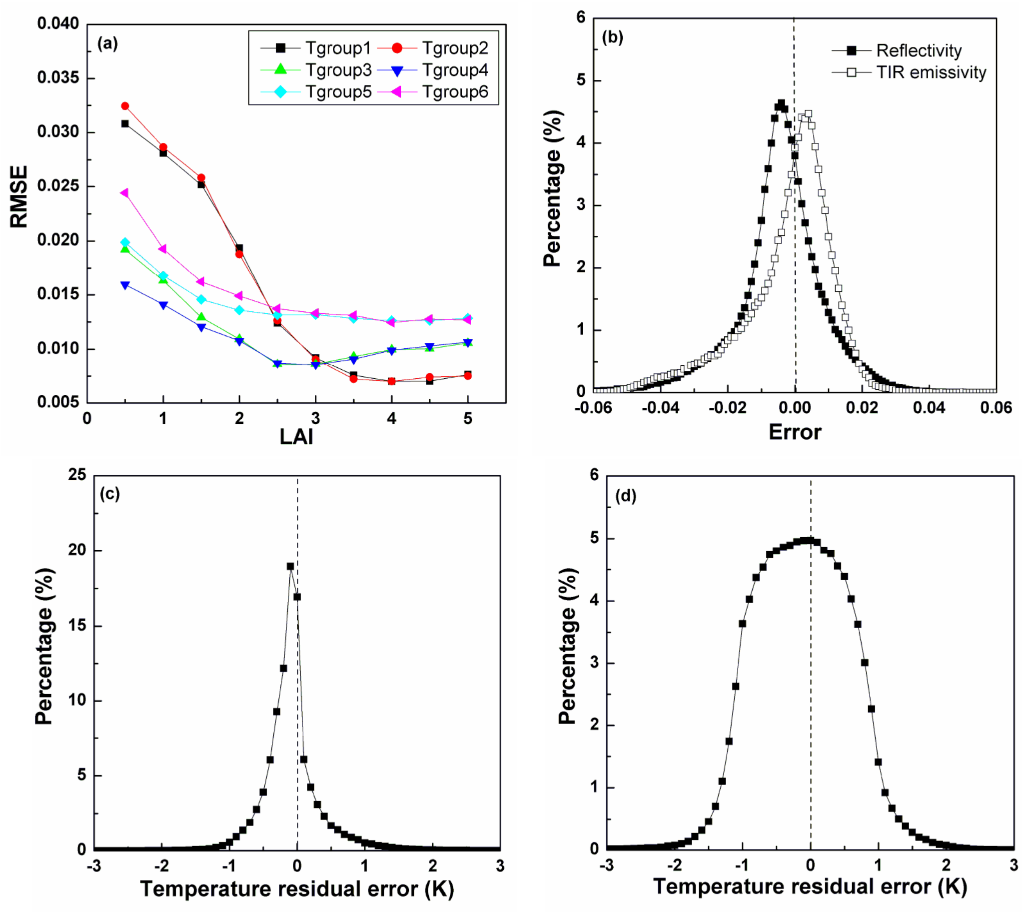

Fig.5-8. (a) RMSE of TIR emissivity at different LAIs and components' temperatures for the WiDAS system. (b) Histograms of the retrieval error for bi-directional reflectivity in MIR channel and emissivity in TIR channel of the WiDAS system. (c) Histogram of the residual error of directional effective temperature ($\boldsymbol{T_e}$) calculated from the retrieved TIR emissivity, and the directional radiance and atmospheric data without noise; (d) Histogram of the residual error of $\boldsymbol{T_e}$ calculated from the retrieved TIR emissivity, and the directional radiance and atmospheric data with noise. Angle case (4) was used for illustration.

Fig.5-8(b) is the corresponding histogram of the residual error of the MIR bi-directional reflectivity and TIR emissivity for the WiDAS system, which indicates that their residual error was distributed widely from -0.06 to 0.06 and that there was a bias of approximately -0.004 and 0.004 for the reflectivity and emissivity, respectively. A comparison between Fig.5-7(a) and Fig.5-8(b) highlights that the retrieval accuracy of the WiDAS system was generally lower than that of the MODIS, most likely due to its broader bandwidths in both the MIR and TIR channels. According to the simulated DBT of the MODIS and WiDAS system using Eqs. (5.11) and (5.12), we observed that the broader bandwidth degraded the retrieved accuracy of the reflectivity and emissivity in two different ways: one, because some response wavelengths of the MIR channel were out of the atmospheric-window of 3 to 5 µm as shown in Fig.5-1, the transmittance of the solar irradiance from space to the surface was reduced and consequently decreased the solar contribution in the MIR channel. As a result, the correlation of the radiative transfer equations between the MIR and TIR channels of the WiDAS system was higher than that of the MODIS at the same atmospheric conditions. Two, the angular variation of the DBT in both the MIR and TIR channels of the WiDAS system was weakened, which caused the retrieved result to be more sensitive to the noise included in the used DBT data. However, as seen from Fig.5-8(b), approximately 80% and 88% of the residual error was respectively within [-0.015, 0.015] and [-0.02, 0.02], which indicates that most of the retrieved error of the MIR reflectivity and TIR emissivity for the WiDAS system was smaller than 0.02 in theory. Fig.5-8(c) and (d) show the histograms of the residual error for the directional effective temperature ($\boldsymbol{T_e}$) calculated from the inversion of the radiative transfer equation using the retrieved TIR emissivity with true DBT and downward atmospheric radiance, and with noised DBT and downward atmospheric radiance, respectively. The results were very similar to the results observed with MODIS, as shown in Fig.5-7(b) and (c).

5.4 Applications to airborne images

An airborne multi-angular images dataset was acquired by the WiDAS system, which was one of the major airborne sensors used in the WATER synthetic field campaign conducted in the spring to summer of 2008 on the Heihe River watershed in west China (Li et al. 2009). The WiDAS system acquired images using four CCD cameras in visible/near-infrared (VNIR) channels and two thermal cameras in the MIR and TIR channels (Fang et al. 2009; Liu et al. 2012). Table 5-5 lists the specification of those cameras. The VNIR image will be used for results analysis.

Table 5-5. Specification of the WiDAS system

	CCD camera	MIR camera	TIR camera
Spectral band	550nm, 650nm,700nm and 750nm(with band width 40nm)	Mainly 3~5 μm	Mainly 8~12 μm
Pixels	1392 ×1040	320×240	
Total view angle	60°	80°	
IFOV	0.8 μrad	4.24 μrad	
Nadir resolution	1.2 m @ 1.5 km	7.9 m @ 1.5 km	
View zenith	Five angels between forward 30° and backward 30°	Seven angles between forward 40° and backward 40°	

5.4.1 Acquirement of multi-angular images

The WiDAS system was designed to observe the surface in the MIR and TIR channels at a total of seven zenith angles: nadir, backward and forward 10°, 20° and 40°(see angle case (4) in Table 5-4).The cameras of the WiDAS system acquired the surface sequential images with a high frequency during the flight (Liu et al. 2012), and the overlap between two sequential images was more than 80% for the VNIR channels and more than 85% in the MIR and TIR channels, which meant that the same ground point can be almost simultaneously observed in several sequential images. After geometric corrections, a multi-angular dataset was obtained from the collections of the same ground point in the sequential WiDAS images.

However, because the time interval between two sequential images was very short (<4 s), the variations of VZA and even VAA were consequently very small, causing the two sequential observations to contain no more angular information about the surface than only one observation did, and the error in the additional observations might influence the final solution of the retrieval. Therefore, we should only use those observations whose VZAs were equal or close to the designed angles. However, because the multi-angular images were obtained from sequential observations at the manner of the central projection, which reduced the angular differences between sequential observations for those pixels far from the central line in the cross-track direction, only the pixels on the central line of the camera along the flight track can be observed with the designed angles. Moreover, for the edge pixels in the cross-track direction, their VZAs were almost the same in all sequential images, and only their VAAs changed. To improve the accuracy of the emissivity and temperature retrieval from those pixels, we had to select a group of angular observations with the maximum VZA or VAA difference from the sequential images with a constraint that the VZA interval between any two angular observations with a similar VAA or the VAA interval between any two observations with a similar VZA must be beyond a threshold value, such as 6° for VZA and 15° for VAA. Therefore, the emissivity and temperature for different pixels were actually retrieved with different combinations of VAA and VZA, rather than the designed combination.

5.4.2 Calibration and atmospheric correction

The recorded temperatures of the MIR and TIR channels were calibrated to blackbody brightness temperatures using a polynomial approximation as expressed in Eq.(5.14):

$$\boldsymbol{BBT} = \boldsymbol{B}_0 + \boldsymbol{B}_1 \cdot \boldsymbol{T}_{\boldsymbol{obs}} + \boldsymbol{B}_2 \cdot \boldsymbol{T}_{\boldsymbol{obs}}^2 , \tag{5.14}$$

where, $\boldsymbol{B_0}$, $\boldsymbol{B_1}$ and $\boldsymbol{B_2}$ are coefficients, regressed from their measurement on a blackbody (Series No. Mikron 340) in the temperature range from 273.16 K to 358.16 K with an interval of 5 K. The value of those coefficients is shown in Table 5-6 (Fang et al. 2009).

Table 5-6. The coefficients from observed temperature of the MIR and TIR channels to blackbody brightness temperature

	$\boldsymbol{B_0}$	$\boldsymbol{B_1}$	$\boldsymbol{B_2}$
MIR	2.87597×10^{-2}	-0.58336	0.00202
TIR	86.19557	0.62729	2.54228×10^{-4}

Radiosounding data were also collected simultaneously to remove atmospheric effects for the VINR images and to simulate the upward and downward atmospheric radiance and solar radiation for both MIR and TIR channels. After atmospheric correction, only surface-leaving radiances (i.e., $\boldsymbol{R_i}$ in Eq.(5.2)) were included in the MIR and TIR data.

5.4.3 Directional emissivity and effective temperature

5.4.3.1 Multi-angular image dataset

The WiDAS image used in this thesis was located in the ZY-YK-HZZ flight zone, which is a typical oasis agricultural area. The main land covers included maize, wheat and vegetable. The WiDAS system acquired data over this area on June 1st, June 29th, and July 7th, 2008. Only the data from July 7th, 2008, were applied because of its clear sky and high quality. Fig.5-9 displays several sequential images of the DBT in the TIR channel and the corresponding VNIR false color image for this area, and those images were acquired at approximately UTC 3:58 (Beijing Time: 11:58, duration < 30 s) on July 7th, 2008. The solar zenith and azimuth angles at that time were approximately 125.7° and 24.4°, respectively. Because the aircraft flew from north-east to south-west at a height of approximately 1.5 km above the surface, the spatial resolutions of the MIR/TIR and the VNIR images were approximately 7.9 m and 1.25 m, respectively. The red pixels of the VNIR image represented the vegetated pixels, and the rest were the non-vegetated pixels, such as bare soil, buildings and man-made road. Four sites composed of 4×4 pixels were chosen for further analysis, and their detailed information can be found in Table 5-7.

Table 5-7. The specification of four sites, and their retrieved BRDF coefficients and TISIE

No.	Land cover	Lon/Lat	f_{geo}	f_{vol}	f_{iso}	TISIE
Site A	Maize	100.411E, 38.857N	0.075	-0.041	0.137	0.978
Site B	Orchard	100.402E, 38.844N	0.052	-0.036	0.134	0.971
Site C	Wheat	100.398E, 38.859N	0.057	-0.038	0.135	0.974
Site D	bare soil	100.398E, 38.847N	0.054	0.027	0.150	0.961

From the TIR images in Fig.5-9, the difference of pixels' DBTs was up to 46 K. Fig.5-10 (filled circles) shows the DBT after atmospheric correction for four sites shown in the VNIR image of Fig.5-8. The changes of VZA (and/or VAA) lead to a temperature variation of approximately 1.0 K, 3.1 K, 2.7 K and 4.4 K for Site A, Site B, Site C, and Site D, respectively. Although the DBT difference of Site A was much smaller than that of other sites, these angular temperature differences were still used for separating emissivity and temperature. Furthermore, the data presented in Fig.5-10 also indicated that the higher DBTs were observed at smaller VZAs, whereas the lower DBTs were obtained at larger VZAs because, for the vegetated canopy, the fractions of soil with higher temperature was generally larger in small VZAs than those in large VZAs. In addition, as reported by some previous studies (Li et al. 2013b; Sobrino and Cuenca 1999), the bare soil emissivity decreased with the increasing VZA, which most likely caused the soil's brightness temperature to decrease with the increasing VZA. However, one should note that because all sites except for Site D were not located near the central line of the flight track, their minimum VZA was not equal to 0° as shown in Fig.5-10.

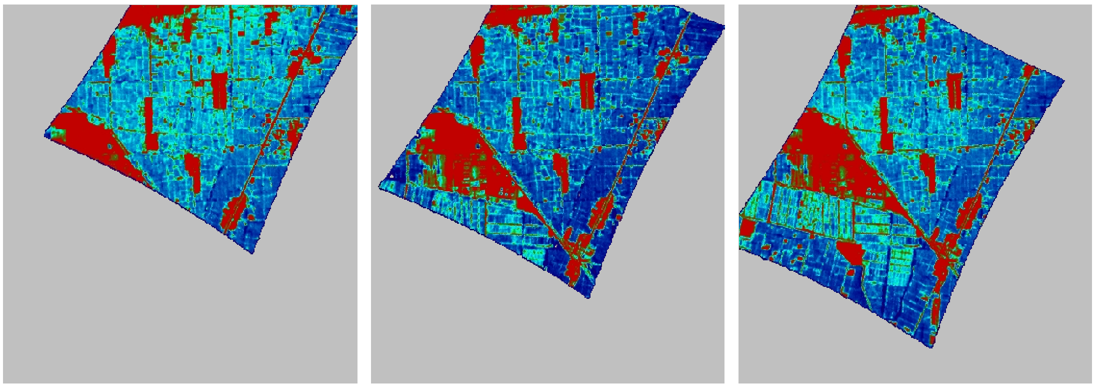

(a) Backward 40° (b) Backward 20° (c) Backward 10°

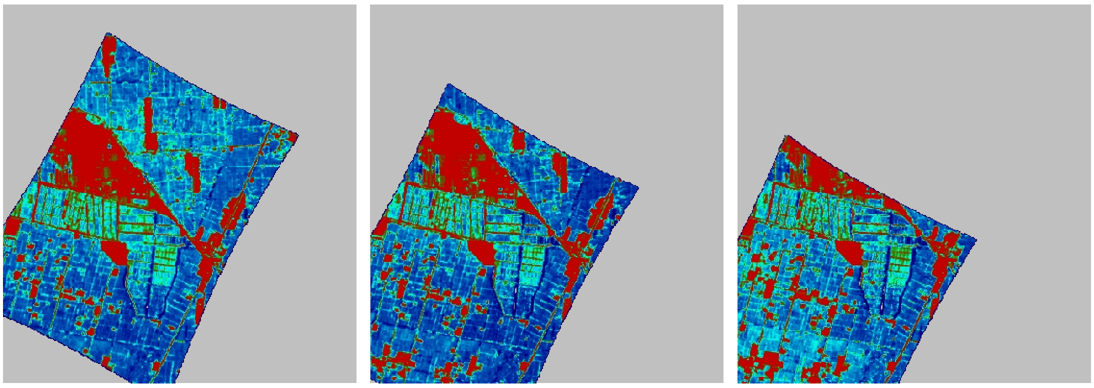

(d) Nadir (e) Forward 10° (f) Forward 20°

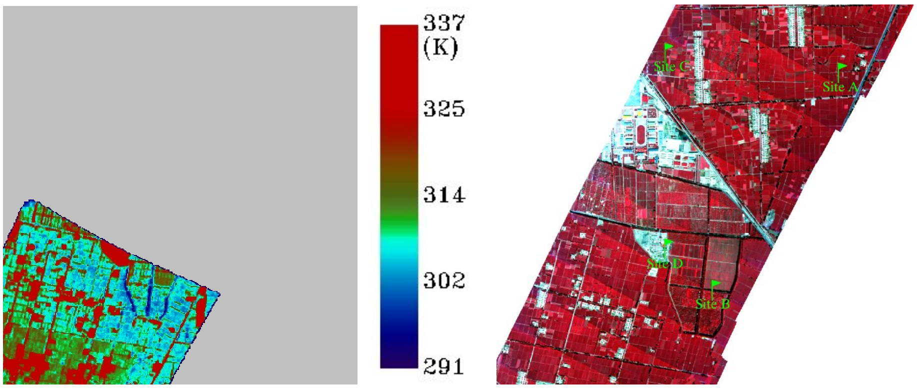

(g) Forward 40° (h) CCD image

Fig.5-9. Multi-angular TIR images and VNIR image over study area

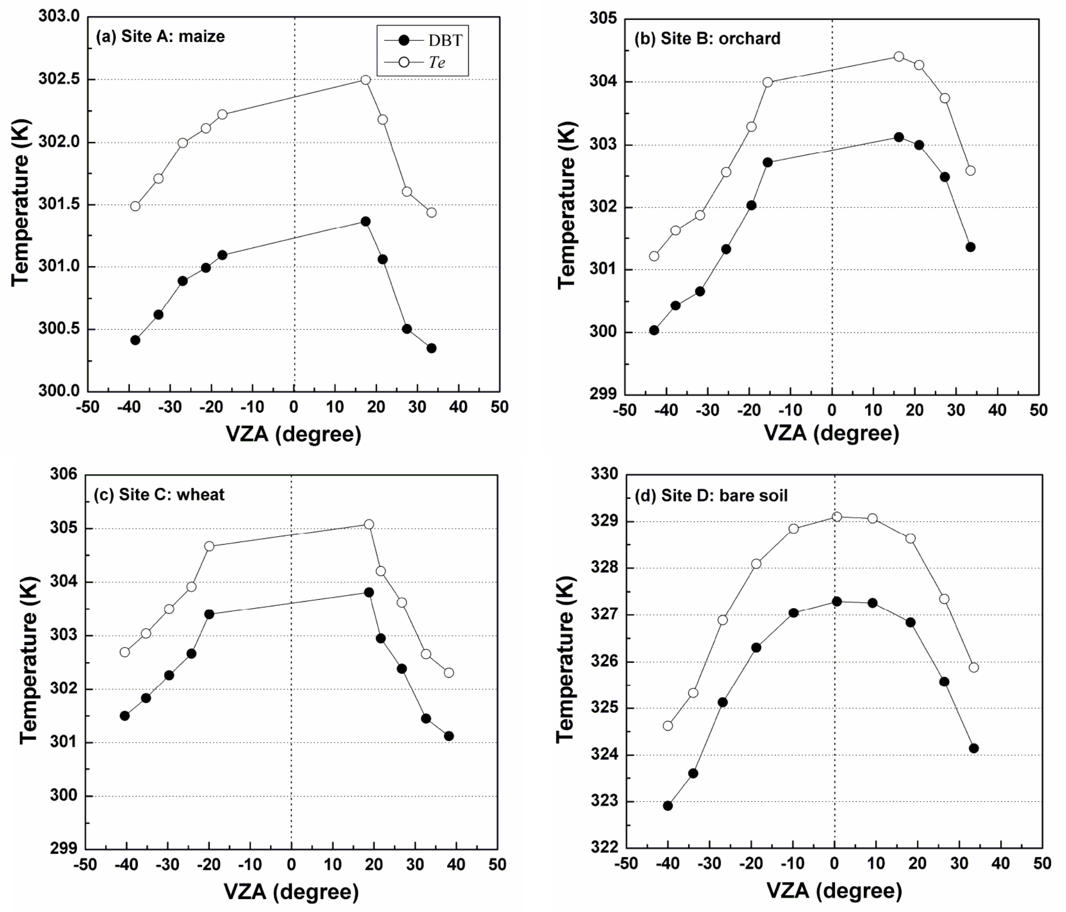

Fig.5-10. The angular variation of the measured directional brightness temperature (DBT, filled circles) after atmospheric correction and the effective temperature (***T_e***, unfilled circles) defined in Eq.(5.12) for four sites. The positive and negative VZAs correspond to nearly opposite VAAs.

5.4.3.2. Retrieval of emissivity and temperature

Fig.5-11 presents the retrieved TISIE and nadir emissivity of the MIR and TIR channels and their histograms. Compared with the area shown in Fig.5-9, the area of Fig.5-11 is smaller because some of the pixels that could not meet the requirement of the angle interval between different VZA and VAA, especially for those pixels near the edge in the cross-track direction, were removed during the retrieval process. As observed in Fig.5-11(a), the TISIE mainly distributed in the range of [0.95, 1.01], similar to the results of (Jiang et al. 2006). According to the VNIR image in Fig.5-9, the TISIE values of vegetated pixels were generally higher than those of bare soil and buildings because the vegetation component in the pixel increased the TISIE values (Li and Becker 1990).

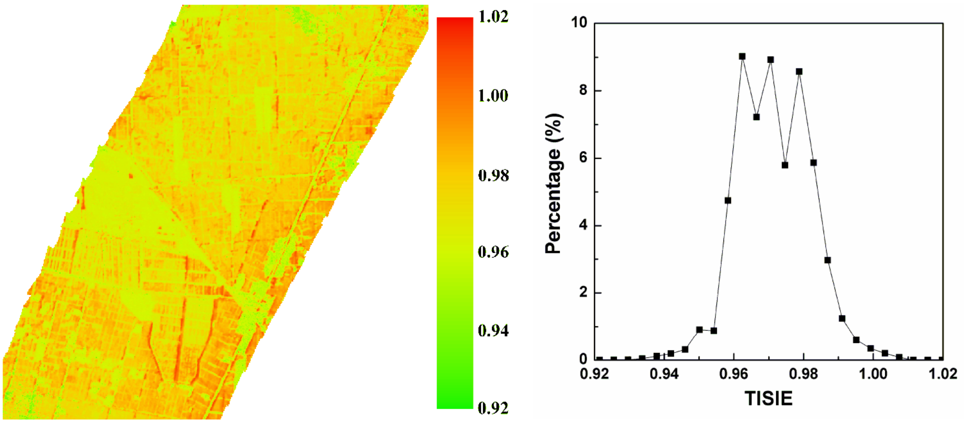

(a) TISIE and its histogram

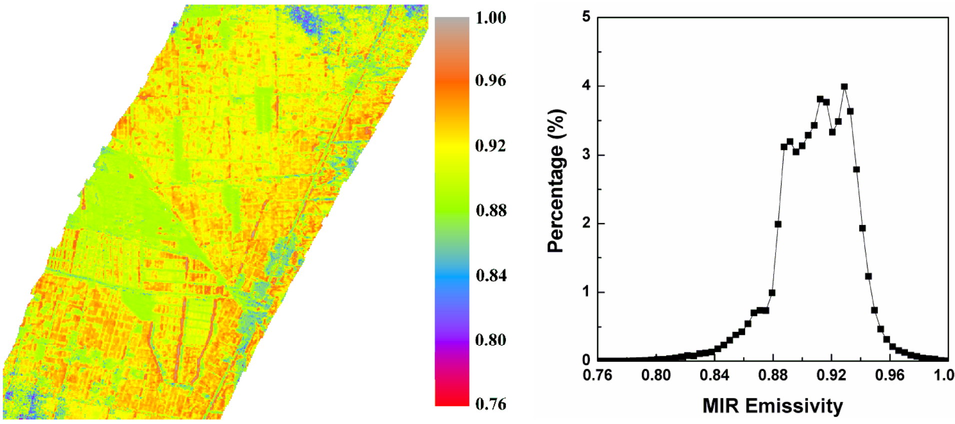

(b) MIR emissivity and its histogram

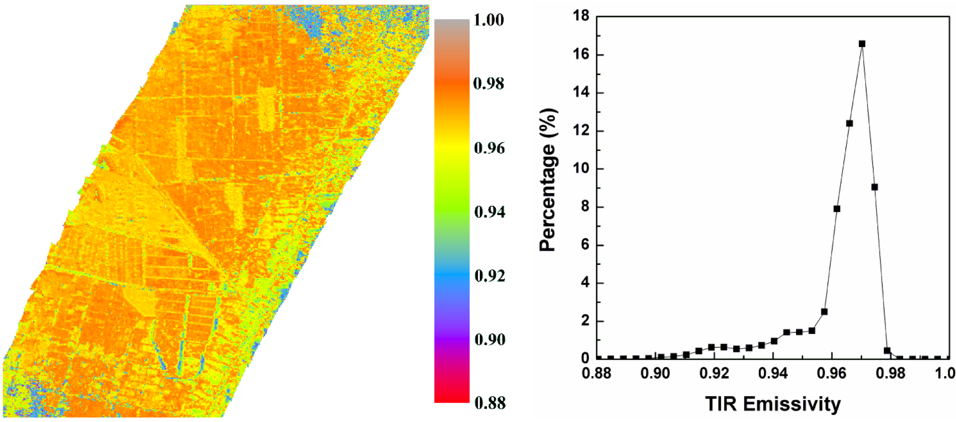

(c) TIR Emissivity and its histogram

Fig.5-11. Retrieved TISIE and nadir emissivities of the MIR and TIR channels

Similar to the TISIE, both the MIR and TIR emissivities of vegetated pixels were higher than those of non-vegetated pixels, as shown in Fig.5-11(b) and (c). However, the emissivity of the MIR channel was generally lower than that of the TIR channel, especially for the non-vegetated pixels, and the MIR emissivity difference between the vegetated and non-vegetated pixels was larger than that of the TIR emissivity. These results might be due to the fact that most soils and man-made materials present a strong spectral emissivity variation in the range of 3 to 6 µm, and the minimum emissivity in this spectral range can be as low as

0.7. Meanwhile, the emissivity of most vegetation in this spectral range was almost flat. In contrast, the spectral emissivity for most land covers is almost flat in the TIR range (e.g., 8 to 14 μm), and their values are usually larger than 0.95. The histogram of Fig.5-11(b) reveals that the retrieved MIR emissivity mainly ranged from 0.88 to 0.94. Compared with the findings of Chapter 3, where the angular emissivities for several types of land covers from MODIS emissivity products were obtained, this emissivity range had the same levels for grass and barren land and only slightly smaller (approximately 0.005) than the latter for cropland. The TIR emissivity shown in the histogram of Fig.5-11(c) is mainly distributed in the range of [0.96, 0.98], which is narrower than the range of the MIR emissivity due to two factors: first, as stated above, both soil and vegetation emissivities in the TIR range were very high, and their differences in such ranges were smaller than that in the MIR range; second, Eq.(5.9) might reduce the range of the TIR emissivity, especially for those pixels with a TISIE larger than 1.0.

The angular variations of the TIR emissivity for the above four sites are presented in Fig.5-12. The solid lines are the emissivity of VZAs within [0°, 90°] that was estimated using the retrieved three coefficients of the BRDF model and TISIE, whereas the squares are the emissivity for those VZAs under which the sites were observed. These results indicate that the directional emissivity for the three vegetated samples increased with VZA, and the emissivity difference between nadir and horizontal (i.e., VZA = 90°) observations was approximately 0.008 in theory. However, this difference turned out to be as small as 0.004 between nadir and VZA = 60° and can almost be ignored for the VZAs varying from nadir to VZA = 40°. The angular variation of the emissivity of bare soil (Site D) was quite different from that of those vegetated samples. First, the emissivity increased with the increasing VZA and then decreased at the larger VZAs. Comparisons of the three BRDF coefficients in Table 5-7 indicate that the positive coefficient $\boldsymbol{f_{vol}}$ produced a different angular pattern for soil emissivity. If the barren pixels were assumed to be isotropic, there would be no difference among the emissivity and brightness temperatures observed at different VZAs, and the BRDF coefficients $\boldsymbol{f_{geo}}$ and $\boldsymbol{f_{vol}}$ should be zero. However, because the DBT of Site D varied significantly with the viewing angle (see Fig.5-10(d)), perhaps due to the roughness and the multiple shadowing effect of itself, the D-TISI method proposed in this thesis finally produced an optimal solution for the three BRDF coefficients and TISIE, which had the minimum residual error of the radiative transfer equation, without considering the types of land cover. Generally, the angular variation of the barren soil can be ignored because the emissivity difference was as small as 0.002. One should note that not all vegetated pixels have the similar angular patterns as shown in Fig.5-12(a)~(c), and not all non-vegetated pixels have similar angular pattern as Fig.5-12(d).

Using the directional emissivity shown in Fig.5-12 and the DBT shown in Fig.5-10 (see filled circles), the directional effective temperatures ($\boldsymbol{T_e}$) defined by Eq.(5.13) were consequently determined by removing the downward atmospheric radiance from the surface-leaving thermal radiance (see Eq.(5.2), where $\boldsymbol{R_{sl\downarrow}}$ and $\boldsymbol{E_{sun}}$ equal 0 for the TIR channel), and presented in Fig.5-10 (see unfilled circles). $\boldsymbol{T_e}$ was generally larger than DBT after removing the reflected downward atmospheric radiance and non-unity effect of the emissivity mainly because the blackbody emission of the surface was larger than that of the atmospheric profile. The average differences between $\boldsymbol{T_e}$ and DBT were approximately 1.1 K, 1.6 K, 1.2 K, and 1.8 K for the four sites, respectively, and Site D (bare soil) had the maximum temperature difference because it had the smallest emissivity, which caused the largest value of the reflected downward atmospheric radiance.

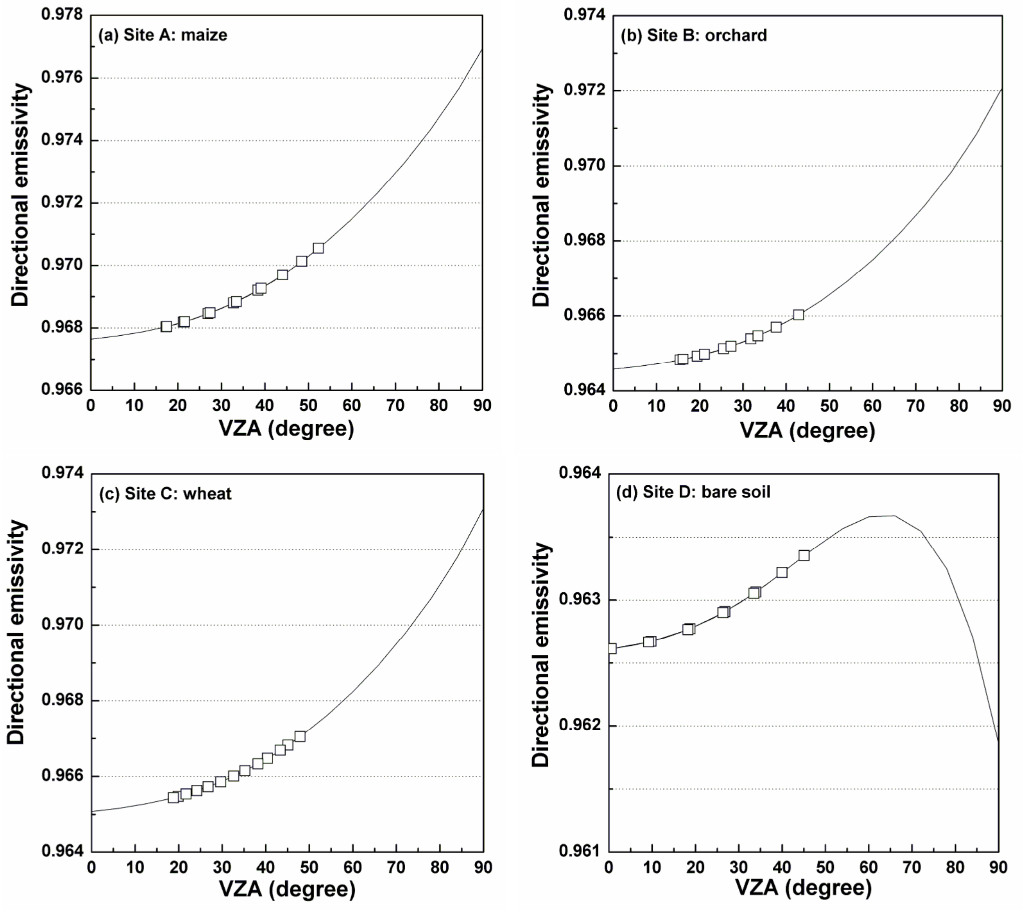

Fig.5-12. Directional TIR emissivities for several cover types. The solid line presents the emissivity in all VZAs calculated from Eq.(5.9) using the retrieved BRDF coefficients and TISIE, while the squares are the emissivity for those VZAs under which the sites were observed.

5.4.3.3. Angular normalization of temperature

As shown in Fig.5-10, the surface directional effective temperature ($\boldsymbol{T_e}$) varied with the VZAs and even with the VAAs because the viewing geometry of sun-target-sensor determined the fractions of different components with different temperatures in the pixel. As a result, this angular effect made the temperature of different pixels in the same image incomparable because they were observed at different directions, which can produce erroneous results. Therefore, it was very crucial to normalize the retrieved effective temperature at various VZAs to a reference VZA (e.g., at nadir).

Unfortunately, no existing study on the angular normalization of temperature has been previously reported. According to the findings in the literature (Peng et al. 2011), we modified the kernel-driven BRDF model addressed in Eq.(5.6) by replacing the bi-directional reflectivity with the directional effective temperature $\boldsymbol{T_e}$ as follows:

$$\boldsymbol{T_e}(\theta_s,\theta_v,\varphi) = \boldsymbol{f}'_{iso} + \boldsymbol{f}'_{vol}\cdot\boldsymbol{k}_{vol}(\theta_s,\theta_v,\varphi) + \boldsymbol{f}'_{geo}\cdot\boldsymbol{k}_{geo}(\theta_s,\theta_v,\varphi)\,. \qquad (5.15)$$

The terms in Eq.(5.15) have similar meanings to the discussions in previous sections. To fit the three coefficients $\boldsymbol{f'_{iso}}$, $\boldsymbol{f'_{vol}}$ and $\boldsymbol{f'_{geo}}$, at least three $\boldsymbol{T_e}$ values are required. As stated previously, four or more angular observations are needed to solve the four unknowns included in Eq.(5.7), and the retrieval process finally generates a $\boldsymbol{T_e}$ for each direction, whose number is equal to that of the observations and larger than three. Therefore, the three coefficients in Eq.(5.15) can be fitted in theory as long as the four unknowns in Eq.(5.7) are mathematically solvable. From this point of view, we first used the retrieved directional emissivity in the TIR channel to calculate $\boldsymbol{T_e}$ of different directions and then fit the three coefficients $\boldsymbol{f'_{iso}}$, $\boldsymbol{f'_{vol}}$ and $\boldsymbol{f'_{geo}}$ and finally extracted the nadir ***T_e-nadir*** from Eq.(5.15). Fig.5-13(a) shows the ***T_e-nadir*** of the study area.

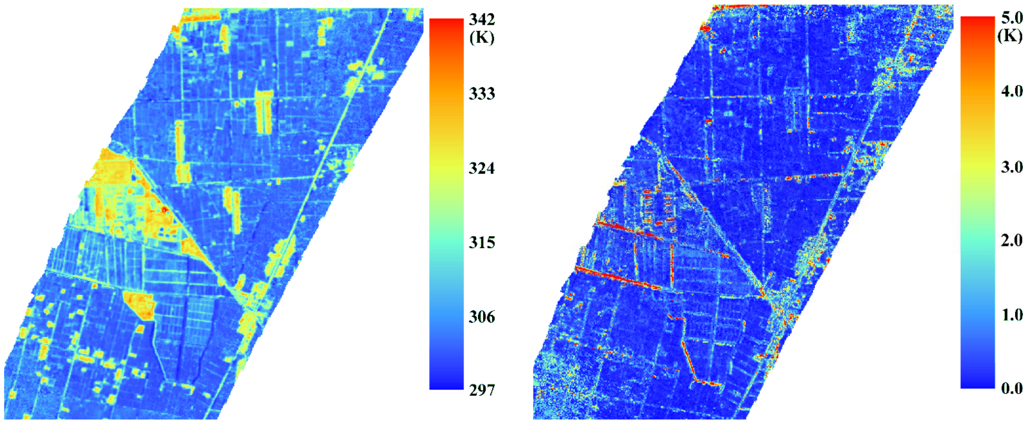

(a) $\boldsymbol{T_e}$-nadir (b) RMSE of BRDF model

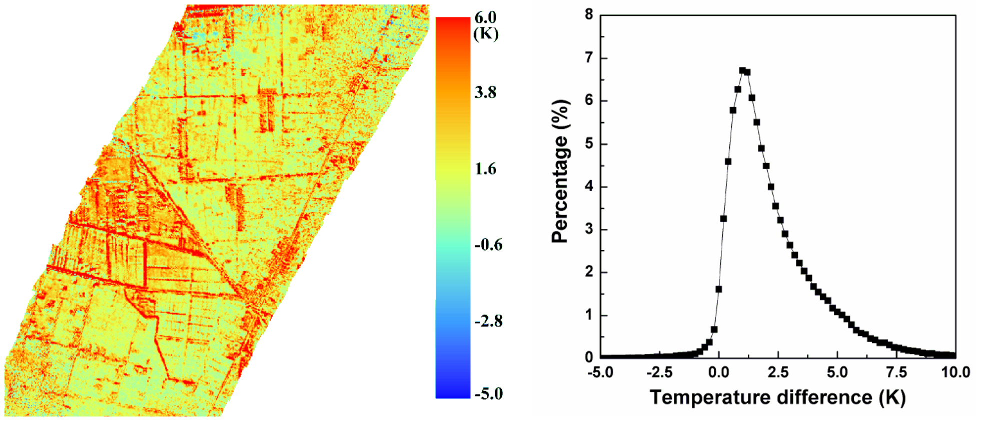

(c) Temperature difference (d) histogram of temperature difference

Fig.5-13. (a) the nadir effective temperature from BRDF model ($\boldsymbol{T_e}$-nadir); (b) the RMSE of the BRDF model for the directional effective temperature; (c) the difference between the nadir effective temperature and the minimum effective temperature of observations. The color scalar was restricted to 6 K and those pixels with a larger value were forced to 6 K for illustration; (d) the histogram of (c).

In addition, to investigate the performance of the BRDF model, the temperature RMSE of this model was also obtained using Eq.(5.16) and displayed in Fig.5-13(b):

$$\boldsymbol{RMSE} = \sqrt{\sum_{\boldsymbol{k}=1}^{\boldsymbol{N}} [\boldsymbol{T_e}(\boldsymbol{k}) - \boldsymbol{T_e}(\boldsymbol{k})']^2 \Big/ \boldsymbol{N}}, \boldsymbol{N} \geq 4, \tag{5.16}$$

where, $\boldsymbol{N}$ is the number of angular observations on the same target, and $\boldsymbol{T_e}(\boldsymbol{k})$ is the $\boldsymbol{k}$th directional effective temperature retrieved from the $\boldsymbol{k}$th observation (see Eq.(5.13)), whereas $\boldsymbol{T_e}(\boldsymbol{k})$’ is the fitted $\boldsymbol{k}$th directional effective temperature from the BRDF model (see Eq.(5.15)).

As seen from Fig.5-13(b), it is determined that the BRDF model produces an error smaller than 1.0 K for most pixels, especially the vegetated pixels. In contrast, this model produced significant error (even larger than 3 K) for some non-vegetated pixels, especially for those non-vegetated pixels near the edge of the image, perhaps because the angle intervals of different observations over those pixels were relatively smaller than the others, which caused the BRDF model to be more sensitive to the error included in the input $\boldsymbol{T_e}$ and viewing angles. However, the BRDF model performed generally well for most pixels in the angular normalization of their directional effective temperature.

Fig.5-13(c) presents the temperature difference between the nadir effective temperature $\boldsymbol{T_e}$***-nadir*** and the minimum value of the effective temperature under different viewing directions, and Fig.5-13(d) is the corresponding histogram of Fig.5-13(c) at a step of 0.2 K. To make the data in Fig.5-13(c) more distinguishable, the color scalar of the figure was restricted to 6 K, and those pixels with a larger value were forced to 6 K for illustration purposes. Both Fig.5-13(c) and (d) indicate that $\boldsymbol{T_e}$***-nadir*** was larger than the minimum temperatures for most pixels (approximately 98%), and their differences mainly fell into the range of [0.0, 5.0] K. Because the temperature difference for most vegetated pixels was in the range of [0.5, 2.0] K, the angular normalization of temperature appeared unnecessary for those pixels if the accuracy of the retrieved temperature is not required to be better than that range. The temperature difference of the non-vegetated pixels was generally larger than that of the vegetated pixels and even exceeded 6.0 K for some cases. Although the BRDF model might cause remarkable temperature error for the non-vegetated pixels as stated above, the results for some pixels (e.g., the barren pixels near Site D in Fig.5-9, with which the BRDF model displayed high accuracy, still illustrated that its angular normalization was strongly required for their temperatures because the temperature difference of those pixels was up to several Kelvin and far from the maximum tolerance of the temperature retrieval accuracy.

5.4.3.4. Cross comparison with ASTER emissivity

Unfortunately, there was no ground-measured emissivity and temperature data available for the validation of the above results. Cross-comparison with satellite data (such as ASTER) was consequently conducted. ASTER generates surface emissivity products in five TIR channels that are retrieved using the TES algorithm (Gillespie et al. 1998). Because of its relatively finer resolution (approximately 90 m), the ASTER emissivity data provide us an opportunity to make cross-comparisons with the WiDAS TIR emissivity data. To remove the influence of the spectral differences between the ASTER and WiDAS TIR channels, we established an empirical relationship for the emissivities of the five ASTER channels with that of the WiDAS channels using the method described in (Ogawa and Schmugge 2004), which can be expressed as the following:

$$\bar{\varepsilon} = 0.129 \cdot \varepsilon_1 - 0.010 \cdot \varepsilon_2 + 0.193 \cdot \varepsilon_3 + 0.628 \cdot \varepsilon_4 + 0.060 \cdot \varepsilon_5 , \tag{5.17}$$

where, $\varepsilon_{\boldsymbol{k}}$ ($\boldsymbol{k}$ = 1, 2…5) is the ***k***th channel's ASTER emissivity. The ASTER sensor observed the study area on June 29, 2008. However, there were only 65 clear-sky pixels that had valid emissivity due to the occurrence of clouds. Fig.5-14 (a) shows the comparison of the average WiDAS TIR emissivity aggregated from 7.9 m to 90 m and the calculated ASTER emissivity $\bar{\varepsilon}$ from Eq.(5.17). The comparison indicates that the WiDAS emissivity was, in total, higher than the transferred ASTER emissivity $\bar{\varepsilon}$, with an RMSE of approximately 0.012. In addition, the WiDAS emissivity and that of ASTER channel 5 (10.8 to 11.8 µm) were relatively closer to each other, as shown in Fig.5-14(b), but still with an RMSE of approximately 0.007. The difference between the ASTER and WiDAS emissivities might be caused by the intrinsic difference of their algorithms, the temporal variation of the emissivity itself from June 29 to July 7, 2008, as well as the spatial scale effect of the two products. However, as reported by some previous studies, the TES algorithm suffers from spectral emissivity contrast with dense vegetation surfaces (Yoriko et al. 2003) and consequently introduces more uncertainty into the retrieved emissivity of those surfaces. According to the results of (Wang and Liang 2009), who found that the ASTER emissivity was 0.01 to 0.02 smaller than the MODIS emissivity retrieved using the day/night algorithm (Wan and Li 1997), and the results reported in Fig.5-14(a), the WiDAS TIR emissivity might be closer to the MODIS emissivity. However, it is almost impossible to perform cross-comparison with the MODIS data because of the coarser resolution (approximately 6 km in Collection 5).

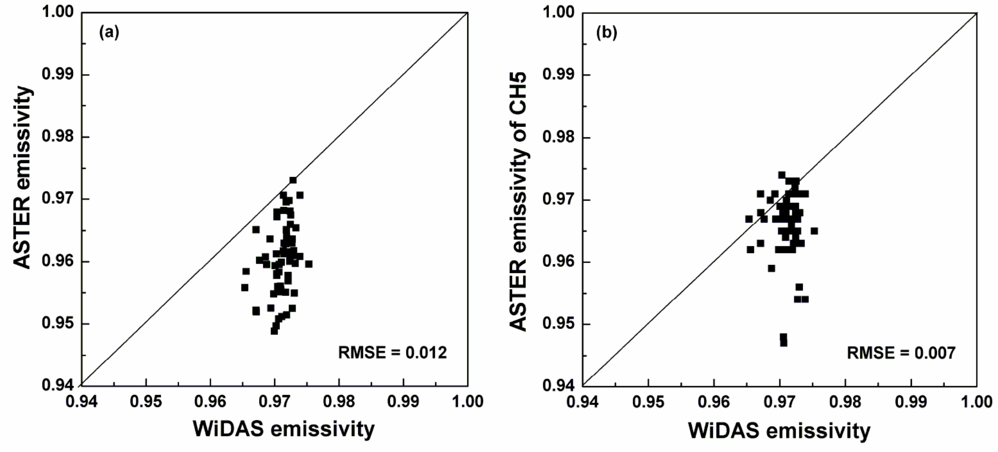

Fig.5-14. Comparison with ASTER emissivity. (a) Transferred ASTER emissivity from Eq.(5.17); (b) the emissivity of ASTER channel 5.

5.5 Conclusions and discussions

This chapter proposed a daytime TISI method (D-TISI) to retrieve directional emissivity and effective temperature from daytime multi-angular observed images in both MIR and TIR channels by combining the kernel-driven BRDF model and the TISI method. In contrast to most previous studies, the non-isothermal surface/canopy was a concern. For model analysis, the canopy's bi-directional reflectivity and emissivity in the MIR and TIR channels were simulated using the SAILH model, and the canopy's directional brightness temperature and radiance were simulated as the weight average of component temperatures and their fractions calculated from a parameterization of the SAILH model by (Li et al. 2010). Two groups of MIR and TIR channels were used for illustration, and they were respectively from the MODIS that had narrow bandwidths, which are more representative of current most sensors, and the airborne WiDAS system that, in contrast, had much boarder bandwidths and whose data were used for validating the D-TISI method. Four groups of angular combinations were designed to investigate the influence of the angular observations on the retrieval accuracy. Generally, large angle intervals among the angular observations and a larger VZA with respect to nadir direction can improve the retrieval accuracy of emissivity and temperature because those angle conditions result in significant variation of component fractions and the DBT under different viewing direction. The influences of canopy LAI, component temperatures and TISIE on the retrieval accuracy were also discussed. The results generally indicated that for DBT noise within [-1.0, 1.0] K and atmospheric data noise within [-10%, 10%], the D-TISI method can obtain emissivity and temperature with an accuracy within 0.015 and 1.5 K for the MODIS channels and within 0.02 and 1.5 K for the WiDAS channels, respectively.

We applied the D-TISI method to retrieve directional emissivity and effective temperature from the multi-angular MIR and TIR images acquired by the airborne WiDAS system at the Heihe River watershed. The results indicated that the vegetated pixels had larger TISIE values and emissivity than the non-vegetated pixels. The retrieved angular variation of the directional emissivity for the vegetated sites from nadir to the horizontal direction was approximately 0.01, larger than that of the bare soil site. Comparison with the ASTER emissivity product at the study area showed that the difference of the retrieved nadir emissivity and the ASTER emissivity was approximately 0.012. Furthermore, we used the kernel-driven BRDF model by replacing the bi-directional reflectivity in the original model with the retrieved directional effective temperature ($\boldsymbol{T_e}$) to normalize $\boldsymbol{T_e}$ from the off-nadir direction to the nadir. The results indicate that the temperature difference between the normalized nadir effective temperature ($\boldsymbol{T_e}$-nadir) and the minimum $\boldsymbol{T_e}$ of the observing directions was 0.5~2.0 K for most vegetated pixels and always several Kelvin for most non-vegetated pixels. Therefore, it is necessary to perform angular normalization on land surface temperature measurements for higher accuracy. However, the retrieved nadir and off-nadir effective temperatures were not validated in this thesis due to the lack of field data.

Note that the land surface temperature also displays temporal variation, except for angular variation, due to the fluctuations of the local meteorological and solar conditions, and this temporal variation is sometimes more significant than the angular variation. However, this thesis ignored this temporal variation and considered the temperature variation fully caused by the changes of viewing angles because, up to now, there has been no operational method developed to allow time normalization of measured DBT data from multi-angular observations and also because the time interval between the two sequential images examined in this thesis was very short (< 4 s). However, we should keep in mind that the lack of consideration of the temporal variation must have degraded the retrieval accuracy. In addition, different VZAs corresponded to ground pixels with different areas, which might cause the pixels observed on the same place to include different components, especially for the heterogeneous surfaces. This problem, along with the mis-registration between different images, might have led to more uncertainty in the retrieval results. Moreover, although we discussed the influence of the angular combination on the retrieval accuracy only from 4 groups of angles (see Table 5-4) and chose angle case (2) as the local optimum combination among those groups, the conclusions based on those angle cases are limited and additional investigation is required in the future to determine the global optimum combination in the upper hemisphere.

In addition, the results of the model analysis in Section 5.3.6 were only suitable for the pixels in the central line of the images along the flight track because the angular combination for those pixels far from this central line in the central projection image or linear-array detecting system was actually different from the designed angular combination and their angle intervals were consequently significantly reduced. As a result, the retrieval accuracy gradually decreased, in theory, for the pixels moving from the central line to the edge. A sensor with the conical scanning method, such as the AMSR-E (Advanced Microwave Scanning Radiometer for EOS, http://aqua.nasa.gov/about/instrument_amsr.php), is expected in the future to ensure that all pixels have the same angular combinations.

Chapter 6

Impact of sensor footprint on the measurement of the directional brightness temperature of the row crop canopies

This chapter focuses on the modeling of directional brightness temperature for row canopy by considering the ground-based sensor’s footprint. A sensor’s footprint determines the target that is observed by the sensor, and influences the angular features of the target’s directional brightness temperature (DBT) at the field site. This thesis describes a new radiative transfer model (FovMod) to simulate the DBT of the row crop canopy by considering the sensor’s footprint in the ground measurements. The FovMod firstly divides the sensor’s circular or elliptical footprint into a few small cells, and then estimates the components’ fractions (e.g., leaves, sunlit soil and shaded soil) in each cell based on the gap probability theory. The canopy’s DBT is finally obtained by weighting the components’ brightness temperatures and their fractions using a Gaussian point spreading function (PSF) of the sensor’s response. Simulation results indicate that a small footprint causes the distribution of the DBT to be strongly dominated by the row direction and a single component’s temperature but little influenced by the solar position. On the contrary, a large footprint smoothes the row-space effect and causes the DBT to distribute as a uniform, continuous canopy. Comparison with a previous parallel model shows that if the diameter of the sensor’s circular footprint extends to 1.5~2.0 times as large as the total width of the row crop canopy, the footprint effect is minimized, and the ground measured DBT can, theoretically, be used to evaluate the parallel model with negligible error. Finally, validations with a maize canopy demonstrated that the new model performed more accurately than the parallel model to simulate the DBT. Moreover, the FovMod also provides an opportunity to assess the measurement uncertainty caused by some unexpected changes in the sensor’s footprint.

6.1 Background

The angular variation in the LST has been measured at ground and satellite levels and has attracted much attention in recent decades (Kimes and Kirchener 1983; Lagouarde et al. 2004; Otterman et al. 1995; Sobrino and Caselles 1990). Previous studies indicate that the angular variation in LST depends strongly on the distribution of the components’ temperatures and emissivities, the geometric structure of the target surface, and the geometry of the locations of the sun, target, and sensor(Jackson et al. 1979; Kimes et al. 1980; Otterman et al. 1999). To investigate the angular effect of LST and to extend the benefits of remotely sensed data in the calculation of LST, many algorithms have been proposed to make angular corrections to LST or to extract the components’ temperatures from multi-angular or multi-channel remotely sensed data (François et al. 1997; Kimes 1983; Li et al. 2001; Liu et al. 2012; Menenti et al. 2001; Otterman et al. 1992; Prata 1993; Song and Zhao 2007; Xu et al. 2001; Zhan et al. 2011).

Modeling the directional brightness temperature (DBT) of homogenous or heterogeneous canopies is a promising approach to enhance our understanding of the angular feature, and this issue has prompted numerous thermal radiative models that can generally be divided into four categories: geometrical optical (GO) models, radiative transfer (RT) models, hybrid models (GORT), and computer/numerical simulation methods. A GO model estimates the thermal radiance by combining the weights of the proportions and thermal radiance from several components. Several studies (Kimes 1983; Kimes and Kirchener 1983; Kimes et al. 1981) have geometrically calculated the optical path length of radiation passing through row crops by treating the row structure as a rectangular cross section for the first time and using the gap probability to calculate the components’ fractions from those optical lengths. Inspired by this concept, several similar models have been developed by considering the bi-directional gap, hotspot effect or crop growth stages (Chen et al. 2002; Du et al. 2007; Huang et al. 2010; Yan et al. 2001; Yan et al. 2003; Yu et al. 2004). In addition to these three types of models, Guillevic et al.(2003) proposed a three-dimensional radiative transfer model that was based on the Discrete Anisotropic Radiative Transfer (DART) model (Gastellu-Etchegorry et al. 1996) to investigate the angular thermal radiance of a vegetated canopy, and Chen et al. (2004) used a Monte Carlo technique to study the angular characteristics of emitted radiance from heterogeneous and nonisothermal surfaces.

DBT modeling of the row canopy, which mainly means the row crop canopy (such as maize and wheat) in this thesis, is generally more difficult than that of the homogeneous canopy because of the row-space effect which causes the varying foliage area volume density (FAVD) and optical length from place to place. A crucial assumption in the current models is that the row canopy has an infinite extension; therefore, the models treat the components’ fractions using a whole row structure. This assumption is reasonable, but the assumption that the viewing direction is a parallel beam is rarely consistent with reality because different regions within the footprint of the sensor’s FOV (field of view) that is used to collect field DBT data have different azimuth and zenith viewing angles rather than one unique angle. Except for Colaizz et al. (2010), who modeled row structure as continuous ellipses and estimated the sunlit and shaded components within the circular or elliptical footprint, there have been no other studies that have considered the footprint effect (i.e., the FOV effect) on a row canopy’s DBT until now, let alone any discussion of the DBT difference between a parallel-beam model and a FOV model that accounts for variations in the viewing angle within the footprint. Consequently, the question is raised: how large the sensor’s footprint should be in order to collect representative DBTs from a row canopy during the field validation of a parallel model with the lowest error? Thus, the objective of this thesis is to develop a new GORT hybrid model that accounts for a sensor’s footprint effect in the DBT of a row canopy and to identify the threshold footprint under which the footprint effect can be ignored and the field measured DBT data can be used to evaluate a parallel model without causing significant error. The modeling results from this chapter are also expected to provide an operational method for assessing the uncertainty in field measurements that is caused by variations of the sensor's footprint.

6.2 Modeling directional brightness temperature

Most DBT models focus on the anisotropy of thermal radiance and are dependent on the components' temperatures and fractions within the footprint. The footprint of a row canopy generally consists of four types of components: sunlit soil and shaded soil, sunlit leaves and shaded leaves. Because stems occupy a small percentage of the footprint, this component can be ignored without causing significant differences. Several authors have reported that the temperature difference between sunlit and shaded leaves is very small compared to the temperature difference between the sunlit and shaded soils (Rasmussen et al. 2011; Yu et al. 2004); the leaves are often assumed to have a unique temperature in the canopy.

The canopy's DBT is often measured by rotating a goniometer around the target of interest in the upper hemisphere. As illustrated in Fig.6-1 (a), the footprint observed by a sensor with a FOV (θ_f) onboard the goniometer is a circle or an ellipse on the top and bottom of the canopy (TOC and BOC). The points A and A', and B and B' are the left and right intersections of the FOV with the BOC and TOC, respectively; C and C' are the centers of the ellipse on the BOC and TOC; and D and D' are the intersections of the central line of the sensor's FOV with the BOC and TOC. In the nadir direction, C and D (or C' and D') are the same locations. If we assume that the width of the vegetated hedgerow and soil ($\boldsymbol{w_c}$ and $\boldsymbol{w_s}$), canopy height ($\boldsymbol{h}$), and the current observation height ($\boldsymbol{H}$) in the viewing direction θ_v are measurable and known as a prior, the semi-major axes of the ellipses on the BOC and TOC can be calculated using Eq.(6.1):

$$\boldsymbol{a_B} = 0.5\boldsymbol{H} \cdot [\tan(\theta_v + 0.5\theta_f) - \tan(\theta_v - 0.5\theta_f)],$$

$$\boldsymbol{a_T} = 0.5(\boldsymbol{H} - \boldsymbol{h}) \cdot [\tan(\theta_v + 0.5\theta_f) - \tan(\theta_v - 0.5\theta_f)]. \tag{6.1}$$

Similarly, the corresponding semi-minor axes on the BOC and TOC are described by Eq.(6.2):

$$\boldsymbol{b_B} = \sqrt{(\boldsymbol{H} \cdot \tan(\theta_v - 0.5\theta_f) + \boldsymbol{a_B})^2 + \boldsymbol{H}^2} \cdot \tan(0.5\theta_f),$$

$$\boldsymbol{b_T} = \sqrt{[(\boldsymbol{H} - \boldsymbol{h}) \cdot \tan(\theta_v - 0.5\theta_f) + \boldsymbol{a_T}]^2 + (\boldsymbol{H} - \boldsymbol{h})^2} \cdot \tan(0.5\theta_f). \tag{6.2}$$

Furthermore, the lengths of C'O' and D'O' are calculated, respectively, with Eq.(6.3):

$$\boldsymbol{l_{C'O'}} = (\boldsymbol{H} - \boldsymbol{h}) \cdot \tan(\theta_v + 0.5\theta_f) - \boldsymbol{a_T} \quad \text{and} \quad \boldsymbol{l_{D'O'}} = (\boldsymbol{H} - \boldsymbol{h}) \cdot \tan(\theta_v). \tag{6.3}$$

However, because of the canopy's three dimensional structure as shown in Fig.6-1, the surface of the target can be regarded as being located on the TOC or BOC. If the surface of the target is on the TOC, the length of SD' is fixed, and the point D' is unchanged on the TOC, but the point D changes with both the viewing zenith angle (VZA) and the viewing azimuth angle (VAA). However, if the surface of the target is on the BOC, the length of SD is fixed, and the location of point D is unchanged on the BOC, but point D' on the TOC varies with the viewing angles. For clarity, this thesis only uses the former case for illustrations. Another key parameter is the central position $\boldsymbol{x_c}$, which is defined as the distance from the edge of a hedgerow to the central point of the sensor's FOV (i.e., the foot point of the FOV's center) on the TOC when the goniometer observes at the nadir, as shown in Fig.6-1(b). This parameter is used to determine whether a point of the footprint is above the vegetated hedgerow or above the soil, which will be discussed in the next section. $\boldsymbol{x_c}$ is positive when this point is above the hedgerow; otherwise, $\boldsymbol{x_c}$ is negative when this point is above the soil. Because the angular observations are made around the sensor's central point on the TOC, the $\boldsymbol{x_c}$ is always the same.

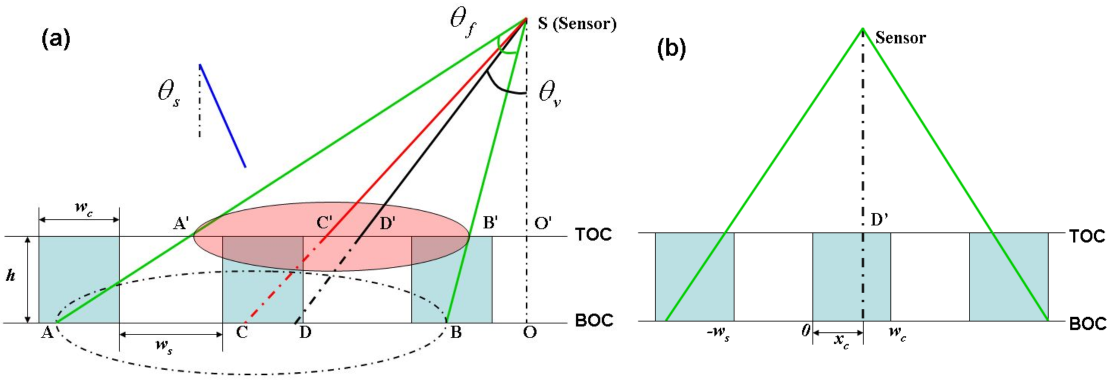

Fig.6-1. (a): the geometry of the sensor and the row canopy. $\boldsymbol{w_c}$ and $\boldsymbol{w_s}$ are the width of the hedgerow and the background soil; $\boldsymbol{h}$ is the height of the canopy. The current observation height $\boldsymbol{H}$ is equal to the length of SO. TOC and BOC relate to the top and the bottom of canopy. θ_f is the sensor's FOV angle, and θ_v is the viewing zenith angle of the goniometer while θ_s is the solar zenith angle. C' and C are the center of the ellipse footprint on the TOC and BOC, respectively; D' and D are the central positions of the sensor's footprint on the TOC and BOC, respectively.
(b): the definition of the relatively central position $\boldsymbol{x_c}$ of the sensor's footprint at nadir observation.

The parallel model often obtains the components' fractions in a row structure by using the geometry of the sun, target, and sensor as well as gap probability theory, with known optical lengths through the canopy in both the solar and viewing directions. This approach is possible because it treats the VZA and VAA as unique values everywhere. However, in reality, the FOV of a sensor during ground measurements causes different locations within the footprint to have different VZAs and VAAs. As a result, the method for calculating the components' fractions in the parallel model should be no longer theoretically effective, and a new model is therefore needed to account for the footprint effect on the row canopy. Inspired by the structure of the DART model (Gastellu-Etchegorry et al. 1996; Guillevic et al. 2003), we followed five steps to develop our new model:

STEP 1: Similar to previous studies (Kimes et al. 1981; Yan et al. 2003; Yu et al. 2004), the row canopy is assumed to be rectangular. The elliptical footprint on the TOC (see Fig.6-1(a)) is first divided into several small cells with an area of ΔS_T (see Fig.6-2), and the location of the $\boldsymbol{i}$th cell ($\boldsymbol{x_i}$, $\boldsymbol{y_i}$) in the X-Y coordinate system, which is created by the major and minor axes of the ellipse, is then calculated. Using this location, the actual VZA and VAA ($\theta_{\boldsymbol{vi}}$ and $\varphi_{\boldsymbol{vi}}$) of the cell is obtained from the geometry that links the current cell to the sensor (point S) and its footprint on the TOC (point O'):

$$\theta_{\boldsymbol{vi}} = \arctan[\boldsymbol{d_i}/(\boldsymbol{H}-\boldsymbol{h})] \text{ and } \varphi_{\boldsymbol{vi}} = \varphi_{\boldsymbol{v}} - \arctan(\boldsymbol{k_i}), \tag{6.4}$$

where, $\boldsymbol{d_i}$ is the distance from the $\boldsymbol{i}$th cell to the point O'; $\varphi_{\boldsymbol{v}}$ is the azimuth viewing angle of the goniometer, which is equal to the angle of the vector O'A' going from the north in a clockwise direction; $\boldsymbol{k_i}$ is the slope of the line from the point O' to the center of the $\boldsymbol{i}$th cell. If the slope $\boldsymbol{k_i}$ does not exist, $\varphi_{\boldsymbol{vi}}$ is equal to $\varphi_{\boldsymbol{v}} \pm 90°$. Because the area of each cell is small enough, it is reasonable to use only one value for the VZA and VAA for the entire cell.

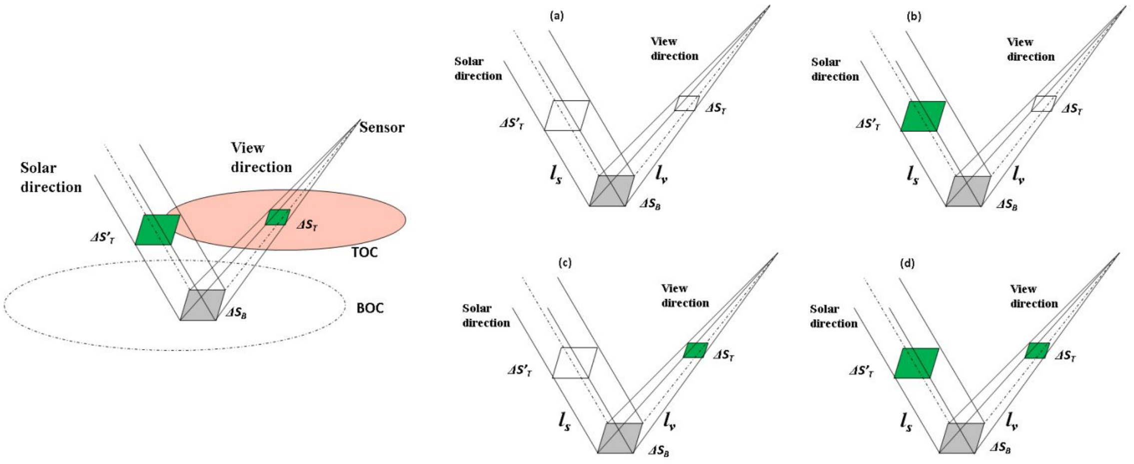

Fig.6-2. Segmentation of sensor’s footprint. Four cases resulting from the combination of the path lengths in the viewing and directions ($\boldsymbol{l_v}$ and $\boldsymbol{l_s}$). (a) $\boldsymbol{l_v} = 0$ and $\boldsymbol{l_s} = 0$: only sunlit soil; (b) $\boldsymbol{l_v} = 0$ and $\boldsymbol{l_s} > 0$: sunlit soil and shaded soils; (c) $\boldsymbol{l_v} > 0$ and $\boldsymbol{l_s} = 0$: the leaves and the sunlit soil; (d) $\boldsymbol{l_v} > 0$ and $\boldsymbol{l_s} > 0$: leaves, sunlit and shaded soils.

STEP 2: With known VZA and VAA ($\theta_{\boldsymbol{vi}}$ and $\varphi_{\boldsymbol{vi}}$) of the $\boldsymbol{i}$th cell ΔS_T, the corresponding cell ΔS_B on the BOC can be determined by projecting ΔS_T in the viewing direction. Once the location of ΔS_B is determined, its corresponding cell $\Delta S'_T$ on the TOC in the solar direction is then defined using the same method that is used in the direction from ΔS_T to ΔS_B. Because the viewing beams of ΔS_T come from a point (i.e., the sensor), the area of ΔS_B is somewhat larger than that of ΔS_T, equal to $\Delta S'_T$. In this case, the path lengths through the vegetated hedgerow of both the viewing and solar beams ($\boldsymbol{l_v}$ and $\boldsymbol{l_s}$) are expressed by Eq.(6.5):

$$\boldsymbol{l_x} = \boldsymbol{n}\cdot\boldsymbol{l}_1 + \Delta\boldsymbol{l} \text{ and } \boldsymbol{n} = \mathrm{int}[\boldsymbol{l}_\theta/(\boldsymbol{l}_1+\boldsymbol{l}_2)], \tag{6.5}$$

where, $\boldsymbol{l}_\theta = \boldsymbol{h}/\cos(\theta)$ is the total slant length from the TOC to the BOC when the zenith angle is θ (i.e., $\theta = \theta_{vi}$ for the viewing beam and $\theta = \theta_s$ for the solar beam); $\boldsymbol{l}_1$ and $\boldsymbol{l}_2$ are the slant lengths when the viewing or solar beam passes through a whole hedgerow and soil row, respectively, and are defined by Eq.(6.6):

$$\boldsymbol{l}_1 = \boldsymbol{w_c} / |\sin(\Delta\varphi)| / \sin(\theta) \text{ and } \boldsymbol{l}_2 = \boldsymbol{w_s} / |\sin(\Delta\varphi)| / \sin(\theta). \tag{6.6}$$

The first step of the formulas in Eq.(6.6) is to convert the widths of the hedgerow and soil to the projected widths in the direction of VAA or SAA, and the second step is to calculate the slant length. The azimuth difference $\Delta\varphi$ is calculated as $\Delta\varphi = \varphi - \varphi_r$, where φ_r is the row azimuth angle and φ represents the viewing azimuth φ_{vi} of the ***i***th cell or the solar azimuth φ_s. However, if φ is equal to φ_r, $\boldsymbol{l}_1$ and $\boldsymbol{l}_2$ are infinite. In this case, Eqs. (6.5) and (6.6) are not used, and $\boldsymbol{l_x}$ is equal to $\boldsymbol{l}_\theta$ if the cell ΔS_T (or $\Delta S'_T$) is directly above the surface of the hedgerow (e.g., the point B' in Fig.6-1), or equal to zero if ΔS_T ($\Delta S'_T$) is directly above the background soil (e.g., the points A', C' and D' in Fig.6-1). In addition, the term $\Delta\boldsymbol{l}$ in Eq.(6.5) represents the remainder of the length $\boldsymbol{l}_\theta$ after several crossings of ($\boldsymbol{l}_1 + \boldsymbol{l}_2$). However, $\Delta\boldsymbol{l}$ is not always equal to the result $\boldsymbol{l}_\theta - \boldsymbol{n}\cdot(\boldsymbol{l}_1 + \boldsymbol{l}_2)$ because this result may still contain the slant length above the soil.

A general way to calculate the position ($\boldsymbol{x_{ri}}$) of the ***i***th cell ΔS_T relative to the vegetated hedgerow (i.e., above the hedgerow or the soil) is provided in Eq.(6.7):

$$\boldsymbol{x_{ri}} = \boldsymbol{d_{ri}} - \boldsymbol{j}\cdot(\boldsymbol{w_c} + \boldsymbol{w_s}),\ \boldsymbol{j} = \mathrm{int}[\boldsymbol{d_{ri}} \big/ (\boldsymbol{w_c} + \boldsymbol{w_s})], \text{ and } \boldsymbol{d_{ri}} = \boldsymbol{d_{ri0}} \cdot \sin(\Delta\varphi_i) + \boldsymbol{x_c}, \tag{6.7}$$

where, $\boldsymbol{d}_{ri0}$ is the distance from the ***i***th cell to the sensor's central point on the TOC (i.e., Point D' in Fig.6-1(a)), the product of $\boldsymbol{d}_{ri0}$ and $\boldsymbol{sin}(\Delta\varphi_i)$ projects this distance in the crossing row direction, and $\Delta\varphi_i$ is the relative azimuth angle between the row direction and the line from the cell to Point D'. The other terms were previously defined.

STEP 3: The combination of $\boldsymbol{l_v}$ and $\boldsymbol{l_s}$ results in four cases, as illustrated in Fig.6-2(a)-(d):

Case (a): $\boldsymbol{l_v} = 0$ and $\boldsymbol{l_s} = 0$. In Case (a), the sunlit soil is viewed directly by the sensor. Neither the solar beam nor the viewing beam is obscured by the canopy. However, if the viewing zenith angle or solar zenith angle (θ_{vi} or θ_s) is large enough, the soil will be obscured by the canopy, and this case will decline or disappear.

Case (b): $\boldsymbol{l_v} = 0$ and $\boldsymbol{l_s} > 0$. Case (b) illustrates the condition where the solar beam is partly obscured by the canopy but the viewing beam continues freely. In this case, two components may be observed: sunlit soil and shaded soil. The fraction of sunlit soil is equal to the gap probability of the canopy in the solar direction $\boldsymbol{P_s}$, and the fraction of shaded soil is then equal to $1 - \boldsymbol{P_s}$.

Case (c): $\boldsymbol{l_v} > 0$ and $\boldsymbol{l_s} = 0$. In Case (c), the sunlit soil can be viewed through the canopy, and two components are observed: the leaves and the sunlit soil. The fraction of sunlit soil is equal to the gap probability of the canopy in the viewing direction $\boldsymbol{P_v}$, and the fraction of the leaves is then equal to $1 - \boldsymbol{P_v}$.

Case (d): $\boldsymbol{l_v} > 0$ and $\boldsymbol{l_s} > 0$. The canopy obscures both the solar and viewing beams. All three components are included in this case: leaves, sunlit and shaded soils. The fraction of the leaves is equal to 1– $\boldsymbol{P_v}$, the fraction of sunlit soil can be estimated from the bi-directional gap probability as $\boldsymbol{P_s P_v Ht}$ (Yu et al. 2004), and the fraction of shaded soil is, finally, $\boldsymbol{P_v}(1-\boldsymbol{P_s P_v Ht})$. $\boldsymbol{Ht}$ is the corresponding bi-directional function.

The directional gap probability throughout the canopy layer depends on the canopy structure, the leaf area index (LAI), the leaf angle distribution (LAD) and the viewing angle. It can be expressed as Eq.(6.8) for a homogeneous canopy (Myneni et al. 1989; Nilson 1971):

$$\boldsymbol{P}(\theta)=\exp[-\lambda(\theta)\frac{\boldsymbol{G}(\theta)}{\cos\theta}\cdot\boldsymbol{LAI}], \tag{6.8}$$

where, the ratio $\boldsymbol{G}(\theta)/\cos\theta$ represents the directional extinction coefficient for a canopy with a random leaf dispersion, and $\boldsymbol{G}(\theta)$ is the fraction of leaves projected in the direction θ**.** $\lambda(\theta)$ is the directional leaf dispersion parameter, which equals 1 if the leaves are randomly distributed but is less than 1 for clumped canopies (Chehbouni et al. 2001; Nouvellon et al. 2000). For a discontinuous canopy, the gap probability can be expanded from Eq.(6.8) as a function of the path length (Li and Strahler 1988):

$$\boldsymbol{P}(\theta)=\exp[-\tau(\theta)\cdot\boldsymbol{l_e}\cdot\boldsymbol{FAVD}], \tag{6.9}$$

where, $\boldsymbol{l_e}$ is the effective path length that passes through the canopy, while the length passing through the adjacent space among rows is ignored. $\boldsymbol{FAVD}$ is the foliage area volume density in a unit of m^{-1}, and $\tau(\theta)=\lambda(\theta)\cdot\boldsymbol{G}(\theta)$ is defined as the attenuation coefficient. According to Eq.(6.9), the gap probability in the viewing and solar directions for the four cases (a – d) can be expressed by Eq.(6.10):

$$\boldsymbol{P_v}=\exp[-\tau\cdot\boldsymbol{l_v}\cdot\boldsymbol{FAVD}] \text{ and } \boldsymbol{P_s}=\exp[-\tau\cdot\boldsymbol{l_s}\cdot\boldsymbol{FAVD}]. \tag{6.10}$$

To calculate the fractions of sunlit and shaded soil in case (d), the bi-directional gap probabilities in the solar and viewing directions are considered. An exponential model for homogeneous canopies, developed by Kuusk (1985), can be applied to estimate the fraction of sunlit soil $\boldsymbol{P}$ (Du et al. 2007; Yu et al. 2004):

$$\boldsymbol{P}=\boldsymbol{P_s P_v Ht}=\exp[-\tau(\boldsymbol{l_s}+\boldsymbol{l_v}-\frac{1-\exp(-\boldsymbol{m}\cdot\boldsymbol{l_{sv}})}{\boldsymbol{m}\cdot\boldsymbol{l_{sv}}}\sqrt{\boldsymbol{l_s l_v}})\cdot\boldsymbol{FAVD}]. \tag{6.11}$$

In Eq.(6.11), $\boldsymbol{Ht}$ is the bi-directional function, and $\boldsymbol{m}=1/\boldsymbol{s}$, where $\boldsymbol{s}$ is the characteristic linear dimension of the foliage. As stated above, $\boldsymbol{l_v}$ and $\boldsymbol{l_s}$ are the path lengths through the canopy in the viewing and solar directions, respectively. $\boldsymbol{l_{sv}}$ is the path length difference between the solar and viewing beams and is defined by Eq.(6.12):

$$\boldsymbol{l_{sv}}=|\vec{\boldsymbol{l}}_s-\vec{\boldsymbol{l}}_v|=\sqrt{\boldsymbol{l}_s^2+\boldsymbol{l}_v^2-2\boldsymbol{l_v l_s}\cos\xi}, \tag{6.12}$$

where, ξ is the scattering angle, which can be calculated from the zenith and azimuth angles of the solar and viewing directions of the $\boldsymbol{i}$th cell:

$$\cos\xi = \cos\theta_s \cos\theta_{vi} + \sin\theta_s \sin\theta_{vi} \cos(\varphi_{vi} - \varphi_s)\,. \tag{6.13}$$

The rest of the terms in Eqs. (6.12) and (6.13) have the same meanings as those used in previous equations.

STEP 4: Using equations from Eq.(6.10) to Eq.(6.13), the components' fractions for each cell can be derived. However, the average fractions for the entire footprint of the ellipse are not the mathematical average of those fractions for all of the cells because of the Point Spreading Function (PSF) effect of the sensor's response to input energy. This effect can be simply understood as the contribution of each cell to the total energy is different, and the closer the cell is to the center of the sensor's FOV, the greater its weight will be. Because it is difficult to measure the sensor's PSF, we used a two-dimensional Gaussian function to determine the relative weight of the $\boldsymbol{i}$th cell (Huang et al. 2002):

$$\boldsymbol{w}(\boldsymbol{i}) = \frac{1}{2\pi\sigma^2}\exp[-\frac{(\boldsymbol{x}_i - \boldsymbol{x}_0)^2 + (\boldsymbol{y}_i - \boldsymbol{y}_0)^2}{2\sigma^2}]\,, \tag{6.14}$$

where, $(\boldsymbol{x}_i, \boldsymbol{y}_i)$ is the location of the $\boldsymbol{i}$th cell within the footprint on the TOC, while $(\boldsymbol{x}_0, \boldsymbol{y}_0)$ is the location of the central point of the sensor's FOV on the TOC, i.e., point D' in Fig.6-1. The term σ is the standard deviation of $\boldsymbol{x}$ and $\boldsymbol{y}$, and is assumed to be the same for both $\boldsymbol{x}$ and $\boldsymbol{y}$. As a result, the components' fractions for the whole FOV are weighted according to Eq.(6.15):

$$\boldsymbol{F}_x(\theta_v, \varphi_v) = \frac{\sum_{\boldsymbol{i}=1}^{\boldsymbol{N}} \boldsymbol{f}_x(\boldsymbol{i}) \cdot \boldsymbol{w}(\boldsymbol{i}) \cdot \Delta \boldsymbol{S}_T(\boldsymbol{i})}{\sum_{\boldsymbol{i}=1}^{\boldsymbol{N}} \boldsymbol{w}(\boldsymbol{i}) \cdot \Delta \boldsymbol{S}_T(\boldsymbol{i})} = \frac{\sum_{\boldsymbol{i}=1}^{\boldsymbol{N}} \boldsymbol{f}_x(\boldsymbol{i}) \cdot \boldsymbol{w}(\boldsymbol{i})}{\sum_{\boldsymbol{i}=1}^{\boldsymbol{N}} \boldsymbol{w}(\boldsymbol{i})}\,, \tag{6.15}$$

where, $\boldsymbol{F}_x$ represents the fractions of leaves ($\boldsymbol{F}_{leaf}$), sunlit soil ($\boldsymbol{F}_{sun\_soil}$) and shaded soil ($\boldsymbol{F}_{shd\_soil}$) within the footprint; $\boldsymbol{f}_x(\boldsymbol{i})$ is the component fraction of the $\boldsymbol{i}$th cell; and $\boldsymbol{N}$ is the number of cells in the footprint. Because the area of each cell is the same, Eq.(6.15) is not sensitive to the term ΔS_T.

STEP 5: Finally, the directional brightness temperature (DBT) from the footprint of the sensor's FOV is related to the components' fractions and corresponding temperatures by the following linear expression (Du et al. 2007; Yu et al. 2004):

$$\begin{aligned} \boldsymbol{L}(\boldsymbol{DBT}) = {} & \boldsymbol{F}_{leaf} \cdot \boldsymbol{L}(\boldsymbol{BT}_{leaf}) + \boldsymbol{F}_{sun\_soil} \cdot \boldsymbol{L}(\boldsymbol{BT}_{sun\_soil}) + \boldsymbol{F}_{shd\_soil} \cdot \boldsymbol{L}(\boldsymbol{BT}_{shd\_soil}) \\ & + \boldsymbol{R}_{multi} + (1 - \varepsilon_c)\boldsymbol{R}_{a\downarrow} \end{aligned}\,, \tag{6.16}$$

where, $\boldsymbol{L}(\boldsymbol{DBT})$ is the thermal radiance from Planck's law, and the inversion of Planck's law to the term $\boldsymbol{L}(\boldsymbol{DBT})$ in Eq.(6.16) will return the DBT. $\boldsymbol{BT}_{leaf}$, $\boldsymbol{BT}_{sun\_soil}$ and $\boldsymbol{BT}_{shd\_soil}$ are the brightness temperatures of the leaves, sunlit soil and shaded soil, respectively, which are defined by the inversion of Planck's law, $\boldsymbol{L}^{-1}[\varepsilon_x \boldsymbol{L}(\boldsymbol{T}_x)]$, where $\boldsymbol{T}_x$ and ε_x are a single component's temperature and emissivity, respectively; $\boldsymbol{R}_{multi}$ is the single and multiple scattering radiance within the canopy and between the soil and leaves (François et al. 1997;

Verhoef et al. 2007). For the row canopy, the term is complex because of the discontinuous structure. Because the reflectivity of leaves and soil in the thermal spectral range is very low, excluding this scattering will not cause significant error in the DBT. The last term is the reflected atmospheric downward radiance; $\boldsymbol{R}_{a\downarrow}$ is the atmospheric downward radiance and ε_c is the canopy directional emissivity. Because atmospheric radiance is related to atmospheric emission, there is much uncertainty in the DBT. Therefore, this study does not consider the reflected atmospheric radiance in the following discussion and only considers the angular variation of DBT, which is mainly dependent on the components' fractions and brightness temperatures.

6.3 Model analysis

As indicated above, the new model treats the sensor's footprint on the TOC as a circle at the nadir or as an ellipse in the slant direction and then divides the footprint into several smaller cells and calculates the actual VZA, VAA, and path lengths for each cell in both the viewing and solar directions. Based on these parameters, the fractions of leaves, sunlit soil and shaded soil are obtained from gap probability theory. The total energy in the footprint is calculated as the sum of the radiation from all of the cells, which is weighted by a Gaussian-distributing PSF. Therefore, the input parameters for the new model include three categories:

(1) Canopy structure parameters: the width of the hedgerow ($\boldsymbol{w_c}$) and soil ($\boldsymbol{w_s}$); the height of the canopy ($\boldsymbol{h}$); LAI or ***FAVD***; the dimension of the foliage elements ($\boldsymbol{s}$ = 0.2 m, as reported in (Yu et al. 2004)); and the row direction (φ_r).

(2) Observational geometric parameters: the solar zenith and azimuth angles (θ_s and φ_s); the zenith and azimuth angles of the goniometer (θ_v and φ_v); the observation height $\boldsymbol{H_0}$ from the sensor to the ground at the nadir, and the slant observation height $\boldsymbol{H} = \boldsymbol{H_0}\cos(\theta_v)$; the angle of the sensor's FOV (θ_f); and the central point ($\boldsymbol{x_c}$) of the sensor's FOV on the TOC.

(3) Brightness temperatures of leaves, sunlit soil and shaded soil: $\boldsymbol{BT_{leaf}}$, $\boldsymbol{BT_{sun\_soil}}$ and $\boldsymbol{BT_{shd\_soil}}$.

Table 6-1 lists the general input parameters that are used for the model analysis. The row direction is assumed to be south/north, $\varphi_r = 0$. Three FOV angles are considered to investigate the effect of the FOV on the DBT of the row canopy: small (6°), medium (16°) and large (28°).

Table 6-1. The input parameters used for model analysis

θ_s (°)	φ_s (°)	FOV (°)	$\boldsymbol{w_c}$ (m)	$\boldsymbol{w_s}$ (m)	$\boldsymbol{h}$ (m)	$\boldsymbol{H_0}$ (m)	φ_r (°)	$\boldsymbol{x_c}$ (m)	LAI	$\boldsymbol{BT_{leaf}}$ (K)	$\boldsymbol{BT_{sun\_soil}}$ (K)	$\boldsymbol{BT_{shd\_soil}}$ (K)
30	270	6,16,28	0.3	0.3	0.3	3.0	0	0.15	1.0	305	320	315

6.3.1 Components' fractions and angular variation in DBT

Fig.6-3 depicts the fractional distribution of several variables: (a) leaves, (b) sunlit soil, (c) shaded soil and (d) DBT for three FOV angles: 6° (FOV6) in column 1, 16° (FOV16) in column 2, and 28° (FOV28) in column 3. Column 4 lists the angular variations in those fractions and the DBT in the solar principle plane (SPP). The SAA and SZA are 270° and 30°, respectively, which indicate that the solar beam is perpendicular to the row direction. For simplicity, the VZA is assumed to be negative in the solar backscattering direction. As a result, the SPP in Fig.6-3 runs from west to east, ranging from VZA = -60° to VZA = 60° by a step of 10°.

The distribution of the leaves fraction ($\boldsymbol{F_{leaf}}$) is presented in Fig.6-3(a), which illustrates that different distributional patterns are caused by these FOVs. Fig.6-3(a-4) indicates that $\boldsymbol{F_{leaf}}$ reaches its local maximum at the nadir in the case of FOV6, decreases until about VZA = 45°, and finally increases with increasing VZA. However, the fractions of both FOV16 and FOV28 always increase with increasing VZA. Although the footprint for large VZAs is larger than that for small VZAs, the path length $\boldsymbol{l_v}$ of the viewing beam for large VZAs of the SPP may be reduced for two reasons in the case of FOV6. First, the row-space effect does not account for the path length through the space of two the adjacent vegetated hedgerow. The footprint of FOV6 encompasses a small area of the TOC at the nadir observation, but the majority the footprint intersects the leaves, and the path length $\boldsymbol{l_v}$ from the TOC to the BOC generally passes through the hedgerow, infrequently intersecting the adjacent soil space due to the small VZAs of all cells. Since the major axis (approximately 0.28 m at the nadir) of the elliptical footprint of FOV6 is less than the total width ($\boldsymbol{w_c}$ + $\boldsymbol{w_s}$) of one whole period of the row canopy, the probability that the footprint includes predominantly vegetation with minimal background or predominantly background with minimal vegetation, actually increases. Therefore, the leaves fraction $\boldsymbol{F_{leaf}}$ decreases while the soil fraction increases with VZAs varying from the nadir to the slant direction. Similar results can be also found in Fig.6-3(b-1) that illustrates the fractional distribution of sunlit soil for FOV6. However, this row-space effect diminishes or disappears when the VZA exceeds the row threshold angle (e.g., 45°, arctan ($\boldsymbol{h/w_s}$)), as indicated in Fig.6-3(a-4). A longer path length is then consistent with large VZAs. The second reason is the previously mentioned PSF effect, in which the cells around the FOV's central point contribute more to the observed DBT than the other cells. As a result, the observed DBT is largely dependent on those cells near the center of the FOV, and their path lengths further rely upon their locations within the hedgerow. From Fig.6-3(a-4), it is apparent that FOV16 and FOV28 have very similar angular variations of $\boldsymbol{F_{leaf}}$ in the SPP. However, comparison between Fig.6-3(a-2) and (a-3) reveals that the directional $\boldsymbol{F_{leaf}}$ of FOV16 and FOV28 are still different, especially in the profile of the row direction. In addition, Fig.6-3 (a-3) also shows that the $\boldsymbol{F_{leaf}}$ of FOV28 is almost independently on the azimuth, and its isolines resemble a series of concentric circles. This result indicates that the FOV28 is large enough to smooth the row-space effect of the row canopy because its footprint contains approximately one to three periods of the row structures. This smoothing causes the final directional components' fractions (Fig.6-3(b-3) and (c-3)) and the final DBT (see Fig.6-3(d-3)) to distribute as a uniform, continuous canopy. Moreover, because the new model does not separate the sunlit and shaded leaves, the distribution of $\boldsymbol{F_{leaf}}$ is independent on the solar position, and only determined by the canopy and viewing geometric parameters. As a result, there is no a local maximum $\boldsymbol{F_{leaf}}$ in the hotspot where the solar and viewing beams are in the same direction.

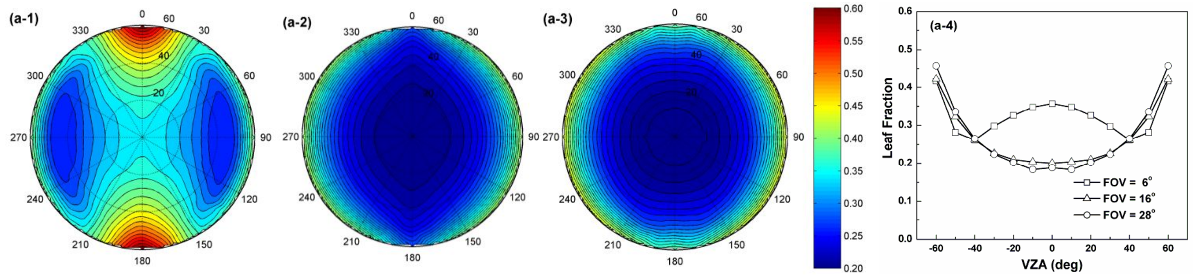

(a) Leaf fractions (Left to right: FOV=6°, 16°, 28° and SPP profile)

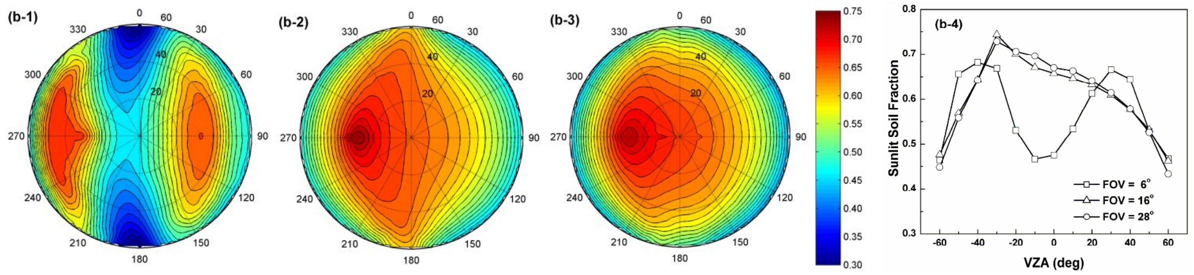

(b) Sunlit soil fractions (Left to right: FOV=6°, 16°, 28° and SPP profile)

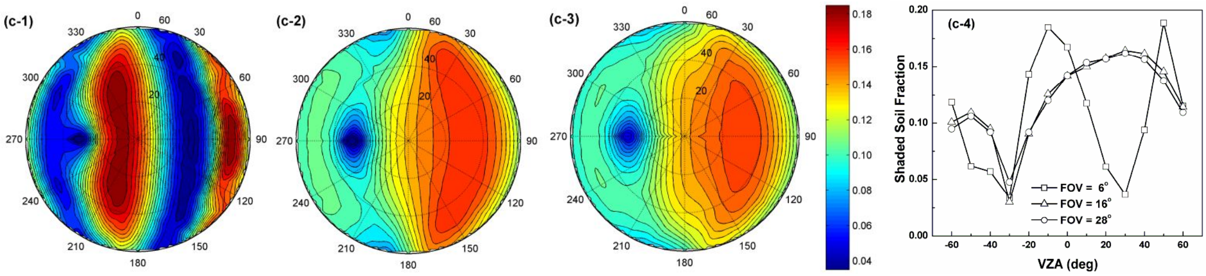

(c) Shaded soil fractions (Left to right: FOV=6°, 16°, 28° and SPP profile)

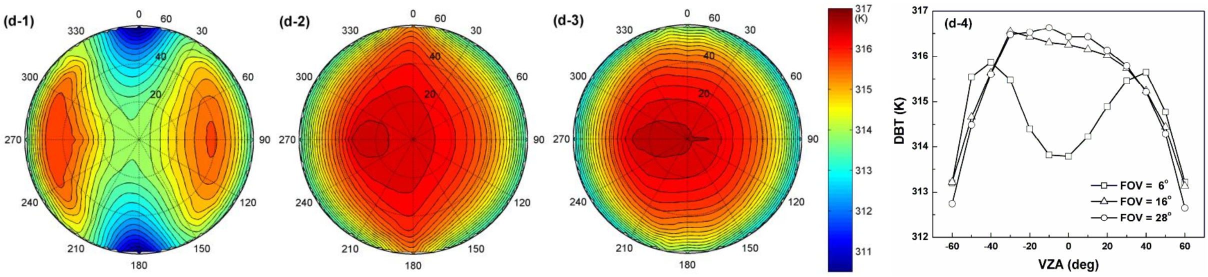

(d) DBT (Left to right: FOV=6°, 16°, 28° and SPP profile)

Fig.6-3. Fraction distribution of several variables: (a) leaves, (b) sunlit soil, (c) shaded soil and (d) DBT for difference FOV angles: 6° in column 1, 16° in column 2, and 28° in column 3. Column 4 shows the angular variations of those fractions and DBT in the principle plane. (SAA = 270°, SZA = 30°, row direction = 0°)

Fig.6-3(b) displays the fractional distribution of the sunlit soil ($\boldsymbol{F_{sun\_soil}}$) for the three FOVs and their comparison in the SPP. The hotspot is obvious for FOV16 and FOV28, while two such spots exist in the FOV6, falling on the forward and backward scattering sides of the SPP. As depicted in Fig.6-3(b-1), the row-space effect is significant in the case of FOV6, especially in the VZA range from 20° to 50° in the SPP. Meanwhile, the angular variations of the $\boldsymbol{F_{sun\_soil}}$ for cases FOV16 and FOV28 in the SPP are quite similar, with a difference less than 0.03. However, the $\boldsymbol{F_{sun\_soil}}$ of the two cases has an obvious discrepancy in the row direction, and this difference has a maximum value 0.1 at VZA = 60°. However, since FOV28 smoothes the row-space effect, the result of FOV16 may be much closer to reality than FOV28. As for the distribution of the shaded soil ($\boldsymbol{F_{shd\_soil}}$) presented in Fig.6-3(c), there is a "cold spot" in the solar direction for FOV16 and FOV28, corresponding to the hotspot of the $\boldsymbol{F_{sun\_soil}}$. Compared to the $\boldsymbol{F_{sun\_soil}}$, the $\boldsymbol{F_{shd\_soil}}$ patterns of FOV16 and FOV28 are more similar, even in the row direction. As expected, the $\boldsymbol{F_{shd\_soil}}$ of FOV6 is still different from the other two cases.

Fig.6-3(d) represents the DBT distribution for the three FOVs, which were calculated from the components' fractions and their brightness temperatures at $\boldsymbol{BT_{leaf}}$ = 305 K, $\boldsymbol{BT_{sun\_soil}}$ = 320 K and $\boldsymbol{BT_{shd\_soil}}$ = 315 K (see Table 6-2). Because the $\boldsymbol{F_{leaf}}$ is beyond the control of the solar position and its distribution is almost symmetric along the row direction, the angular behaviors of DBT are predominantly determined by the distribution of sunlit soil that has the largest brightness temperature. Consequently, similar to the distribution of the $\boldsymbol{F_{sun\_soil}}$, two hotspots appear in the forward and backward SPP of the DBT distribution of FOV6, while only one such hotspot falls within the solar beam direction for FOV16 and FOV28. However, from Fig.6-3(d-4), it is apparent that the DBT of VZA = -10° is larger than that of VZA = -30°, perhaps because the leaf temperature is lower than that of shaded soil, and the increased temperature due to the increase of the leaves and sunlit soil fractions is smaller than the decreased temperature due to the decrease of the shaded soil fraction when VZA changes from -10° to -30°. The same reasons can be used to explain the DBT's fluctuation in the range of VZAs from the nadir to forward 20°.

Table 6-2 lists some comparison of the components' fractions and the DBT among the three FOVs. It indicates that the results of FOV16 and FOV28 are generally similar, but different from those of FOV6: the root mean square errors (RMSE) of the leaves, sunlit and shaded soils fractions between FOV6 and the other two FOVs are respectively 0.13, 0.14 and 0.06, which causes their temperature difference up to 1.9 K, and even results in an larger difference at the nadir observation (e.g., approximately 2.5 K). Furthermore, the nadir DBT of FOV6 is lower than that of both FOV16 and FOV28 because the footprint of FOV6 mainly contains the leaf component at the nadir, while the soil covers a relatively larger percent in the footprint of the two other FOVs.

Table 6-2. Difference of components' fractions and DBT caused by different FOVs

Cases	RMSE				DBT difference (K)	
	$\boldsymbol{F_{leaf}}$	$\boldsymbol{F_{sun\_soil}}$	$\boldsymbol{F_{shd\_soil}}$	DBT (K)	@Hotspot	@Nadir
FOV6 - FOV16	0.13	0.14	0.06	1.9	-1.1	-2.5
FOV6 - FOV28	0.13	0.14	0.06	1.9	-1.0	-2.6
FOV16 - FOV28	0.02	0.02	0.01	0.3	0.1	-0.2

From the discussion above, we learn that different sensors' FOVs can result in significantly different patterns in the directional distribution of the component fractions and DBT. A small FOV, such as FOV6, whose footprint is less than one period of the row canopy, can cause DBT to be predominantly contributed by one component and row direction, while a large FOV, such as FOV28, whose footprint is more than two periods of the row canopy, can smooth the row-space effect and cause the DBT's angular variation of the row canopy to perform as a uniform, continuous canopy. Therefore, a question is raised: what FOV (or footprint) can be used to obtain a representative DBT for the row canopy? To answer this question, the next sections will analyze the model's sensitivity to some key parameters and compare the new model with the parallel model developed by Yu et al.(2004).

6.3.2 Model sensitivity to key parameters

This section will evaluate the new model's sensitivity and consistency with several key input parameters: the widths of the hedgerow and the background, LAI, the central location of the sensor's FOV, the solar position and the components' brightness temperatures.

A. Effect of the ratio of the hedgerow width to the background soil width r. The hedgerow width determines the gap distributions within the canopy. For a narrow hedgerow, gaps are largely concentrated along the hedgerows; otherwise, gaps may be generally within the hedgerows for a wide hedgerow. We fix the total width of a whole row period (i.e., $\boldsymbol{w_c}+\boldsymbol{w_s}$ = 0.6 m) and evaluate the influence of the ratio $\boldsymbol{r} = \boldsymbol{w_c}/(\boldsymbol{w_c}+\boldsymbol{w_s})$ on the DBT. Different $\boldsymbol{r}$s correspond to crop's different growth stages, and $\boldsymbol{r}$ = 1.0 means that the row canopy is fully vegetated and becomes a uniform, continuous canopy. In order to investigate the influence of $\boldsymbol{r}$ on DBT, we changes $\boldsymbol{r}$ from 0.1 to 1.0 at a step of 0.1 and keep the other input parameters the same as those in Table 6-1. Fig.6-4(a), (b) and (c) display the directional distribution of DBT at $\boldsymbol{r}$ = 0.2 and $\boldsymbol{r}$ = 0.8 for the three FOVs, as well as the DBT variation in SPP and the cross principal plane (CPP). As shown in those figures, the DBTs for the case of $\boldsymbol{r}$ = 0.2 are significantly higher than those of $\boldsymbol{r}$ = 0.8 because a small $\boldsymbol{r}$ indicates that more soil is contained in the footprint. As seen from the DBT profiles in column 3 of Fig.6-4, the range of the DBT for the case $\boldsymbol{r}$ = 0.8 in both SPP and CPP is larger than that of $\boldsymbol{r}$ = 0.2, which shows that the fractional variations in soil have a greater influence on the DBT of a dense canopy than that of a sparse canopy. In addition, the distribution of DBTs generally depends on the FOV at a small $\boldsymbol{r}$ (e.g., 0.2) but gradually exceeds the control of the FOV with increasing $\boldsymbol{r}$, especially when $\boldsymbol{r}$ remains high. For the FOV6, an increasing $\boldsymbol{r}$ diminishes the hotspot in the forward direction of the SPP and only retains the normal hotspot in the solar direction. For the FOV16, a hot stripe appears in the row direction at $\boldsymbol{r}$ = 0.2 but gradually changes to a pattern similar to the FOV28. For the FOV28, although some slight changes can be found in the SPP, the distribution pattern of the DBT is nearly unchanged because of its huge footprint.

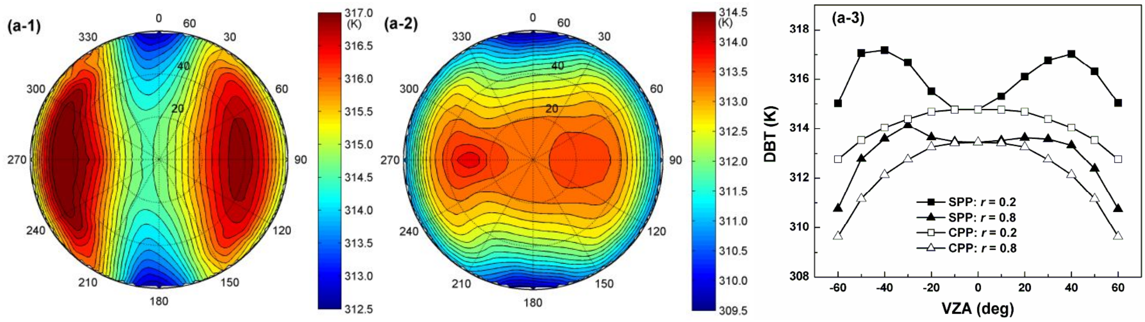

(a) FOV6, Left: ***r*** =0.2, Mid: ***r*** = 0.8, Right: SPP and CPP profiles

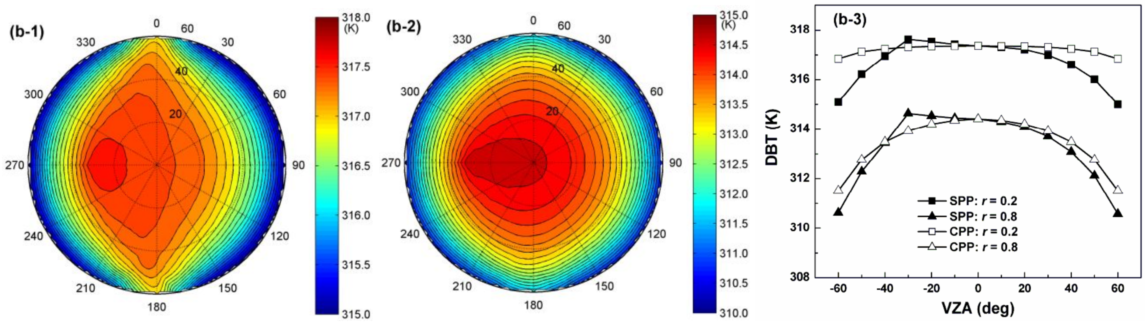

(b) FOV16, Left: ***r*** =0.2, Mid: ***r*** = 0.8, Right: SPP and CPP profiles

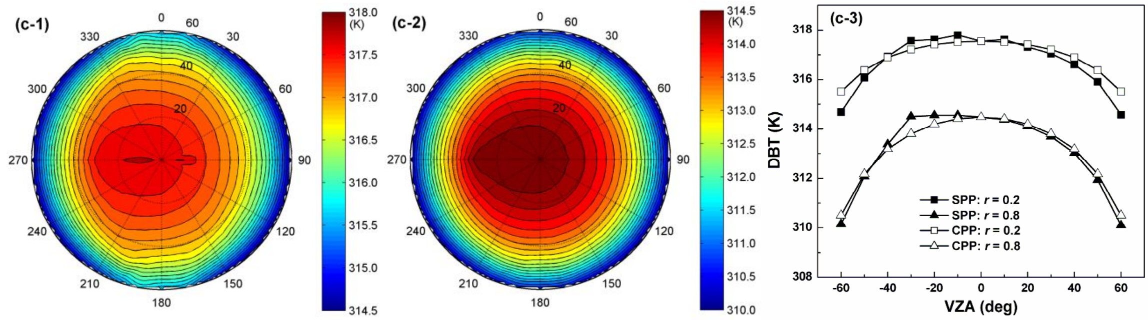

(c) FOV28, Left: ***r*** =0.2, Mid: ***r*** = 0.8, Right: SPP and CPP profiles

Fig.6-4. Directional distribution of DBT for FOV6, FOV16 and FOV28 at ***r*** (=$w_c/(w_c+w_s)$) = 0.2 (column 1) and 0.8 (column 2), and their corresponding angular variation of DBT (column 3) in solar principle plane (SPP) and cross-principle plane (CPP).

Fig.6-5 presents the comparison of the components' fractions and the DBT from different FOVs by taking the values of FOV28 at each ***r*** as the reference. It indicates that the differences of the components' fractions (leaves and sunlit soil) and DBT between FOV16 and FOV28 are generally less than 0.03 and 0.3 K, respectively, while the difference between FOV6 and FOV28 is significant: the RMSE of the components' fractions first increases rapidly, then reaches its maximum (0.13 for leaves and 0.14 for sunlit soil) near ***r*** = 0.4 and decreases to less than 0.03. Similarly, the DBT RMSE reaches its maximum (approximately 2 K) around ***r*** = 0.4, and most of ***r*** results in a RMSE larger than 1 K. In theory, the distribution of the DBT should be independent on FOV for a fully vegetated footprint (e.g., ***r*** =1.0), but there are still some DBT discrepancies between FOVs, as shown in Fig.6-5. This result might be caused by the non-linear PSF of the different FOVs. If PSF is assumed to be 1 for each cell, their difference will be removed. Based on these results, we know that the DBT of a narrow-hedgerow canopy (a small ***r***) depends on the FOV and has one or two small hotspot peaks for different FOVs, while the DBT of a broad-hedgerow canopy (a large ***r***) becomes independent on the FOV and has a sharper hotspot compared to a proper ratio ***r***. A similar result was also described by (Yu et al. 2004).

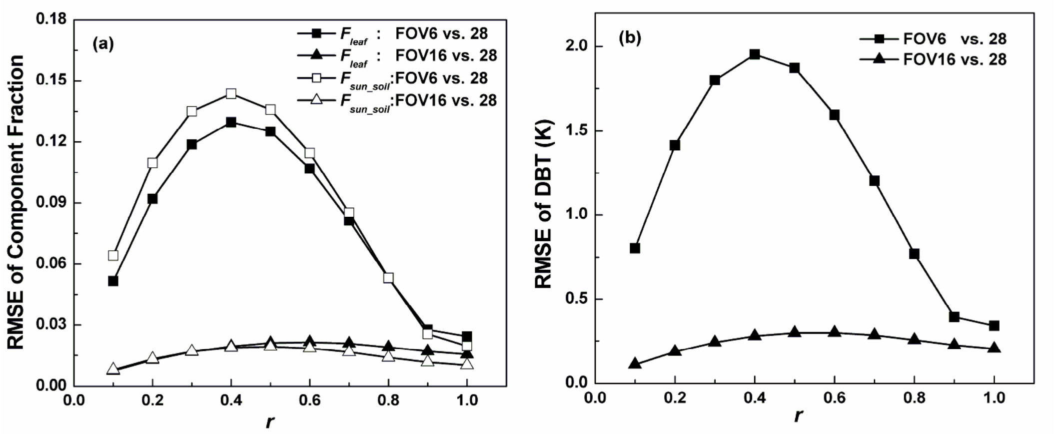

Fig.6-5. RMSE for the difference of components' fractions (a) and DBT (b) between FOV6, FOV16 and FOV28 with ***r*** varying from 0.1 to 1.0.

B. Effect of LAI. As reported in other papers (Chehbouni et al. 2001; Du et al. 2007; Yu et al. 2004), LAI is the key parameter that influences the gap probability in the canopy. Fig.6-6 displays the directional distribution of the DBT for the three FOVs with LAI = 0.5 and 5.0, corresponding to sparse and dense leaves in the hedgerow. The other input parameters are the same as those listed in Table 6-1. It shows that a lower LAI results in an obvious hotspot and hot region around the solar direction. The DBT in this region is similar to the soils' temperatures (BT_{sun_soil} = 320 K and BT_{shd_soil} = 315 K) because it is mainly determined by the soil components. However, in the case of a larger LAI, the dense hedgerow is almost opaque and consequently decreases the gap probability of sunlit soil. This condition causes the hotspot to nearly disappear in FOV16 and FOV28, and their hot regions are finally distributed in the row direction rather than the solar direction, but closer to the side of the solar position. Nevertheless, a different result is obtained for FOV6 that the increase of LAI in the hedgerow sharpens the hot stripe in the solar direction but reduces the hot stripe in forward directions, as shown in Fig.6-6(a-1). On the contrary, a cold stripe rather than the hot stripe appears in the row direction for LAI =5.0 (see Fig.6-6(a-2)) because the small footprint of FOV6 is mainly covered by leaves, causing the DBT to be determined by the leaves' brightness temperature. Therefore, for a smaller LAI, the DBT is largely dependent on the soil components and has minimal variation over large viewing zeniths, especially for large FOVs. On the other hand, a larger LAI can cause the DBT to be dominated by the hedgerow structure and leaves' brightness temperatures, and result in a lower average DBT, a small hotspot and a hot stripe in the row direction.

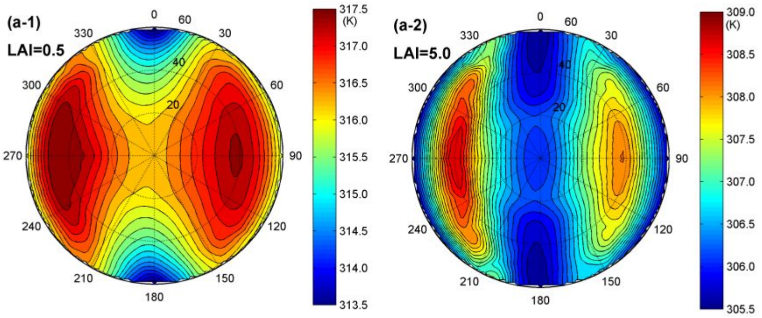

(a) FOV6

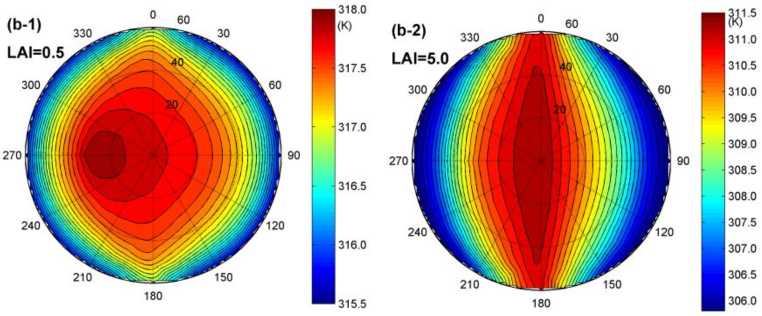

(b) FOV16

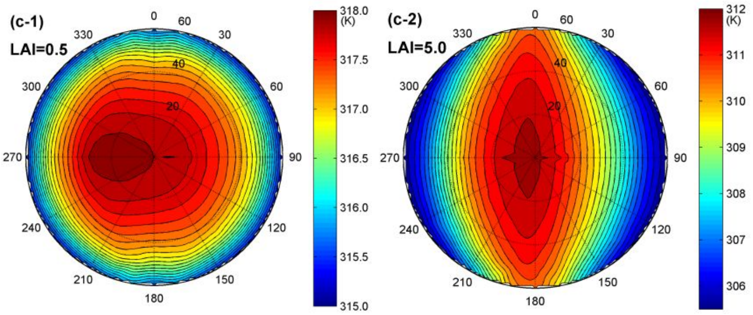

(c) FOV28

Fig.6-6. Influence of LAI on the DBT distribution for FOV6 (a), FOV16 (b) and FOV28 (c). Left column: LAI =0.5; Right column: LAI = 5.0.

C. Effect of the central position of the sensor's footprint x_c. The x_c that is defined in Fig.6-1(b) plays a key role in the DBT distribution because it is used to determine each cell's relative position above the hedgerow or the soil within the sensor's footprint, as described by Eq.(6.7). We illustrate the influence of x_c by varying its value from $-w_s$ (i.e., -0.3 m) to w_c (0.3 m) with an interval of 0.03 m. The other parameters remain unchanged from Table 6-1. Generally, if x_c is closer to the center position above the soil (the hedgerow) the DBT will be higher (lower). Fig.6-7 displays the DBT distribution at $x_c = -0.15$ m, meaning that x_c is in the middle part above the soil, and $x_c = 0.0$ m, meaning that x_c is on the common boundary between the hedgerow and the soil rows. Only FOV6 and FOV16 are presented in Fig.6-7 because the DBT for FOV28 rarely varies with the x_c positions. The RMSE of FOV28 DBT difference caused by different values of x_c is less than 0.2 K, and the corresponding maximum difference is less than 0.8 K. Compared to the DBT in Fig.6-3(d), whose x_c is 0.15 m, the FOV16 has a small variation in DBT (< 0.4 K) caused by the variation of x_c moving from the hedgerow to the soil but it is found that this variation of x_c changes the DBT distribution from a VAA-dependent pattern to an almost VAA-independent pattern. However, as for FOV6, the DBT distribution changes significantly, as expected. The variation of $\boldsymbol{x_c}$ from the hedgerow to the soil causes the two hotspots in Fig.6-3(d-1) to get closer to each other, and finally produces a hot region along the row direction, as shown in Fig.6-7(a-1) at $\boldsymbol{x_c}$ = -0.15 m. In this case, the component observed in the directions around the nadir is predominantly covered by the soil due to the small footprint of FOV6, and the DBT is, therefore, dominated by soil.

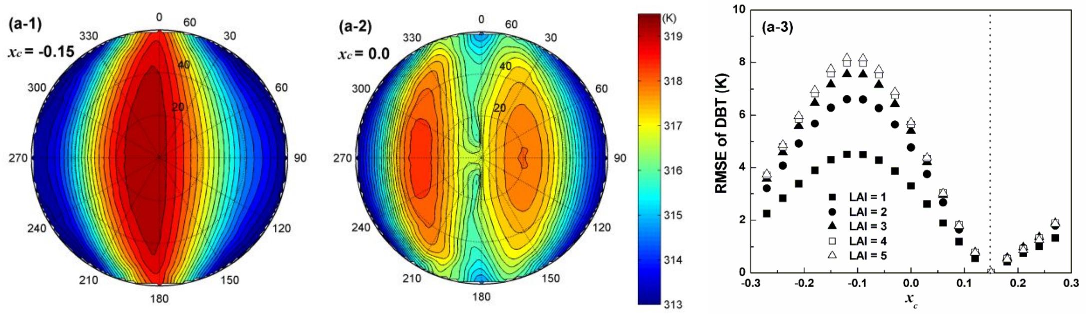

(a) FOV6

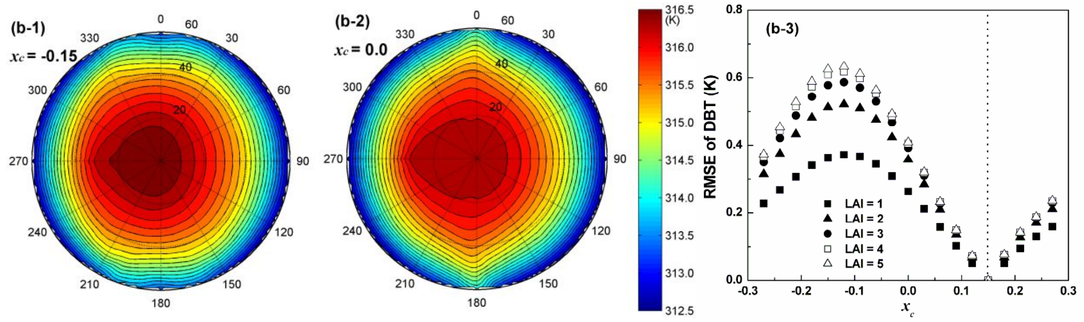

(b) FOV16

Fig.6-7. Influence of the central position $\boldsymbol{x_c}$ on the DBT distribution. (a) FOV6; (b) FOV16. Column 1 is the case of $\boldsymbol{x_c}$ = -0.15 m (above the middle of soil) and column 2 is the case of $\boldsymbol{x_c}$= 0.0 m (above the common boundary of hedgerow and soil). Column 3 is the comparison between DBT at $\boldsymbol{x_c}$ = 0.15 m and those of other $\boldsymbol{x_c}$, with LAI varying from 1.0 to 5.0.

Fig.6-7 also highlights the DBT difference between $\boldsymbol{x_c}$ = 0.15 m and other $\boldsymbol{x_c}$ varying from -0.3 to 0.3, with LAI varying from 1.0 to 5.0. Results indicate that FOV6 has a higher RMSE than FOV16 due to the limitation of its footprint, and the DBT difference is generally significant when $\boldsymbol{x_c}$ falls above the soil and reached the local maximum at $\boldsymbol{x_c}$ = -0.15. Besides, the DBT difference is also influenced by the LAI and increases with the increasing LAI, especially for the cases $\boldsymbol{x_c} < 0$. Although a larger LAI is related to a larger leaves fraction within the footprint and consequently reduces the DBT, the DBT difference is actually enlarged with the increasing LAI, because the decreased DBT caused by increasing the LAI is larger than the decreased DBT caused by the variation of $\boldsymbol{x_c}$ with respect to the case of $\boldsymbol{x_c}$ = 0.15 m (i.e., the reference case, in the middle range above the hedgerow). Fortunately, the influence of LAI on the DBT difference nearly disappears when LAI exceeds 4 for a dense canopy. Therefore, the $\boldsymbol{x_c}$ has a little influence on the DBT with a large FOV, but affects the DBT distribution with a small FOV. Since the shift of $\boldsymbol{x_c}$ can change the pattern of the DBT distribution for the small FOV, an accurate input of this parameter is highly required for accurately simulating the DBT.

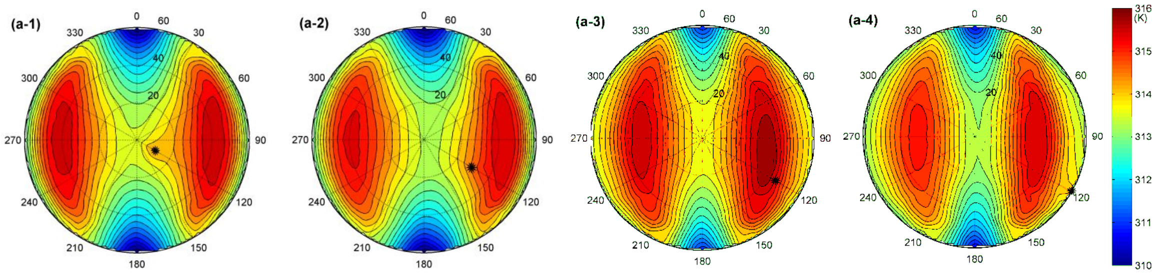

(a) FOV6

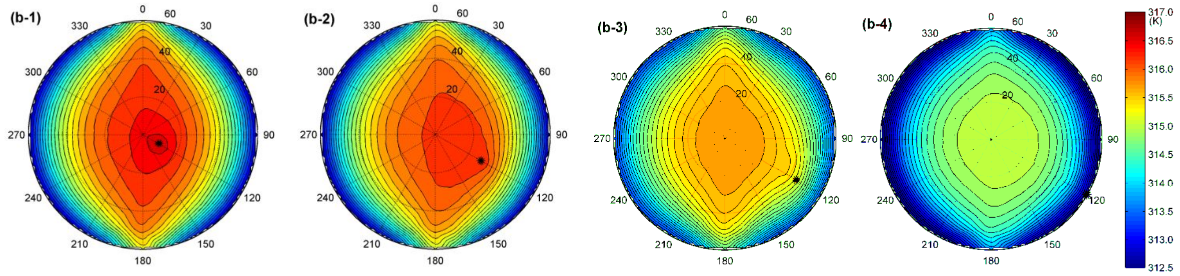

(b) FOV16

Fig.6-8. Influence of solar position (marked with a star) on the DBT for (a) FOV6 and (b) FOV16. Left to right presents the solar position at 120°/10° (SAA/SZA), 120°/30°, 120°/45° and 120°/60°, respectively.

D. Effect of solar position. The solar position (SZA and SAA) determines the fractions of sunlit and shaded soils and the components' brightness temperatures. However, it has no effect on the leaves fraction because the leaves are not separated into sunlit and shaded components, and their fractions are only dominated by the canopy parameters and the viewing direction. Fig.6-8 displays the influence of the solar position on the DBT by changing the SAA and SZA from Table 6-1 to 120°/10° (SAA/SZA), 120°/30°, 120°/45° and 120°/60°, respectively. It shows that the increase of the SZA in the same azimuth plane reduces the value of the DBT because the longer path length through the leaves in the solar direction results in a larger shaded soil fraction. The position of the hotspot for FOV16 is almost consistent with the solar position (marked with a star) at both SZA = 10° and 30°, but the hot stripe became wider, and the hot peak is consequently reduced. However, the hotspot becomes far from the solar position at both SZA = 45° and 60°, and their hot stripes distribute around the nadir direction, perhaps because all solar beam is obscured by the leaves (i.e., $\boldsymbol{l_s} > 0$ for each cell in Fig.6-2) at a SZA equal or beyond the threshold angle (=arctan ($\boldsymbol{h}/\boldsymbol{w_s}$), i.e., 45°) of the row canopy, and the soil fractions with higher brightness temperature in the solar direction are consequently reduced and even less than those in the directions around the nadir. FOV28 has a pattern similar to that of FOV16 and is not presented here. On the contrary, both Fig.6-8(a) and Fig.6-3(d-1) indicate that the solar position does not change the position of the two hot stripes and has little impact on the DBT of FOV6. The DBT difference between the four simulations of FOV6 in Fig.6-8(a) has a RMSE of less than 0.3 K and a maximum of approximately 1.1 K. In fact, the DBT distribution of such a small FOV is largely determined by the row structure because its footprint is too small to collect representative DBT data. Similar results are obtained even if the solar beam follows along the row direction.

E. Effect of components' brightness temperatures. If all of the components have a unique brightness temperature, the DBT will be independent of the geometry of the sun, target, and sensor. However, this condition seldom occurs in sunny days. Because the DBT is a weighted average of its components' fractions and brightness temperatures, and those fractions are calculated from the canopy and viewing geometrical parameters, the components' temperatures predominantly determine the value of the DBT, with little impact on the pattern of the DBT distribution. Taking Fig.6-3(d-4) for example, the hot peak is not sharp enough in FOV28, and the DBT in the hotspot is a little lower than that of the other VZAs in the SPP, such as VZA = -10° and -20°. The leaf temperature is lower than the shaded soil, and the increased temperature due to the increase in the leaves and sunlit soil fractions is smaller than the decreased temperature due to the decrease in the shaded soil fraction when VZA changes from -10° to -30°. If we reduce the brightness temperature of the shaded soil in Table 6-1 to 310 K, the hotspot in Fig.6-3(d-3) will be sharper and, consequently, the DBT of VZA = -10° and -20° in the SPP will be lower than that of the hotspot.

6.3.3 Comparison with the parallel model

Because a parallel model always assumes that the row canopy is large enough and distributed in period, it is therefore reasonable to model the directional components' fractions and DBT within only one row period. However, as indicated above, the FOV influences the DBT distribution in the row canopy; a small FOV (e.g., 6°) of the sensor causes the DBT distribution to be dominated by the row direction and infrequently by the solar position, while a large FOV (e.g., 28°) smoothes the row-space effect and causes the DBT to distribute as a uniform, continuous canopy. As a result, the field validation of the parallel models becomes puzzling: which FOV should be used for the DBT measurement in the row canopy? Although many field studies have been conducted for validation (Chen et al. 2002; Menenti et al. 2001; Yu et al. 2004), there has been no discussion about their validity until now. Thus, the next section is devoted to identifying a proper FOV (or footprint) for the validation of the parallel model through a comparison with our new model (hereafter called FovMod).

We simulate the components' fractions and DBT using the model proposed by Yu et al. (2004) (hereafter called YuMod), with the same canopy parameters (i.e., $\boldsymbol{H}$=0.3, $\boldsymbol{L}$ = 0.6, $\boldsymbol{a}$= 0.3 in YuMod) as those in Table 6-1 but without the height of the hedgerow's bottom edge (i.e., $\boldsymbol{h}$ = 0 in YuMod), and using the FovMod at different FOVs, LAIs and other input parameters from Table 6-1. Fig.6-9 displays the comparison of the two models. The RMSEs of the DBT difference at different FOVs and LAIs (see Fig.6-9(a)) indicate that the RMSEs first decrease rapidly, and reach their local minimums at approximately FOV = 18°, and finally, increase slowly with increasing FOV. The DBT difference between the two models is slightly sensitive to the LAI value, and the influence of the LAI also depends on the FOV; the RMSE increases with increasing LAI at a FOV smaller than 18° but decreases slowly with increasing LAI at a FOV larger than 18°. A larger LAI generally reduces both models' DBT, but the YuMod's DBT is reduced more than that of the FovMod when FOV is small because the FovMod's footprint includes fewer fractions of leaves in many cases. Fig.6-9(b) displays the variations in the maximum absolute DBT difference. The curves in this figure have similar patterns to those in Fig.6-9(a), and the minimum difference is less than 1 K at FOV = 18°.

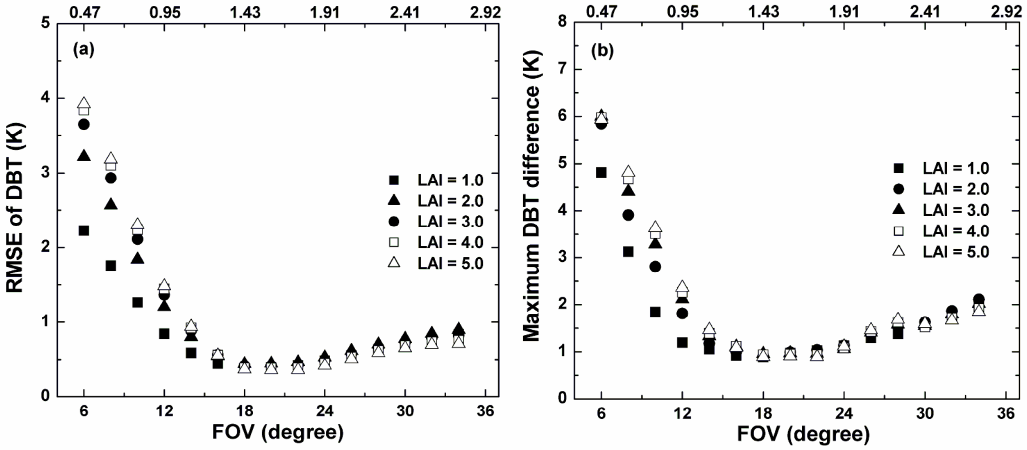

Fig.6-9. Comparison between the FovMod and YuMod. (a) and (b) are respectively DBT RMSE and maximum difference between the FovMod and the YuMod for different FOVs. The top of the horizontal axis is the number of period (NP) corresponding with the FOVs.

As seen in Fig.6-9, the FOV effect reaches its minimum at FOV = 18°, and the simulated DBT of the two models is closest in this case. However, this result does not imply that an FOV = 18° is the optimum FOV for all cases because this optimum FOV further depends on many other parameters: the width of the hedgerow and the soil, the height of the canopy, LAI, the observation height, etc. The simulation results suggest that the optimum FOV is almost independent of the solar position, so we ignore the influence of the solar position. To identify a quasi-universal optimum FOV that can reduce or eliminate the FOV effect for most cases, we introduce an index called the number of period (NP), which is defined as the ratio of the footprint's diameter $\boldsymbol{d_n}$ at the nadir observation to the total width of one row period of the canopy:

$$\boldsymbol{NP} = \boldsymbol{d_n} / (\boldsymbol{w_c} + \boldsymbol{w_s}) \text{, with } \boldsymbol{d_n} = 2(\boldsymbol{H}_0 - \boldsymbol{h}) \cdot \tan(0.5 \cdot \theta_f) . \qquad (6.17)$$

All of the terms in Eq.(6.17) are defined in Fig.6-1. The top horizontal axis in Fig.6-9 describes the NP that corresponds to the FOV displayed on the bottom axis. The optimum NP (ONP) is, theoretically, equal to the NP that results in the minimum DBT difference between YuMod and FovMod. Once the ONP is discovered, the corresponding sensor's FOV (θ_f) and footprint can be computed from the inversion of Eq.(6.17), using a known $\boldsymbol{H_0}$ and $\boldsymbol{h}$ from a field study.

Simulations are made by varying NP, $\boldsymbol{r}$ (defined in Section 6.3.2), the height-width ratio $\boldsymbol{r_{hw}}$ (=$\boldsymbol{h}$ / ($\boldsymbol{w_c}$+$\boldsymbol{w_s}$)), and LAI, as listed in Table 6-3. The other input data are the same as those in Table 6-1. Fig.6-10 displays the variations between the two models' DBT differences using a series of combined NP and $\boldsymbol{r}$, where $\boldsymbol{r_{hw}}$ equals 0.25, 0.50 and 0.75. LAI is 2.0 in all of these figures. As indicated by this figure, a larger $\boldsymbol{r_{hw}}$ can result in a bigger DBT RMSE when $\boldsymbol{r}$ is small (such as 0.1), but this effect gradually disappears with increasing $\boldsymbol{r}$. Although the RMSE is influenced by different $\boldsymbol{r}$ and $\boldsymbol{r_{hw}}$, it nearly reaches the local minimum (< 0.3 K) when NP ranges from 1.5 to 2.0 and has a larger DBT difference outside of this range, especially when NP is less than 1.5. By examining the influence of different LAIs, we found that the NP was also in the range of 1.5 ~ 2.0 when their DBT difference reached its local minimum. Therefore, the ONP should be within this range. Considering the slight variation of the ONP due to the influence of different $\boldsymbol{r}$, $\boldsymbol{r_{hw}}$ and even LAI values, we recommend taking the middle value of this range as the ONP. This value is 1.8, which suggests that if the nadir footprint of the sensor covers 1.8 times the width of one whole row structure, the DBT collected by a ground sensor on a row canopy can be regarded as the brightness temperature observed in a unique view direction. In this case, the FOV effect is essentially removed, and the measured DBT from the field study can be used to validate a parallel model with the smallest error. However, we do not recommend using a sensor whose footprint covers significantly more area than 1.8 times the row width because a larger FOV will cause the DBT distribution to resemble a uniform, continuous canopy, as discussed above.

Table 6-3. Simulation conditions for model comparison

Variables	Description	Values
NP	number of period	1.0 ~ 2.0 with a step 0.1
$\boldsymbol{r}$	ratio of the hedgerow width to the row width, $\boldsymbol{w_c}/(\boldsymbol{w_c}+\boldsymbol{w_s})$	0.1 ~ 1.0 with a step 0.1
$\boldsymbol{r_{hw}}$	height-width-ratio, $\boldsymbol{h}/(\boldsymbol{w_c}+\boldsymbol{w_s})$	0.25, 0.5, 0.75, 1.0
LAI	leaf area index	0.5, 1.0 ~ 5.0 with a step 1.0

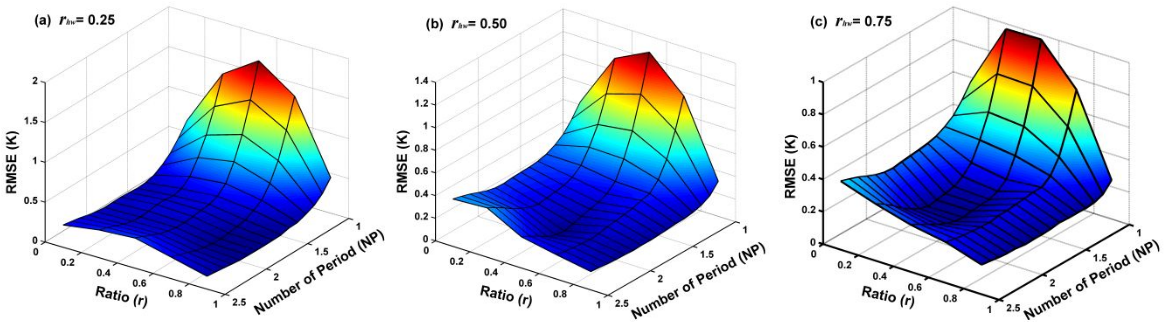

Fig.6-10. Combined influence on DBT difference between the two models from different NP (the number of period) and $\boldsymbol{r}$ with $\boldsymbol{r_{hw}}$ equal (a) 0.25, (b) 0.5 and (c) 0.75, respectively. $\boldsymbol{r_{hw}} = \boldsymbol{h}/(\boldsymbol{w_c} + \boldsymbol{w_s})$.

Note that the ONP that is recommended above was determined from only one group of components' brightness temperatures that are listed in Table 6-1. In fact, the DBT difference between the two models displayed in Fig.6-9 will vary with the components' brightness temperatures. However, because the DBT difference is caused by the different components' fractions in the two models, the variations of the components' brightness temperatures can only change the value of the DBT difference but will seldom influence the value of NP that has the local minimum difference. Therefore, the ONP of 1.8, described above, is theoretically still available for other combinations of components' brightness temperatures.

6.4 Validation

A field study was conducted on a row structured maize canopy on June 22, 2012 at Wu-xingcun (100°24' E, 38°48' N), ZhangYe City in Gansu province, China. A Multi-Angle Observation System (MAOS) was designed to automatically collect the DBT of the canopy at different azimuth and zenith angles (Yan et al. 2012), shown in Fig.6-11. The MAOS was driven by a two-dimensional automatic goniometer to take more than 13 zenith measurements in approximately six minutes at arbitrary azimuth planes, with an angle accuracy of better than 2°. One infrared thermometer (CS-LT series, manufactured by Optris Inc, Germany, with a spectral range of 8~14 μm, a temperature resolution of 0.1 K, and a FOV = 28°) was used to collect DBT on four important azimuth planes: the solar principal plane (SPP), the cross principal plane (CPP), the row azimuth plane (RAP), and the cross-row azimuth plane (CAP). Zenith measurements were made every 10° from -60° to 60°, and additional measurements were prescribed in the direction of the hotspot. The solar position was dynamically calculated from the local time and geographic data. Because the MAOS was supported by a tripod and the height of the tripod was adjustable rather than fixed, the tripod was set to have the same height with the maize canopy's average height in order to make the sensor's central point stay on the TOC all the time.

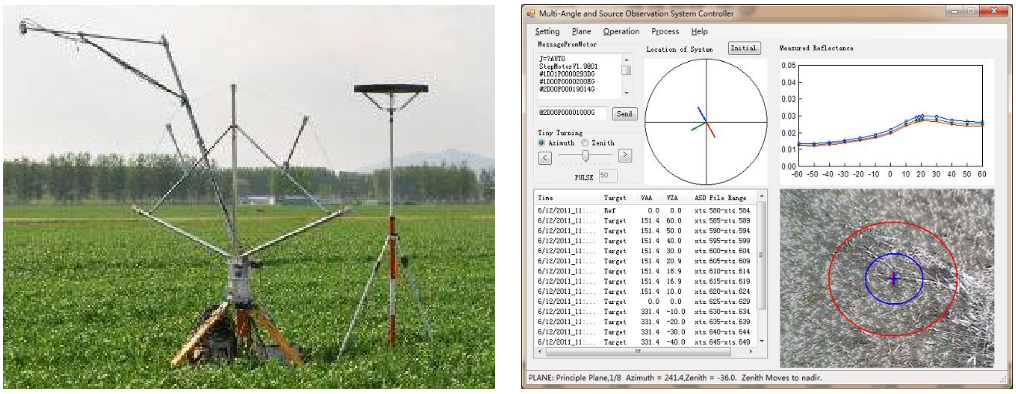

```
J=?AUTO
StepMotorV1.9@01
#1D01P0000293DG
#1D00P0000200EG
#2D00P00019014G
```

@2D00P00001000G

Time	Target	VAA	VZA	ASD File Range
6/12/2011_11:...	Ref	0.0	0.0	xts.580~xts.584
6/12/2011_11:...	Target	151.4	60.0	xts.585~xts.589
6/12/2011_11:...	Target	151.4	50.0	xts.590~xts.594
6/12/2011_11:...	Target	151.4	40.0	xts.595~xts.599
6/12/2011_11:...	Target	151.4	30.0	xts.600~xts.604
6/12/2011_11:...	Target	151.4	20.9	xts.605~xts.609
6/12/2011_11:...	Target	151.4	18.9	xts.610~xts.614
6/12/2011_11:...	Target	151.4	16.9	xts.615~xts.619
6/12/2011_11:...	Target	151.4	10.0	xts.620~xts.624
6/12/2011_11:...	Target	0.0	0.0	xts.625~xts.629
6/12/2011_11:...	Target	331.4	-10.0	xts.630~xts.634
6/12/2011_11:...	Target	331.4	-20.0	xts.635~xts.639
6/12/2011_11:...	Target	331.4	-30.0	xts.640~xts.644
6/12/2011_11:...	Target	331.4	-40.0	xts.645~xts.649

PLANE: Principle Plane,1/8 Azimuth = 241.4,Zenith = -36.0. Zenith Moves to nadir.

Fig.6-11. MAOS in operation for a field campaign (left) and its controlling system (right)

A thermal camera was used at a similar place near the MAOS, and the components' brightness temperatures can be manually extracted from the camera image, which was simultaneously collected with each angular measurement of the MAOS. This camera had a FOV of 24°×18°, corresponding to an image of 320 ×240 pixels and a temperature resolution of 0.08 K at 300 K. Both the thermometers and the camera were calibrated using a BODACH BOD series blackbody after the field measurements. The canopy and observation parameters were measured and the row direction was approximately 90°. Table 6-4 lists several input parameters for the model simulations, and. According to Eq.(6.17), the NP at the nadir of this observation was about 1.3.

Table 6-4. Some input parameters of model simulations for the maize canopy

FOV (°)	w_c (m)	w_s (m)	h (m)	H_0 (m)	φ_r (°)	x_c (m)	LAI
28	0.6	0.3	0.87	2.2	90	-0.15	3.35

Because of the storage limitation of the thermal camera and the cloud effect, only six cloud-free azimuth planes' DBT were successfully collected simultaneously with the thermal images on that day: 2 in SPP, 2 in CPP, 1 in RAP and 1 in CAP. Fig.6-12 (a) shows the DBT distribution, which was interpolated from the four-plane measurements from 12:07 to 12:24 when the average SAA and SZA were equal to 128.8° and 22.0°, respectively. The solar position was marked by a star. Unfortunately, the expected hotspot was not observed, but a hot stripe did appear in the CAP. This result may be caused by the high temporal variation in the components' brightness temperatures due to the solar illumination and local meteorological conditions. In this case, a time normalization should be applied to the DBT dataset using the four nadir measurements of each plane, as reported by Du et al. (Du et al. 2007). However, we did not apply such correction because of the strong fluctuation in the measured nadir DBT, which first decreased and then increased along the sequence of these planes, and also because the components' temperatures were extracted from simultaneous thermal images for each DBT.

Fig.6-12(b) and (c) are the simulated DBT distributions from FovMod and YuMod, respectively. They illustrate that the FovMod's DBT distribution pattern was closer to the measurements than the YuMod, especially in the CAP. The details of their differences in those azimuth planes will be described in Fig.6-13. Fig.6-12(d) displays the scatter of the measured DBT against the DBT simulated by the two models. It suggests that most of the FovMod's DBTs fell within ±1.0 K of the measurement, with a RMSE 1.2 K, which was 0.5 K lower than the YuMod (RMSE = 1.7K).

Fig.6-13 compares the measured and simulated DBT from the FovMod and YuMod in four planes, corresponding to Fig.6-12(a). The simulated DBT from both models in the SPP (128.8°/308.8°) and CPP (38.8°/218.8°) were very close to each other, as shown in Fig.6-13(a) and (b), and had angular variations that were similar to the measurement. For VZA < 0 in the SPP, the FovMod's DBTs fit the measurements with higher accuracy than the YuMod as the FovMod's results had a similar curve as the real data, especially for the VZAs from the nadir to the solar direction, while the YuMod resulted in a much smoother pattern. The measured DBTs in the middle VZAs (20°~50°) of the CPP were generally larger than the simulated values, but a relatively small DBT difference was still obtained by the FovMod.

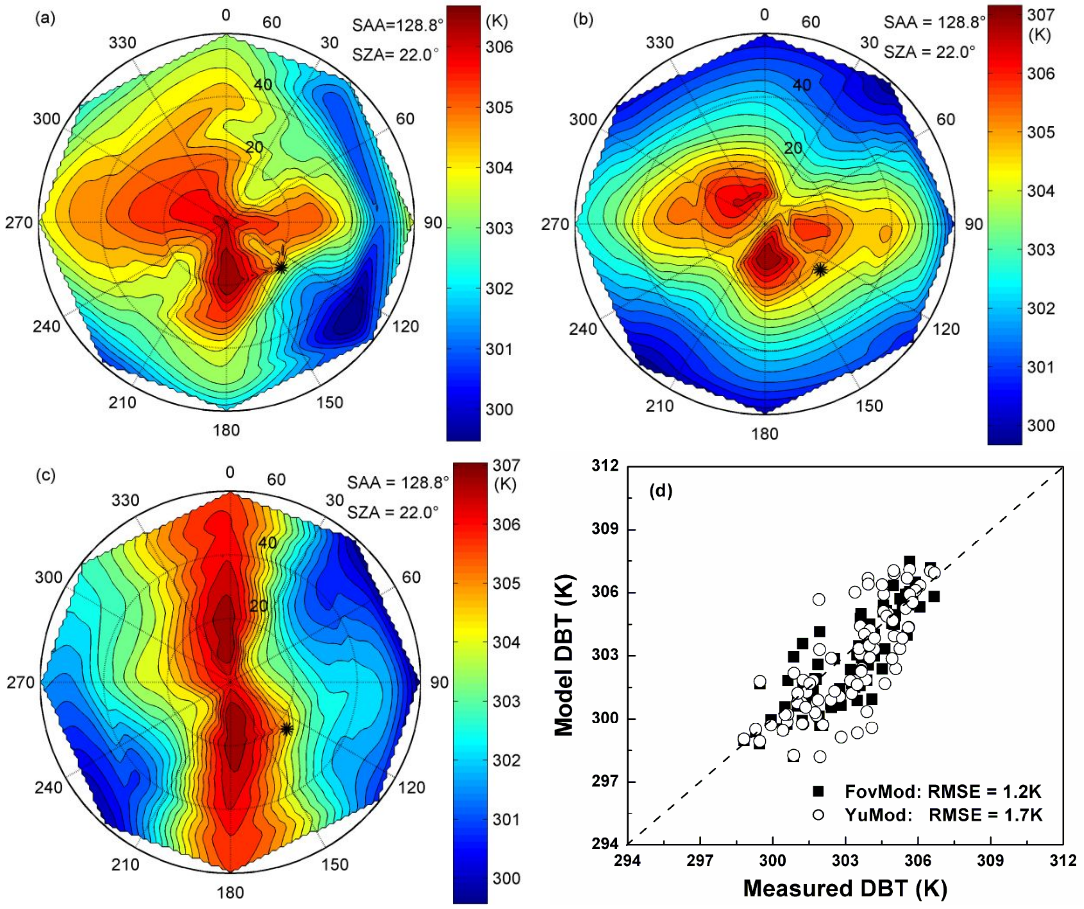

Fig.6-12. DBT distribution (a) from field measurement, (b) from FovMod simulation and (c) from YuMod simulation. The row direction was about 90° and the solar position was marked with a star. (d) Scattering of the measured DBT against the DBT simulated by FovMod and YuMod, respectively.

In the RAP (90°/270°) and CAP (0°/180°), the FovMod was generally superior to the YuMod. First, the DBT RMSEs in the FovMod were approximately 1.2 K and 1.4 K for the two planes, which was much lower than those of the YuMod (2.0 K for RAP and 2.1 K for CAP). Second, the angular variation in the FovMod was substantially similar in shape to the measurements, while the shape of the YuMod's angular variation was significantly different, especially in the curve of the CAP (Fig.6-13(d)). Fig.6-13(c) also indicates that the YuMod had a lower DBT than both the FovMod and the measured values because the central point of the thermometer's footprint fell above the background soil ($\boldsymbol{x}_c$ = -0.15 m in Table 6-4) and, consequently, the soil fraction in the footprint increased, resulting in relatively larger DBTs. However, since the YuMod simulated DBT from a whole period with regardless of the sensor's position, the components' fractions were generally dominated by the canopy structure itself and the viewing angle. Furthermore, as illustrated in Fig.6-13(d), the YuMod's DBTs in the CAP were generally larger than those of FovMod and the measurements. After examining the components' fractions respectively from FovMod and YuMod, we found that the RMSE of their leaves fraction difference ranged up to 0.14, and a larger VZA caused a larger difference. Besides, we noted that the measured DBTs had a "strange" change in the larger VZA of each plane (i.e., VZA = -60° in the SPP, 60° in the CPP and RAP, and 40° in the CAP), perhaps because the canopy did not extend infinitely, and bare soil outside of the field site covered a section of the footprint.

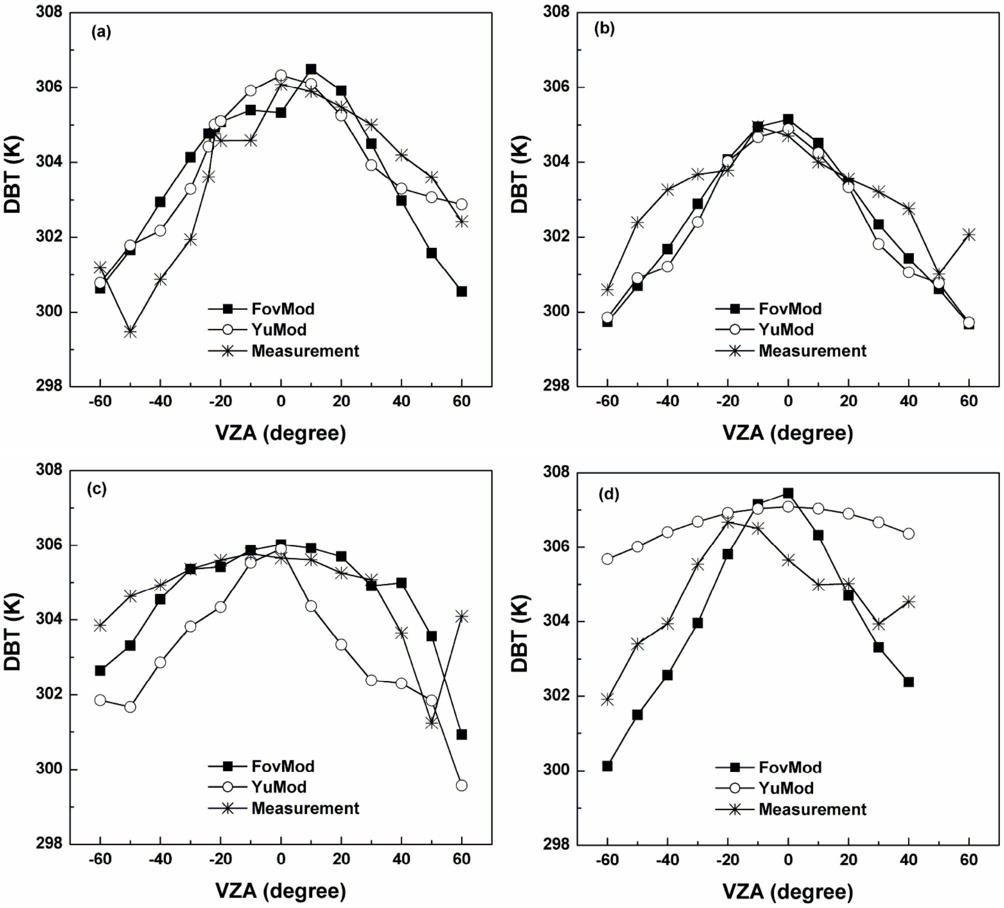

Fig.6-13. Comparison of the simulated DBT and measurement. (a) solar principle plane (SPP); (b) cross solar principle plane (CPP); (c) row azimuth plane (RAP); (d) cross-row azimuth plane (CAP). (Solar position: SAA = 128.8°, SZA = 22.0°)

The above comparison demonstrates that if the DBTs measured by the current thermometer are used to validate the YuMod, a reliable result cannot be obtained, especially in the RAP and CAP. On the other hand, the footprint effect of the thermometer for the row canopy was significant in our validation; the FovMod can simulate the DBT closer to reality than the YuMod for the row maize canopy because the FovMod concerns on the footprint of the thermometer and its central position. However, the DBT difference between the measured data and the FovMod should not be ignored. For example, the DBT in the SPP reached the local maximum at VZA = 0° of the measurements but at VZA = 10° for the FovMod. Similar cases occurred in the CPP. These differences might come from the error that was included in the input parameters of the FovMod, the components' temperatures from the thermal image as well as the calibration accuracy of the thermometer and the thermal camera.

6.5 Discussions

6.5.1 Model application and future studies

Field measurements always suffer from the unexpected changes in the footprint and, consequently, produce some strange results, but there is no practical way to eliminate them. Because the FovMod focuses on the footprint effect of the ground sensor and the calculation of the DBT is close to reality, it therefore provides an opportunity to evaluate the uncertainty of the field measurements of the row canopy. Additionally, this model can be extended to the visible and near infrared (VNIR) ranges by replacing the components’ temperatures with the components’ reflectance, but additional work is needed to investigate the transmittance and multiple scattering effects in the canopy because these two issues are larger in the VNIR than in the TIR.

The inversion of the components’ temperatures (e.g., leaves, sunlit soil and shaded soil) is possible using the new model if the canopy and observation parameters are known as a prior to calculate the component fractions in at least three viewing directions. However, because some of the parameters that are needed in the current model can be only obtained at ground level, such as $\boldsymbol{x_c}$, the inversion is currently available only for ground measurements. Future work can focus on the parameterization or simplification of the model to extend its applications.

6.5.2 Field validation in the future

This thesis validated the developed model on a maize canopy for the first time. Although the FovMod performed better than another parallel model, the footprint effect was actually reduced largely by the nearly dense canopy because the LAI was up to 3.35 at the time of the observations. In addition, the dataset for the validation was not huge enough for several reasons (i.e., the device’s storage limitation and cloudy sky). Therefore, additional validations must be made in the future on different crop canopies, such as maize and wheat. An ideal dataset should be composed of different canopy structures, observation geometries, footprints and components’ temperatures. A time-series measurement of the row canopy under different growth stages is promising and is planned as part of our future validation work.

6.6 Conclusions

This chapter proposes a new model (FovMod) to describe the directional brightness temperature (DBT) for a row canopy (mainly for the row crop canopy) by considering the footprint effect of the sensor’s FOV at ground measurement. The new FovMod divides the sensor’s footprint into numerous small cells, calculates the components’ fractions (e.g., leaves, sunlit soil and shaded soil) in each cell using the theory of gap probability, and then averages those fractions with a Gaussian PSF for the sensor’s response. The canopy’s DBT is finally obtained from the components’ fractions and their corresponding brightness temperatures. We evaluate the FovMod’s sensitivity and consistency with several key input parameters: the widths of the hedgerow and the background, LAI, the central position of the sensor’s footprint, the solar position and components’ brightness temperatures. Simulation results indicate that a small footprint of the sensor causes the DBT fraction to be dominated by the row direction and a single component’s temperature but seldom by the solar position, while a large footprint smoothes the row-space effect, causing the DBT to be distributed as a uniform, continuous canopy. Taking the parallel model developed by Yu et al.(Yu et al. 2004) for example, we introduce an index, called the number of period (NP) that is independent of the observations and canopy height to investigate the optimum footprint that can result in the smallest DBT difference between the FovMod and the parallel model. The results demonstrate that the DBT difference between the two models always reaches its minimum when NP is in the range of [1.5, 2.0], which suggests that if the diameter of a sensor’s circular footprint at the nadir covers 1.5~2.0 times the total width of a row canopy, the sensor’s footprint effect will be essentially eliminated, and the sensor measured DBT can theoretically be used to evaluate the parallel model. Finally, a validation was performed using a maize canopy, with the observing NP equal to approximately 1.3. Simultaneously measured DBTs indicated that the FovMod performed better than the YuMod. Therefore, we recommend the FovMod to simulate the DBT of a row canopy when the NP falls outside of the range of 1.5~2.0.

Chapter 7

Summary and prospective

The main work of this thesis includes: (1) finding the directional emissivity of natural surface at pixel scales and presenting the angular effect of the emissivity on land surface temperature (LST); (2) parameterizing the directional emissivity using the BRDF models and gap-frequency-based models, and validating the kernel-driven BRDF (K-BRDF) model in the angular normalization of surface temperature and investigating its requirement of the viewing angles; (3) retrieving directional emissivity and effective temperature for non-isothermal surface from daytime multi-angular middle and thermal infrared (MIR and TIR) data, and performing normalization on effective temperature from off-nadir to nadir; (4) investigating the footprint effect in the measurement of directional brightness temperature for the row canopy and providing the optimum footprint for the ground measurement and a new method to access the uncertainty in the field data. These contributions will enhance our understanding of the anisotropy of the surface thermal radiation and improve the accuracy of separating emissivity and temperature from remotely sensed data for land surface, especially for the heterogeneous surface. However, some problems are still required more work in the future.

7.1 The major finding and discussions

7.1.1 Angular effect of emissivity at pixel scale and its impact on LST

Directional emissivity for several natural land covers were extracted at pixel scale from MODIS emissivity products, driven from the day/night algorithm, and MODIS land cover products. Result showed that emissivity increased in MIR channels but decreased in TIR channels with the increase of viewing angle, and the angular variation was in a range of 0.01~0.02 in MIR channels and about 0.01 in TIR channels, but this variation can be almost ignored at viewing zenith angle (VZA) smaller than 45°. The directional emissivity was applied to the split-window algorithm to retrieve LST at 1km resolution from MODIS two adjacent TIR channels' brightness temperatures. By comparing the retrieved LST with the original MODIS LST products, it was found that the new LSTs were generally larger than the original one and their temperature discrepancy ranged from -1.0 to +3.0 K. Large viewing angles caused bigger temperature differences than smaller ones. Finally, this thesis also discussed the spatial scale effects between the retrieved LST at 1 km and 5 km, and its results denoted that the spatial scale effects of emissivity could be ignored from 5 km to 1 km in our study region probably because there was no scale effect included in the linear split-window algorithm. Besides, two look-up tables of the directional emissivity were created for further use in the future and other colleagues.

However, one should note that the directional emissivity at pixel scale from space might be partly caused or influenced by other two factors except for the viewing angle: one was residual error of the atmospheric correction although the day/night algorithm adjusted the column water vapor and near-surface air temperature; the other was the temporal and spatial variation of the emissivity itself because the directional emissivities of land covers were obtained from the statistical results of five years MODIS products in a large study area (most part of China, Mongolia and Russia). Besides, the result of the directional emissivity had to ignore the influence of soil moisture because we did not have such data at 5 km scale.

7.1.2 Parameterization of the directional emissivity and brightness temperature

Based on the directional emissivity simulated from the thermal SAIL model (TIR-SAIL) and the bi-directional reflectivity simulated from the SAILH model, we compared four parameterization models (2 BRDF models and 2 gap-frequency-based models) in the parameterization of the directional emissivity. Results showed that the kernel-driven BRDF (K-BRDF) model accurately presented the angular variation of the canopy directional emissivity, and it had to refine the cavity effect factor, which related to the multiple scattering of the canopy, in the analytical model proposed by (François et al, 1997). On basis of the new cavity effect factor and the parameterization way of the SAILH model that can estimate the components' fractions in viewing direction (Li et al, 2010), a new method was proposed to simulate the directional brightness temperature (DBT) of the canopy as the weight of several components' fractions (leaves, sunlit and shaded soils) and their temperatures as well as the multiple scattering contribution among those components. Furthermore, this thesis also investigated the application of the K-BRDF model in the angular normalization of the DBT. Results presented the local optimum three-angle combination of the K-BRDF model, and released the requirement of the VZA in the designed three arrays (nadir, forward and backward) detector system. Those findings perhaps provided some suggestions for the future design of the multi-angular thermal infrared sensor.

However, the new cavity effect factor in this thesis only be used for the SAIL series models and it may causes uncertainty if this factor is used for other radiative transfer models. The new method of simulating the DBT for the canopy was inherited from the calculation manners in the VNIR channels, but it was not validated due to the lack of the field data. Besides, since this thesis only discussed the case of three angular observation and found out the local optimum one for the K-BRDF model in the angular normalization of the temperature, more work was still needed to solve the question "what is the global angular combinations for the kernel-driven BRDF model to fit the DBT accurately?". Besides, those findings mainly concerns on the case of homogeneous canopy, so it may be not suitable for the barren or heterogeneous surface.

7.1.3 Angular moralization of emissivity and temperature using multi-angular images

In order to use the TISI (temperature-independent spectral indices) method with only daytime observed data, we combined the K-BRDF model and the TISI method to retrieve directional emissivity and effective temperature for non-isothermal surface from daytime multi-angular observed images in both middle and thermal infrared (MIR and TIR) channels. In the new daytime TISI method (called D-TISI), it has to retrieve only four unknowns: three kernel coefficients for the BRDF model, and TISIE. The MIR emissivity was obtained as the complementary to the hemispheric-directional reflectivity integrated from the BRDF model with the three kernel coefficients, and the TIR emissivity was further calculated from the MIR emissivity and TISIE. Finally, the directional effective temperature was recovered from the inversion of the radiative transfer equation in the TIR channels. Model analysis on the influence of the angular observations and the bandwidth on the retrieval accuracy showed that (1) large angle intervals among the angular observations and a larger viewing zenith angle (VZA) with respect to nadir direction can improve the retrieval accuracy of emissivity and temperature, and (2) narrow channels lead to a better result than the broad ones. Generally, the D-TISI method can obtain emissivity and temperature with an error less than 0.015 and 1.5 K if the noise included in the measured directional brightness temperature and atmospheric data was no more than 1.0 K and 10%, respectively. At last, the new method was applied to a multi-angular MIR and TIR dataset acquired by an airborne system, and a modified kernel-driven BRDF model was used to make angular normalization on the surface temperature for the first time. Results showed that it was necessary to make angular normalization on surface temperature for a higher accuracy.

However, we did not validate the retrieved nadir and off-nadir effective temperatures due to the lack of field data, and also ignored the temporal variation of surface temperature and considered the temperature variation fully caused by the changes of viewing angles because up to now there has no operational method that can be used to make time normalization of the measured DBT data from multi-angular observation. As for the multi-angular observations, pixels under different VZA had different areas, which might cause the pixels observed over the same place in different directions included different components, especially for the heterogeneous surface. This problem, along with the mis-registration between different images, might lead more uncertainty to the retrieval result. Furthermore, although this thesis discussed the influence of the angular combination on the retrieval accuracy from 4 groups angles (see Table 5-4), and recommended the optimum combination among those groups, our conclusion was very limited and more investigation is expected in the future to find the global optimum combination in the upper hemisphere.

7.1.4 Impact of sensor footprint in the measurement of the DBT for the row canopy at ground

A sensor’s footprint determines the target that is observed by the sensor and influences the angular features of the target’s DBT at the field site. Accuracy measurement of surface’s DBT at field campaign and its reasonable quality assessment is crucial for the validation of the model and the result retrieved from space. From this point of view, this thesis proposed a new model (FovMod) to describe the angular DBT for a row canopy by considering the footprint effect of the sensor’s FOV at ground measurement. The FovMod firstly divided the sensor’s circular or elliptical footprint into a few small cells, and then estimated the components’ fractions (e.g., leaves, sunlit soil and shaded soil) in each cell based on the gap probability theory. The canopy's DBT was finally obtained by weighting the components' brightness temperatures and their fractions using a Gaussian point spreading function (PSF) of the sensor's response. Simulation results indicated that a small footprint caused the distribution of the DBT to be strongly dominated by the row direction and a single component's temperature but little influenced by the solar position. On the contrary, a large footprint smoothed the row-space effect and caused the DBT to distribute as a uniform, continuous canopy. Comparison with a previous parallel model showed that if the diameter of the sensor's circular footprint extended to 1.5~2.0 times as large as the total width of the row canopy, the footprint effect was minimized, and the ground measured DBT can, theoretically, be used to evaluate the parallel model with negligible error. Finally, validations with a maize canopy demonstrated that the new model performed more accurately than the parallel model to simulate the DBT.

Actually, the FovMod provides an opportunity to assess the uncertainty in field measurements that is caused by unexpected changes in the sensor's footprint. However, because some of the parameters needed in this model can be only obtained at ground level, the inversion of the components' temperatures is currently available only for ground measurements. Therefore, the parameterization or simplification of the model is expected in the future in order to extend its applications. Besides, because the FovMod ignores the single and multiple scattering in the canopy, its expansion to VNIR channels needs more investigation because the single and multiple scattering contributions in these channels are much stronger than in the TIR channel. Moreover, more validations over different types of the row canopy were required to check the performance of the FovMod.

7.2 Prospective

The proposed D-TISI method can be also applied to the geostationary satellite data, which measures the same place at a high time frequency and it is easy to obtain multi-angular observations on the basis of the changes of solar positions as long as the atmospheric correction is operational. Additionally, it is also available for the polar-orbiting satellite sensor, such as MODIS and AVHRR, if the sensor can observe the same pixel in a short period and the emissivity of the pixel is assumed to keep unchanged. Besides, the result from the D-TISI method should be validated using field data or using the products from other sensors.

This thesis achieved this angular correction in two ways: using directional emissivity in the split-window algorithm and using the modified kernel-driven BRDF model in the multi-angular MIR and TIR data. However, the two methods are unavailable for the sensor that has neither directional emissivity nor enough multi-angular observations. Consequently, new ways are therefore still needed. Since directional effective temperature is significantly influenced by the fraction of the vegetation (FVC), it is possible to establish a relationship between the directional temperature and FVC based on the temperature-FVC triangle space method from the spatial distribution of the two variables in the study area, and use the relationship to normalize the directional temperature to that of the nadir direction. For the case that only one channel (e.g. TIR) is observed at different viewing angles, the temperature at nadir can be analytically related to those of the viewing angles based on the measured data or simulation data from thermal radiative transfer model. Besides, the combination of the polar-orbiting and geostationary satellites may be another way for angular correction on LST if they observe the same place at different directions simultaneously or quasi-simultaneously, but more attentions must be paid on the geo-registration and crossing radiative calibration between the two kinds of sensors. Besides, hyperspectral TIR data may be helpful in the angular correction to the LST because its hundreds of narrow channels' data hold much more information about the land surface than the multi-channel data.

In addition, more validation of the FovMod on different canopies, such as maize and wheat, should be conducted in the future. An ideal dataset can be composed of different canopy structures, observation geometries, footprints and components' temperatures. A time-series measurement of the row canopy under different growth stages is promising and is planned as part of our future validation work. Moreover, the comparison with other models may improve the accuracy of the FovMod.

Appendix: Acronyms

4A/OP	Operational release for 4A radiative transfer model
AATSR	Advanced Along Track Scanning Radiometer
AMSR-E	Advanced Microwave Scanning Radiometer for EOS
ASTER	Advanced Spaceborne Thermal Emission and Reflection Radiometer
AVHRR	Advanced Very High Resolution Radiometer
BOC	Bottom Of Canopy
BRDF	Bi-directional Reflectance Distribution Function
CAP	Cross-row Azimuth Plane
CBEM	Classification-Based Emissivity Retrieval Method
CPP	Cross solar Principal Plane
D/N	Day/Night algorithm
DART	Discrete Anisotropic Radiative Transfer model
DBT	Directional Brightness Temperature
D-TISI	Daytime TISI method
ECMWF	European Centre for Medium-Range Weather Forecasts
ESDR	Earth System Data Records
FAVD	Foliage Area Volumetric Density
FOV	Field Of View
FWHM	Full Width at Half Maximum
FY	FengYun sensor
GO	Geometrical Optical model
GOES	Geostationary Operational Environmental Satellite
HDF	Hierarchical Data Format
IASI	Infrared Atmospheric Sounding Interferometer
IGBP	International Geo-sphere and Biosphere Program
ISSTES	Iterative Spectrally Smooth Temperature Emissivity Separation Method
K-BRDF	Kernel-driven BRDF model
LAD	Leaf Angle Distribution
LAI	Leaf Area Index
LSE	Land Surface Emissivity
LST	Land Surface Temperature
LUT	Look-Up table

MAOS	a Multi-Angle Observation System
MIR	Middle Infrared
MODIS	Moderate Resolution Imaging Spectroradiometer
MODTRAN	MODerate spectral resolution atmospheric TRANsmittance and radiance code
MGP	Modified Geometric Projection model
MSG	Meteosat Second Generation
NASA	National Aeronautics and Space Administration
NCEP	National Centers for Environmental Prediction
NDVI	Normalized Difference Vegetation Index
NP	Number of the Period of the row canopy
PSF	Point Spreading Function
RAP	Row Azimuth Plane
RMSE	Root Mean Square Error
RT	Radiative Transfer model
SAA	Solar Azimuth Angle
SAIL	Scattering by Arbitrarily Inclined Leaves
SEVIRI	Spinning Enhanced Visible and InfraRed Imager
SPP	Solar Principal Plane
SST	Sea Surface Temperature
SZA	Solar Zenith Angle
TES	Temperature and Emissivity Separation
TIGR	Thermodynamic Initial Guess Retrieval
TIR	Thermal Infrared
TIR-SAIL	Thermal SAIL model
TISI	Temperature-Independent Spectral Indices
TM	Thematic Mapper
TOA	Top of Atmosphere
TOC	Top Of Canopy
TTM	Two-Temperature Method
UCSB	University of California Santa Barbara library
VAA	Viewing Azimuth Angle
VNIR	Visible/Near infrared
VZA	Viewing Zenith Angle
WATER	Watershed Allied Telemetry Experimental Research campaign
WiDAS	Wide-angle infrared Dual-mode line/area Array Scanner
WV	Water Vapor

Reference

Atitar, M., & Sobrino, J.A. (2009). A split-window algorithm for estimating LST from Meteosat 9 data: Test and comparison with in situ data and MODIS LSTs. ***IEEE Geosicence and Remote Sensing Letters, 6***, 122-126

Baldridge, A.M., Hook, S.J., Grove, C.I., & Rivera, G. (2009). The ASTER spectral library version 2.0. ***Remote Sensing of Environment, 113***, 711-715

Barducci, A., & Pippi, I. (1996). Temperature and emissivity retrieval from remotely sensed images using the grey body emissivity method. ***IEEE Transactions on Geoscience and Remote Sensing, 34***, 681-695

Becker, F. (1987). The impact of spectral emissivity on the measurement of land surface temperature from a satellite. ***International Journal of Remote Sensing, 8***, 1509-1522

Becker, F., & Li, Z.-L. (1995). Surface temperature and emissivity at various scales: Definition, measurement and related problems. ***Remote Sensing Reviews, 12***, 225-253

Becker, F., & Li, Z.-L (1990a). Temperature-independent spectral indices in thermal infrared bands. ***Remote Sensing of Environment, 32***, 17-33

Becker, F., & Li, Z.-L (1990b). Towards a local split window method over land surfaces. ***International Journal of Remote Sensing, 11***, 369-393

Berk, A., Anderson, G.P., Acharya, P.K., Hoke, M.L., Chetwynd, J.H., Bernstein, L.S., Shettle, E.P., & Matthew, M.W. (2003). MODTRAN4 version 3 revision 1 user's manual. ***Air Force Research Lab. Hanscom AFB, MA***

Borel, C.C. (1998). Surface emissivity and temperature retrieval for a hyperspectral sensor. ***IEEE International Geoscience and Remote Sensing Symposium, 1***, 546-549

Carlson, T.N., & Ripley, D.A. (1997). On the relation between NDVI, fractional vegetation cover, and leaf area index. ***Remote Sensing of Environment, 62***, 241-252

Caselles, E., Valor, E., Abad, F., & Caselles, V. (2012). Automatic classification-based generation of thermal infrared land surface emissivity maps using AATSR data over Europe. ***Remote Sensing of Environment, 124***, 321-333

Chaumat, L., Standfuss, C., Tournier, B., Armante, R., & Scott, N. (2009). 4A/OP reference documentation ***NOV-3049-NT-1178-v4.0. NOVELTIS, LMD/CNRS, CNES***

Chehbouni, A., Y.Nouvellon, Kerr, Y.H., Moran, M.S., Watts, C., Prevot, L., D.C, G., & Rambal, S. (2001). Directional effect on radiative surface temperature measurements over a semiarid grassland site. ***Remote Sensing of Environment, 76***, 360-372

Chen, L., Yan, G., Li, J., & Yu, Y. (2009). Footprint uncertainty analysis for ground-based multiangular measurement of row crops. ***Advances in Earth Science, 24***, 793-802

Chen, L.F., Liu, Q., Fan, W., Li, X., Xiao, Q., Yan, G., & Tian, G. (2002). A bi-directional gap model for simulating the directional thermal radiance of row crops. ***Science in China (Series D), 45***, 1087-1098

Chen, L.F., Li, Z.-L., Liu, Q.H., Chen, S., Tang, Y., & Zhong, B. (2004). Definition of component effective emissivity for heterogeneous and non-isothermal surfaces and its approximate calculation. ***International Journal of Remote Sensing, 25***, 231-244

Chen, S.-S., Chen, X.-Z., Chen, W.-Q., Su, Y.-X., & Li, D. (2011). A simple retrieval method of land surface temperature from AMSR-E passive microwave data-Case study over Southern China during the strong snow disaster of 2008. ***International Journal of Applied Earth Observation and Geoinformation, 13***, 140-151

Cheng, J., Liang, S., Wang, J., & Li, X. (2010). A stepwise refining algorithm of temperature and emissivity separation for hyperspectral thermal infrared data. ***IEEE Transactions on Geoscience and Remote Sensing, 48***, 1588-1597

Cheng, J., Liu, Q., Li, X., Xiao, Q., Liu, Q., & Du, Y. (2008). Correlation-based temperature and emissivity separation algorithm. ***Science in China(Series D), 51***, 363-372

Colaizz, P.D., O'Shaughnessy, S.A., Gowda, P.H., Evett, S.R., Howell, T.A., Kustas, W.P., & Anderson, M.C. (2010). Radiometer footprint model to estimate sunlit and shaded components for row crops. ***Agronomy journal, 102***, 942-955

Coll, C., & Caselles, V. (1997). A split-window algorithm for land surface temperature from advanced very high resolution radiometer data: Validation and algorithm comparison. ***Journal of Geophysical Research, 102***, 16697-16713

Coll, C., Caselles, V., Valor, E., Niclòs, R., Sánchez, J.M., Galve, J.M., & Mira, M. (2007). Temperature and emissivity separation from ASTER data for low spectral contrast surfaces. ***Remote Sensing of Environment, 110***, 162-175

Coret, L., Briottet, X., Kerr, Y.H., & Chehbouni, A. (2004). Simulation study of view angle effects on thermal infrared measurements over heterogeneous surfaces. ***Geoscience and Remote Sensing, IEEE Transactions on, 42***, 664-672

Dash, P., Gottsche, F.-M., Olesen, F.-S., & Fischer, H. (2005). Separating surface emissivity and temperature using two-channel spectral indices and emissivity composites and comparison with a vegetation fraction method. ***Remote Sensing of Environment, 96***, 1-17

Du, Y., Liu, Q., Chen, L., Liu, Q., & Yu, T. (2007). Modeling directional brightness temperature of the winter wheat canopy at the ear stage. ***IEEE Transactions on Geoscience and Remote Sensing, 45***, 3721-3739

Duan, S., Yan, G., Qian, Y., Li, Z.-L., Jiang, X., & Li, X. (2008). Retrieval of land surface temperature from simulated HJ-1B data using two different single channel methods. ***Progress in Natural Science(Chinese Journal with English abstract), 18***, 1001-1008

Fang, L., Liu, Q., Xiao, Q., Liu, Q., & Liu, Z. (2009). Design and implementation of airborne Wide-angle Infrared Dual-mode line/area Array Scanner in Heihe experiment. ***Advances in Earth Science(Chinese Journal with English abstract), 24***, 696-704

François, C. (2002). The potential of directional radiometric temperatures for monitoring soil and leaf temperature and soil moisture status. ***Remote Sensing of Environment, 80***, 122-133

François, C., Ottlé, C., & Prévot, L. (1997). Analytical parameterization of canopy directional emissivity and directional radiance in the thermal infrared. Application on the retrieval of soil and foliage temperatures using two directional measurements. ***International Journal of Remote Sensing, 18***, 2587-2621

Friedl, M.A., Mciver, D.K., Hodges, J.C.F., Zhang, X.Y., Muchoney, D., Strahler, A.H., Woodcock, C.E., Gopal, S., Schneider, A., Cooper, A., Baccini, A., Gao, F., & Schaaf, C. (2002). Global land cover mapping from MODIS: Algorithms and early results. ***Remote Sensing of Environment, 83***, 168-182

Gastellu-Etchegorry, J.P., Demarez, V., Pinel, V., & Zagolski, F. (1996). Modeling radiative transfer in heterogeneous 3-D vegetation canopies. ***Remote Sensing of Environment, 58***, 131-156

Gillespie, A. (1995). Lithologic mapping of silicate rocks using TIMS. ***in TIMS Data Users’ Workshop. Pasadena, CA: Jet Propul. Lab., JPL Publication 86-38***, 29-44

Gillespie, A., Rokugawa, S., Matsuuaga, T., Cothern, J.S., Hook, S., & Kahle, A.B. (1998). A temperature and emissivity separation algorithm for Advanced Spaceborne Thermal Emission and Reflection Radiometer (ASTER) images. ***IEEE Transactions on Geoscience and Remote Sensing, 36***, 1113-1126

Gillespie, A.R., Abbott, E.A., Gilson, L., Jiménez-Muñoz, J.-C., & Sobrino, J.A. (2011). Residual errors in ASTER temperature and emissivity standard products. ***Remote Sensing of Environment, 115***, 3681-3694

Goïta, K., & Royer, A. (1997). Surface temperature and emissivity separability over land surface from combined TIR and SWIR AVHRR data. ***IEEE Transactions on Geoscience and Remote Sensing, 35***, 718-733

Griend, V.D., & Owe, M. (1993). On the relationship between thermal emissivity and the normalized difference vegetation index for natural surfaces. ***International Journal of Remote Sensing, 14***, 1119-1131

Gustafson, W.T., Gillespie, A.R., & Yamada, G. (2006). Revisions to the ASTER temperature/emissivity separation algorithm. ***in Proc.2nd Recent Advance Quantitative Remote Sensing, Valencia, Spain***, 770-775

Hansen, M.C., DeFries, R.S., Townshend, J.R.G., Carroll, M., Dimiceli, C., & Sohlberg, R.A. (2003). Global percent tree cover at a spatial resolution of 500 meters: First results of the MODIS vegetation continuous fields algorithm. ***Earth Interactions, 7***, 1-15

Huang, C., Townshend, J.R.G., Liang, S., Kalluri, S.N.V., & DeFries, R.S. (2002). Impact of sensor's point spread function on land cover characterization: assessment and deconvolution. ***Remote Sensing of Environment, 80***, 203-212

Huang, H., Liu, Q., & Qin, W. (2010). Thermal emission hot-spot effect of crop canopies-part I: Simulation. ***IEEE Journal of Selected Topics in Applied Earth Observations and Remote Sensing, 3***, 313-322

Hulley, G.C., & Hook, S.J. (2011). Generating consistent land surface temperature and emissivity products between ASTER and MODIS data for earth science research. ***IEEE Transactions on Geoscience and Remote Sensing, 49***, 1304-1315

Hulley, G.C., Hook, S.J., & Schneider, P. (2011). Optimized split-window coefficients for deriving surface temperatures from inland water bodies. ***Remote Sensing of Environment, 115***, 3758-3769

Ingram, P.M., & Muse, A.H. (2001). Sensitivity of iterative spectrally smooth temperature/emissivity separation to algorithmic assumptions and measurement noise. ***IEEE Transactions on Geoscience and Remote Sensing, 39***, 2158-2257

Jackson, R.D., Reginato, R.J., Paul J. Pinter, J., & Idso, S.B. (1979). Plant canopy information extraction from composite scene reflectance of row crops. ***Applied Optics, 18***, 3775-3782

Jacob, F., Petitcolin, F.o., Schmugge, T., Vermote, É., French, A., & Ogawa, K. (2004). Comparison of land surface emissivity and radiometric temperature derived from MODIS and ASTER sensors. ***Remote Sensing of Environment, 90***, 137-152

Jacquemoud, S., Verhoef, W., Baret, F., Bacour, C., Zarco-Tejada, P.J., Asner, G.P., François, C., & Ustin, S.L. (2009). ROSPECT+SAIL models: A review of use for vegetation characterization. ***Remote Sensing of Environment, 113***, S56-S66,doi:10.1016/j.rse.2008.1001.1026

Jia, L., Li, Z.-L., Menenti, M., Su, Z., Verhoef, W., & Wan, Z. (2003). A practical algorithm to infer soil and foliage component temperatures from bi-angular ATSR-2 data. ***International Journal of Remote Sensing, 24***, 4739-4760

Jiang, G.-M., & Li, Z.-L. (2008a). Intercomparison of two BRDF models in the estimation of the directional emissivity in MIR channel from MSG1-SEVIRI data. ***Optic Express, 16***, 19310-19321

Jiang, G.-M., & Li, Z.-L. (2008b). Split-window algorithm for land surface temperature estimation from MSG1-SEVIRI data. ***International Journal of Remote Sensing, 29***, 6067-6074

Jiang, G.-M., Li, Z.-L., & Nerry, F. (2006). Land surface emissivity retrieval from combined mid-infrared and thermal infrared data of MSG-SEVIRI. ***Remote Sensing of Environment, 105***, 326-340

Jiménez-Muńoz, & Cristóbal, J. (2009). Revision of the single-channel algorithm for land surface temperature retrieval from Landsat thermal-infrared data. ***IEEE Transactions on Geoscience and Remote Sensing, 47***, 339-349

Jimenez-Munoz, J.C., & Sobrino, J.A. (2007). Feasibility of retrieving land-surface temperature from ASTER TIR bands using two-channel agorithms: A case study of agricultural areas. ***IEEE Geoscience and Remote Sensing Letters, 4***, 60-64

Jiménez-Muńoz, J.C., & Sobrino, J.A. (2003). A generalized single-channel method for retrieving land surface temperature from remote sensing data. ***Journal of Geophysical Research, 108***, 4688, doi:4610.1029/2003JD003480

Kealy, P.S., & Hook, S.J. (1993). Separating temperature and emissivity in thermal infrared multispectral scanner data: Implications for recovering land surface temperatures. ***IEEE Transactions on Geoscience and Remote Sensing, 31***, 1155-1164

Kerr, Y.H., Lagouarde, J.P., & Imbernon, J. (1992). Accurate land surface temperature retrieval from AVHRR data with use of an improved split window algorithm. ***Remote Sensing of Environment, 41***, 197-209

Kimes, D.S. (1981). Remote sensing of temperature profiles in vegetation canopies using multiple view angles and inversion techniques. ***IEEE Transactions on Geoscience and Remote Sensing, GE-19***, 85-90

Kimes, D.S. (1983). Remote sensing of row crop structure and component temperatures using directional radiometric temperatures and inversion techniques. ***Remote Sensing of Environment, 13***, 33-55

Kimes, D.S., Idso, S.B., Pinter Jr, P.J., Reginato, R.J., & Jackson, R.D. (1980). View angle effects in the radiometric measurement of plant canopy temperatures. ***Remote Sensing of Environment, 10***, 273-284

Kimes, D.S., & Kirchener, J.A. (1983). Directional radiometric measurements of row-crop temperatures. ***International Journal of Remote Sensing, 4***, 299-311

Kimes, D.S., Smith, J.A., & Link, L.E. (1981). Thermal IR exitance model of a plant canopy. ***Applied Optics, 20***, 624-642

Kuusk, A. (1985). The hot spot effect on a uniform vegetative cover. ***Soviet Journal of Remote Sensing, 3***, 645-658

Lagouarde, J.-P., Hénon, A., Kurz, B., Moreau, P., M.Irvine, Voogt, J., & P.Mestayer (2010). Modelling daytime thermal infrared directional anisotropy over Toulouse City centre. ***Remote Sensing of Environment, 114***, 87-105

Lagouarde, J.-P., Moreaua, P., Irvine, M., Bonnefonda, J.-M., & Coll, C. (2004). Airborne experimental measurements of the angular variations in surface temperature over urban areas: case study of Marseille (France). ***Remote Sensing of Environment, 93***, 443-462

Lagouarde, J.-P., & Irvine, M. (2008). Directional anisotropy in thermal infrared measurements over Toulouse city centre during the CAPITOUL measurement campaigns: First results. ***Meteorology and Atmospheric Physics, 102***, 173-185

Lagouarde, J.P., Kerr, Y.H., & Brunnet, Y. (1995). An experimental study of angular effects on surface temperature for various plant canopies and bare soils. ***Agricultural and Forest Meteorology, 77***, 167-190

Li, F., Jackson, T.J., Kustas, W.P., Schmugge, T.J., French, A.N., Cosh, M.H., & Bindlish, R. (2004a). Deriving land surface temperature from Landsat 5 and 7 during SMEX02/SMACEX. ***Remote Sensing of Environment, 92***, 521-534

Li, J., Yan, G., & Mu, X. (2010). A parameterized SAILH model for LAI retrieval. ***Journal of Remote Sensing, 14***, 1182-1195

Li, X., Li, X., Li, Z., Ma, M., Wang, J., Xiao, Q., Liu, Q., Che, T., Chen, E., Yan, G., Hu, Z., Zhang, L., Chu, R., Su, P., Liu, Q., Liu, S., Wang, J., Niu, Z., Chen, Y., Jin, R., Wang, W., Ran, Y., Xin, X., & Ren, H. (2009). Watershed Allied Telemetry Experimental Research. ***Journal of Geophysical Research, 114, D22103, doi:10.1029/2008JD011590***

Li, X., & Strahler, A.H. (1988). Modeling the gap probability of a discontinuous vegetation canopy. ***IEEE Transactions on Geoscience and Remote Sensing, 26***, 161-170

Li, X., & Strahler, A.H. (1992). Geometric-optical bidirectional reflectance modeling of the discrete crown vegetation canopy: Effect of crown shape and mutual shadowing. ***IEEE Transactions on Geoscience and Remote Sensing, 30***, 276-292

Li, X., Strahler, A.H., & Fried, M.A. (1999). A conceptual model for directional effective emissivity from nonisothermal surfaces. ***IEEE Transactions on Geoscience and Remote Sensing, 37***, 2508-2517

Li, Z.-L., & Becker, F. (1990). Properties and comparison of temperature-independent thermal infrared spectral indices with NDVI for HAPEX data. ***Remote Sensing of Environment, 33***, 165-182

Li, Z.-L., & Becker, F. (1993). Feasibility of land surface temperature and emissivity determination from AVHRR data. ***Remote Sensing of Environment, 43***, 67-85

Li, Z.-L., Tang, B.-H., Wu, H., Ren, H., Yan, G., Wan, Z., Trigo, I.F., & Sobrino, J.A. (2013a). Satellite-derived land surface temperature: Current status and perspectives. ***Remote Sensing of Environment, 131***, 14-37

Li, Z.-L., Wu, H., Wang, N., Qiu, S., Sobrino, J.A., Wan, Z., Tang, B.-H., & Yan, G. (2013b). Land surface emissivity retrieval from satellite data. ***International Journal of Remote Sensing, 34***, 3084-3127

Li, Z.-L., Zhang, R., Sun, X., Su, H., Tang, X., Zhu, Z., & Sobrino, J.A. (2004b). Experimental system for the study of the directional thermal emission of natural surfaces. ***International Journal of Remote Sensing, 25***, 195-204

Li, Z.-L, Petitcolin, F., & Zhang, R. (2000). A physically based algorithm for land surface emissivity retrieval from combined mid-infrared and thermal infrared data. ***Science in China Series E: Technological Sciences, 43***, 23-33

Li, Z.-L., Stoll, M.P., Zhang, R.H., Jia, L., & Su, Z.B. (2001). On the separate retrieval of soil and vegetation temperatures from ATSR data. ***Science in China Series D: Earth Sciences, 44***, 97-111

Liu, Q., Chen, L., Liu, Q., & Xiao, Q. (2003). A radiation transfer model to predict canopy radiation in thermal infrared band. ***Journal of Remote Sensing, 7***, 161-167

Liu, Q., Yan, C., Xiao, Q., Yan, G., & Fang, L. (2012). Separating vegetation and soil temperature using airborne multiangular remote sensing image data. ***International Journal of Applied Earth Observation and Geoinformation, 17***, 66-75

Lucht, W., & Roujean, J. (2000). Considerations in the parametric modeling of BRDF and albedo from multiangular satellite sensor observations. ***Remote Sensing Reviews, 18***, 343-379

Ma, X.L., Wan, Z., Moeller, C.C., Menzel, W.P., & Gumley, L.E. (2002). Simultaneous retrieval of atmospheric profiles, land-surface temperature, and surface emissivity from Moderate-Resolution Imaging Spectroradiometer thermal infrared data: Extension of a two-step physical algorithm. ***Applied Optics, 41***, 909-924

Ma, X.L., Wan, Z., Moeller, C.C., Menzel, W.P., Gumley, L.E., & Zhang, Y. (2000). Retrieval of geophysical parameters from Moderate Resolution Imaging Spectroradiometer thermal infrared data: Evaluation of a two-step physical algorithm. ***Applied Optics, 39***, 3537-3550

Mannstein., H. (1987). Surface energy budget, surface temperature, and thermal inertia. ***Remote Sensing Applications in Meteorology and Climatology, R.A Vaughan and D.Reidel, Eds., Netherlands:Dordrecht***

Mao, K., Shi, J., Tang, H., Guo, Y., Qiu, Y., & Li, L. (2007). A neural-network technique for retrieving land surface temperature from AMSR-E passive microwave data. ***IEEE International Geoscience and Remote Sensing Symposium***, 4422-4425

Matsunaga, T. (1994). A temperature-emissivity separation method using an empirical relationship between the mean, the maximum, and the minimum of the thermal infrared emissivity spectrum. ***Journal of the Remote Sensing Society of Japan, 14***, 230-241

McMillin, M.L. (1975). Estimation of sea surface temperatures from two infrared window measurements with different absorption. ***Journal of Geophysical Research, 80***, 5113-5117

Menenti, M., Jia, L., Li, Z.-L., Djepa, V., Wang, J., Stoll, M.P., Su, Z., & Rast, M. (2001). Estimation of soil and vegetation temperatures with multiangular thermal infrared observations: IMGRASS, HEIFE, and SGP 1997 experiments. ***Journal of Geophysical Research, 106***, 11997-11912,11010

Mildrexler, D.J., Zhao, M., & Runing, S.W. (2011). Satellite finds highest land skin temperatures on earth. ***Bulletin of the American Meteorological Society, 92***, 855-860

Minnaert, M. (1941). The reciprocity principle in lunar photometry. ***Astrophysical Journal, 93***, 403-410

Minnis, P., & Khaiyer, M.M. (2000). Anisotropy of land surface skin temperature derived from satellite data. ***Journal of Applied Meteorology, 39***, 1117-1129

Momeni, M., & Saradjian, M.R. (2007). Evaluating NDVI-based emissivities of MODIS bands 31 and 32 using emissivities derived by Day/Night LST algorithm. ***Remote Sensing of Environment, 106***, 190-198

Myneni, R.B., Ross, J., & Asrar, G. (1989). A review on the theory of photo transport in leaf canopies. ***Agricultural and Forest Meteorology, 45***, 1-153

Nerry, F., Petitcolin, F., & Stoll, M.P. (1998). Bidirectional Reflectivity in AVHRR Channel 3: Application to a Region in Northern Africa. ***Remote Sensing of Environment, 66***, 298-316

Nilson, T. (1971). A theoretical analysis of the frequency of gaps in plant stands. ***Agricultural Meteorology, 8***, 25-38

Norman, J., & Becker, F. (1995). Terminology in thermal infrared remote sensing of natural surface. ***Agriculture and Forest Meteorology, 77***, 154-176

Nouvellon, Y., Bégué, A., Moran, M.S., Seen, D.L., Rambal, S., Luquet, D., Chehbouni, G., & Inoue, Y. (2000). PAR extinction in shortgrass ecosystems: Effects of clumping, sky conditions and soil albedo. ***Agricultural and Forest Meteorology, 105***, 21-42

Otterman, J., Brakke, T.W., Fuchs, M., Lakshmi, V., & Cadeddu, M. (1999). Longwave emission from a plant/soil surface as a function of the view direction: Dependence on the canopy architecture. ***International Journal of Remote Sensing, 20***, 2195-2201

Otterman, J., Brakke, T.W., & Susskind, J. (1992). A model for inferring canopy and underlying soil temperatures from multi-directional measurements. ***Boundary-Layer Meteorology, 61***, 81-97

Otterman, J., Starr, D., Brakke, T., Davies, R., Jacobowitz, H., Mehta, A., Cheruy, F., & Prabhakara, C. (1997). Modeling zenith-angle dependence of outgoing longwave radiation: Implication for flux measurements. ***Remote Sensing of Environment, 62***, 90-100

Otterman, J., Susskind, J., Brakke, T., Kimes, D., Pielke, R., & Lee, T.J. (1995). Inferring the thermal-infrared hemispheric emission from a sparsely-vegetated surface by directional measurements. ***Boundary-Layer Meteorology, 74***, 163-180

Ottlé, C., & Stoll, M. (1993). Effect of atmospheric absorption and surface emissivity on the determaination of land surface temperature from infrared satellite data. ***International Journal of Remote Sensing, 14***, 2025-2037

Payan, V., & Royer, A. (2004). Analysis of temperature emissivity separation (TES) algorithm applicability and sensitivity. ***International Journal of Remote Sensing, 25***, 15-37

Peng, J., Liu, Q., Liu, Q., Li, J., Ma, H., & Li, F. (2011). Kernel-driven model fitting of multi-angle thermal infrared brightness temperature and its applicaion. ***Journal of Infrared and Millimeter Waves, 30***, 361-365

Peres, L.F., & DaCamara, C.C. (2004a). Inverse problems theory and application: analysis of the Two-Temperature Method for land-surface temperature and emissivity estimation. ***IEEE Geoscience and Remote Sensing Letters, 1***, 206-210

Peres, L.F., & DaCamara, C.C. (2004b). Land surface temperature and emissivity estimation based on the two-temperature method: sensitivity analysis using simulated MSG/SEVIRI data. ***Remote Sensing of Environment, 91***, 377-389

Peres, L.F., & DaCamara, C.C. (2005). Emissivity maps to retrieve land-surface temperature from MSG/SEVIRI. ***IEEE Transactions on Geoscience and Remote Sensing, 43***, 1834-1844

Peres, L.F., & DaCamara, C.C. (2006). Improving two-temperature method retrievals based on a nonlinear optimization approach. ***IEEE Geosicence and Remote Sensing Letters, 3***, 232-236

Perry, E.M., & Moran, M.S. (1994). An evaluation of atmospheric corrections of radiometric surface temperatures for a semiarid rangeland watershed. ***Water Resources Research, 30***, 1261-1269

Petitcolin, F., Nerry, F., & Stoll, M.-P. (2002a). Mapping temperature independent spectral indices of emissivity and directional emissivity in AVHRR channels 4 and 5. ***International Journal of Remote Sensing, 23***, 3473-3491

Petitcolin, F., Nerry, F., & Stoll, M.-P. (2002b). Mapping directional emissivity at 3.7 μm using a simple model of bi-directional reflectivity. ***International Journal of Remote Sensing, 23***, 3443-3472

Petitcolin, F., & Vermote, E. (2002). Land surface reflectance, emissivity and temperature from MODIS middle and thermal infrared data. ***Remote Sensing of Environment, 83***, 112-134

Phinheiro, A.C.T., Mahoney, R., Privette, J.L., & Tucker, C.J. (2006). Development of a daily long term record of NOAA-14 AVHRR land surface temperature over Africa. ***Remote Sensing of Environment, 103***, 153-164

Pinheiro, A.C.T., Privette, J.L., Mahoney, R., & Tucker, C.J. (2004). Directional effects in a daily AVHRR land surface temperature dataset over Africa. ***IEEE Transactions on Geoscience and Remote Sensing, 42***, 1941-1954

Prata, A.J. (1993). Land surface temperatures derived from the Advanced Very High Resolution Radiometer and the Along-Track Scanning Radiometer 1. Theory. ***Journal of Geophysical Research, 98***, 16689-16702

Prata, A.J., Caselles, V., Coll, C., Sobrino, J.A., Ottlé, C., & C.Jiménez-Muńoz (1995). Thermal remote sensing of land surface temperature from satellites: Currents status and future prospects. ***Remote Sensing Reviews, 12***, 175-224

Prévot, L. (1985). Modélisation des échanges radiatifs au sein des couverts végétaux. Application a la télédétection. Validation sur un couvert de mais. ***Doctoral Thesis, University of Paris VI, France***

Qin, Z., Karnieli, A., & Berliner, P. (2001). A mono-window algorithm for retrieving land surface temperature from Landsat TM data and its application to the Israel-Egypt border region. ***International Journal of Remote Sensing, 22***, 3719-3746

Rasmussen, M.O., Göttsche, F.-M., Olesen, F.-S., & Sandholt, I. (2011). Directional effects on land surface temperature estimation from Meteosat Second Generation for savanna landscapes. ***IEEE Transactions on Geoscience and Remote Sensing, 49***, 4458-4468

Rasmussen, M.O., Pinheiro, A.C., Proud, S.R., & Sandholt, I. (2010). Modeling angular dependences in land surface temperatures from the SEVIRI instrument onboard the Geostationary Meteosat Second Generation satellites. ***IEEE Transactions on Geoscience and Remote Sensing, 48***, 3123-3133

Rodriguez-Galiano, V., & Chica-Olmo, M. (2012). Land cover change analysis of a Mediterranean area in Spain using different sources of data: Multi-seasonal Landsat images, land surface temperature, digital terrain models and texture. ***Applied Geography, 35***, 208-218

Ross, J. (1981). The radiation regime and architecture of plant stands. ***Dr. W. Junk Publishers, The Hague, 392***

Roujean, J.-L. (2000). A parametric hot spot model for optical remote sensing applications. ***Remote Sensing of Environment, 71***, 197-206

Roujean, J.-L., Leroy, M., & Deschamps, P.Y. (1992). A bidirectional reflectance model of the Earth's surface for the correction of remote sensing data. ***Journal of Geophysical Research, 97***, 20455-20468

Rubio, E., Caselles, V., & Badenas, C. (1997). Emissivity measurements of several soils and vegetation types in the 8-14 µm wave band: Analysis of two field methods. ***Remote Sensing of Environment, 59***, 490-521

Rubio, E., Caselles, V., Coll, C., Valour, E., & Sospedra, F. (2003). Thermal-infrared emissivities of natural surfaces: Improvements on the experimental set-up and new measurements. ***International Journal of Remote Sensing, 24***, 5379-5390

Sabol, J., Gillespie, A.R., Abbott, E., & Yamada, G. (2009). Field validation of the ASTER Temperature-Emissivity Separation algorithm. ***Remote Sensing of Environment, 113***, 2328-2344

Salisbury, J.W., & D'Aria, D.M. (1992). Emissivity of terrestrial materials in the 8-14 μm atmospheric window. ***Remote Sensing of Environment, 42***, 83-106

Schmugge, T., Hook, S.J., & Coll, C. (1998). Recovering surface temperature and emissivity from thermal infrared multispectral data. ***Remote Sensing of Environment, 65***, 121-131

Shi, Y. (2011). Thermal infrared inverse model for component temperatures of mixed pixels. ***International Journal of Remote Sensing, 32***, 2297-2309

Sims, D.A., Rahman, A.F., Cordova, V.D., El-Masri, B.Z., Baldocchi, D.D., Bolstad, P.V., Flanagan, L.B., Goldstein, A.H., Hollinger, D.Y., Misson, L., Monson, R.K., Oechel, W.C., Schmid, H.P., Wofsy, S.C., & Xu, L. (2008). A new model of gross primary productivity for North American ecosystems based solely on the enhanced vegetation index and land surface temperature from MODIS. ***Remote Sensing of Environment, 112***, 1633-1646

Smith, J.A., & Ballard, J.R. (2001). Thermal infrared hot spot and dependence on canopy geometry. ***Optical Engineering, 40***, 1435-1437

Snyder, W.C., & Wan, Z. (1998). BRDF models to predict spectral reflectance and emissivity in the thermal infrared. ***IEEE Transactions on Geoscience and Remote Sensing, 36***, 214-225

Snyder, W.C., Wan, Z., & Feng, Y.-Z. (1998). Classification-based emissivity for land surface temperature measurement from space. ***International Journal of Remote Sensing, 9***, 2753-2774

Sobrino, J.A., & Caselles, V. (1990). Thermal infrared radiance model for interpreting the directional radiometric temperature of a vegetative surface. ***Remote Sensing of Environment, 33***, 193-199

Sobrino, J.A., & Cuenca, J. (1999). Angular variation of thermal infrared emissivity for some natural surfaces from experimental measurements. ***Applied Optics, 38***, 3931-3936

Sobrino, J.A., Jiménez-Muñoz, J.C., Balick, L., Gillespie, A.R., Sabol, D.A., & Gustafson, W.T. (2007). Accuracy of ASTER level-2 thermal-infrared standard products of an agricultural area in Spain. ***Remote Sensing of Environment, 106***, 146-153

Sobrino, J.A., Jiménez-Muñoz, J.C., El-Kharraz, J., Gómez, M., Romaguera, M., & Sòria, G. (2004a). Single-channel and two-channel methods for land surface temperature retrieval from DAIS data and its application to the Barrax site. ***International Journal of Remote Sensing, 25***, 215-230

Sobrino, J.A., Jiménez-Muñoz, J.C., & Paolini, L. (2004b). Land surface temperature retrieval from LANDSAT TM 5. ***Remote Sensing of Environment, 90***, 434-440

Sobrino, J.A., Jiménez-Muñoz, J.C., Sòria, G., Romaguera, M., & Guanter, L. (2008). Land surface emissivity retrieval from different VNIR and TIR sensors. ***IEEE Transactions on Geoscience and Remote Sensing, 46***, 316-327

Sobrino, J.A., Jimenez-Munoz, J.C., Verhoef, W., & Bendikov, T.A. (2005). Canopy directional emissivity: Comparison between models. ***Remote Sensing of Environment, 99***, 304-314

Sobrino, J.A., Kharraz, J.E., & Li, Z.-L. (2003). Surface temperature and water vapor retrieval from MODIS data. ***International Journal of Remote Sensing, 24***, 5161-5182

Sobrino, J.A., Li, Z.-L., Marc P. Stoll, & Becker, F. (1994). Improvements in the split-window technique for land surface temperature determination ***IEEE Transactions on Geoscience and Remote Sensing, 32***, 243-253

Sobrino, J.A., Raissouni, N., & Li, Z.-L (2001). A comparative study of land surface emissivity retrieval from NOAA data. ***Remote Sensing of Environment, 75***, 256-266

Sobrino, J.A., & Romaguera, M. (2004). Land surface temperature retrieval from MSG1-SEVIRI data. ***Remote Sensing of Environment, 92***, 247-254

Sobrino, J.A., Caselles, C., & Coll, C. (1993). Theoretical split-window algorithms for determining the actual surface temperature. ***IL NUOVO CIMENTO, 16C***, 219-236

Song, X., & Zhao, Y. (2007). Study on component temperatures inversion using satellite remotely sensed data. ***International Journal of Remote Sensing, 28***, 2567-2579

Su, Z. (2002). The Surface Energy Balance System (SEBS) for estimation of turbulent heat fluxes. ***Hydrology and Earth System Sciences, 16***, 85-99

Sun, D., & Pinker, R.T. (2003). Estimation of land surface temperature from a Geostationary Operational Environmental Satellite (GOES-8). ***Journal of Geophysical Research, 108***, 4326

Sun, D., & Pinker, R.T. (2007). Retrieval of surface temperature from the MSG-SEVIRI observations: Part I. Methodology. ***International Journal of Remote Sensing, 28***, 5255-5272

Tang, B., Bi, Y., Li, Z.-L., & Xia, J. (2008). Generalized split-window algorithm for estimate of land surface temperature from Chinese geostationary FengYun meteorological satellite (FY-2C) data. ***Sensors, 8***, 933-951

Tang, R., Li, Z.-L, & Tang, B. (2010). An application of the Ts-VI triangle method with enhanced edges determination for evapotranspiration estimation from MODIS data in arid and semi-arid regions: Implementation and validation. ***Remote Sensing of Environment, 114***, 540-551

Tonooka, H. (2001). An atmospheric correction algorithm for thermal infrared multispectral data over land—A water-vapor scaling method. ***IEEE Transactions on Geoscience and Remote Sensing, 39***, 682-692

Tonooka, H. (2005). Accurate atmospheric correction of ASTER thermal infrared imagery using the WVS method. ***IEEE Transactions on Geoscience and Remote Sensing, 43***, 2778-2792

Townshend, J.R.G., Justice, C.O., Skole, D., Malingreau, J.P., Cihlar, J., Teillet, P., Sadowski, F., & Ruttenberg, S. (1994). The 1 km resolution global data set: needs of the International Geosphere Biosphere Programme. ***International Journal of Remote Sensing, 15***, 3417-3441

Trigo, I.F., Peres, L.F., DaCamara, C.C., & Freitas, S.C. (2008). Thermal land surface emissivity retrieved from SEVIRI/Meteosat. ***IEEE Transactions on Geoscience and Remote Sensing, 46***, 307-315

Valor, E., & Caselles, V. (1996). Mapping land surface emissivity from NDVI: Application to European, African, and South American areas. ***Remote Sensing of Environment, 57***, 167-184

Van Leeuwen, T.T., Frank, A.J., Jin, Y., Smyth, P., Goulden, M.L., van der Werf, G.R., & Randerson, J.T. (2011). Optimal use of land surface temperature data to detect changes in tropical forest cover. ***Journal of Geophysical Research, 116***, G02002

Verhoef, W. (1984). Light scattering by leaf layers with application to canopy reflectance modeling:The Sail model. ***Remote Sensing of Environment, 16***, 125-141

Verhoef, W. (1989). Theory of radiative transfer models applied in optical remote sensing of vegetation canopies. ***Ph.D. dissertation, Wageningen Agricultural University, Wageningen, Netherlands***

Verhoef, W., Jia, L., Xiao, Q., & Su, Z. (2007). Unified optical-thermal four-stream radiative transfer theory for homogeneous vegetation canopies. ***IEEE Transactions on Geoscience and Remote Sensing, 45***, 1808-1822

Wan, Z. (1999). MODIS Land-Surface Temperature Algorithm Theoretical Basis Document (LST ATBD), Version 3.3. ***Greenbelt MD, USA: NASA/GSFC***, 1-77

Wan, Z. (2008). New refinements and validation of the MODIS land-surface temperature/emissivity products. ***Remote Sensing of Environment, 112***, 59-74

Wan, Z., & Dozier, J. (1996). A generalized split-window agorithm for retrieving land-surface temperature from space. ***IEEE Transactions on Geoscience and Remote Sensing, 34***, 892-905

Wan, Z., & Li, Z.-L (1997). A physics-based algorithm for retrieving land-surface emissivity and temperature from EOS/MODIS data. ***IEEE Transactions on Geoscience and Remote Sensing, 35***, 980-996

Wan, Z., Zhang, Y., Zhang, Q., & LI, Z.-L. (2004). Quality assessment and validation of the MODIS global land surface temperature. ***International Journal of Remote Sensing, 25***, 261-274

Wan, Z., Zhang, Y., Zhang, Q., & Li, Z.-L (2002). Validation of the land-surface temperature products retrieved from Terra Moderate Resolution Imaging Spectroradiometer data. ***Remote Sensing of Environment, 83***, 163-180

Wang, J., Anderson, G.P., Revercomb, H.E., & Knuteson, R.O. (1996). Validation of FASCOD3 and MODTRAN3: Comparison of model calculations with ground-based and airborne interferometer observations under clear-sky conditions. ***Applied Optics, 35***, 6028-6040

Wang, K., & Liang, S. (2009). Evaluation of ASTER and MODIS land surface temperature and emissivity products using long-term surface longwave radiation observations at SURFRAD sites. ***Remote Sensing of Environment, 113***, 1556-1565

Wang, K., Wan, Z., Wang, P., Sparrow, M., Liu, J., & Haginoya, S. (2007). Evaluation and improvement of the MODIS land surface temperature/emissivity products using ground-based measurements at a semi-desert site on the western Tibetan Plateau. ***International Journal of Remote Sensing, 28***, 2549-2565

Wang, N. (2011). Simultaneous retrieval of land surface temperature, emissivity and atmospheric profiles from hyperspectral thermal infrared data ***Doctoral Thesis, Institute of Geographic Sciences and Natural Resources Research, CAS, China***

Wang, W. (2009). Estimation of component temperatures of vegetative canopy with VIS/NIR and TIR multiple-angular data through inversion of vegetative canopy radiative transfer model. ***Doctoral Thesis, University of Strasbourg, France***

Wanner, W., Li, X., & Strahler, A. (1995). On the derivation of kernels for kernel-driven models of bidirectional reflectance. ***Journal of Geophysical Research, 100***, 21077

Watson, K. (1992). Two-temperature method for measuring emissivity. ***Remote Sensing of Environment, 42***, 117-121

Xu, X., Chen, L., & Zhuang, J. (2001). Genetic inverse algorithm for retrieval of component temperature of mixed pixel by multi-angle thermal infrared remote sensing data. ***Science in China (Series D), 44***, 363-372

Yan, G., Jiang, L., Wang, J., Chen, L., & Li, X. (2003). Thermal bi-directional gap probability model for row crop canopies and validation. ***Science in China (Series D), 46***, 1241-1249

Yan, G., Ren, H., Hu, R., Yan, K., & Zhang, W. (2012). A portable muti-angle observation system. ***IEEE International Geoscience and Remote Sensing Symposium, IGARSS 2012, Munich, Geomany***, 6916-6919

Yoriko, S., Tsuneo, M., Shuichi, R., & Akira, H. (2003). Temperature and emissivity separation for multi-band radiometer and validation ASTER TES algorithm. ***Journal of Remote Sensing Society of Japan, 23***, 364-375

Yu, T., Gu, X., Tian, G., Legrand, M., Baret, F., Hanocq, J.-F., Bosseno, R., & Zhang, Y. (2004). Modeling directional brightness temperature over a maize canopy in row structure. ***IEEE Transactions on Geoscience and Remote Sensing, 42***, 2290-2304

Yu, Y., Privette, J.L., & Pinheiro, A.C. (2008). Evaluation of split-window land surface temperature algorithms for generating climate data records. ***IEEE Transactions on Geoscience and Remote Sensing, 46***, 179-192

Zhan, W., Chen, Y., Zhou, J., & Li, J. (2011). An algorithm for separating soil and vegetation temperatures with sensors featuring a single thermal channel. ***IEEE Transactions on Geoscience and Remote Sensing, 49***, 1796-1809

Zhou, L., Dickinson, R.E., Ogawa, K., Tian, Y., Jin, M., Schmugge, T., & Tvetsinskaya, E. (2003). Relations between albedos and emissivities from MODIS and ASTER data over north African desert. ***Geophysical Research Letters, 30***, 2026, doi:2010.1029/2003GL018069

List of publications

[1] **Huazhong Ren**, Guangjian Yan, Rongyuan Liu, Françoise Nerry and Zhao-Liang Li. (2013). Impact of sensor footprint on measurement of directional brightness temperature of row crop canopies. ***Remote Sensing of Environment, 134***, 135-151.

[2] **Huazhong Ren,** Shunlin Liang, Guangjian Yan, and Jie Cheng.(2013). Empirical algorithms to map global broadband emissivities over vegetated surfaces. ***IEEE Transactions on Geoscience and Remote Sensing, 51***, 2619-2631.

[3] **Huazhong Ren**, Guangjian Yan, Rongyuan Liu, Ronghai Hu, Tianxing Wang, and Xihan Mu. (2013). Spectral recalibration for in-flight broadband sensor using man-made ground targets. ***IEEE Transactions on Geoscience and Remote Sensing, 51***, 4316-4329.

[4] **Huazhong Ren**, Guangjian Yan, Ling Chen, and Zhao-Liang Li. (2011). Angular effect of MODIS emissivity products and its application to split-window algorithm. ***ISPRS Journal of Photogrammetry and Remote Sensing, 66***, 498-507.

[5] Zhao-Liang Li, Bo-Hui Tang, Hua Wu, **Huazhong Ren**, Guangjian Yan, Zhengming Wan, Isabel F. Trigo, and José A. Sobrino. (2013). Satellite-derived land surface temperature: Current status and perspectives. ***Remote Sensing of Environment, 131***, 14-37.

[6] Ling Chen, Guangjian Yan, Tianxing Wang, **Huazhong Ren**, Josep Calbó, Jing Zhao, and Richard McKenzie. (2012). Estimation of surface shortwave radiation components under all sky conditions: Modeling and sensitivity analysis. ***Remote Sensing of Environment, 123***, 457-469.

[7] Tianxing Wang, Guangjian Yan, **Huazhong Ren**, and Xihan Mu. (2010). Improved methods for spectral calibration of on-orbit imaging spectrometers. ***IEEE Transactions on Geoscience and Remote Sensing, 48***, 3924-3931.

[8] Guangjian Yan, **Huazhong Ren**, Ronghai Hu, Kai Yan, and Wuming Zhang. (2012). A portable muti-angle observation system. in the proceeding of ***IEEE International Geoscience and Remote Sensing Symposium(IGARSS),*** pp.6916-6919, Munich, Germany.